Influence of tropical instability waves on climate variability in the eastern tropical Pacific

Lisa Maillard

Université Fédérale
Toulouse Midi-Pyrénées

THÈSE

En vue de l'obtention du

DOCTORAT DE L'UNIVERSITÉ DE TOULOUSE

Délivré par : *l'Université Toulouse 3 Paul Sabatier (UT3 Paul Sabatier)*

Présentée et soutenue le *30/11/2022* **par :**

Lisa MAILLARD

Influence des ondes tropicales d'instabilité sur la variabilité climatique du Pacifique tropical Est

---

JURY

Matthieu LENGAIGNE	Directeur de recherche (IRD)	Rapporteur
Pierrick PENVEN	Directeur de recherche (IRD)	Rapporteur
Xavier CAPET	Directeur de recherche (CNRS)	Examinateur
Patrick MARCHESIELLO	Directeur de recherche (IRD)	Examinateur
Claire MENESGUEN	Chargée de recherche (IFREMER)	Examinatrice
Julien BOUCHAREL	Chargé de recherche (IRD)	Directeur de thèse
Lionel RENAULT	Chargé de recherche (IRD)	Co-directeur de thèse

---

École doctorale et spécialité :
SDU2E : Océan, Atmosphère, Climat
Unité de Recherche :
LEGOS (UMR 5566)
Directeur(s) de Thèse :
Julien BOUCHAREL et *Lionel RENAULT*
Rapporteurs :
Matthieu LENGAIGNE et *Pierrick PENVEN*

Résumé — Les tropiques sont des régions d'intense variabilité climatique impliquant une large gamme d'échelles temporelles. Dans le Pacifique tropical, l'Oscillation Australe - El Niño (ENSO) est le principal moteur de la variabilité interannuelle. En modulant la thermodynamique océanique et la circulation atmosphérique, ENSO peut avoir de désastreux impacts écologiques et socio-économiques. Il est donc primordial de pouvoir prévoir cet évènement à l'avance, et d'améliorer la fiabilité de ses projections dans notre climat futur. Pour ce faire, il est nécessaire de comprendre ses interactions avec les processus océaniques et atmosphériques de fine échelle. Dans l'océan Pacifique tropical Est, les ondes tropicales d'instabilité (TIWs) sont la principale source de variabilité mésoéchelle et intrasaisonnière. Ces ondes, de ∼1000 km de longueur d'onde et de période de ∼40 jours, se propagent vers l'Ouest le long de l'équateur, advectant et mélangeant chaleur, quantité de mouvement, salinité et traceurs biologiques, et modulant la variabilité climatique du Pacifique tropical.
L'objectif de cette thèse est d'améliorer notre compréhension des interactions qui relient TIWs et variabilité tropicale. Pour ce faire, une méthodologie supprimant subtilement les TIWs des simulations numériques océaniques est développée et implémentée dans le modèle océanique CROCO. Cette méthodologie repose sur le rappel des courants méridiens de surface vers une climatologie prescrite. Bien qu'ayant un potentiel impact sur les ondes de Rossby, cette méthodologie donne des résultats satisfaisants. En comparant ces expériences à des simulations de contrôle dans lesquelles les TIWs se propagent librement, nous pouvons évaluer et quantifier l'impact des TIWs sur l'état moyen et la variabilité du Pacifique tropical. Cette méthodologie est appliquée sur un modèle océanique forcé au 1/12°, et dans un modèle couplé océan (1/14°) – atmosphère (1/4°), utilisant CROCO comme composante océanique, WRF comme composante atmosphérique et OASIS comme coupleur.
L'analyse de ces simulations révèle les effets directs et indirects qu'ont les TIWs sur de plus grandes et longues échelles spatiales et temporelles du Pacifique tropical. Premièrement, les TIWs modifient la répartition de la température équatoriale de surface via (1) un réchauffement non linéaire direct de 0.34°C mois^{-1} et (2) un refroidissement indirect de -0.10°C mois^{-1} lié à l'affaiblissement et à l'approfondissement du sous-courant équatorial (EUC) en présence de TIWs. Deuxièmement, en raison de leur synchronisation avec le cycle saisonnier, les TIWs rétroagissent sur le cycle saisonnier des principales composantes thermodynamiques du bassin. L'amplitude saisonnière de la température équatoriale de surface est réduite de 0.4°C en raison du réchauffement induit par les TIWs en été et en automne boréaux. Les TIWs modulent également le cycle saisonnier de l'EUC, stabilisant et affaiblissant le courant tout au long de l'année, et empêchant sa ré-intensification probablement irréaliste en automne boréal, obtenue par certains modèles basse résolution. Troisièmement, une étude préliminaire du cycle ENSO de 2015-2018 pointe une modulation complexe de l'amplitude et de la durée de La Niña par les TIWs. Cette modulation semble résulter de l'augmentation de l'advection non linéaire de chaleur et du mélange vertical par les TIWs. Les TIWs semblent également moduler les rétroactions qui déterminent le cycle de vie des événements ENSO.
Dans cette thèse, les interactions entre les TIWs et la variabilité climatique à plus grande échelle sont étudiées. La méthodologie et les résultats qui en découlent peuvent servir à

l'amélioration des paramétrisations des TIWs dans les modèles climatiques globaux de basse résolution.

Mots clefs : *Ondes Tropicales d'Instabilité; Variabilité Climatique; Pacifique Tropical Est; Oscillation Australe – El Niño; Cycle Saisonnier; Modélisation Régionale Couplée Océan-Atmosphère; Intéractions d'échelles Temporelles*

Abstract — Tropics are regions of strong air-sea coupling, in which disturbances of the apparent steady state lead to intense oceanic and atmospheric responses, resulting in a strong climate variability over a wide range of time scales. In the tropical Pacific, the El Niño – Southern Oscillation (ENSO) is the main driver of the interannual variability. By modulating the ocean thermodynamics and atmospheric circulation, ENSO can have disastrous ecological and socio-economical impacts. It is therefore of the utmost importance to forecast ENSO events well in advance, and improve the reliability of its projections in our future climate. One way to improve our understanding of ENSO dynamics is to assess its interactions with fine and short scale processes in the ocean and atmosphere. In the eastern tropical Pacific Ocean, Tropical Instability Waves (TIWs) are the main source of mesoscale and intraseasonal variability. These long waves characterized by a wavelength of ∼1000 km and time scales of ∼40 days propagate westward along the equator, advecting and mixing heat, momentum, salinity, and biological tracers. As such, they are a source of non-linearity that affects the tropical spatio-temporal variability.

The purpose of this thesis is to provide a better picture of the interactions between the transient mesoscale activity associated with TIWs, and larger scale climate variability in the eastern tropical Pacific. To do so, a methodology to subtly remove TIWs in oceanic numerical simulations is developed and implemented in the CROCO model. This methodology, which relies on the online nudging of meridional surface currents toward a prescribed climatology, is thoroughly validated. Limitations are discussed, in particular regarding its potential impact on Rossby waves. Nevertheless, the methodology gives satisfying results while barely impacting other processes. Comparing these experiments to similar control simulations in which TIWs freely develop makes it possible to evaluate and quantify the impact of TIWs on the eastern tropical Pacific mean state and variability. This methodology is applied on an $1/12^\circ$ ocean-only forced model, and in a $1/14^\circ$ ocean – $1/4^\circ$ atmosphere coupled model, using CROCO as the oceanic component, WRF as the atmospheric component and OASIS as the coupler.

The analysis of these simulations reveals the existence of direct and indirect effects of TIWs on larger spatial scales and longer time scales of the eastern tropical Pacific. First, TIWs modify the mean near-surface equatorial temperature through (1) a direct nonlinear dynamical heating at a rate of 0.34°C month^{-1} and (2) an indirect cooling effect of -0.10°C month^{-1} linked to the weakening and deepening of the equatorial undercurrent (EUC) in presence of TIWs. Second, due to their phase locking with the seasonal cycle, TIWs feed back onto the seasonal cycle of the main thermodynamic components of the basin. The seasonal amplitude of the near-surface equatorial temperature is decreased by 0.4°C, due to the TIW-induced warming of equatorial waters in boreal summer and fall. TIWs also modulate the EUC seasonal cycle by stabilizing and weakening the current year-round, preventing what appears to be an unrealistic re-intensification found in boreal fall in some non-eddy resolving models. Third, a preliminary study based on the 2015-2018 ENSO case study tends to show a complex TIW-induced modulation of La Niña amplitude and duration arising from a combination of increased nonlinear dynamical heating and mixing. TIWs also seem to modulate the typical ENSO feedbacks which determine the life cycle of ENSO events.

In this thesis, the interactions between TIWs and larger scale climate variability are studied, and the methodology and results that have emerged could serve as a basis for improving parameterizations of non-resolved TIW effects in low-resolution global climate models.

Keywords: *Tropical Instability Waves; Climate Variability; Eastern Tropical Pacific; El Niño – Southern Oscillation; Seasonal Cycle; Regional Coupled Ocean-Atmosphere Modeling; Time scale Interactions*

Remerciements

Après un peu plus de trois ans de travail, ma thèse touche à sa fin. Repenser à ces trois années, c'est repenser à une multitude de souvenirs. Certes, il y aura beaucoup de souvenirs de covid, de confinements, de couvre-feux, de masques, de tests, de cas contact, de laboratoire fermé. Mais ce que je retiendrai avant tout, ce sont tous ces moments de joie, de rires, de fêtes, de concerts, de danse, de chant, de vélo, de grimpe, de randonnée, de bivouac. Et au milieu de tout cela, beaucoup de travail sur les cyclones ... Oh pardon, sur les TIWs [tiouises]. Ces souvenirs n'auraient pu exister sans les nombreuses personnes qui m'ont entourées et à qui je tiens à exprimer toute ma gratitude.

Pour ouvrir le bal des remerciements, je tiens à saluer mes deux formidables directeurs de thèse, Julien Boucharel et Lionel Renault. Merci de m'avoir soutenue tout au long de ces trois années, d'avoir géré avec patience mon stress et mes doutes, d'avoir toujours été disponibles, de m'avoir pourrie-gâtée en disques durs et autre matériel informatique, et de m'avoir permis de faire cette incroyable mission à Hawai'i. Du Mai Tai de Waikiki, au club de la zone industrielle, en passant par le ping-pong chez des inconnus... Merci de m'avoir fait découvrir les recoins les plus undergrounds de l'archipel et surtout merci à vous deux d'avoir rendu cette thèse possible.

Je tiens à remercier Julien Jouanno, Sébastien Masson et Swen Jullien pour leurs précieux conseils lors des comités de thèse. Sébastien, merci infiniment de m'avoir parlé de cette offre de thèse. Swen, merci pour toutes ces discussions au téléphone ou autour d'un verre. Merci également à Pierrick Penven et Matthieu Lengaigne pour leur lecture attentive de ce manuscrit, et merci à Patrick Marchesiello, Claire Menesguen, et Xavier Capet pour leur évaluation de mon travail de thèse et leurs retours constructifs. Un grand merci également à Rachid Benshila, qui m'a débloquée de nombreuses galères numériques. Je souhaite aussi remercier Fei-Fei Jin et Malte Stuecker qui m'ont accueillies à l'Université d'Hawai'i, et tous les collaborateurs et collaboratrices avec qui j'ai pu travailler de près ou de loin, j'espère pouvoir continuer à travailler avec vous dans le futur.

Je tiens également à remercier toute l'équipe de la Direction et du GESSEC, et en particulier Brigitte, Catherine et Agathe qui ont toujours été présentes, réactives et pleines de bons conseils. Merci à Frédéric Marin et Geneviève Soucail pour leur attention et soutien aux doctorants. Un grand merci à Caroline pour toute l'aide informatique qu'elle m'a apportée.

Les heures passées au LEGOS m'auraient paru bien longues sans toute l'équipe de doctorant·e·s, CDD et autres « précaires » du laboratoire. C'est pourquoi je tiens à dire un grand grand merci à mes co-bureaux préféré·e·s : Pierre et Gabriela, pour les discussions, les conseils, les rires, les pauses café/thé/chocolat. Merci d'avoir supporté mes bruits de grignotage à toute heure de la journée. Pierre, merci pour cette mémorable fin de thèse. Je remercie aussi Manon d'avoir été une cheffe de choeur hors pair, et de m'avoir fait découvrir la chorale malgré mes réticences. Merci à Adé, Lise, Audrey, Marion et Manon pour toutes les conversations et conseils. Un grand merci à toutes celles et tous ceux avec qui j'ai pu discuter et passer des

moments au LEGOS: Morgane, Antonin, Alexandra, Adrien, Alice, Arne, Elisa, Julia, Juliette, Marco, Benjamin, Marion B, Simon T, Simon B, Amélie, Quentin, Wassim, et la liste est encore longue.

Ces trois années à Toulouse ont été riches de nombreux moments entre ami·e·s. Merci à la team Adé, Pierre, Romain, Manon et Flo pour m'avoir initiée aux soirées jeux, aux fondues à 2000m, et surtout au Buzet à la bouteille. Quentin, merci d'avoir été mon acolyte et meilleur ami pendant la (quasi) totalité de cette thèse, d'avoir écouté mes interminables répétitions, mais surtout d'avoir partagé mille aventures, fous rires, papotages, soirées, confinements, vacances. Merci à Alex A. pour tous les bons moments passés ensembles. Merci à mes colocataires de la rue Mercadier, Lise, Doriane et Quentin, pour tous les souvenirs dans cet appartement. Je pense aussi très fort à la team grimpe de SiB qui m'a permis de faire des rencontres incroyables. Enfin, un grand merci à Alex pour sa patience et son amour, et pour toutes ces soirées à refaire le monde.

Bien sûr, je tiens à dire un grand grand merci à mes parents et à ma sœur de m'avoir toujours soutenue et encouragée dans la bienveillance, l'amour et la rigolade. Morgane, tu illumines ma vie. Merci également à mes tantes et ma grand-mère, qui ont suivi tant bien que mal cette soutenance de thèse. Je vous aime.

Et finalement, merci à vous, lecteur·rice, qui allez parcourir cette thèse. Bonne lecture !

Lisa

Contents

List of Figures

Acronyms

IPCC	*Intergovernmental Panel on Climate Change*
ITCZ	*Intertropical Convergence Zone*
CMIP	*Coupled Model Intercomparison Project*
CFB	*Current Feedback*
CEOF	*Complex Empirical Orthogonal Function*
CMIP	*Coupled Model Intercomparison Project*
CROCO	*Coastal and Regional Ocean Community Model*
CP El Niño	*Central Pacific El Niño*
EOF	*Empirical Orthogonal Function*
EP El Niño	*Eastern Pacific El Niño*
EUC	*Equatorial Undercurrent*
GCM	*Global Coupled Model*
KPP	*K-Profile Parameterization*
LH	*Latent Heat Flux*
NECC	*North Equatorial Countercurrent*
MLD	*Mixed Layer Depth*
MUSIC	*MUlti Scale Interactions in the PacifiC*
SEC	*South Equatorial Current*
SSH	*Sea Surface Height*
SST	*Sea Surface Temperature*
STD	*Standard Deviation*
SPCZ	*South Pacific Convergence Zone*
SW	*Shortwave radiation*
TFB	*Thermal Feedback*
TIW	*Tropical Instability Waves*

TIV	*Tropical Instability Vortices*
ENSO	*El Niño – Southern Oscillation*
WWBs	*Westerly Wind Bursts*
WFR	*Weather and Research Forecast Model*

General introduction

The Ocean is a major driver of the water, heat and carbon cycles. It contains 97% of the Earth's water, has a large heat capacity, and can absorb carbon dioxide through carbon dissolution. At the air-sea interface, the ocean exchanges water, heat, and gases with the atmosphere, which are redistributed horizontally and vertically through ocean circulation and mixing. As such, oceans are a key driver of the weather and climate system variability (Abram et al. (2019)).

In tropical oceans (30°S – 30°N), a tight coupling with the overlying atmosphere results in an apparent equilibrium state. In the tropical Pacific, several positive feedbacks maintain the oceanic state in an apparent equilibrium: easterly winds drive a zonal surface current that pushes warm water westward, lifting the thermocline in the east and producing a pressure gradient that generates an eastward equatorial undercurrent. The easterly winds also drive an equatorial upwelling in the east, known as the cold tongue, and the resulting zonal and meridional surface temperature gradients support the two main circulation cells in the atmosphere, the Walker and Hadley cells. Disturbances of this apparent steady state lead to intense oceanic and atmospheric responses, resulting in a strong climate variability over a wide range of time scales (Kessler (2006)).

The main driver of the tropical Pacific interannual variability is the El Niño – Southern Oscillation (ENSO). This climate phenomenon, which can be seen as a disturbance of the seasonal cycle, is a major and well-studied example of ocean-atmosphere coupling: stochastic disturbances of easterly winds can drive anomalous temperatures in the eastern Pacific, which result in the zonal displacement of the Walker circulation. The ecological and socio-economical impacts of ENSO can be disastrous, and are not limited to tropical areas. Therefore, it is of the utmost importance for populations to forecast ENSO events well in advance, and improve the reliability of ENSO projections in our future climate (Karamperidou et al. (2020)).

One way to improve our understanding of ENSO dynamics is to assess its interactions with fine and short scale processes in the ocean and atmosphere. In the tropical oceans, Tropical Instability Waves (TIWs) are the main source of mesoscale and intraseasonal variability. These long waves characterized by a wavelength of a thousand kilometers and time scales of ∼40 days propagate westward in the equatorial Pacific ocean, advecting and mixing heat, momentum, salinity, and biological tracers (Fig. 1). As such, they are a source of non-linearity that affects the tropical spatio-temporal variability (Willett et al. (2006)).

The purpose of this thesis is to provide a better picture of the interactions between the transient mesoscale activity associated with TIWs, and larger scale climate variability in the eastern tropical Pacific. In the First Chapter of this thesis, I give a detailed presentation of the main features of the tropical Pacific environment and its climate variability. In particular, I present the coupled ocean-atmosphere background state by describing the main oceanic and atmospheric circulations, the surface and subsurface ocean thermal distributions, and the feedbacks that contribute to maintaining this state

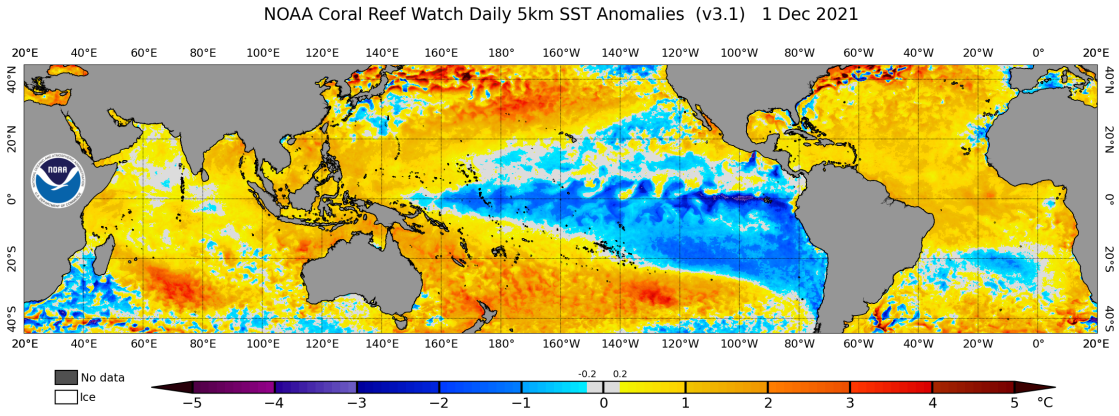

Figure 1: Tropical Instability Waves (TIWs) seen in the snapshots of anomaly of sea surface temperature (*i.e.,* departure from the long-term average) of December 1st 2021, from the NOAA Coral Reef Watch product. TIWs are these meandering of cold water observed at the surface of the equatorial Pacific ocean.
Les ondes tropicales d'instabilité (TIWs) visibles sur cette image de l'anomalie de température de surface (i.e., anomalie vis-à-vis de la moyenne à long terme), du 1er Décembre 2021, obtenue à partir du produit NOAA Coral Reef Watch. Les TIWs sont ces méandres d'eau froide que l'on distingue à la surface de l'océan Pacifique équatorial.

in an apparent equilibrium. I then describe the different time scales of variability around which this tropical Pacific background state can evolve, from interannual to intraseasonal. In particular, I present the ENSO phenomenon as the main source of interannual variability in the Pacific, then the seasonal variability of large scale thermodynamic components, and finally the intraseasonal variability with a special focus on TIWs. I also highlight the main sources of interactions occurring between these different temporal and spatial scales.

The Second Chapter discusses the oceanic and atmospheric models used in this thesis: the Coastal and Regional Ocean Community Model (CROCO), and the Weather Research and Forecast Model (WRF). I also explain in details the main methodology used throughout the manuscript, which consists in (i) subtly removing TIWs in different oceanic simulations of the eastern tropical Pacific, the so-called NOTIW-RUNs; and (ii) comparing these experiments to similar control simulations in which TIWs freely develop (TIW-RUN), which will make it possible to evaluate and quantify the impact of TIWs on the eastern tropical Pacific mean state and variability.

In the Third Chapter, the interactions between TIWs and the ocean background state are investigated using the methodology described in Chapter 2, in a forced ocean-only simulation of the eastern tropical Pacific spanning the period 1980 to 2019. In this work published in *Journal of Physical Oceanography* (Maillard et al. (2022a)), I identify, using a kinetic energy transfer diagnostic and a heat budget analysis, a direct (*i.e.,* induced directly by TIWs) and indirect (or rectified) TIW effect on the eastern tropical Pacific mean state. In particular, I show that while the direct effect of TIWs tends to warm the cold tongue through horizontal heat advection, the weakening of the equatorial undercurrent by TIWs leads to a rectified

cooling feedback on the cold tongue.

From the same set of forced ocean-only simulations, I then assess in Chapter Four the impacts of TIWs on the eastern tropical Pacific seasonal variability, which have been little documented so far despite the strong connection to large scale climate variability such as ENSO. Results show that TIWs induce a modulation of the seasonal amplitude of the upper temperature in the cold tongue region, by warming equatorial waters in boreal summer and fall. I have also highlighted a new pathway by which TIWs modulate the seasonal cycle of the equatorial undercurrent, stabilizing and weakening it throughout the year, thus preventing what appears to be an unrealistic re-intensification in boreal autumn, and found in some low resolution climate models. This work (Maillard et al. (2022b)) has been published in *Geophysical Research Letters*.

In my Last Chapter, I use coupled ocean-atmosphere simulations of the 2015 – 2018 ENSO cycle in the eastern tropical Pacific to assess the ENSO – TIWs interaction. This cycle is composed of one major warm phase (El Niño) and two successive cold phases (La Niña) of ENSO that are reproduced by the coupled simulations, yet with a weaker amplitude compared to observations. Understanding the origins of El Niño/La Niña asymmetry, and in particular the temporal asymmetry with the existence of multi-year La Niña events, is a very current issue. As I write this manuscript, the Pacific is indeed heading into its third consecutive year of La Niña. Since TIWs are more active during the cold phase of ENSO than during its warm phase, they may be involved in the asymmetry of ENSO events. Although my preliminary results tend to show significant differences in the impact of TIWs between the first and second La Niña, further work is needed to fully understand the intricacy of processes involved.

Introduction Générale

L'Océan est l'un des principaux moteurs des cycles de l'eau, de la chaleur et du carbone. Il contient 97% de l'eau présente sur la Terre, a une grande capacité thermique et peut absorber le dioxyde de carbone via la dissolution du carbone. À l'interface air-mer, l'Océan échange de l'eau, de la chaleur, et des gaz avec l'atmosphère, qui sont ensuite redistribués horizontalement et verticalement par la circulation et le mélange océaniques. Ainsi, les océans sont un acteur clef de la variabilité du système climatique (Abram et al. (2019)).

Dans les océans tropicaux (30°S – 30°N), un couplage étroit avec l'atmosphère conduit à un état d'apparent équilibre. Dans le Pacifique tropical, plusieurs rétroactions positives maintiennent l'Océan dans cet état d'apparent équilibre. Les vents d'est, ou Alizés, génèrent un courant zonal de surface qui pousse les eaux chaudes vers l'ouest, soulevant la thermocline à l'est et produisant un gradient de pression qui génère à son tour un sous-courant équatorial dirigé vers l'est. Les Alizés entraînent également une remontée des eaux équatoriales dans l'est du bassin, connue sous le nom de "cold tongue". Les gradients de température de surface zonaux et méridiens qui en résultent alimentent ainsi les deux principales cellules de circulation de l'atmosphère, les cellules de Walker et de Hadley. Les perturbations de cet état d'apparent équilibre entraînent d'intenses réponses océaniques et atmosphériques, ce qui se traduit par une forte variabilité climatique sur une large gamme d'échelles temporelles (Kessler (2006)).

Le principal moteur de la variabilité interannuelle du Pacifique tropical est l'Oscillation Australe – El Niño (ENSO). Ce phénomène climatique, pouvant être considéré comme une perturbation du cycle saisonnier, est un exemple remarquable et bien connu du couplage entre l'océan et l'atmosphère: les perturbations stochastiques des vents d'est peuvent générer des anomalies de températures dans l'est du Pacifique, qui se traduisent par un déplacement zonal de la circulation de Walker. Les impacts écologiques et socio-économiques d'ENSO peuvent être désastreux, et ne se limitent pas aux zones tropicales. Il est donc de la plus haute importance pour les populations impactées de pouvoir prévoir les événements ENSO à l'avance, et d'améliorer la fiabilité de ses projections dans notre climat futur (Karamperidou et al. (2020)).

L'une des façons d'améliorer notre compréhension de la dynamique d'ENSO est d'évaluer ses interactions avec les processus de fine et courte échelle dans l'océan et l'atmosphère. Dans les océans tropicaux, les ondes tropicales d'instabilité (TIWs) sont la principale source de variabilité de mésoéchelle et intrasaisonnière. Ces longues ondes, caractérisées par une longueur d'onde de mille kilomètres et des échelles de temps de l'ordre de 40 jours, se propagent vers l'ouest dans l'océan Pacifique équatorial, advectant et mélangeant chaleur, quantité de mouvement, salinité et traceurs biologiques (Fig. 1). Ainsi, elles sont une source de non-linéarité qui affecte la variabilité spatio-temporelle tropicale (Willett et al. (2006)).

L'objectif de cette thèse est d'améliorer notre compréhension des interactions entre l'activité mésoéchelle associée aux TIWs, et la variabilité climatique à plus grande échelle, du Pacifique tropical Est. Dans le Premier Chapitre de cette

thèse, les principales caractéristiques du Pacifique tropical et de sa variabilité climatique sont présentées. L'état moyen du couplage océan-atmosphère est d'abord décrit, puis les différentes échelles temporelles de variabilité autour desquelles cet état moyen peut évoluer, de l'interannuel à l'intrasaisonnier. En particulier, le phénomène ENSO est présenté comme principale source de variabilité interannuelle dans le Pacifique, puis la variabilité saisonnière des composantes thermodynamiques de grande échelle, et enfin la variabilité intrasaisonnière en se focalisant sur les TIWs. Les principales interactions entre ces différentes échelles temporelles et spatiales sont également mises en avant.

Le Second Chapitre présente les modèles océaniques et atmosphériques utilisés dans cette thèse : le Coastal and Regional Ocean Community Model (CROCO), et le Weather Research and Forecast Model (WRF). La principale méthodologie utilisée tout au long du manuscrit est ensuite expliquée, qui consiste à (i) supprimer les TIWs dans différentes simulations océaniques du Pacifique tropical oriental, appelées NOTIW-RUN; et (ii) comparer ces expériences à des simulations de contrôle dans lesquelles les TIWs se propagent librement (TIW-RUN). Cela permettra ainsi d'évaluer et de quantifier l'impact des TIWs sur l'état moyen et la variabilité du Pacifique tropical Est.

Dans le Troisième Chapitre, les interactions entre les TIWs et l'état moyen océanique sont étudiées via la méthodologie décrite dans le Chapitre 2 et implémentée dans une simulation océanique forcée du Pacifique tropical Est, simulant la période 1980 – 2019. Dans ce travail, publié dans *Journal of Physical Oceanography* (Maillard et al. (2022a)), j'identifie à l'aide d'un diagnostic de transfert d'énergie cinétique et d'une analyse du bilan thermique, un effet direct (induit directement par les TIWs) et indirect (ou rectifié) des TIWs sur l'état moyen du Pacifique tropical Est. Si l'effet direct des TIWs tend à réchauffer la "cold tongue" par advection horizontale de chaleur, l'affaiblissement du sous-courant équatorial par les TIWs conduit à un refroidissement de la "cold tongue".

À partir du même ensemble de simulations océaniques forcées, le Chapitre Quatre évalue les impacts des TIWs sur la variabilité saisonnière du Pacifique tropical Est. Ces impacts ont en effet été peu documentés jusqu'à présent malgré leur lien étroit avec la variabilité climatique à grande échelle telle qu'ENSO. Les résultats montrent que les TIWs induisent une modulation de l'amplitude saisonnière de la température de surface de la "cold tongue", en réchauffant ces eaux en été et en automne boréaux. Ce travail a également permis de mettre en évidence la modulation du cycle saisonnier du sous-courant équatorial par les TIWs, stabilisant et affaiblissant le courant tout au long de l'année, empêchant ainsi ce qui semble être une ré-intensification en automne boréal irréaliste, et que l'on retrouve dans certains modèles climatiques de basse résolution. Ce travail (Maillard et al. (2022b)) a été publié dans la revue *Geophysical Research Letters*.

Dans mon Dernier Chapitre, j'utilise des simulations couplées océan-atmosphère du cycle ENSO 2015 – 2018 dans le Pacifique tropical Est afin d'évaluer l'interaction ENSO – TIWs. Ce cycle est composé d'une phase chaude (El Niño) et de deux phases froides successives (La Niña) d'ENSO. Les simulations couplées parviennent à reproduire ce cycle, avec toute fois une amplitude plus faible que les observations. Comprendre les origines de l'asymétrie El Niño/La Niña, et en particulier l'asymétrie temporelle avec en particulier l'existence d'événements

pluriannuels La Niña, est une question très actuelle. Au moment où j'écris ce manuscrit, le Pacifique se dirige en effet vers sa troisième année consécutive de La Niña. Puisque les TIWs sont plus actives pendant la phase froide d'ENSO que pendant sa phase chaude, il est possible qu'elles soient impliquées dans l'asymétrie des événements ENSO. Les premiers résultats présentés dans ce chapitre mettent en avant des différences dans l'impact qu'ont les TIWs sur la première et la deuxième année La Niña simulée. Des travaux supplémentaires sont nécessaires pour comprendre pleinement la complexité des processus impliqués.

Chapter 1

Background

Contents

1.1 Background state in the tropical Pacific

As we approach the equator, the Coriolis parameter $f = 2\Omega sin\theta$ (Ω the Earth angular rotation speed, θ the latitude) decreases in amplitude, vanishes at the equator and changes sign in the other hemisphere. This singularity of the Coriolis parameter near the equator determines the dynamic and the wave propagation in this oceanic region. An other important factor driving the equatorial ocean circulation is the wind forcing. The vertical structure of the tropical waters is characterized by a surface layer of sun-warmed water overlying a deep layer of cold water. This strong vertical ocean stratification allows a high coupling between air and sea, with in particular an upper oceanic circulation driven by low-level winds. These two specificities of equatorial regions (low Coriolis parameter, and strong air-sea coupling) shape the equatorial ocean background, generating currents shears, tracers and pressure gradients, which plays an important role on the ocean dynamics.

In the Pacific, the atmospheric Hadley circulation (Fig. 1.1a, red arrows) delivers the heat accumulated in the tropics to higher latitudes through a closed loop: warm sea surface temperature (SST) in the western equatorial Pacific and on each side of the equator creates zonal and meridional gradients of SST, which in turn generate convergence of winds and ascending motions of warm and moist air that reaches the tropopause and forms cumulus. This zone of convergence and ascending motions is known as the Intertropical Convergence Zone (ITCZ) in the northern hemisphere, and the South Pacific Convergence Zone (SPCZ) in the southern hemisphere (*e.g.,* Hastenrath and Lamb (1978)). The air in altitude then moves polewards, being deflected to the east by the increasing Coriolis parameter. As it becomes cooler and dryer, the air sinks and returns to the tropics with a westward deviation. These north/south-easterlies that close the Hadley circulation are commonly called trade winds (Fig. 1.1a, thin grey arrows). South-easterly trade winds from the southern hemisphere cross the equator and reach the northern hemisphere, where they meet north-easterly trade winds in the ITCZ.

By generating an Ekman transport, these south-easterly trade winds move the surface water to their right (*i.e.,* northward) in the northern hemisphere and to their left (*i.e.,* southward) in the southern hemisphere, which causes surface water to diverge at the equator (Fig. 1.1b). This divergence induces an upwelling, *i.e.,* a vertical transport of cold water from the deeper layers to the surface (Cromwell (1953)). This cold upwelled water is known as the *cold tongue*, and expands from the Ecuadorian coast to the center of the Pacific Ocean. On the other side of the basin, the western pacific *warm pool* is an area of warm surface waters that are pushed westward by trade winds. This zonal SST gradient is overlaid by a zonal atmospheric circulation called the Walker circulation (Fig. 1.1a, black arrows, Bjerknes (1969)). It shares its ascending western branch with that of the Hadley circulation, above the warm pool. Its subsiding branch is located above the cold tongue, in the eastern part of the basin. The loop is closed by the trade winds blowing toward the west at the ocean surface along the equator.

The warm water being pushed by winds to the west, and the cold water being upwelled to the east, shapes the zonal slope of both the sea level and the thermocline depth, with higher

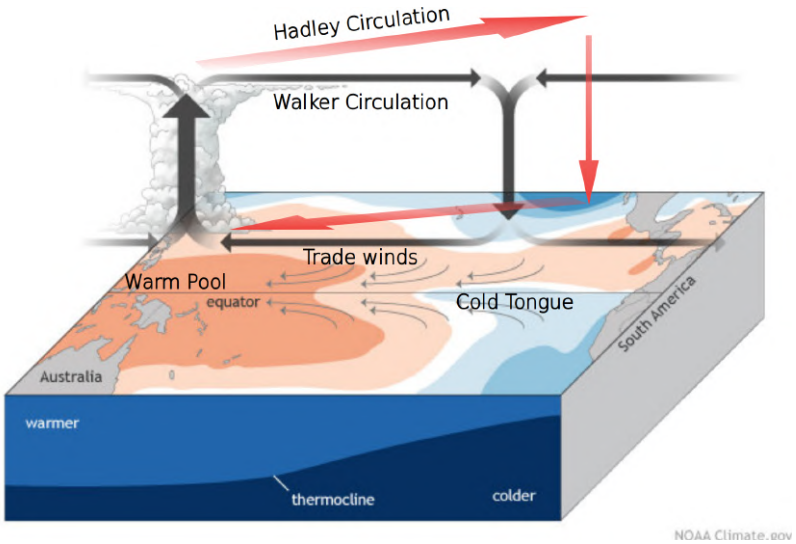

(a) Mean ocean temperature and atmospheric circulation

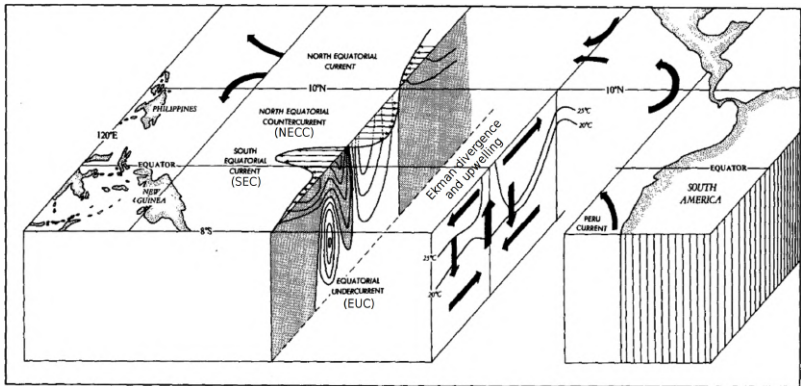

(b) Mean ocean circulation

Figure 1.1: Schematics of average atmospheric and oceanic conditions across the tropical Pacific Ocean. (a) Ocean temperature and atmospheric circulation. Reprinted and adapted from Climate.gov schematic by Emily Eng, https://www.climate.gov/news-features/blogs/enso (b) Horizontal and vertical circulation. Grey shaded areas show westward currents (SEC) and white shaded areas show eastward currents (EUC, NECC). Reprinted and adapted from Philander et al. (1987)

sea levels and deeper thermocline in the west than in the east.

Several positive feedbacks help maintaining this mean state. First, the shallow thermocline to the east allows surface waters to be efficiently cooled by vertical mixing and advection, while the deep thermocline to the west isolates the surface warm waters from the cold deeper water. Second, the zonal SST gradient leads to a surface pressure gradient with low pressure above the warm pool due to convection, and high pressure above the cold tongue due to subsidence of air. This pressure gradient reinforces the trade winds, which in turn reinforce the temperature gradient through a positive feedback loop.

The trade winds are also driving the zonal westward South Equatorial Current (SEC, Cromwell and Bennett (1959); Wyrtki (1965)), which splits into two lobes on either side of the equator (Fig. 1.1b). Below, at the equator, the geostrophic Equatorial Undercurrent (EUC, Cromwell et al. (1954)) flows eastward in the thermocline, driven by the zonal ocean pressure gradient generated by trade winds. To the north of the equator, the North Equatorial Counter Current (NECC, Cromwell and Bennett (1959); Wyrtki (1965)) flows eastward between 5° and 10°N. For a review of the eastern equatorial Pacific circulation, the reader is invited to refer to Kessler (2006).

This background equatorial state is not a steady state as it is modulated at decadal, interannual, seasonal and intraseasonal time scales, which can interact with each other creating a rather broad continuous spectrum of variability. As a reminder, the scheme on Figure 1.2 lists all time and space scales of ocean variability as well as their potential overlaps. Some of these time scales will be discussed in further details in this manuscript, with a particular focus on the mesoscale variability associated with tropical instability waves (≈ 1000 km, 1-month) and their interactions with the seasonal and interannual variability.

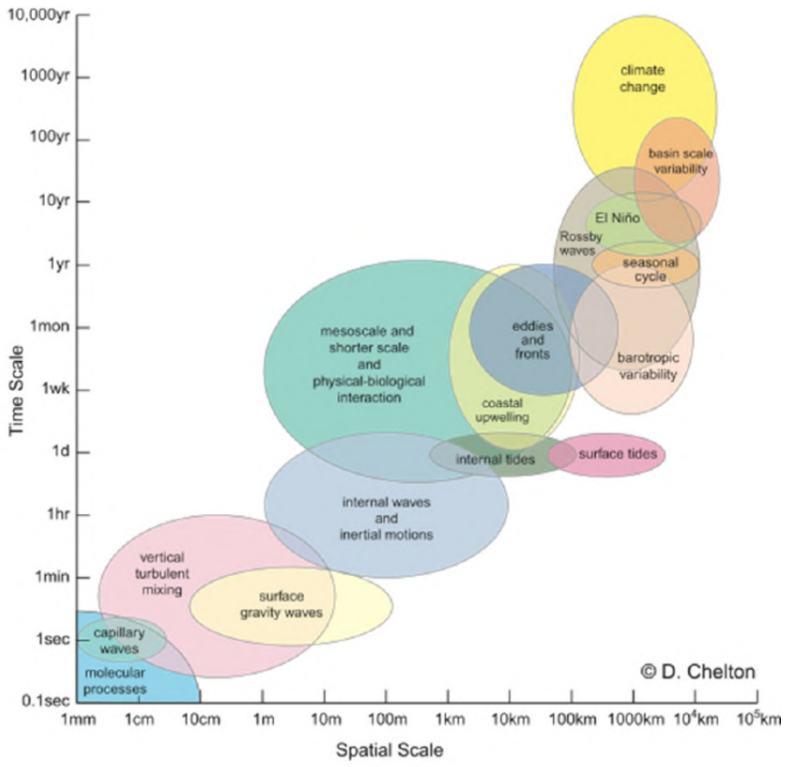

Figure 1.2: Time and space scales of ocean variability. Copyright by D. Chelton

1.2 Interannual variability: The El Niño - Southern Oscillation (ENSO)

1.2.1 The life cycle of ENSO

Growth and development

The El Niño - Southern Oscillation (ENSO) is the main driver of interannual variability in the tropical Pacific basin. Chaotic – but state-dependent – westerly wind bursts (WWBs) events can generate a relaxation of the western warm pool, *i.e.,* the warm pool is less constrained to the west due to weaker trade winds, which causes warm water to move eastward and leads to anomalous warming in the central-to-eastern Pacific (Fig. 1.3a, see also *e.g.,* Menkes et al. (2014)). This anomalous zonal SST gradient modifies the zonal pressure gradient, intensifying the anomalous westerly winds, which further strengthen the temperature gradient. This positive feedback loop in air-sea interactions is known as the *Bjerknes feedback* (Bjerknes (1966)), and plays a central role in the onset of ENSO (Fig. 1.3b). As trade winds weaken, the warm pool is more relaxed and the thermocline slope flatten. Warm water is then advected eastward by anomalous currents, the equatorial upwelling weaken and eastern upwelled waters are warmer due to the deeper thermocline. These reinforcements of the initial anomalous warming due to oceanic feedbacks are called respectively the *zonal advective feedback*, *the upwelling feedback* and the *thermocline feedback* and can lead to an El Niño event, the warm phase of ENSO (Fig. 1.3c). La Niña events, the cold phase of ENSO, starts with an intensification of trade winds generating an increased zonal temperature gradient. The feedbacks mentioned above are also involved in the development of La Niña, in the opposite way (although with some differences, see next section) to El Niño (Fig. 1.3, left panels). For a review of explanation of each feedback, the reader is invited to refer to the review of the ENSO glossary in Box 1 of Timmermann et al. (2018). Overall, the average states of El Niño and La Niña conditions are shown in Figure 1.4. The El Niño state consists in weaker than usual trade winds, warmer SST in the central-to-eastern Pacific and decline of the cold tongue, a deeper thermocline in the east and an eastward displacement of the convective branch of the Walker cell. Conversely, the La Niña state consists in reinforced trade winds, cooler SST in the cold tongue, a shallower thermocline in the east and an westward displacement of the convective branch of the Walker circulation (Philander (1990)).

Decay: oscillator theories

All of the above ocean and atmosphere feedbacks are positive, *i.e.,* they reinforce the initial anomaly. Delayed negative feedbacks are needed to stop this infinite growth, begin the decay of the anomalous state and promote the transition towards the opposite state. Since the 1970s, scientists have built several conceptual models in order to identify possible origins of these negative feedbacks. Oscillator models are based on the principle of an oscillation between (i) fast positive ocean and atmosphere feedbacks favoring the growth of ENSO, and

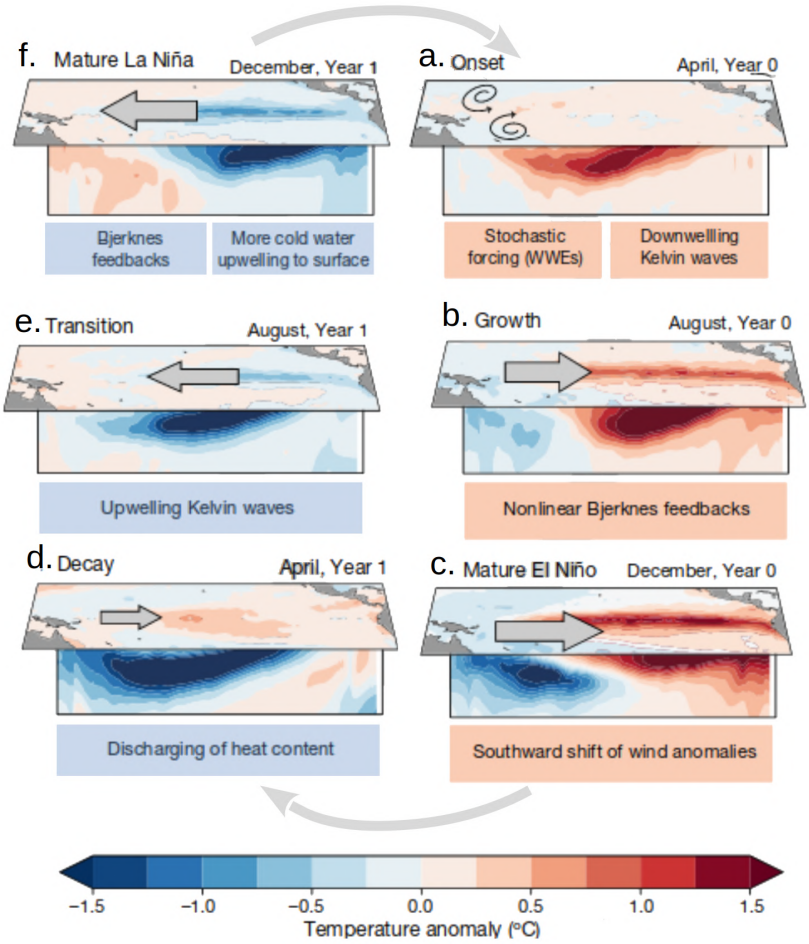

Figure 1.3: Composites temperatures of the life cycle of a typical El Niño, followed by a typical La Niña. Reprinted and adapted from Timmermann et al. (2018). See paper for more details on the composites

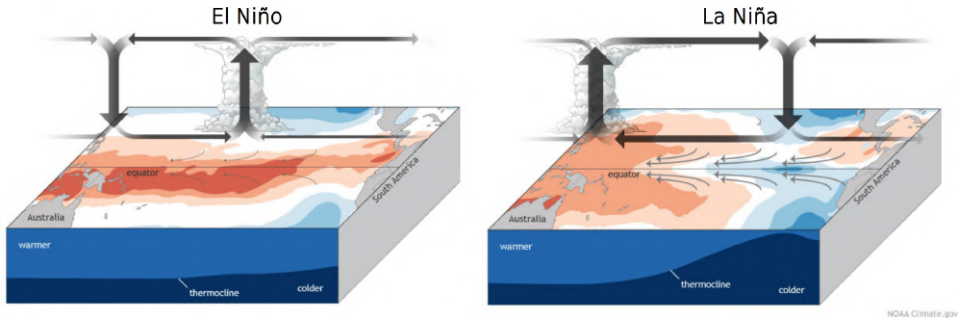

Figure 1.4: Schematic of ENSO conditions. Reprinted and adapted from Climate.gov schematic by Emily Eng, https://www.climate.gov/news-features/blogs/enso

(ii) slow negative ocean feedbacks leading to its decay. For example, the *delayed oscillator* model (Suarez and Schopf (1988); Battisti and Hirst (1989)) invokes the negative feedbacks

of a delayed Rossby wave reflected in a Kelvin wave. In the widely used *recharge oscillator* model (Jin (1997a)), it is the slow meridional discharge or recharge of heat content that follows the Sverdrup dynamics and control the growth and transition of ENSO events.

These simple oscillator theories allow understanding and modeling the main ENSO life cycle. They are described in detail in the review of Jin et al. (2020) and in the first chapter of the thesis of Carreric (2019). French speakers are also invited to refer to the thesis of Boucharel (2010).

1.2.2 Diversity of ENSO events

ENSO events are very diverse in terms of their temporal evolution, spatial pattern and amplitude. Moreover, El Niño and La Niña events do not mirror each other, as El Niño events tend to be stronger and shorter than La Niña events. These irregularities and asymmetries arise from non-linearities in the ocean and atmosphere feedbacks, which are not accounted for in the simple oscillator theories.

Spatial diversity

ENSO has been shown to exhibit diverse spatial patterns. Two different flavors of El Niño events have been noticed (Kao and Yu (2009)): (i) The Central Pacific (CP, Fig. 1.5b) El Niño, characterized by warm anomalous SST located in the center of the basin and a strong contribution of the zonal advective feedback and (ii) the Eastern Pacific (EP, Fig. 1.5a) El Niño, characterized by warm anomalous SST reaching the far eastern part of the basin and with a stronger contribution of the thermocline feedback. The EP El Niño events are more likely to become extreme events, such as the famous 1997/98 El Niño or the more recent 2015/16 El Niño, although the latter has recently been categorized as a mixed event (Paek et al. (2017)). EP events are also more likely to transition to La Niña events, owing to the strong meridional discharge of equatorial heat content that terminates EP events. While El Niño events have different spatial patterns, La Niña events have a unique pattern that lies between those of EP and CP events.

Temporal diversity

Aside from the spatial diversity, another notable fact about the evolution of the ENSO cycle is its irregularity that even prompted researchers to question its oscillatory nature and consider it potentially as a succession of random events (Kessler (2002)). Regardless, ENSO obvious non-periodicity/irregularity (Fig. 1.6) still remains an open question given the short temporal record of observed events. Two theories attempt to explain this temporal irregularity, either through deterministic large scale non-linear dynamics or through external stochastic forcing, the latter leading to less predictability than the former.

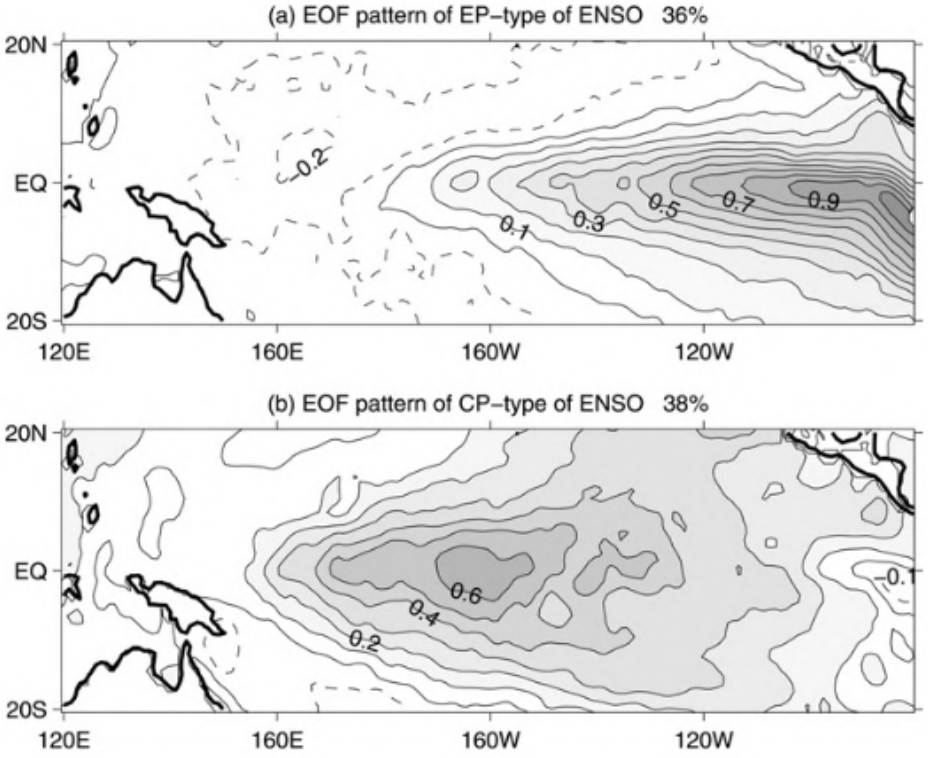

Figure 1.5: Leading Empirical Orthogonal Function (EOF) patterns from an EOF-regression analysis of SST interannual anomalies from HadISST observations, corresponding to (a) eastern Pacific El Niño events and (b) central Pacific El Niño events. Reprinted from Kao and Yu (2009).

Supporters of the non-linear deterministic theories rely in part on the ENSO phase locking with the seasonal cycle. ENSO events usually start to grow in boreal spring, are the most intense in winter, and decay in spring of the following year (Timmermann et al. (2018)). This synchronization with the seasonal cycle is due to the seasonally modulated strength of air-sea coupling and a seasonal meridional shift in wind anomaly. The phase locking drives a non-linear interaction between ENSO and the seasonal cycle, generating new time scales of variability and explaining ENSO irregularity (Jin et al. (1994)), which has important repercussions for improving predictability of events and their impacts. More details on the non-linear interaction between ENSO and the seasonal cycle will be given in section 1.3.

El Niño/ La Niña asymmetries

Another irregularity of ENSO is expressed in the strong asymmetry between El Niño and La Niña events, with differences not only observed in the spatial patterns but also in the amplitude and temporal evolution between the warm and cold phases of ENSO.

While many El Niño events have reached strong warm anomalous states and some of them

can be defined as very strong – or extreme – El Niño (Nino 3.4 index > 2°C), only few La Niña events can be defined as strong events, and no extreme La Niña has ever been recorded (Fig. 1.6). This asymmetry is due to non-linearities.
These non-linearities arise from oceanic processes, such as the non-linear dynamical heating (NDH, advection of anomalous temperature by anomalous currents, An and Jin (2004)), the non-linear oceanic wave response (Im et al. (2015)), an asymmetrical biophysical feedback impacting solar penetration in the mixed layer (Marzeion et al. (2005)), and the asymmetrical Tropical Instability Waves (TIWs) activity (An (2008)). TIWs are transient features that propagate in the upper equatorial Pacific. Their properties, mechanisms of formation, and interaction with the ENSO cycle will be described in more details in the next section.
The non-linearities also arise from atmospheric processes such as the asymmetrical response of wind stress to SST anomalies (Kang and Kug (2002)), a non-linear shortwave feedback (Im et al. (2015)), and higher frequency of WWBs during El Niño (Levine and Jin (2010)).

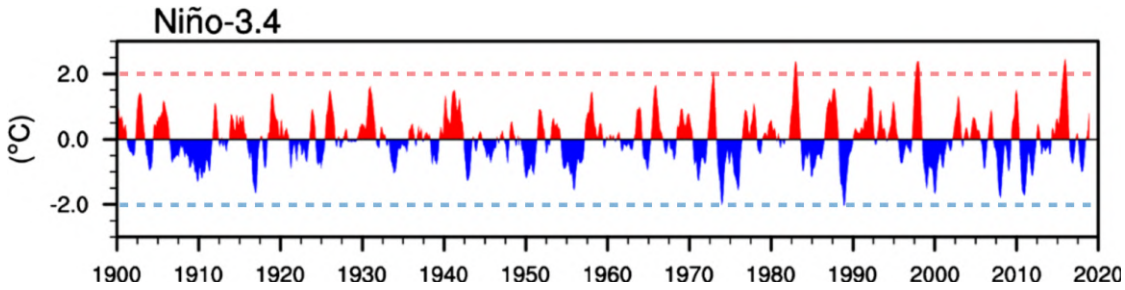

Figure 1.6: The Niño 3.4 index (3-month running mean of SST anomaly averaged in 5°S – 5°N, 170°– 120°W) shows El Niño (red) and La Niña (blue) events. Reprinted and adapted from Okumura (2019)

In addition to this amplitude asymmetry, La Niña differs from El Niño in terms of temporal evolution. While a sharp phase transition occurs after the decay of two over three of moderate-to-strong El Niño (Fig. 1.7, left panel), half of La Niña events are followed by at least a second year of La Niña (Fig. 1.7 1.7, right panel). This "double-dip", or multiyear La Niña mostly occurs after a strong El Niño event with an important meridional discharge of heat that favors La Niña (Wu et al. (2019)). Other non-linear atmospheric and oceanic processes are also at play, such as asymmetric strength of surface wind anomalies and asymmetric negative thermocline feedbacks (DiNezio and Deser (2014)).

Ocean and atmosphere non-linear processes are therefore key to understanding the irregularity, diversity and asymmetry of ENSO. For an up-to-date review of these non-linear processes responsible for ENSO diversity, the reader is invited to refer to the reviews of Okumura (2019) and An et al. (2020).

1.2.3 ENSO impacts and Societal challenges

On February 2022, the working group II of the Intergovernmental Panel on Climate Change (IPCC) published the second study of the Sixth Assessment Report, untitled *Impact, Adap-*

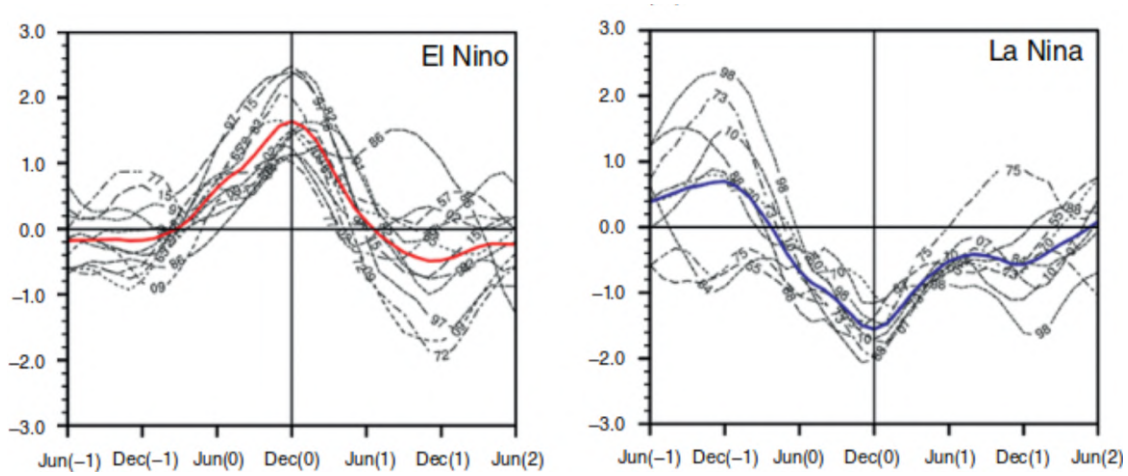

Figure 1.7: Time series of the Niño 3.4 index (3-month running mean and linear trend removed) for (left) El Niño events and (right) La Niña events during 1948–2018 (from HadISST dataset, Rayner (2003)). Only events with Niño 3.4 index higher than 1 standard deviation in December(0) are selected for El Niño, and lower than -1 for La Niña. Composites are shown in tick colored curves. Reprinted from An et al. (2020).

tation and Vulnerability (Pörtner et al. (2022)). One of the objectives of this report is to give an up-to-date picture of the impacts of climate change on our planet and human lives. Combined with the other two studies of Group I and Group III that focus on the scientific basis of climate change and on the mitigation measures, the full report is based on peer-reviewed literature and is an urgent call to action for our policymakers.

In this second study of the Sixth Assessment Report, the ecological and socio-economical impacts of ENSO are extensively described. Among ecological impacts, we can mention floods and landslides, droughts, tropical cyclone, marine heatwaves, coral bleaching. Among human impacts, ENSO drives diseases (cholera in Africa, Dengue in Venezuela), and can lead to children underweight, poverty, monetary losses, and overall impacts on populations' well-being.

Given the severe repercussions of this large scale phenomenon on our societies, it is necessary to understand the life cycle of ENSO, from its onset to its decline and transition, in order to provide accurate predictions with sufficient lead time and warning. Moreover, in a context of increasing greenhouse gases, understanding how ENSO events will evolve in our changing climate is essential for risk management. The study of working group I (Arias et al. (2021)), and several new peer-reviewed studies published since then, focus on these topics. As summarized in Cai et al. (2020),

> There appear to be three factors that are key toward an understanding of how ENSO would change under global warming: (1) the tropical Pacific mean-state change; (2) changes in non-linear processes that interact with the mean climate; and (3) climate model fidelity.

In particular, the mean state change under greenhouse forcing leads to a robust increase in the variability of ENSO driven precipitation, but no consensus was reached on the tendency of ENSO driven SST. Indeed, most climate models of the 5th and 6th phase of the Coupled Model Intercomparison Project (CMIP5 and 6) that are used for climate projection still show (i) strong mean-state biases, such as a cold tongue bias in the eastern Pacific and an underestimated precipitation rate in the western Pacific (Li et al. (2015)), and (ii) unrealistic ENSO dynamics (Bayr et al. (2018); Hayashi et al. (2020)). However, in a recent study, Cai et al. (2018) found that the most accurate CMIP5 models that include non-linear forcing and are able to simulate distinct EP and CP El Niño events converge toward an increased frequency of extreme events. But it should be noted that error compensations among key ENSO dynamical mechanisms result in many climate models simulating seemingly correct ENSO amplitude for the wrong reasons. Incorrect seasonality of ENSO feedbacks also plays a role in poor simulations of the observed tendency of ENSO events to peak in boreal winter. These errors are consequential, because strong interactions between interannual and seasonal time scales can cause rapid climate fluctuations (*i.e.,* the combination mode at near annual time scale, see section 1.3).

Therefore, it is of the utmost importance for forecasting and risk management to fully understand the processes driving the life cycle of ENSO, its interaction with other time scales such as the seasonal and intraseasonal, and the process behind its non-linearity, using both observations and high resolution regional modeling in order to parameterize the unresolved processes in lower resolution global climate models.

1.3 Seasonal variability

The seasonal cycle

In the tropics, the sun "crosses" the equator twice a year, at the end of the austral summer in March and of the boreal summer in September. In addition, the southeasterly trade winds are weak in boreal spring when the ITCZ gets closer to the equator, and intensify in the second half of the year when the ITCZ migrates polewards (Philander et al. (1987)). As a result, the spectra of equatorial oceanic features often display annual and semiannual harmonics (Fiedler and Talley (2006)). The relative importance of these two harmonics depends on the combination of the external forcing (*i.e.,* heat fluxes and winds), and other oceanic processes such as vertical mixing and upwelling. For instance, SST in the eastern Pacific cold tongue has a strong unique annual cycle (Horel (1982)), with coldest waters in boreal autumn. This arises from combinations of several factors such as a stronger wind-driven upwelling (Fig.. 1.8a; Kessler (2006)); an increased strato-cumulus formation over the cold SST which damps solar radiation and further reduces the SST (Mitchell and Wallace (1992); Klein and Hartmann (1993); and an increased mixing above the EUC core that cools the SST (Fig. 1.8b; Moum et al. (2013).

At the equator, the SEC exhibits strong seasonal variations, with a semiannual component

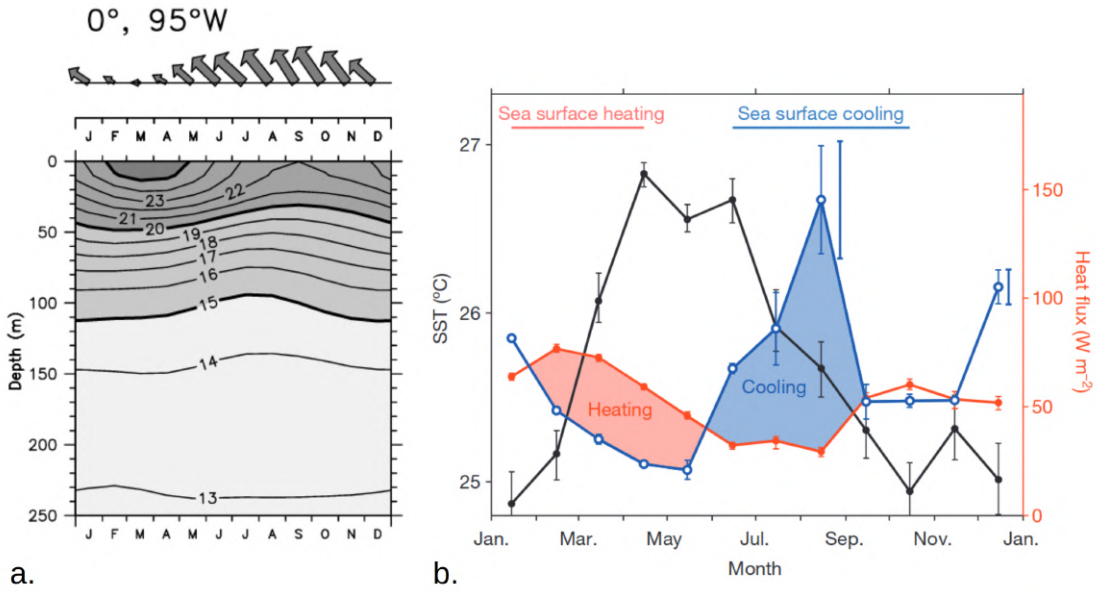

Figure 1.8: Seasonal cycle of temperature in the eastern equatorial Pacific. The intensification of wind stress (a, upper panel; scatterometer winds) in boreal fall favors the equatorial upwelling, bringing deep cold to the surface (b, lower panel; temperatures from XBT measurements). Reprinted from Kessler (2006). The balance between sea surface heating by solar radiative heat fluxes (b, red) and sea surface cooling through turbulent heat flux (b, blue, from multi-year turbulence measurements) drives the SST tendency in the cold tongue. Reprinted from Moum et al. (2013).

in the central-to-western Pacific (Fig. 1.9a,b). In boreal spring, when trade winds are the weakest, the EUC intensifies and shoals in the far eastern Pacific. This seasonal shoaling then propagates to the west (Fig. 1.9c) like most equatorial Pacific surface features (*e.g.,* SST, zonal currents, winds) but opposed to the eastward thermocline depth seasonal propagation. These seasonal westward and eastward propagation of currents and thermal structures are driven by a combination of wind-forced equatorial Kelvin and long Rossby waves (*e.g.,* Yu and McPhaden (1999), Yang et al. (2022)).

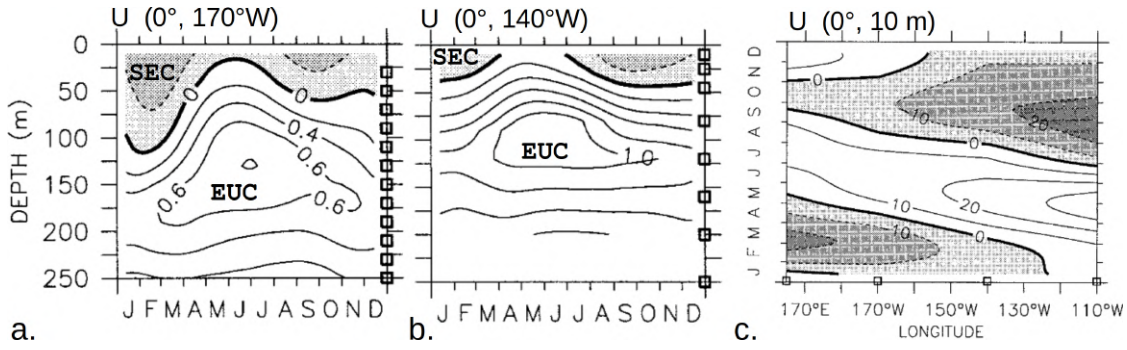

Figure 1.9: Seasonal cycle of zonal currents in the equatorial Pacific, from observations of the Tropical Atmosphere Ocean array. Reprinted and adapted from Yu and McPhaden (1999).

ENSO and the seasonal cycle

As briefly mentioned in Section 1.2.2, ENSO and the seasonal cycle are closely interacting. ENSO events usually start in spring, grow in boreal autumn, reach their maximum intensity in December and decay in the following spring (Fig. 1.10, bars). This cycle is associated with a high variance in SST anomaly at the peak of the event, as depicted by the red curve in Figure 1.10. This phase locking is thought to arise from either (1) a non-linear interaction between the seasonal cycle and the frequency of ENSO (Jin et al. (1994); Tziperman et al. (1994)), or (2) a seasonal modulation of the growth rate of ENSO (*e.g.,* Chen and Jin (2020)). Therefore, in both cases, it is clear that ENSO interacts with the seasonal cycle of the equatorial Pacific region. In the first case, the non-linear interaction gives rise to new time scales of variability of ENSO, explaining its irregularity. As originally detailed in Stuecker et al. (2013), a combination mode arises from this interaction: an ENSO cycle at a frequency of f_E year^{-1}, forced by an annual frequency of 1 year^{-1}, will dominantly responds at the near-annual frequencies $1-f_E$ and $1+f_E$ (Stuecker et al. (2013, 2015, 2017)). This interplay between time scales underscores the need to accurately represent the variability of each time scale in equatorial regions in order to understand ENSO dynamics, predict upcoming events, and project them onto future climates.

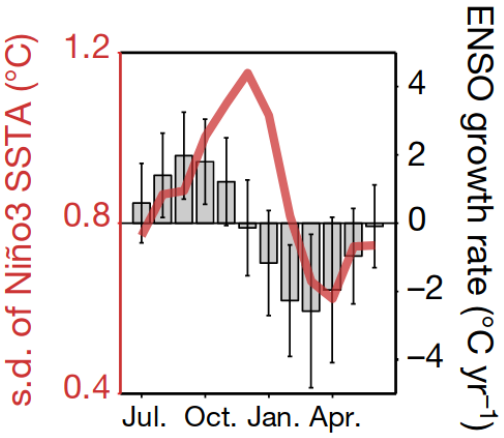

Figure 1.10: ENSO phase locking. Standard deviation of the NOAA Extended Reconstructed Sea Surface Temperature dataset v5 SST interannual anomalies averaged in the Niño 3 region (red), and ENSO growth rate (bars). Reprinted from Timmermann et al. (2018). See paper for more details.

1.4 Intraseasonal Variability and Transient Mesoscale Features

1.4.1 Rossby, Yanai and Kelvin waves

Tropical areas are the place of propagation of many equatorial waves, trapped in the equatorial waveguide induced by the variation of the Coriolis parameter strength around the equator (Fig. 1.11, see also Gill (1982)). To name a few, the eastward equatorial Kelvin waves, the westward equatorial planetary or Rossby waves, the mixed planetary-gravity or Yanai waves. All these waves have been shown to have important effects on the equatorial background from intraseasonal to interannual time scales. For instance, downwelling Kelvin waves are fast (phase speed of 2.7 m s^{-1}, Cravatte et al. (2003)), intraseasonal (period of 60-90 days)

eastward propagating waves that have no meridional velocity and are often generated by westerly wind bursts in the western Pacific. As described in previous sections, they can trigger a warm El Niño - Southern Oscillation (ENSO) event by deepening the thermocline in the eastern Pacific, counteracting the equatorial upwelling and resulting in an anomalously warm SST in that region. Equatorially trapped Rossby waves are slower (phase speed of ≈ 1 m s^{-1}, Gill (1982)) westward propagating waves, and are responsible for the decay of ENSO in the recharge oscillator model described previously.

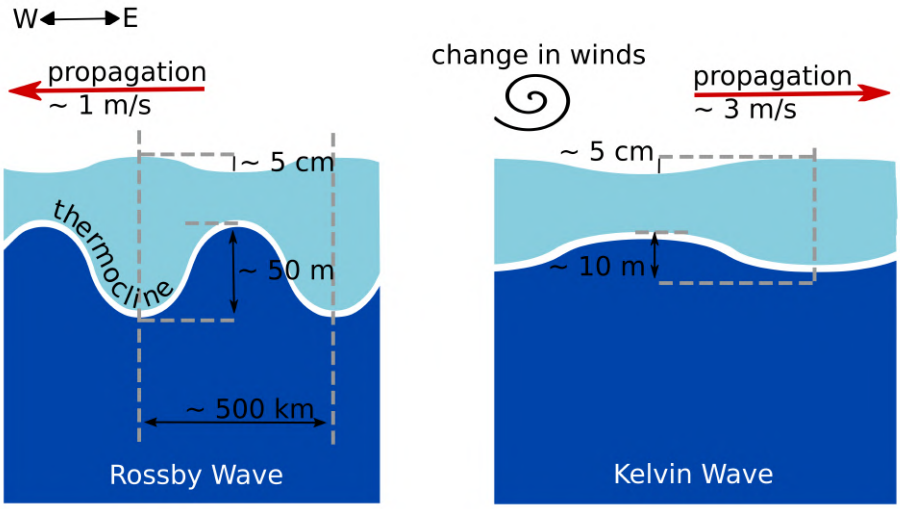

Figure 1.11: Schematics of the main properties of intraseasonal equatorial Kelvin and Rossby Waves.

1.4.2 Focus on Tropical Instability Waves

Along the equator, long meanders of the equatorial cold tongue front propagate westward, arising from instability processes in the Atlantic and Pacific Oceans. These Tropical Instability Waves (TIWs) were first noticed in the Atlantic Ocean in 1974 through current meter measurements showing oscillations of the SEC and EUC (Düing et al. (1975)). The following year, in the Pacific Ocean, infrared images from a geostationary satellite revealed similar long waves in the meandering of SST (Legeckis (1977)). Since these pioneering studies, several others have focused their research on TIWs, emphasizing that the interactions of these waves with the ocean and the atmosphere, from intraseasonal to interannual time scales and from submesoscale to basin scale, make them a key element of the climate system that must be properly understood.

Main properties

TIWs are intraseasonal westward propagating waves with averaged wavelengths of 1000-2000 km, periods of 15-40 days and phase speed 0.5 $m.s^{-1}$ (Qiao and Weisberg (1995); Contreras (2002)). Their relatively large spatial scale classifies them as mesoscale features, while their large Rossby number – the ratio of inertial forces to Coriolis force $Ro = U/fL$ with U and L the characteristic speed and length of the TIWs – in the vicinity of the equator makes them more similar to mid-latitude 1-km submesoscale features (Thomas et al. (2008); Holmes (2016)). Their temporal scale consists in two main peaks, at $\sim$ 17- and $\sim$ 33-days, rather than a continuous broad spectrum. These two modes have been shown to share characteristics with respectively mixed planetary-gravity Yanai waves and unstable first meridional mode of Rossby waves (Lyman et al. (2007); Wang et al. (2020)), and have differences in terms of location, pattern and impacts on the mean flow (*e.g.,* Liu et al. (2019b)). In particular, the 33-day TIWs are near 5°N and often evolve as anticyclonic eddies of $\sim$ 500-km of diameter, called Tropical Instability Vortices (TIVs, Flament et al. (1996); Kennan and Flament (2000)). In this study, we will focus on the full TIW flow field rather than on one specific TIW mode. TIWs are generated in the surface and subsurface layers (Liu et al. (2019a); Specht et al. (2021)), but can propagate downward and meridionally as barotropic Rossby (Farrar (2011); Lee et al. (2022)) and downward Yanai waves (Delpech et al. (2020)), generating intraseasonal variability down to 2000 meters (Tuchen et al. (2018)) which could potentially trigger the generation of deep jets in the Pacific Ocean.

Since the initial studies from Düing et al. (1975) and Legeckis (1977), TIWs have been observed through a variety of oceanic and atmospheric fields. Tracers measurements show transient westward-propagating meanders of the temperature front of the cold tongue, with cold edges and warm cusps (Fig. 1.12a). TIWs are also observed through oscillations of the sea surface salinity with salty edges and fresh cusps (Düing et al. (1975); Lee et al. (2012); Olivier et al. (2020)), as well as high and low Chlorophyll-A concentrated edges and cusps (Fig. 1.12b, Yoder et al. (1994)). At the ocean surface, the sea surface height also displays alternating high and lows (Miller et al. (1985); Périgaud (1990); Escobar-Franco et al. (2022a)), and the ocean currents turn in the clockwise direction in the anticyclonic TIVs (Kennan and Flament (2000)). All these features are translated to the west as the wave propagates in time. In the atmosphere, the amplitude and directions of low-level trade winds are modulated above TIW-induced SST and currents anomalies (Xie et al. (1998); Hashizume et al. (2001); Chelton et al. (2001)).

TIW growth and decay

TIWs draw their energy from the background state through two main energy conversion processes. The shear of zonal currents between the westward SEC and the eastward EUC and NECC generates a barotropic energy conversion and a Kelvin-Helmoltz conversion from the mean kinetic energy into eddy kinetic energy ($K_m K_e$). In total, this energy conversion is

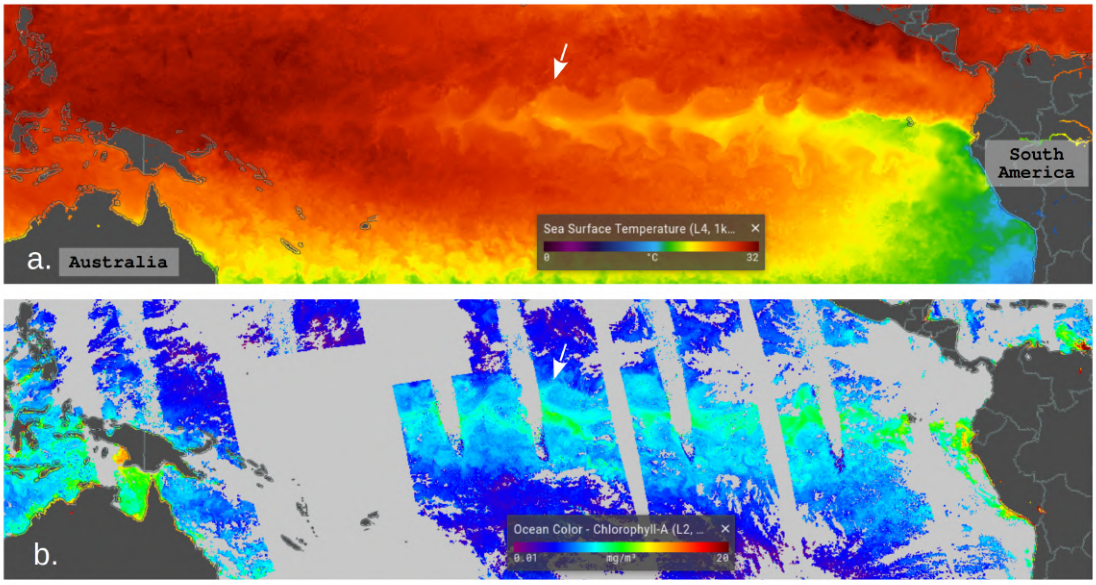

Figure 1.12: Observed fields of (a) SST and (b) Chlorophyll-A in the Pacific Ocean, August 31st, 2016. Maps obtained from the State Of The Ocean interactive web-based tool. The SST is obtained from the daily 1km Multiscale Ultrahigh Resolution Level 4 dataset that combined several instruments (radiometers and in situ observations). The Chlorophyll-A is obtained from the daily 1km chlorophyll-A measurements from MODIS on the Aqua Satellite

$$K_m K_e = -\overline{u'u'}\partial_x\overline{u_m} - \overline{v'v'}\partial_y\overline{v_m} - \overline{u'v'}(\partial_y\overline{u_m} + \partial_x\overline{v_m}) \quad (1.1)$$
$$- \overline{u'w'}\partial_z\overline{u_m} - \overline{v'w'}\partial_z\overline{v_m} \quad (1.2)$$

where (u, v, w) are the 3-dimensional ocean currents, $(\partial_x,\partial_y,\partial_z)$ are the 3-dimensional spatial partial derivatives, and each field is decomposed into a time-fluctuating x' and time-mean x_m part. Typically, for transient features like TIWs, the fluctuations are the perturbations from a 30-day running mean. The over-line $\overline{x}$ depicts the long time average.

In the above equation, the terms 1.1 correspond to horizontal barotropic conversion terms and 1.2 correspond to vertical Kelvin-Helmoltz conversion terms. At the equator, the dynamics is driven by zonal flows. Therefore, the term $\partial_y\overline{u_m}$ is large, making $-\overline{u'v'}\partial_y\overline{u_m}$ the dominant term of the $K_m K_e$ conversion (Qiao and Weisberg (1998)).

The second dominant source of eddy kinetic energy available for TIWs growth and development arises from a barotropic conversion which comes from the meridional gradient of ocean temperature that exists between the cold tongue and the warm off-equatorial waters. This temperature gradient is a reservoir of available potential energy, that can be converted in EKE when the temperature front is unstable (Masina et al. (1999)). This barotropic

conversion of eddy potential energy into EKE (P_eK_e) is

$$P_eK_e = -\frac{g}{\rho_0}\overline{w'\rho'} \tag{1.3}$$

where $g = 9.81$ m.s^{-1} is the gravitational acceleration constant, $\rho_0 = 1025$ kg.m^{-3} and ρ' is the perturbed density.

The relative contribution of each conversion term depends on the mean state, as detailed in the study of Xue et al. (2021b). Using observational and reanalysis products, they found that the generation of TIWs in May-June of 1998 was made possible by a balance between baroclinic and barotropic energy conversions, whereas it was largely dominated by a baroclinic conversion in May-June of 2016. This high baroclinic conversion in 2016 was due to a high anomalous meridional temperature gradient, in particular related to warm anomalies in the northeastern off-equatorial Pacific.

In addition to not having the same amplitude, each conversion term does not occur at the same location. While baroclinic conversion occurs primarily at the northern temperature front between 0°– 5°N (Fig. 1.13b), barotropic conversion is significant at the equator and near 5°N (Fig. 1.13c). In total, it gives rise to a TIW-induced EKE located between 5°S – 8°N (Fig. 1.13a).

Other processes also impact the EKE budget, such as the eddy wind work :

$$F_eK_e = \frac{1}{\rho_0}(\tau'_x u' + \tau'_y v') \tag{1.4}$$

where τ_x and τ_y are the zonal and meridional surface wind stress. As described in Baturin and Niiler (1997), this conversion term is negative which indicates a sink of EKE for TIWs, and a source of energy for the atmosphere.

Using an ocean model at 1/4° horizontal resolution, Holmes and Thomas (2016) established a complete EKE budget. They found that TIWs mainly gain energy from K_mK_e and P_eK_e conversions, and lose energy from frictional processes and the radiation of waves, in particular related to the meridional propagation of Rossby waves de-

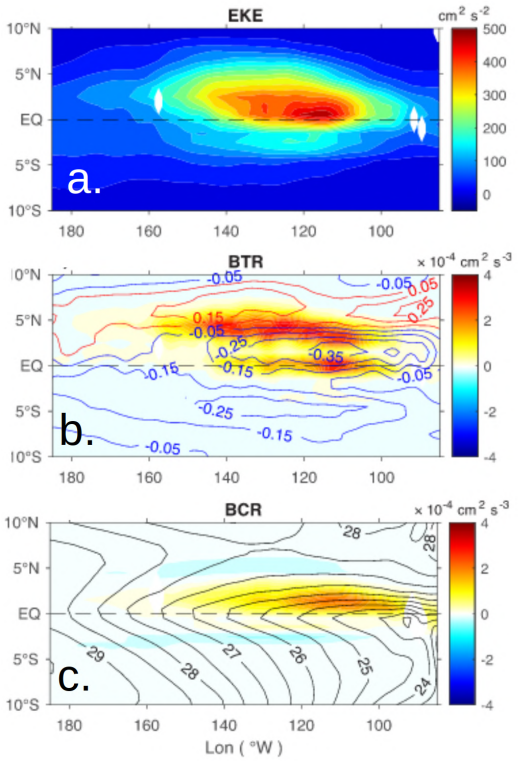

Figure 1.13: Observed mean (a) EKE, (b) barotropic conversion rate (shading) and zonal currents (contours), and (c) baroclinic conversion rates (shading) and SST (contours), over the period 1993–2018. Reprinted and adapted from Wang et al. (2020).

scribed in Farrar (2011) and Lee et al. (2022), and of the radiation of internal waves at the TIW fronts (Tanaka et al. (2015)).

Influence of TIWs on the eastern Pacific SST

A few years after the discovery of TIWs in the Pacific Ocean, Hansen and Paul (1984) used data from 20 drifting buoys to estimate the meridional eddy heat flux due to TIWs. They found an important near surface equatorward eddy heat transport equivalent to two thirds of the heat transport related to the equatorial Ekman divergence. Since then, several studies have focused on establishing the impact of TIWs on the cold tongue SST.

Using a forced ocean-only simulation of the tropical Pacific ocean from 1993 to 1996 at a horizontal resolution of $dx = 1°$ and $dy = 0.5°$ at the equator, Menkes et al. (2006) provided a complete 3-dimensional heat budget of the mixed layer in the eastern Pacific Ocean (2°S – 6°N, 160°– 90°W), separating the advective processes into the contribution by the mean flow and the contribution by TIWs. Their results highlighted the important contribution of TIWs to the horizontal advection of heat in the mixed layer, by driving a warming of 0.84°C.month^{-1} (Fig. 1.14b) that counteracts the horizontal cooling of -0.59 °C month^{-1} by mean currents (Fig.. 1.14a), and resulting in a total warming of 0.24 °C month^{-1} (Fig. 1.14c).

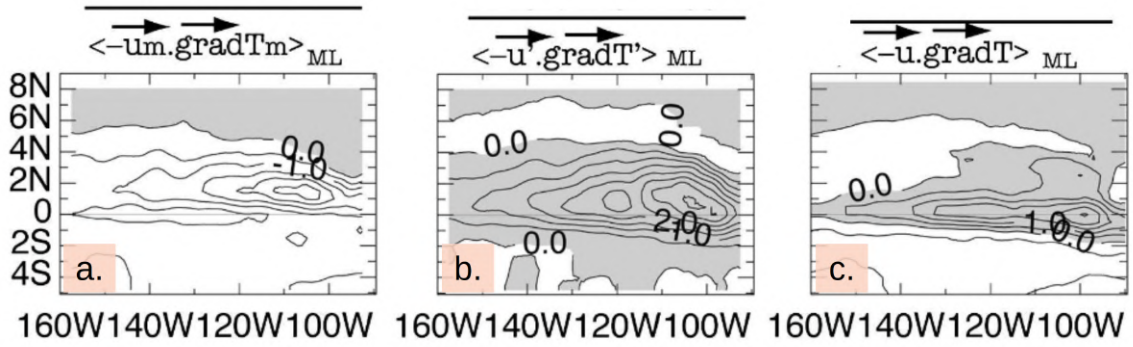

Figure 1.14: Modeled heat advection in the mixed layer between 1993 – 1996, by (a) the mean currents, (b) TIWs and (c) total. Contours are every 0.5 °C month^{-1}. Reprinted and adapted from Menkes et al. (2006)

Based on satellite and in situ observations of SST and currents from year 2002 to 2005, the study of Jochum et al. (2007a) confirmed the estimate of the TIW-induced horizontal heat advection of previous modelling studies. In particular, they emphasized the large contribution of the TIW-induced meridional heat advection in the cold tongue, and the (previously neglected) important contribution of the TIW-induced zonal heat advection, representing 25% of the heating at 0°N, 110°W. Jochum and Murtugudde (2006) suggested that this TIW-induced heating of the cold tongue was in fact a "TIW heat pump" that implies modulations of the air-sea heat fluxes, and vertical entrainment.

The modification of air-sea fluxes by TIWs can arise from different processes. TIWs can for instance modify the surface stress through the current feedback (CFB, *e.g.,* Renault et al. (2016b)) or the thermal feedback (TFB), corresponding to changes in wind stress induced respectively by anomalous currents, or by anomalous temperatures that destabilise the atmospheric boundary layer (*e.g.,* Seo et al. (2007a); Small et al. (2009)). TIWs can also modify the net ocean heat uptake by modulating the latent heat flux above anomalous warm and cool TIW-SST patches (Thum et al. (2002); Jochum and Murtugudde (2006)).

Several observational and modeling studies pointed out an enhancement of oceanic turbulent mixing by TIWs at the equator (Lien et al. (2008); Moum et al. (2009); Inoue et al. (2012); Holmes and Thomas (2015); Inoue et al. (2019)) and off-equator (Cherian et al. (2021)), that may be due to the enhancement of shear instability over the EUC core (Holmes and Thomas (2015)) and to the generation of internal waves at TIW fronts (Tanaka et al. (2015)) that could trigger turbulence. The mean integrated effect of this enhanced TIW-induced turbulent mixing on the SST is not yet understood, with for instance in situ measurements by Moum et al. (2009) indicating a 1-2 °C month^{-1} SST cooling, while the modeling study by Menkes et al. (2006) finds a 0.37 °C month^{-1} SST warming. To better delineate this effect, several modeling and observation projects are in preparation. For instance, a future project leaded by Dr. Ryan Holmes (University of Sydney) will aim at testing several mixing schemes in coupled regional ocean-atmosphere simulations to test TIW-induced mixing sensibility to the choice of turbulent mixing parameterization (personal communication). Two future field works leaded by Dr. Caitlin Whalen (University of Washington) are planned in Fall 2023/2024, along with a year long mooring deployment, that will help understanding the processes responsible for enhanced mixing below TIWs (US CLIVAR Process Study and Model Improvement Panel 2021 [1]).

In addition to their effect on the SST, the waves have been shown to redistribute salinity (Vialard et al. (2002); Olivier et al. (2020)), momentum and kinetic energy (Bryden and Brady (1989)), and biological tracers (Yoder et al. (1994); Strutton et al. (2001); Gorgues et al. (2005); Evans et al. (2009); Shi and Wang (2021)) in the ocean.

Therefore, through horizontal advection, turbulent mixing enhancement, and modification of air-sea fluxes, TIWs have a non-negligible effect on the SST and currents of the eastern tropical Pacific. More work is needed to capture the full picture, in particular related to integrated effects of TIWs on the large scale climate environment.

Interactions between TIWs and seasonal to interannual time scales

Since the background state of the Ocean is responsible for the baroclinic and barotropic instability conditions that generate TIWs, the temporal evolution of these favorable conditions will modulate the characteristics (*e.g.,* amplitude) of the instability waves. Throughout the year, the generation and activity of TIWs is phase-locked with the seasonal cycle (Im et al. (2012)): the activity is enhanced from July to February (Fig. 1.15a, see also Contreras (2002))

[1] https://www.youtube.com/watch?v=ZsVNYq3n9sc

when the cold tongue is the coldest, the meridional temperature gradient is the strongest, and the shear of zonal currents is the highest. On the interannual scale, La Niña events bring together all of the aforementioned favorable conditions necessary to the generation of intense TIW activity. Conversely, their activity is reduced or non-existent during El Niño events (Wang and Mcphaden (2000); Wang and McPhaden (2001); An (2008)). These ENSO-driven interannual variations of TIW activity can be seen in the monthly variance of TIW activity shown in Figure 1.15b).

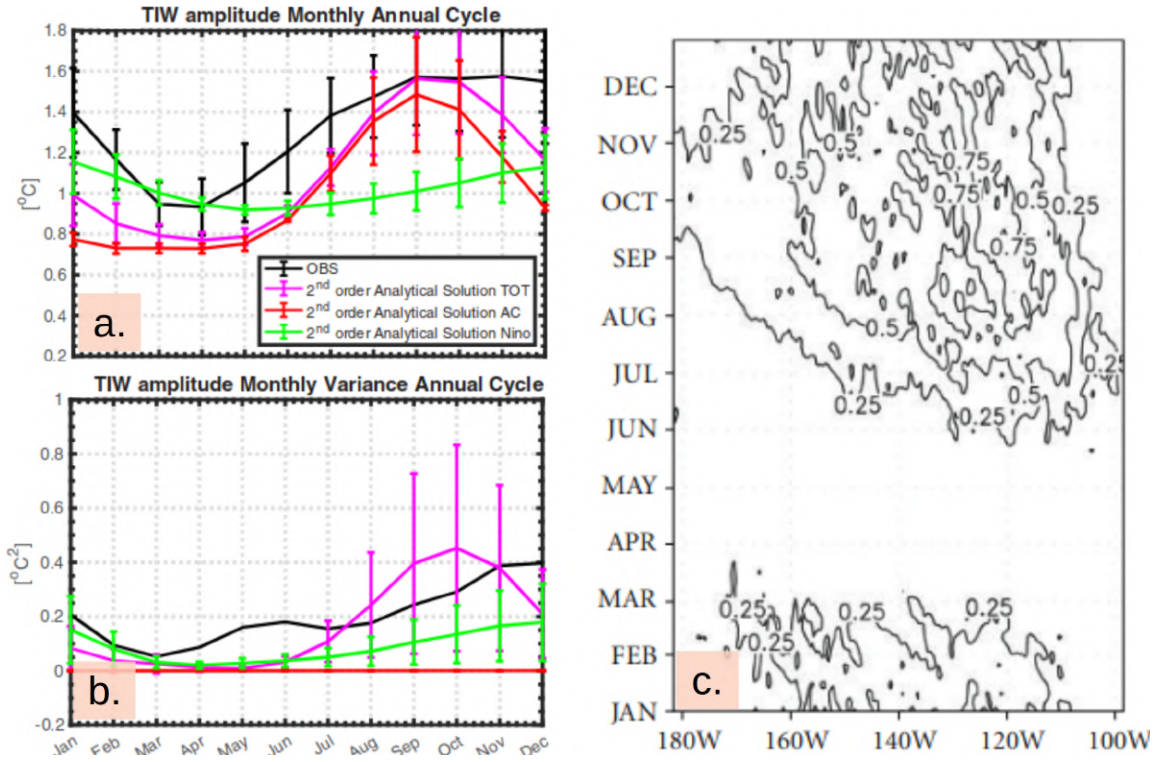

Figure 1.15: (a,b) Seasonal cycle of TIW (a) amplitude and (b) variance in NOAA SST observations (black line). Reprinted from Boucharel and Jin (2020) (see paper for more details). (c) Hovmöller diagram of the seasonal TIW-induced heat advection (°C month^{-1}) averaged between 4°S – 4°N, in the first 50 m. Data are obtained from an oceanic numerical simulation from 1958 – 2007. Reprinted from Im et al. (2012)

In turn, TIWs feed back on climate variability at longer time scales. The SST is warmed by TIW-induced horizontal heat advection during the active season of the instability waves (Im et al. (2012)), and as described in Kessler et al. (1998) using an ocean model:

> "Warming due to tropical instability waves is largest in the second half of the year [...] when upwelling is largest and equatorial SST is coolest, so the effect of this eddy mixing is to moderate the annual variation of cold tongue SST that would otherwise be caused by upwelling"

However, this effect still needs to be quantified, and other effects of TIWs on the equatorial

dynamics are lacking in the literature, in particular related to their connection with the seasonal cycle of zonal currents.

The evolution of ENSO can also be modulated by TIWs. For instance, TIWs could interact with equatorial waves such as Kelvin waves (Holmes and Thomas (2016); Escobar-Franco et al. (2022a)) which could in turn affect the onset of ENSO events. TIWs could also increase ENSO irregularity due to the stochastic nature of the instability waves (Holmes et al. (2019)). Finally, TIW-induced horizontal heat advection in the cold tongue favors La Niña events, while the absence of TIWs during the warm phase of ENSO inhibits El Niño events. An (2008) showed that this anomalous TIW effect on ENSO is stronger during La Niña than El Niño. Therefore, TIWs act as a negative feedback onto ENSO (Fig. 1.16. See also Wang and Mcphaden (2000); Wang and McPhaden (2001); Boucharel and Jin (2020); Xue et al. (2020)), and could participate in the amplitude asymmetry of the ENSO cycle (An and Jin (2004)).

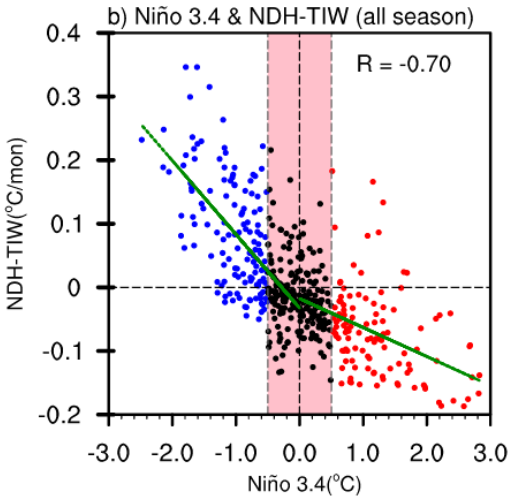

Figure 1.16: TIW-induced heat advection as a function of SST anomalies averaged in the Niño 3.4 region. SST and currents data are obtained from the NCEP Global Ocean Data Assimilation System product from 1980 to 2018. The TIW-induced anomalous warming during La Niña events (negative Niño 3.4) is stronger than the TIW-induced anomalous cooling during El Niño events (positive Niño 3.4). Reprinted from Xue et al. (2020)

TIWs in ocean models

Despite the long wavelength of TIWs extending over several hundred kilometers, their sharp and narrow structures at the TIW cusps and edges make their simulation inaccurate in low-resolution models (Fig. 1.17). Increasing the spatial resolution of ocean models often leads to an increase in the horizontal eddy heat flux related to TIWs, which reduces the cold tongue bias (a common bias in models, in which equatorial waters are too cold relative to observations) and improves ENSO amplitude asymmetry (Roberts et al. (2004, 2009); Sakamoto et al. (2012); Graham (2014)). Most global circulation models (GCMs) used in the scientific community, such as CMIP5 and 6 models, have horizontal ocean resolution close to $dx = 1°$, which does not allow them to fully capture the dynamics of TIWs. However, increasing the spatial resolution of such models would result in high computational costs and an unwelcome large carbon footprint. As a trade-off, one solution is to develop parameterizations of unresolved processes such as TIWs, and incorporate it into low-resolution models. For instance, Imada and Kimoto (2012) incorporated a parameterization of TIWs, based on an eddy diffusion that varies with the local baroclinicity, in a coupled ocean-atmosphere GCM with $dx = 1.48°$ and $dy = 0.58°$ at the equator and decreasing to $0.98°$ at the pole. This simple parameterization significantly reduced the cold tongue bias and improved the amplitude asymmetry of ENSO.

Other studies develop analytical formulation of TIW impacts on the climate that could be incorporated into conceptual ENSO models (*e.g.,* Boucharel and Jin (2020); Xue et al. (2020)). In parallel, deep learning techniques have been tested to find new parameterizations, or even to replace traditional numerical modeling in forecasting operations (Zheng et al. (2020)).

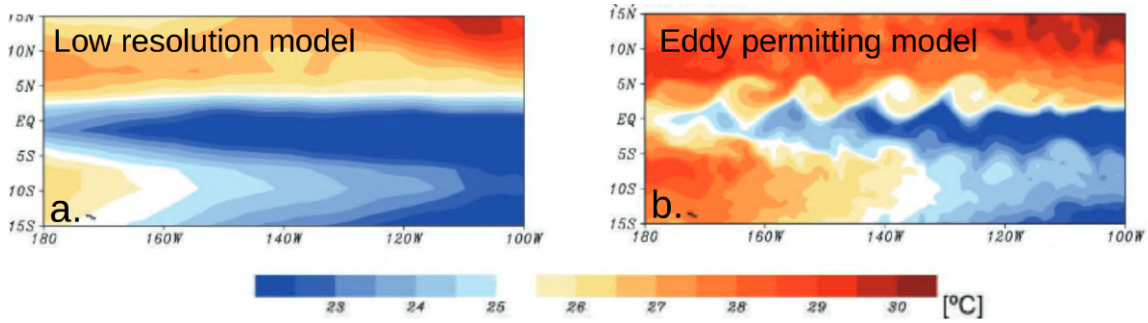

Figure 1.17: Snapshots of SST (2-4 September, 1999) from the ocean-atmosphere coupled Model for Interdisciplinary Research on Climate, at (a) medium ocean horizontal resolution $1.3° \times 0.56°$ (b) eddy permitting ocean resolution $0.28° \times 0.18°$. The resolution of the atmospheric component is also increased, from 2.8° to 0.56°. Reprinted and adapted from Sakamoto et al. (2012)

In any case, there is a need to understand the underlying processes that link TIWs to the mean climatological state and the seasonal cycle of thermodynamic components, and to understand in depth their interactions with the ENSO cycle. This is the purpose of this thesis. By comparing regional simulations with (TIW-RUN) and without TIWs (NOTIW-RUN), the feedbacks of the instability waves on (1) the background state of the eastern tropical Pacific, (2) the seasonal cycle of the main thermodynamic components of the ocean, and (3) on ENSO events will be assessed (Fig. 1.18)

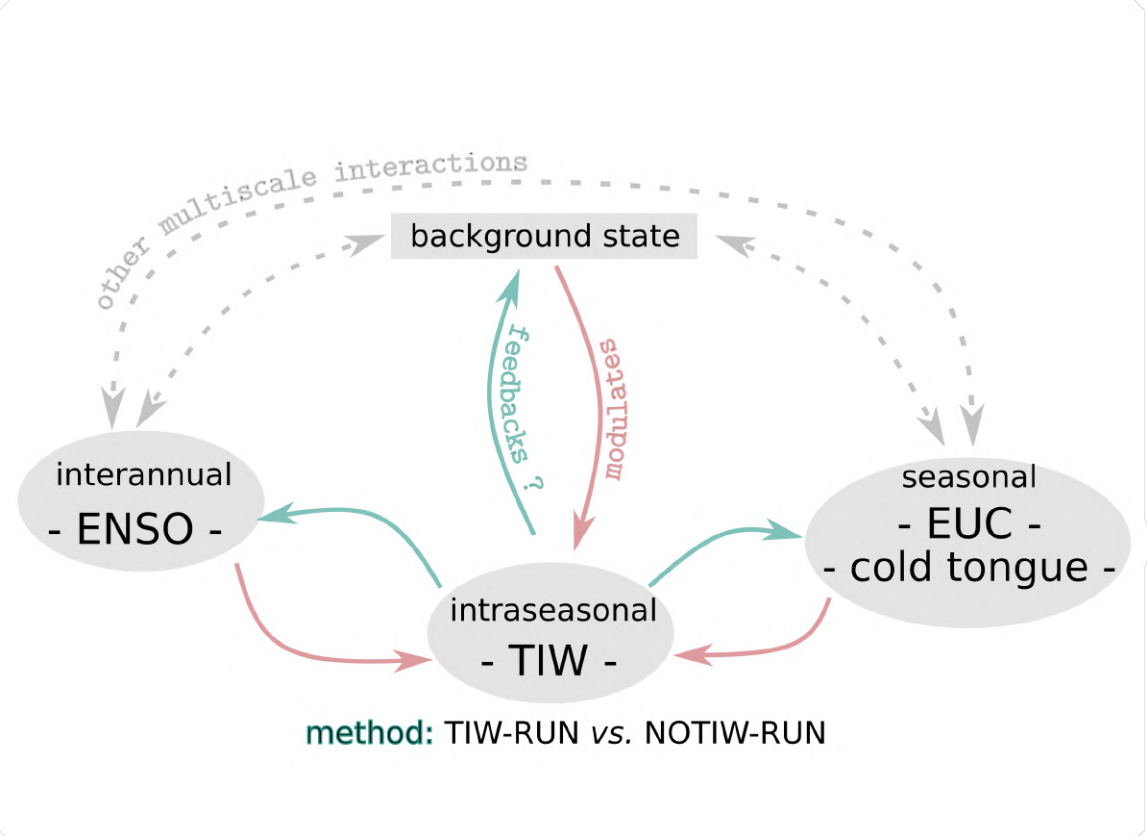

Figure 1.18: Schematics of the multi-scale interactions that will be discussed in this manuscript. Red arrows indicate a modulation of the background state, seasonal variability and interannual variability onto TIWs. Green arrows indicate possible feedbacks of TIWs, that will be assessed in this thesis by comparing a TIW-RUN with a NOTIW-RUN, *i.e.*, simulations with and without the instability waves. Grey arrows indicate other interactions existing between the various time scales presented here.

Chapter 2

Materials and Methods

Contents

2.1 Preamble

Why removing TIWs in an ocean model ? The motivation comes from the need to properly disentangle the effects of these oceanic waves on the thermodynamics of the eastern tropical Pacific Ocean and its variability. As described in the First Chapter, TIWs are at the heart of 2-way interactions as (1) they are modulated by the background environment, and (2) their rapid fluctuations can feedback onto these large scale features.

First, TIWs are generated by baroclinic and barotropic conversions of energy that are respectively linked to instabilities generated by the meridional temperature gradient and the shear of zonal currents. Because these unstable conditions occur primarily from July to February and during La Niña events, the instability waves are seasonally and interannually modulated.

Second, TIWs in turn modulate the ocean thermodynamics through fine-scale processes, usually computed as fluctuations (u', v', T' and so on) from a temporal or spatial average of typically 30 days and 1000 km. When averaged over time or space, these fluctuations disappear by definition. However these waves, usually described by their variances v'^2 or T'^2, have a large imprint on the eddy kinetic energy ($EKE = (u'^2 + v'^2)/2$) and cause turbulent heat and momentum fluxes ($v'T'$ and $u'v'$). By definition, all these variant and covariant eddy fields do not vanish when integrated over time, and thus can lead to basin-wide and slow changes through nonlinear rectification processes. In order to better understand the large scale modulation of thermodynamics driven by TIWs, I will compare a simulation in which TIWs are resolved and freely propagating, *i.e.,* a control simulation that I will call **TIW-RUN**, with a simulation in which TIWs are generated but damped, which I will call **NOTIW-RUN**.

As it will be detailed thoroughly in next Chapters, TIWs can have several direct and indirect impacts on the ocean. First of all, there is a **direct effect** of TIWs which corresponds to the instantaneous nonlinear eddy processes (*e.g.,* $v'T'$) and the time-integration of these instantaneous fields (*e.g.,* $\overline{v'T'}$ where the over-line denotes a long-term average) that will potentially affect the large scale thermodynamics of the ocean. This rectification of the large scale due to the direct effect of TIWs can then lead to other large scale changes, in a more indirect way. This **indirect or rectified effect** can be for instance the difference in $\overline{u_m T_m}$ between TIW- and NOTIW-RUN, where the subscript m denotes a 30-day running mean (see Chapter 3). It can also be the difference in large scale processes such as ENSO between the two simulations. The set of TIW- and NOTIW-RUN simulations will allow me to disentangle the instantaneous fields, the time-integration of these instantaneous fields, and the rectification of the large scale (*e.g.,* modulation of ENSO).

In this Chapter, I will first introduce the ocean and atmosphere models used in this PhD work. I will then describe the different methodologies that I have tested to remove TIWs from a regional simulation of the eastern tropical Pacific Ocean. In the following Chapters, both forced ocean-only and coupled ocean-atmosphere simulations are used. The methodology for TIW damping has been developed on the ocean-only simulations described in Chapter 3 and

Chapter 4, but the same methodology will also be applied on the coupled ocean-atmosphere simulations used in Chapter 5.

2.2 Ocean and Atmosphere Models

In this thesis, regional ocean and atmosphere models were used to simulate the eastern tropical Pacific climate variability. Hereafter, I provide succinct descriptions of each model.

2.2.1 Coastal and Regional Oceanic Community Model: CROCO

The ocean model is the Coastal and Regional Oceanic Community (CROCO) model (Shchepetkin and McWilliams (2005, 2009); Debreu et al. (2012); Shchepetkin (2015)). This ocean model solves the simplified Navier-Stokes equations (*i.e.,* the primitive equations), based on several hypotheses, including the hydrostatic hypothesis (vertical pressure gradient is balancing the buoyancy force) and the Boussinesq hypothesis (density variation are neglected except in their contribution to buoyancy force), and a turbulence closing (turbulent fluxes not resolved by the model are parameterized using large scale features). From these hypotheses, the following primitive equations in Cartesian coordinates are obtained:

$$\begin{array}{lll}
\partial_t u + \mathbf{u}.\nabla u - fv &= -\frac{1}{\rho_0}\partial_x P + \nabla_h(A_h.\nabla_h u) + \partial_z(A_v\partial_z u) & \text{momentum equation} \\
\partial_t v + \mathbf{u}.\nabla v + fu &= -\frac{1}{\rho_0}\partial_y P + \nabla_h(A_h.\nabla_h v) + \partial_z(A_v\partial_z v) & \text{momentum equation} \\
\mathrm{div}(\mathbf{u}) &= 0 & \text{continuity equation} \\
\rho &= \rho(S,T,p) & \text{equation of state} \\
\partial_t T + \mathbf{u}.\nabla T &= \nabla_h(K_{Th}.\nabla_h T) + \partial_z(K_{Tv}\partial_z T) & \text{temperature equation} \\
\partial_t S + \mathbf{u}.\nabla S &= \nabla_h(K_{Sh}.\nabla_h S) + \partial_z(K_{Sv}\partial_z S) & \text{salinity equation}
\end{array} \tag{2.1}$$

And closure conditions at surface ($z=\zeta$) and bottom ($z=-h$):

$$z=\zeta \begin{cases} A_v\partial_z u &= \tau_s^x \\ A_v\partial_z v &= \tau_s^y \\ K_{Tv}\partial_z T &= \frac{Q}{\rho_0 C_p} \\ K_{Sv}\partial_z S &= \frac{(E-P)S}{\rho_0} \\ w &= \partial_t\zeta + u\partial_x\zeta + v\partial_y\zeta \end{cases} \qquad z=-h \begin{cases} A_v\partial_z u &= \tau_b^x \\ A_v\partial_z v &= \tau_b^y \\ K_{Tv}\partial_z T &= 0 \\ K_{Sv}\partial_z S &= 0 \\ w &= -u\partial_x h - v\partial_y h \end{cases} \tag{2.2}$$

Where (u,v) are the horizontal component of currents, p is the pressure, (T,S) are the temperature and salinity tracers, $\rho_0+\rho$ is the total in situ density, f is the Coriolis parameter, (K_{Th},K_{Tv},K_{Sh},K_{Sv}) are the horizontal and vertical diffusive coefficients for temperature and salinity, (A_h,A_v) are the horizontal and vertical viscosity coefficients for momentum, (τ_s,τ_b) are the surface and bottom stress, (Q,$E-P$) are the net heat fluxes and net evaporation fluxes at the surface, ζ is the free surface, and h is the depth of the ocean.

CROCO is a terrain-following coordinate model, which means that the vertical levels follow the bottom topography. Therefore, the primitive equations are modified with a new vertical coordinate σ that ranges from -1 at the bottom to 0 at the surface. The user can chose the number N and stretching parameters (h_{cline},θ_S,θ_b) of these σ-levels, in order to increase the surface and bottom vertical resolution.

In horizontal directions, an Arakawa C-grid, *i.e.,* with a shift in the locations of the variables (density, tracers in the center of the grid; momentum in the center of the edges). A similar shift of variable is done on the vertical grid.

In terms of temporal discretization, the model is "split-explicit" which consists in using different time-steps to allow for the separation of fast surface elevation and barotropic momentum, and slow tracers and baroclinic momentum, which optimise computational time.

In the forced ocean-only simulations performed in this PhD, the atmospheric forcing is performed using the bulk formulation of atmospheric fluxes, with fluxes that adapt to the SST computed in the model.

For more details on CROCO, the reader is invited to refer to the CROCO website[1]. French speaking readers can also read the Appendix A of Renault (2008).

2.2.2 Weather Research and Forecast Model: WRF

The atmosphere model is the Weather Research and Forecast (WRF) Model. WRF solves the Euler equations with compressible and nonhydrostatic hypotheses (see Skamarock et al. (2019) for the detailed equations). The version 4 of WRF is in hybrid sigma-pressure vertical coordinate, which is a terrain-following coordinate that is rapidly de-coupled from the terrain variations with height. As for CROCO, WRF uses a time-splitting scheme for high and low frequency waves, and an Arakawa C-grid for spatial discretization. In WRF, numerous physical paramaterizations can be chosen, for the following physics categories:

- *Microphysics*: explicitly resolves water vapor, clouds and precipitation.
- *Cumulus parameterization*: for unresolved sub-grid convective effects and clouds.
- *Surface layer scheme:* for the calculation of friction velocities and exchange coefficients, used in the heat and moisture fluxes estimation.
- *Land Surface Model:* provides heat and moisture fluxes over land points.
- *Planetary Boundary Layer:* for sub-grid vertical fluxes induced by eddy transport, over the entire atmospheric column.
- *Atmospheric Radiation scheme:* for estimation of the temperature evolution due to longwave and shortwave radiations.

[1] https://www.croco-ocean.org

The reader is invited to refer to Skamarock et al. (2019) and Renault (2008) (for french-speakers) for more details on WRF model.

2.2.3 Coupling WRF and CROCO: OASIS Coupler

In this manuscript, Chapter 3 and Chapter 4 are based on forced ocean-only simulations using CROCO. In Chapter 5, a coupled ocean-atmosphere simulation using CROCO and WRF is used. This coupling is done using the coupler OASIS3-MCT Craig et al. (2017). OASIS allows synchronised hourly exchanges of hourly-averaged heat (net shortwave, net heat flux), momentum, and freshwater fluxes from WRF to CROCO, and SST and currents from CROCO to WRF (Fig. 2.1).

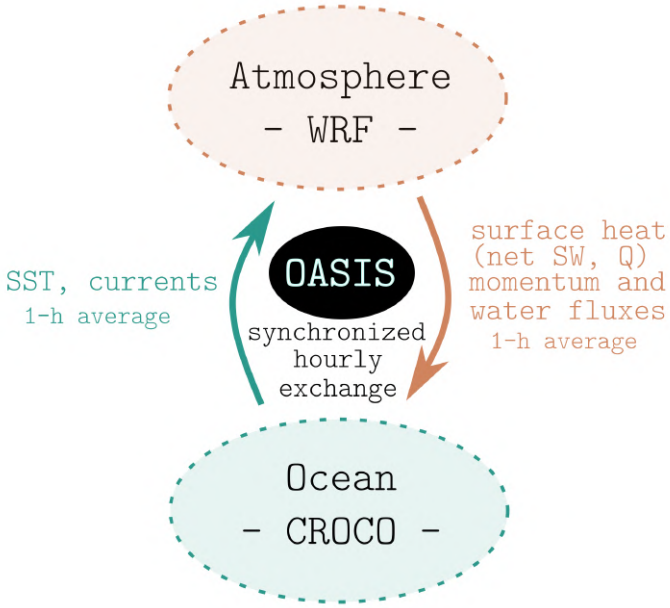

Figure 2.1: Schematics of the coupled ocean-atmosphere procedure. Surface heat fluxes include the net shortwave (SW) and the net heat flux (Q)

2.3 Removing TIWs in an Ocean Model

A significant portion of my three years of PhD has been dedicated to develop an efficient strategy to remove TIWs in an ocean model, and to implement it in CROCO. Hereafter, I will present the different methods that I tried, and their limitations.

2.3.1 First method: increasing the horizontal viscosity

The first method of TIW damping that I have tried to implement in CROCO consists in increasing the horizontal viscosity in the region of active TIWs. In the past decades, several studies have suggested that the viscosity has an impact on the representation of TIWs in an ocean model (Cox (1980); Jochum et al. (2004, 2008)). For instance, Cox (1980) uses an regional oceanic model with a zonal spatial resolution of 1° and meridional spatial resolution of 1/2°, and carries out simulations of the tropical Pacific Ocean with varying horizontal viscosity. While TIW characteristics in terms of wavelength and period were similar, the TIW energy was larger when decreasing viscosity. Consistently, using long term simulations from a global coupled climate model, Jochum et al. (2008) show that decreasing the horizontal viscosity leads to an increase in TIW activity and results in an better representation of the cold tongue in the eastern tropical Pacific Ocean. Based on these assumptions, one could assume that removing TIWs from an oceanic model could be achieved by simply increasing the horizontal viscosity. To test this hypothesis, I used a sponge layer in the oceanic model configuration. Traditionally, sponge layers are used in ocean model to enhance viscosity and diffusivity at open boundaries. These sponge layers act as absorbing layers for oceanic internal waves, preventing them from reflecting off these non-physical open boundaries. They also allow a smooth transition when downscaling a coarser-resolution simulation by damping fine-scale structures at the boundaries. Here I take advantage of this feature that is already implemented in CROCO and apply a sponge layer over the active TIW region (approximately 10°S – 10°N, 185°– 90°W, 0-200 m, see Fig. 2.4) of an eddy-resolving (1/12°) ocean-only simulation of the eastern tropical Pacific Ocean (details on the configuration is described in Chapter 3).

In order to damp TIWs, the additional sponge is used to increase the viscosity coefficient only (and not diffusivity) over the active TIW region. Several viscosity coefficients were tested, and the resulting surface EKE is illustrated in Figure 2.2. The stronger the sponge coefficient (*i.e.,* the horizontal viscosity), the lower the EKE. It indicates that increasing the viscosity coefficient causes indeed a decrease in mesoscale activity. However the efficiency of this method reaches a plateau: increasing the viscosity coefficient from 22000 to 24000 $m^2\ s^{-1}$ does not lead to a significant damping of the EKE. In addition, peaks in EKE (corresponding to peaks in TIW activity) are still present in simulations characterized by increased viscosity, suggesting a failure of the procedure in effectively suppressing TIW activity. Snapshots of SST anomaly during a period of high TIW activity (December 2016) are shown in Figure 2.3 and confirm that the sponge layer only smooths out fine-scale activity associated with TIWs, but not the TIW mesoscale feature in itself. TIW cusps seem even better defined than those simulated without adding the sponge layer. In Cartesian coordinates, the horizontal dissipation of momentum through Reynolds stress can be approximated by $\nabla_h(K_h \nabla_h \mathbf{U})$, where ∇_h is the horizontal divergence operator, K_h is the horizontal viscosity coefficient (in units $m^2\ s^{-1}$) and $\mathbf{U}$ is the horizontal current field. To solve our problem, a solution could lie in performing the spatial second derivatives on a larger amount of grid points in the ocean model. This could smooth out TIW cusps, and not only very fine scales features. However, this requires to adapt the parallelization procedure of the model and, in particular, to increase

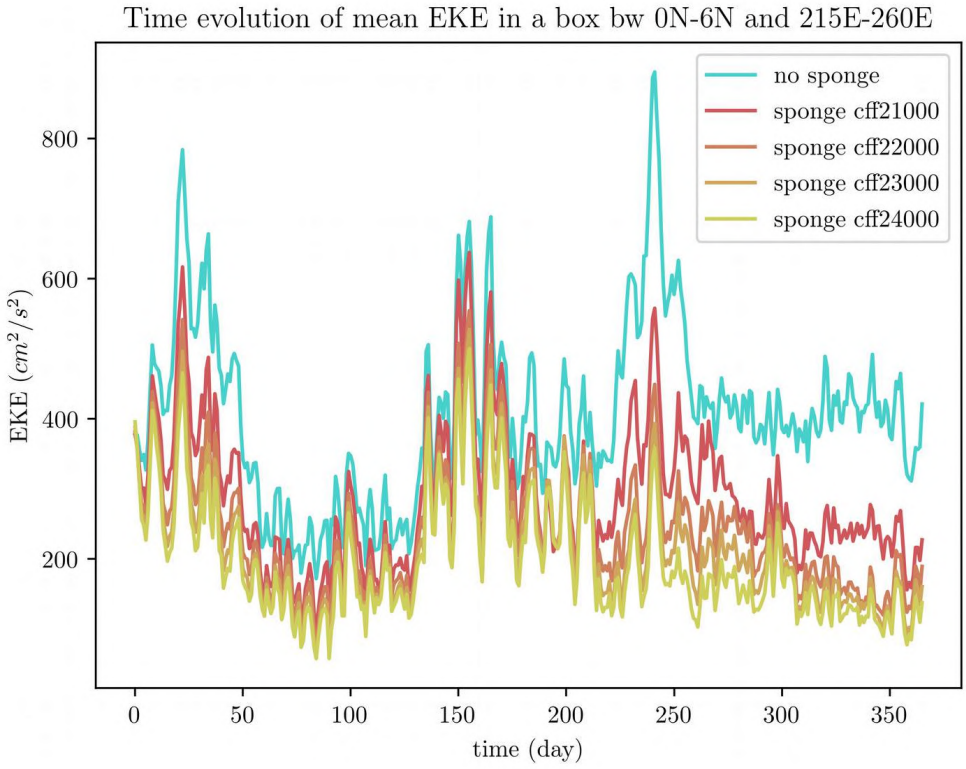

Figure 2.2: Time series of simulated EKE averaged in (145°– 100°W, 0°– 6°N) for year 2011, for various strength of the viscosity sponge.

the number of shadow points (*i.e.,* shared grid points between processors), which would allow to transfer information between several processors online. This work would require skills in numerical developing that are beyond my capabilities. In addition, such approach would likely result in artificial changes in the mean zonal equatorial circulation that would make difficult to properly isolate effects from TIWs only.

2.3.2 Second method: nudging the meridional currents

The second method for TIW damping takes advantage of a nudging methodology which consists in relaxing a selected variable X towards a value X_0, at a relaxation time scale τ. The time evolution of the variable X is given by:

$$\frac{dX}{dt}(t) = f(X) + \underbrace{\frac{X_0 - X(t)}{\tau}}_{nudging} \tag{2.3}$$

where $f(X)$ includes all classic processes that impact the variable X (i.e., advection, diffusion, pressure gradient and Coriolis force). This nudging methodology has been widely used in

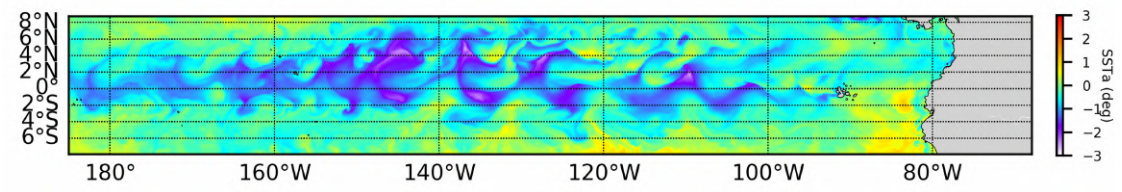

(a) Without sponge

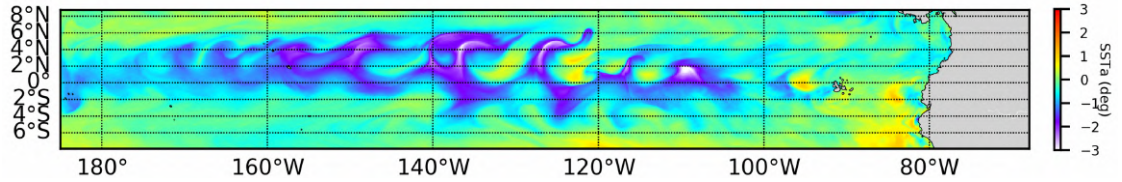

(b) With sponge

Figure 2.3: Snapshots of simulated SST intraseasonal anomaly from 31st of December 2016 in (a) the simulation without viscosity sponge and (b) a simulation with viscosity sponge (coefficient of zonal and meridional viscosity are 12000 and 2200 $m^2\ s^{-1}$).

Earth system modeling. For instance, some regional climate models are nudged toward GCM outputs, so that the fields from regional models do not deviate too much from large scale fields. In regional atmospheric models, a nudging above the planetary boundary layer can be used to constrain the model with reanalyses or GCM outputs while keeping small scale processes near the surface. In oceanic models, a nudging can be added to tracers and momentum at open boundaries in order to better match the boundary dataset. A nudging can also be done toward observations, to improve forecasts.

As TIWs are fluctuating features whose period ranges from 15 to 40 days, their signal is expected to be smoothed out in the monthly mean climatology of tracers and/or currents obtained from the control simulation (TIW-RUN). In addition, in order to remove all traces of TIWs in the NOTIW-RUN, the relaxation towards the TIW-RUN climatology should be done at a short relaxation time scale τ, set to 5 days.

Nudging geometry

To minimize the intrusion of the nudging procedure in our simulation, and in particular not to affect the fine-scale dynamics in the coastal zone, the nudging is restricted to the region of TIW activity by using a window function. TIWs are found between the Galapagos Islands and the central Pacific Ocean along the equatorial band (approximately 8°S – 8°N, see Fig. 2.3a) and in a 200 meters surface layer of the ocean. The window function is noted $G(x, y, z)$, and Eq. 2.3 becomes

$$\frac{dX}{dt}(t) = f(X) + G(x, y, z)\frac{X_0 - X(t)}{\tau} \tag{2.4}$$

The window function G modulates the intensity of the nudging relaxation time scale τ,

in particular by decreasing its strength away from the region of TIW activity. It can be decomposed into the product of normalized individual functions varying with depth $J(z)$, latitude $I(y)$ and longitude $H(x)$ (Fig. 2.4).

The depth function $J(z)$ is maximum from the surface down to $z_1 = 100$-m depth, then decreases until it reaches zero below $z_2 = 200$-m depth:

$$J(z) = \begin{cases} 1 & \text{if } z \leq z1 \\ 3\left(\frac{z-z_2}{z_1-z_2}\right)^2 - 2\left(\frac{z-z_2}{z_1-z_2}\right)^3 & \text{if } z_1 \leq z \leq z_2 \\ 0 & \text{if } z \geq z_2 \end{cases} \tag{2.5}$$

The longitude function $H(x)$ is maximum between the western boundary and the Galapagos Islands at $x_1 = 90°$W, then decreases and reaches zero at $x_2 = 85°$W.

$$H(x) = \begin{cases} 1 & \text{if } x \leq x_1 \\ 3\left(\frac{x-x_2}{x_1-x_2}\right)^2 - 2\left(\frac{x-x_2}{x_1-x_2}\right)^3 & \text{if } x_1 \leq x \leq x_2 \\ 0 & \text{if } x \geq x_2 \end{cases} \tag{2.6}$$

The latitude function $I(y)$ is maximum at $\mu = 1°$N and decreases following a Gaussian profile with a standard deviation σ.

$$I(y) = \exp\left[-\frac{1}{2}\left(\frac{y-\mu}{\sigma}\right)^2\right] \tag{2.7}$$

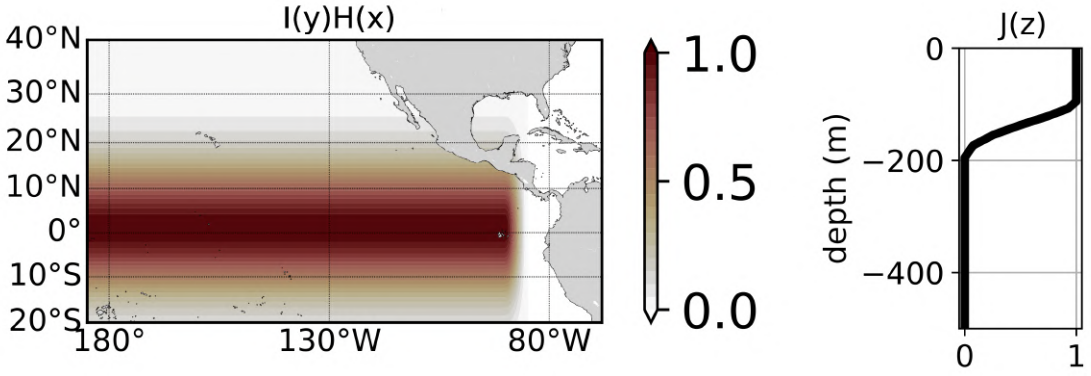

Figure 2.4: Window function $G(x, y, z) = H(x)I(y)J(z)$ with a Gaussian standard deviation of $\sigma = 10°$ latitude.

Nudging tracers and/or momentum ?

TIWs have a strong signature in temperature, salinity and currents. Therefore, in order to remove TIWs from NOTIW-RUN, either tracers, currents, or both can be nudged. I chose to nudge only the meridional currents to their climatological values for several reasons. First of all, TIWs project mostly onto meridional currents v'. Second, the zonal current and tracer fields will not be directly altered by the nudging, but rather will adjust to changes induced by this method, making them more physical, hence more reliable. Third, following the long-wave approximation of shallow water equations (Cane and Sarachik (1977)), Kelvin waves, which play an important role in ENSO's onset, propagate along the equator with no signature in meridional currents. Therefore, nudging v toward their climatological values will allow to damp TIWs while letting Kelvin waves propagate and leaving the equatorial dynamics unaltered. This will be carefully evaluated in the next chapter. Thus, Eq. 2.4 becomes

$$\frac{dv}{dt}(t) = f(v) + G(x,y,z)\frac{v_0 - v(t)}{\tau} \tag{2.8}$$

However, Rossby waves also play an important role in ENSO's onset and termination. As shown by several studies (*e.g.,* Lyman et al. (2007); Wang et al. (2020)), TIWs share characteristics with Yanai (or mixed Rossby-Gravity) waves at the equator, and with the first meridional mode of Rossby waves near 5°N. Thus, removing TIWs while keeping the important Rossby wave modes relatively untouched presents another challenge.

Impact on Rossby waves

Two techniques were tested to preserve the dynamics of the Rossby waves:

- The first method consists in nudging v toward the monthly climatology of v (v_0) estimated from TIW-RUN, but using a smaller value σ for the meridional extent of the window applied in $I(y)$: $\sigma = 5°$.
- The second method nudges v toward $v_0 + v_a$ where v_a are the anomalies of v from the previous month of NOTIW-RUN, hypothesized to contain most of the signal associated with intraseasonal Rossby waves, with a fixed $\sigma = 5°$.

Both methods show similar capabilities to damp TIWs (Fig. 2.5) while preserving Kelvin waves intact (Fig. 2.6). Their effect on Rossby waves is shown in the Hovmöller diagrams of intraseasonal (*i.e.,* band-passed between 90-150 days) sea surface height (SSH) anomalies and averaged between 7.5°N and 8.5°N (Fig. 2.7). While the TIW-RUN (Fig. 2.7a) exhibits clear eastward propagation of Rossby waves, the simulation from NOTIW-RUN with the original nudging method (fixed climatology and $\sigma = 10°$, Fig. 2.7b) shows strongly reduced Rossby wave intensity. However, the two other techniques tested also display a significantly dampened Rossby wave intensity, yet less than with the original nudging method. In particular, the

propagating fluctuation method (Fig. 2.7d) shows no significant improvement compared to the fixed climatology nudging method with $\sigma = 5°$ (Fig. 2.7c).

Unfortunately, I performed this sensitivity experiment during the last year of my PhD. Thus, the studies presented in Chapter 3 and Chapter 4 are based on the same 40-year ocean-only simulations in which the nudging is made toward v_0 with the original meridional nudging scale $\sigma = 10°$. However, for the Chapter 5, which focuses on the ENSO phenomenon and therefore needs the most accurate Rossby wave propagation, the meridional nudging scale is reduced to $\sigma = 5°$, allowing for a slightly better representation of Rossby waves.

Overall, none of the methods leaves Rossby wave propagation perfectly intact, for the simple reason that TIWs are a kind of Rossby waves. This is a drawback of our method that must be taken into account when analyzing the results from the NOTIW-RUN simulations.

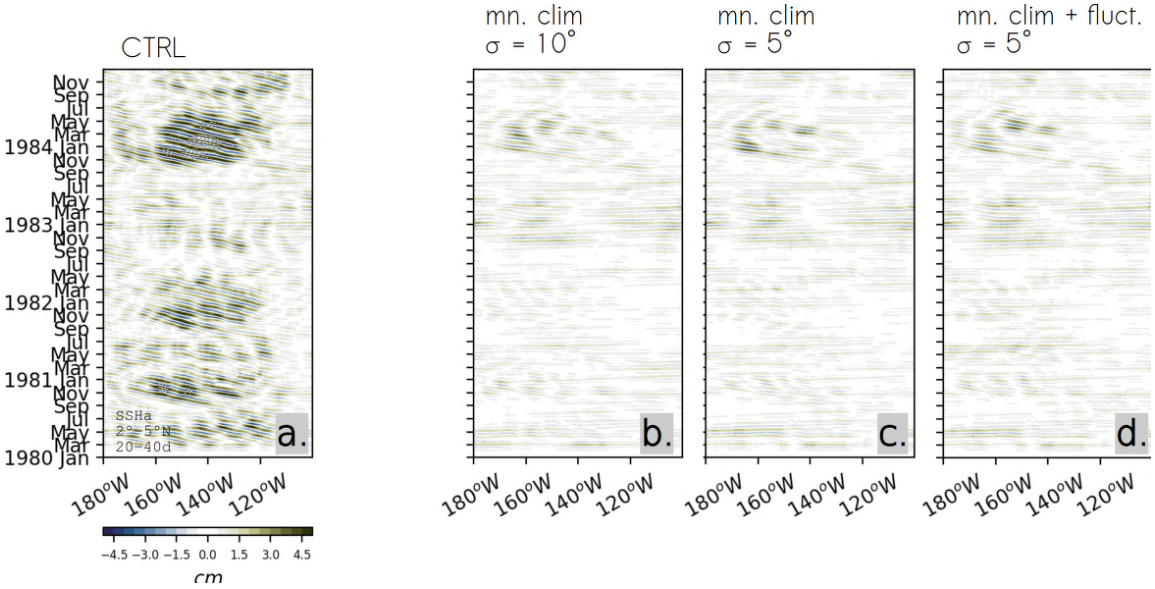

Figure 2.5: Hovmöller diagrams of intraseasonal anomalies of SSH band-passed in the typical TIW periods (20-40 days), and averaged between 2°– 5°N, in ocean-only simulations of (a) TIW-RUN and (b–d) NOTIW-RUN. The NOTIW-RUN are obtained using several methodologies for the nudging of meridional velocities (see details in text)

In practice, in CROCO

The nudging is done online, following this procedure:

- Compute the monthly climatology of the currents u and v (for instance, using `ncra` command from NCO) and concatenate all 12 outputs in the same NetCDF file (for instance, using `ncrcat` command from NCO)
- Put this NetCDF file in the right format, so that it matches the convention of CROCO. To do so, use the python script in Appendix A `clim_u_v_nudging.py`, or `clim_u_v_nudging_xios.py`

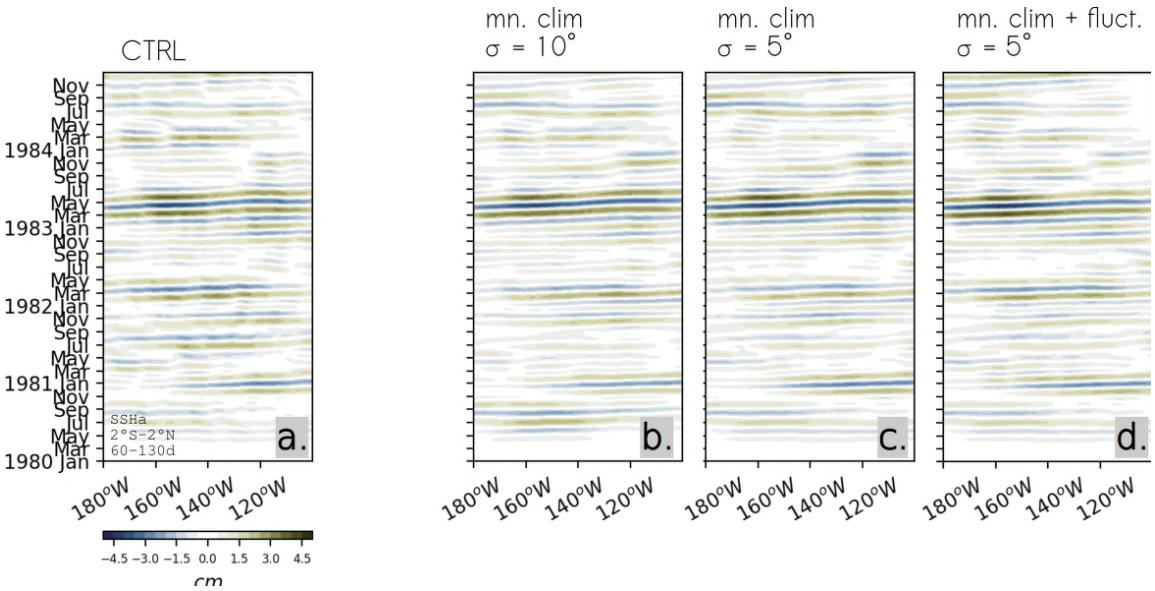

Figure 2.6: Hovmöller diagrams of intraseasonal anomalies of SSH band-passed in the typical Kelvin wave periods (60-130 days), and averaged between 2°S – 2°N, in ocean-only simulations of (a) TIW-RUN and (b–d) NOTIW-RUN. The NOTIW-RUN are obtained using several methodologies for the nudging of meridional velocities (see details in text)

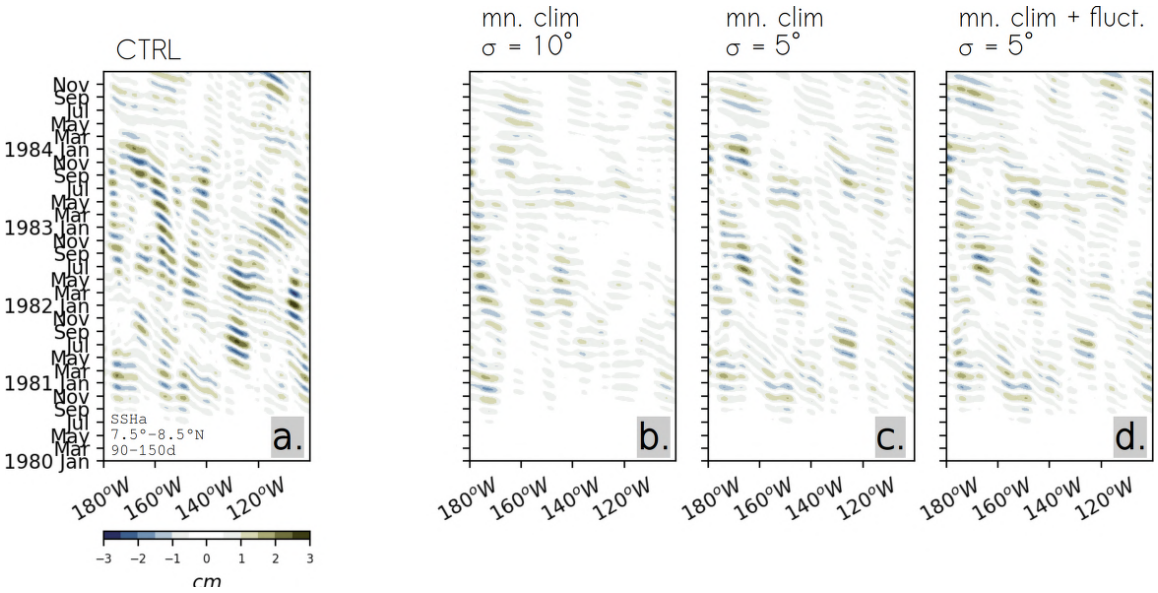

Figure 2.7: Hovmöller diagrams of intraseasonal anomalies of SSH band-passed in the typical Rossby wave periods (90-150 days), and averaged between 7.5°– 8.5°N, in ocean-only simulations of (a) TIW-RUN and (b–d) NOTIW-RUN. The NOTIW-RUN are obtained using several methodologies for the nudging of meridional velocities (see details in text)

if the climatological files are in XIOS convention. Note that in XIOS convention, errors can arise in CROCO if both `_FillValue` and `missing_value` are indicated in the

NetCDF file.

- Define the cpp keys `M3NUDGING`, `CLIMATOLOGY` and `M3CLIMATOLOGY`, and add the new cpp keys `NUDGIN_TIWS` and `NUDGIN_VONLY`, in the `cppdefs.h` file of CROCO.
- Modify the CROCO file `climat.h` and the Fortran scripts `step3d_uv2.F`, and `set_nudgcof.F` to take into account the new cpp keys for nudging v (see Appendix A).

When they are read by the ocean model during a NOTIW-RUN simulation, the monthly climatologies correspond to the 15^{th} of each month, and are interpolated online at each time-step. For instance, if the simulation time is the 1^{st} of July, the nudging is made toward a linear interpolation between the climatological June (corresponding to the 15^{th} of June) and the climatological July (corresponding to the 15^{th} of July).

2.4 Synthesis

In this Chapter, I introduced two techniques to remove TIWs from an ocean model.

Increasing horizontal viscosity

Horizontal viscosity has been found to impact TIW activity in literature. A sponge layer was applied in the ocean in order to increase the horizontal viscosity in the first 200-m. It resulted in the damping of very fine scale structures, but left TIWs still active. One way to improve this method would be to increase the spatial extent of zonal derivatives in the equation of horizontal dissipation of momentum through Reynolds stress. However, it would have required a long dedicated time to develop this method. I preferred to focus on the development of another promising method based on nudging, which required less time and allowed me to go further in the scientific analyses.

Nudging the meridional velocities

Nudging in climate models consists in relaxing a variable toward a prescribed value. Here, because TIWs are fast and transient features vanishing from long-term average, the meridional velocities are nudged toward the monthly climatology v_0 from the control simulation called TIW-RUN that is run over a long time-period and in which TIWs freely propagate. Nudging the new simulation toward v_0 at a short relaxation time scale (5 days) is expected to smooth out all form of TIWs while keeping the basin-scale equatorial dynamics untouched. This nudging is applied to the region of active TIWs by the use of a window function which depends on longitude, latitude and depth (active in the first 200 m and centered at 1°N but decreasing poleward and deactivated east of Galapagos Islands). In terms of TIW damping and Kelvin wave propagation, this method shows very good results that will be extensively

detailed in next Chapters. I tested several adaptations of this method in order to keep Rossby waves as intact as possible. Although some of these methods are better than others, they all show reduced Rossby wave intraseasonal activity, an important point that should be kept in mind when studying the TIWs-ENSO interactions (Chapter 5).

This first method based on the increase of viscosity proved to be technically complex to implement during this thesis. However, pursuing this route could serve as a second independent method to suppress TIWs. It would give robustness to the results presented in the following chapters, in which TIWs are damped using the most suitable strategy both in terms of ease of implementation and results: the nudging method.

Chapter 3

TIWs & the Background State

Contents

3.1 Preamble

In this Chapter, the interactions between TIWs and the ocean background state are investigated. As introduced in Chapter 1, TIWs are generated through baroclinic and barotropic instabilities in the tropical Pacific mean circulation and temperature (Qiao and Weisberg (1995); Masina et al. (1999)). In turn, TIWs modulate these large scale features. While several studies have focused on the impact of TIWs on the temperature (Jochum and Murtugudde (2006); Jochum et al. (2007a); Menkes et al. (2006)), few have looked at their impact on circulation. Moreover, these TIW-induced effects and their consequences on the large scales are difficult to quantify from observations and numerical simulations.

In this work, published in *Journal of Physical Oceanography* (Maillard et al. (2022a)), I use the methodology described in Chapter 2, in a forced ocean-only simulation of the eastern tropical Pacific carried out over the period 1980-2019, using the oceanic model CROCO. With this tool, the effect of TIWs are easily quantified by comparing the control TIW-RUN simulation with the NOTIW-RUN simulation that damp the propagation of TIWs. I first evaluate the simulated spatial distribution and temporal evolution of the main features of the eastern tropical Pacific Ocean (temperature, salinity, currents) against observations. I also validate the damping methodology by using complex empirical orthogonal functions (CEOF) that identify the main modes of variability of transient features, and using a Hovmöller analysis to visualize the wave propagation. I then assess the contribution of TIWs to the thermodynamic changes in the ocean mean state over the 40 years of simulation, and I investigate the direct and indirect pathways by which TIWs modulate this background state, using kinetic energy transfer diagnostics and heat budget analysis. I provide below a copy of the published study as well as a summary of this study.

3.2 Paper published in *Journal of Physical Oceanography*

Direct and Rectified Effects of Tropical Instability Waves on the Eastern Tropical Pacific Mean State in a Regional Ocean Model

LISA MAILLARD,[a] JULIEN BOUCHAREL,[a,b] AND LIONEL RENAULT[a,c]

[a] *LEGOS, University of Toulouse, IRD, CNRS, CNES, UPS, Toulouse, France*
[b] *Department of Atmospheric Sciences, School of Ocean and Earth Science and Technology, University of Hawai'i at Mānoa, Honolulu, Hawaii*
[c] *Department of Atmospheric and Oceanic Sciences, University of California, Los Angeles, Los Angeles, California*

(Manuscript received 7 December 2021, in final form 27 April 2022)

ABSTRACT: Tropical instability waves (TIWs) are oceanic features propagating westward along the northern front of the Pacific cold tongue. Observational and modeling studies suggest that TIWs may have a large impact on the eastern tropical Pacific background state from seasonal to interannual time scales through heat advection and mixing. However, observations are coarse or limited to surface data, and modeling studies are often based on the comparison of low- versus high-resolution simulations. In this study, we perform a set of regional high-resolution ocean simulations (CROCO 1/12°) in which we strongly damp (NOTIWs-RUN) or not (TIWs-RUN) TIW propagation, by nudging meridional current velocities in the TIW region toward their monthly climatological values. This approach, while effectively removing TIW mesoscale activity, does not alter the model internal physics in particular related to the equatorial Kelvin wave dynamics. The impact of TIWs on the oceanic mean state is then assessed by comparing the two simulations. While the well-known direct effect of TIW heat advection is to weaken the meridional temperature gradient by warming up the cold tongue (0.34°C month^{-1}), the rectified effect of TIWs onto the mean state attenuates this direct effect by cooling down the cold tongue (−0.10°C month^{-1}). This rectified effect occurs through the TIW-induced deepening and weakening of the Equatorial Undercurrent, which subsequently modulates the mean zonal advection and counterbalances the TIWs' direct effect. This approach allows quantifying the rectified effect of TIWs without degrading the model horizontal resolution and may lead to a better characterization of the eastern tropical Pacific mean state and to the development of TIW parameterizations in Earth system models.

SIGNIFICANCE STATEMENT: Tropical instability waves (TIWs), meandering features at the surface of the equatorial Pacific Ocean, have long been recognized as a key component of the climate system that can even impact marine ecosystems. Yet, they are still hardly simulated in coupled global climate models. Here, we introduce a new framework to isolate and quantify their complex influence on the tropical Pacific background climate. This approach allows revealing a so far overlooked effect of TIWs on the mean circulation and heat transport in this region that should be accounted for in the next generation of global coupled climate models through parameterization or increased resolution.

KEYWORDS: Mesoscale processes; Ocean models; Tropical variability; Ocean dynamics; Heat budgets/fluxes

1. Introduction

Tropical instability waves (TIWs) are prominent oceanic mesoscale features that have been first observed in the 1970s in the eastern equatorial Pacific (Legeckis 1977) and Atlantic (Düing et al. 1975) Oceans. Since these seminal studies based on satellite and in situ measurements of sea surface temperature (SST) and currents, many efforts have been made to characterize the TIW cusp-shaped and meandering features through satellite and in situ observations of many other oceanic and atmospheric variables such as sea surface height (Miller et al. 1985; Malardé et al. 1987; Musman 1989; Périgaud 1990; Escobar-Franco et al. 2022), velocity (Halpern et al. 1988; Bryden and Brady 1989; Qiao and Weisberg 1995; McPhaden 1996; Kennan and Flament 2000), low-level wind and wind stress (Xie et al. 1998; Chelton et al. 2001; Hashizume et al. 2001), subsurface temperature (McPhaden 1996; Flament et al. 1996; Kennan and Flament 2000), and ocean color and related biogeochemical properties as well (Yoder et al. 1994; Chavez et al. 1999; Strutton et al. 2001; Legeckis et al. 2004; Evans et al. 2009). All these observational studies have contributed to a better understanding of the main properties of TIWs, which essentially represent the dominant form of eddy variability in the equatorial regions. In particular, TIWs are westward-propagating oscillations along the sharp temperature front between the cold upwelled equatorial waters and the warmer waters to the north. They usually appear in the eastern equatorial Pacific in June and persist until the beginning of the following year. Their wavelength is 800–2000 km, and their period is on the order of 15–40 days (Qiao and Weisberg 1995; Lyman et al. 2007). TIWs have very sharp fronts on the order of 100 km at their leading and trailing edges (Warner et al. 2018), associated with strong changes in temperature within a few kilometers.

Complementing these observational studies, early numerical studies (Philander 1976, 1978) started to investigate TIW

Denotes content that is immediately available upon publication as open access.

Corresponding author: Lisa Maillard, lisa.maillard@univ-tlse3.fr

DOI: 10.1175/JPO-D-21-0300.1

generating mechanisms. These forerunner modeling studies first revealed that TIWs arise from barotropic instability (i.e., a conversion from the mean kinetic energy to the eddy kinetic energy, EKE) due to the strong shears between the Equatorial Undercurrent (EUC) and South Equatorial Current (SEC), as well as between the SEC and North Equatorial Countercurrent (NECC), yet to a lesser extent. Later, other idealized modeling and linear stability analyses (Cox 1980; Yu et al. 1995) suggested that baroclinic, Kelvin–Helmholtz, and frontal instabilities also greatly contributed to the generation of TIWs. The induced conversion from available eddy potential energy to EKE was shown to be caused by the sharp meridional gradient of SST between the cold tongue and the surrounding warmer waters (Masina et al. 1999; Im et al. 2012). TIWs have been shown to strongly interact with the atmosphere by exchanging momentum and heat fluxes. Seo et al. (2007) show that TIWs affect the turbulent heat fluxes while Small et al. (2009) demonstrate that TIWs, through the influence of the surface current on the atmosphere (current feedback, e.g., Renault et al. 2016), are damped by 10% or more.

TIW activity is strongly modulated by changes in the climate background over a wide range of time scales. At seasonal time scales, the trade winds intensification during the second half of the year increases the Ekman divergence of surface water. This promotes a colder cold tongue through intensified equatorial upwelling and therefore a stronger meridional SST gradient. In addition, the intensified trade winds also strengthen the SEC. This triggers an increase in both frontal and current shear instabilities, resulting in more kinetic energy production and thus enhanced TIW activity from July to February of the following year (Contreras 2002; von Schuckmann et al. 2008; Wang et al. 2017, 2019). At interannual time scale, TIW activity in the Pacific Ocean is mostly modulated by El Niño–Southern Oscillation (ENSO). In particular, La Niña conditions are accompanied by an increase in meridional SST gradient and intensified currents near the eastern tropical Pacific, which strengthen TIW variability (Hashizume et al. 2001; Yu and Liu 2003). On the other hand, during the warm El Niño phase, the thermocline deepens in the east and warmer waters are brought into the cold tongue, reducing the meridional temperature gradient and concurrently the TIW activity (Philander 1990; Vialard et al. 2001). At intraseasonal time scales, Harrison and Giese (1988) and Giese and Harrison (1991) uncovered changes in TIW amplitude as a response to the passage of Kelvin waves. More recently, the theoretical work by Holmes and Thomas (2016) further revealed that the presence of Kelvin waves could disrupt zonal currents background and in turn modulate the lateral shear production and related TIW generation, with in particular a decreased (strengthened) TIW activity during the downwelling (upwelling) intraseasonal Kelvin waves phase, which has been further confirmed by Escobar-Franco et al. (2022) in satellite observations.

TIWs have been shown to influence the climate state through eddy heat flux convergence and induced nonlinear dynamical heating (Holmes and Thomas 2015; Jin 2003). TIWs have a direct effect on the mean state through nonlinear eddy processes and a rectified effect through upscaling feedbacks, i.e., integrated effects of eddies over a long period of time. For instance, TIWs have been shown to warm up the equatorial cold tongue through the direct effect of horizontal advection of heat by anomalous currents at a rate of approximately 1°C month^{-1}, counterbalancing the cooling induced by mean currents and vertical mixing (Menkes et al. 2006; Im et al. 2012), and highlighting a seasonally modulated negative feedback in the eastern tropical Pacific. Similarly, the ENSO–
TIWs relationship described above has been shown to be modulated at interannual time scales, this feedback being stronger during La Niña than during El Niño, therefore promoting an anomalous mean state warming (cooling) during ENSO negative (positive) phase (An 2008; Imada and Kimoto 2012; Graham 2014). This suggests that TIWs act as an asymmetric negative feedback onto ENSO and influence the cold tongue interannual mean state through a nonlinear rectifying feedback (Boucharel and Jin 2020; Xue et al. 2020, 2021). To sum up, TIWs are at the heart of complex two-way cascading multiscale interactions playing out in the eastern tropical Pacific, which makes it extremely difficult to properly disentangle the direct from the rectified TIW effects onto this region's mean state.

Nonetheless, a few modeling studies have attempted to tackle this issue opting for two different avenues to characterize TIW effects onto the mean, seasonal and interannual cold tongue climate: 1) through the comparison of eddy-permitting or resolving (in which TIWs are free to develop) versus eddy-nonpermitting (i.e., with a resolution too coarse for TIWs to be generated) global ocean model (Graham 2014; Roberts et al. 2004, 2009) and 2) through the implementation of a simple TIW parameterization (mesoscale eddy parameterization of the isopycnal-layer thickness diffusion coefficient, originally developed for baroclinic fronts at mid- or high latitudes; Gent and McWilliams 1990; Gent et al. 1995; Bryan et al. 1999) into an eddy-nonpermitting atmosphere–ocean general circulation model (Imada and Kimoto 2012). The results of these studies suggest that the presence of TIWs (either parameterized or at least partly resolved in the higher spatial resolution model) acts to reduce the equatorial cold tongue well-known cold bias and improve ENSO asymmetry. Yet, one can wonder if these observed differences really originate from only TIW-induced effects or also from a combination of counterbalancing effects due to the altered dynamic triggered by drastic changes in spatial resolution or by the parameterization's intrusive effects?

In this study, motivated by these legitimate interrogations, we develop a new framework to accurately delineate the direct and rectified effects of TIWs onto the ocean mean dynamics. This method is based upon the removal of TIWs in the eastern tropical Pacific by nudging the meridional currents toward their monthly climatological values in an eddy-rich oceanic model. This approach contrasts with the usual technique involving comparison of low- versus high-resolution simulations evoked above, in the sense that small-scale processes and other potential bathymetry-induced instabilities are kept untouched here. This allows quantifying the direct and rectified effects

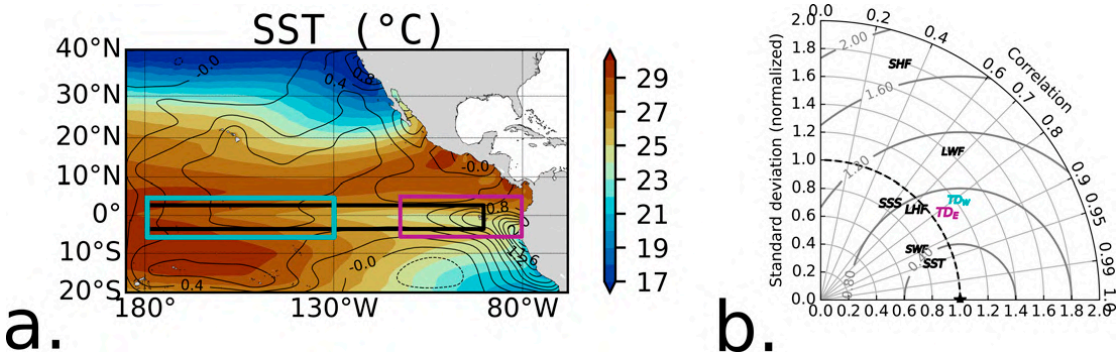

FIG. 1. Evaluation of simulated SST, SSS, and heat fluxes in the control experiment TIWs-RUN. (a) Shading shows the mean SST in the model. Solid and dashed contours (every 0.2°C) show, respectively, the positive and negative mean bias between the model and observed SST. (b) Taylor diagram of SST, SSS, latent heat flux (LHF), sensible heat flux (SHF), shortwave radiation (SWF), and longwave radiation (LWF) monthly time series averaged in the region [2°S–2°N, 180°–90°W, black box in (a)] and thermocline depth (calculated as the depth of the 20°C isotherm) averaged in eastern [TD_E: 3°S–3°N, 110°–80°W, purple box in (a)] and western [TD_W: 3°S–3°N, 180°–140°W, blue box in (a)] regions. Tracers are compared to SODA v3.4.2 during 1980–2019 and fluxes are compared to TropFlux during 1980–2018. Observations are indicated by the black star in the diagram. The angular coordinate shows the Pearson correlation coefficient between the model and observations. The radial coordinate shows the standard deviation normalized by the observations. Gray circles indicate the root-mean-square error between model and observations.

associated with TIW variability on the eastern Pacific mean state and circulation. The paper is structured as follows: section 2 describes the data and model. In section 3, an evaluation of the model performance is done by comparing simulated temperature, fluxes, currents, and mesoscale activity to available observational data. Section 4 describes and validates thoroughly our methodology. In section 5, TIW direct and rectified effects on the oceanic mean state and dynamics are assessed through a heat budget analysis. Results are summarized and discussed in section 6.

2. Model configuration and methods

a. Coastal and Regional Ocean Community model

The oceanic simulations were performed with the Coastal and Regional Ocean Community (CROCO) model (Shchepetkin and McWilliams 2005, 2009; Debreu et al. 2012; Shchepetkin 2015). CROCO is a free-surface, terrain-following coordinate model with split-explicit time stepping and with Boussinesq and hydrostatic approximations. CROCO is implemented over the eastern tropical Pacific from the central Pacific to the American continent (Fig. 1a) i.e., from 185° to 68°W and from 20°S to 40°N at a spatial resolution of 1/12°, corresponding roughly to 9.3 km at the equator. Tracers, surface elevation, and horizontal velocity initial and boundary information are derived from the Simple Ocean Data Assimilation 5-day reanalysis (SODA v3.4.2 on a 1/4° × 1/4° grid; Carton et al. 2019). Because the SODA and model grids rely on different coordinate systems (terrain following vs z coordinates), pressure gradient artifacts can appear, potentially creating spurious rim currents. To avoid this issue, the model grid is merged toward SODA's along the open boundaries (over approximately a 3° band in latitude and a 6° band in longitude). A sponge layer is also applied to enhance the viscosity and diffusivity near the boundary. The configuration has 50 vertical σ levels and the vertical grid is stretched for increased boundary layer resolution using stretching surface and bottom parameters of h_{cline} = 200 m, θ_b = 2, and θ_s = 7. The bathymetry is obtained from the Shuttle Radar Topography Mission (SRTM30 plus; Becker et al. 2009). To avoid aliasing and to ensure the smoothness of the topography at the grid scale, a Gaussian smoothing kernel with a width of 8 times the topographic grid spacing is used.

Vertical mixing of tracers and momentum is done with a K-profile parameterization (KPP; Large et al. 1994). The surface freshwater, heat, and momentum fluxes are estimated using the COARE bulk formulae (Fairall et al. 2003). The atmospheric surface fields are derived from the hourly Climate Forecast System Reanalysis (CFSR; Saha et al. 2010, 2011). We use in particular CFSR from 1980 to 2010 and CFSRv2 onward. The essential atmospheric fields for the ocean-only models are the precipitation rate, the wind field at 10 m, the shortwave and longwave radiation flux, and the temperature and specific humidity at 2 m. To have a realistic representation of the mesoscale activity and of the momentum exchange between the ocean and the atmosphere, the surface oceanic current feedback to the atmosphere (Renault et al. 2016) is parameterized using the stress-correction approach described in Renault et al. (2020).

Two simulations are carried out over the period 1980–2019 after a spinup of seven years, until the total kinetic energy stabilizes. The control simulation, where TIWs are free to develop and propagate, is called TIWs-RUN. The simulation in which TIWs are damped is called NOTIWs-RUN. Offline calculations are made using model outputs at daily average and 1/12° spatial resolution.

b. Observational data

We use a variety of in situ and satellite observational data to validate the model control simulation:

- SST data come from the NOAA 1° Optimal Interpolation of SST version 2 (OI SST v2) data product obtained from in situ and satellite measurements from 1981 to nowadays.
- The SST, sea surface salinity (SSS), and thermocline temporal variabilities are evaluated using SODA v3.4.2 reanalysis on a 1/4° × 1/4° grid, over the 1980–2019 period.
- Heat and momentum fluxes are obtained from TropFlux product on a 1° × 1° grid, from 1980 to 2018. This product combines ERA-Interim and International Satellite Cloud Climatology (ISCCP) data to derive air–sea fluxes (Praveen Kumar et al. 2012). We also used the COREv2 product on a 1° × 1° grid (Yeager and Large 2008).
- In-depth currents come from Johnson's climatology (Johnson et al. 2002), which is derived from in situ measurements of upper-ocean currents in the tropical Pacific during the 1990s.
- Surface currents are obtained from the NOAA 1/4° drifter database (Laurindo et al. 2017), in which the global near-surface currents are derived from satellite-tracked surface drifting buoy observations.
- The eddy kinetic energy is computed using daily mean surface currents from the Copernicus Marine Environment Monitoring Service (CMEMS) on a 1/4° × 1/4° grid (Rio et al. 2014).

c. Intraseasonal anomalies

To capture the variability associated with TIWs, which have periods ranging from 15 to 35 days (Lyman et al. 2007; Wang et al. 2020), anomalies are defined as fluctuations from a 30-day running mean.

d. Statistical significance

The significance of differences between the two simulations is evaluated by generating 40 samples of annual differences (i.e., one for each of the simulation's 40 years) on which a two-tailed Student's t test at 99% is performed, the null hypothesis being a difference of zero. The significance of curves is done using a bootstrapping of the annual means of the variable of interest, i.e., 40 samples, and repeated 1000 times.

e. Heat budget

To assess how TIWs impact the eastern Pacific mean state through changes in the dynamical processes balance, the following temperature heat budget is computed:

$$\underbrace{\frac{\partial T}{\partial t}}_{\text{Tendency}} = -\underbrace{(\mathbf{u}\nabla T)}_{\text{Advection}} + \underbrace{D_l(T)}_{\text{Lateral mixing}} + \underbrace{D_z(T)}_{\text{Vertical mixing}} + \underbrace{I(z)}_{\text{Atmospheric forcing}}, \tag{1}$$

where T is the ocean temperature; $\mathbf{u}$ is the current vector; ∇ is the spatial gradient; $D_l(T)$ and $D_z(T) = \partial_z(k\partial_z T)$ the lateral and vertical mixing terms, respectively; and $I(z)$ is the heating by atmospheric forcing (i.e., solar radiation and its penetration in depth).

We focus on the 50-m surface layer. The integration with depth is denoted $\langle x\rangle = (1/h)\int_0^h x\,dz$ with $h = 50$ m. It gives

$$\frac{\partial\langle T\rangle}{\partial t} = -\langle\mathbf{u}\nabla T\rangle + \langle D_l(T)\rangle + \langle D_z(T)\rangle + \langle I(z)\rangle. \tag{2}$$

Averaging Eq. (2) over the long-term mean (40 years, denoted by an overline), the tendency is found negligible, therefore:

$$-\overline{\langle\mathbf{u}\nabla T\rangle} + \overline{\langle D_l(T)\rangle} + \overline{\langle D_z(T)\rangle} + \overline{\langle I(z)\rangle} \approx 0. \tag{3}$$

Using a classic Reynolds decomposition, each variable can be decomposed into a low-frequency (subscript m) and eddy (prime) part (departure from a 30-day running mean):

$$X = X_m + X'. \tag{4}$$

Note that the eddy part might still contain some variability associated with Kelvin waves. However, TIWs are dominant in this monthly frequency range. Moreover, as detailed later, the TIW effects are evaluated from the difference between TIWs-RUN and NOTIWs-RUN, therefore processes not impacted by TIWs will not affect our analysis. The advective term can be decomposed as

$$\mathbf{u}\nabla T = \mathbf{u}_m\nabla T_m + \mathbf{u}'\nabla T' + \mathbf{u}_m\nabla T' + \mathbf{u}'\nabla T_m. \tag{5}$$

Averaging Eq. (5) on the long term, it becomes

$$\overline{\mathbf{u}\nabla T} = \overline{\mathbf{u}_m\nabla T_m} + \overline{\mathbf{u}'\nabla T'}. \tag{6}$$

As the mean is a linear operation (when weighted by the right ratio), cross terms $\overline{\mathbf{u}'\nabla T_m}$ and $\overline{\mathbf{u}_m\nabla T'}$ are equivalent to $\overline{(\mathbf{u}'\nabla T_m)_m}$ and $\overline{(\mathbf{u}_m\nabla T')_m}$, which vanish by definition.

The mixing, tendency, and forcing terms were computed online by the model as monthly averages. However, for technical reasons, the advective terms were computed offline from daily average fields. These offline advection terms were compared to online advection terms obtained from a short test run of TIWs-RUN, confirming the accuracy of our estimate from daily averages. We verified the closure of the budget averaged over the first 50 m and over the 40 years: the sum of advective, mixing, and atmospheric forcing terms are close to zero, as well as the tendency term.

3. Validation of the model

In this section, we assess the control simulation (TIWs-RUN) with regards to the variety of observational products described in section 2, with a particular focus on equatorial currents and associated mesoscale activity at intraseasonal time scales, the central point of this study.

a. Validation of tracers and heat fluxes

Figure 1a shows the SST long-term mean obtained from 40 years of simulation. Consistent with the literature, the

TABLE 1. Mean values from time series used in the Taylor diagram, for the model and observations. Last line shows the model biases (i.e., model minus observations).

	SST (°C)	SSS (psu)	TD_W (m)	TD_E (m)	SW (W m^{-2})	LW (W m^{-2})	LHF (W m^{-2})	SHF (W m^{-2})
Model	26.8	35.08	154.5	71.7	262.1	−56.5	−111.6	−8.4
Observation	26.1	34.97	146.2	47.3	251.8	−47.8	−82.7	−3.9
Bias	0.7	0.11	8.3	24.4	10.3	−8.7	−28.9	−4.5

typical features of the eastern tropical Pacific can be observed as, e.g., the presence of the cold tongue, a patch of cold water along the equator that lies between 140°W and the Ecuadorian coast and extends along South America shorelines due to the Peruvian coastal upwelling. The cold tongue is flanked on each side by warmer waters, in particular in the Northern Hemisphere, where the eastern Pacific warm pool extends from the tip of Baja California to the northern edge of the cold tongue (Wang and Fiedler 2006). Contours on Fig. 1a indicate a warm bias between the model and the climatology computed from OISST that reaches 0.6°C in the equatorial band and 1.6°C in the eastern part of the cold tongue. This bias can be explained by at least two factors:

- On the one hand, from a too weak equatorial upwelling caused by a thermocline too flat along the equator as indicated by the strong bias in the simulated thermocline depth (TD_W) overestimated by 8.3 m (i.e., 5.7% of the observation) in the west, and by almost 25 m (i.e., more than 50%) in the east (TD_E) (Table 1). This could result from a poor wind stress curl representation in CFSR along with an inaccurate equatorial dynamic at the open boundaries forced with SODA v3.4.2.
- On the other hand, from a positive shortwave radiation bias of roughly 4%, which can contribute to the excessive SST warming and in turn explains the too strong latent and sensible heat flux amplitudes (−28.9 and −4.5 W m^{-2}, respectively; Table 1). The bias in shortwave fluxes is a known bias in CFSR, especially in the western part of the eastern Pacific (Wang et al. 2011). It is most likely due to the deficiency in cloudiness in CFSR (Dolinar et al. 2016). We also note a positive bias of 18.2% for the longwave radiation.

The SSS is only slightly biased as compared to observations (0.11 psu) despite the overestimation of precipitation in CFSR noted by Dolinar et al. (2016). This might result from bias compensations between too strong precipitations and evaporation related to the overestimation of latent heat fluxes.

Overall, the Taylor diagram (Taylor 2001) reveals that the model simulates accurately the eastern tropical Pacific variability, as most variables are well correlated with observations (correlations higher than 0.6) and have normalized standard deviations close to 1, indicating amplitudes similar to observational time series. The sensible heat flux (SHF), however, has a poor correlation coefficient of 0.3 and its standard deviation is 1.8 times higher than observations. Yet, this result has to be taken with caution, as fluxes observations are problematic, which might hinder an accurate representation of their variability. Indeed, a similar analysis of fluxes [SHF, latent heat flux (LHF), and shortwave radiation (SWF)] variability using the COREv2 dataset (Yeager and Large 2008) displays very contrasted results for latent and sensible heat flux. The correlation coefficient for SHF becomes slightly negative (−0.02) and the standard deviation is 1.6 times higher than observations. These results also vary spatially. For the intertropical convergence zone (ITCZ) region (2°–15°N and 180°–90°W), the normalized standard deviation of TropFlux SHF is close to 1, whereas the COREv2 SHF is 1.4. For the same region, the correlation coefficient reaches 0.5 for the TropFlux SHF, but stays under 0.3 for the COREv2 SHF, confirming the strong dependence of the results to the observational product considered (Valdivieso et al. 2017).

b. *Validation of mean circulation and mesoscale activity*

The 40-yr averaged mean zonal circulation is then compared to the drifters-derived climatology at the surface (Fig. 2a) and to Johnson's for their vertical structure (Fig. 2c). Figure 2a exhibits a good agreement with observations for both the position and intensity of the SEC and NECC. In addition, the model captures well their vertical extension at 125°W as indicated by the good match between simulated (shading) and observed (contours) zonal velocity on Fig. 2c. In particular, the SEC extends coherently poleward with its southern and northern branches centered near 3°S and 3°N, and reaching −0.3 and −0.5 m s^{-1}, respectively, the latter being slightly underestimated by 0.2 m s^{-1} in the eastern part of the basin (Fig. 2a). In addition, the SEC/NECC surface front is located at 5°N consistently with Johnson's observations. The EUC vertical structure and intensity also matches well with observations from Johnson, in particular exhibiting a similar maximum value of 0.8 m s^{-1} at the equator. The maximum value is located slightly deeper than Johnson's, which is likely due to the too weak equatorial upwelling in our simulation.

To complement this evaluation and as a preliminary diagnostic of TIW activity, the mean mesoscale activity is then assessed using the eddy kinetic energy [EKE = $(1/2)(u'^2 + v'^2)$]. Shading on Fig. 2b shows the mean simulated EKE from the control configuration (TIWs-RUN). Note that in order to compare to CMEMS, the 1993–2019 average is shown here. Consistent with the literature (Baturin and Niiler 1997; Wang et al. 2020), a strong mesoscale activity is found along the equator, spreading northward up to 5°N, a characteristic signature of TIWs. Contours show the bias between the model EKE and the EKE derived from CMEMS daily currents. The simulated EKE is overestimated by up to 100 cm^2 s^{-2} in the equatorial band. This is not surprising as the CMEMS currents contain only the geostrophic and Ekman currents. A more detailed validation of TIW characteristics in the control experiment will be performed in the next section.

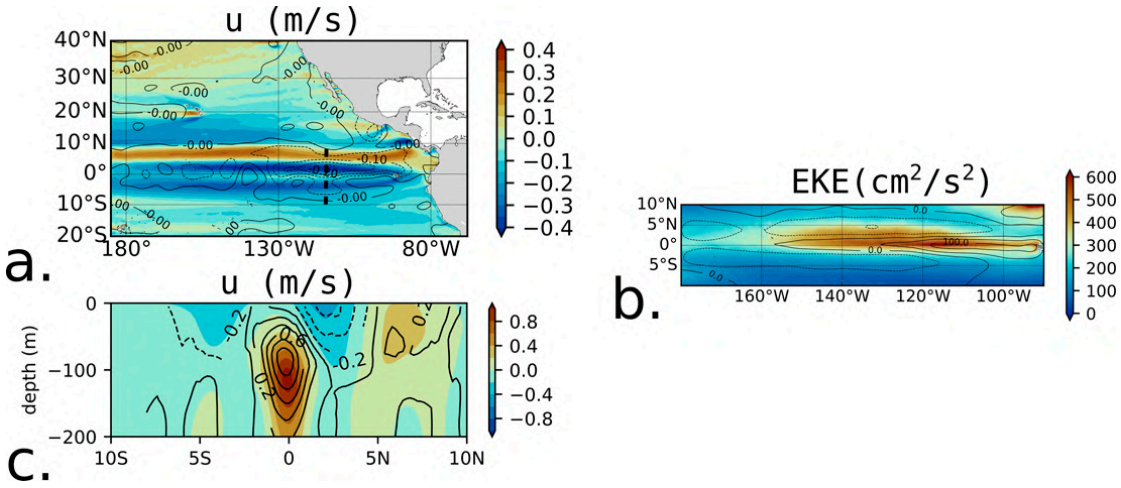

FIG. 2. Evaluation of TIWs-RUN dynamics. Maps of mean surface (a) zonal currents and (b) EKE calculated using fluctuations of horizontal currents from a 30-day running mean. Shading represents the control experiment (TIWs-RUN) mean zonal surface currents from 1980 to 2019 in (a) and mean surface EKE from 1993 to 2019 in (b). Solid and dashed contours show respectively the positive and negative mean amplitude bias between the model and the climatology obtained from the NOAA drifter database in (a) and the 1993–2019 CMEMS currents in (a). Contours are every 0.05 m s^{-1} in (a) and every 50 cm^2 s^{-2} in (b). (c) Depth–latitude section of zonal currents at 125°W [represented in dashed line in (a)] for model (shading) and observations from Johnson (contours). Eastward (westward) currents are shown with solid (dashed) lines.

Overall, despite the presence of some biases, in particular related to the zonal tilt of the equatorial thermocline, the mean state and circulation of the eastern tropical Pacific are well represented in the control configuration, which testifies to the model's ability to simulate adequately the complex equatorial dynamics (Kessler 2006). Regardless, hereafter, the control configuration is compared to a sensitivity experiment in which only the TIW activity is altered. In that sense, the aforementioned mean biases should be similar in both experiments and therefore cancel out when evaluating the specific TIW effect on the eastern tropical Pacific mean state.

4. A framework for damping TIWs in an ocean model

This section is dedicated to describing and validating the methodology employed to smooth out TIWs in the sensitivity experiment (NOTIWs-RUN).

a. *TIW characteristics and associated mesoscale activity in TIWs-RUN*

TIWs have a clear and spatially coherent signature between surface meridional velocity and temperature intraseasonal anomalies, as indicated by snapshots taken during the boreal winter of a La Niña year (i.e., both extremely TIW active periods) (Figs. 3a,b). In particular, we observe alternating positive and negative velocity anomalies localized in the equatorial band (Fig. 3a) and around which filaments of SST anomalies are seen to meander (Fig. 3b). This TIW-induced mesoscale activity is then assessed by calculating the intraseasonal EKE. The highest values of EKE are found along the equator, spreading northward with a maximum at 1°N (Fig. 2b), the region where TIWs are the most active. In addition, EKE is found to be strong (250–500 cm^2 s^{-2}) within the first 100 m (Fig. 3c) and drop to almost zero below 200 m.

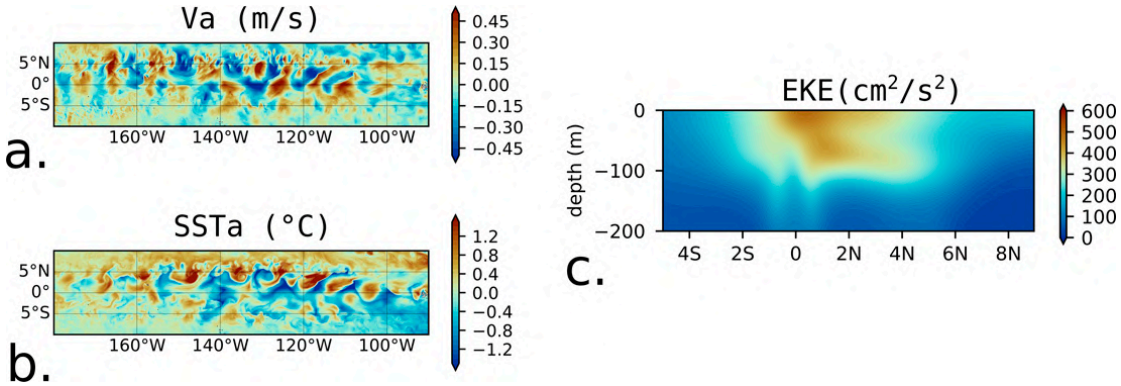

FIG. 3. Illustration of TIW activity. Snapshots (31 Dec 2017) of (a) surface meridional velocity anomaly (m s^{-1}) and (b) surface temperature anomaly (°C), and (c) meridional section of EKE (cm^2 s^{-2}) averaged between 160° and 100°W.

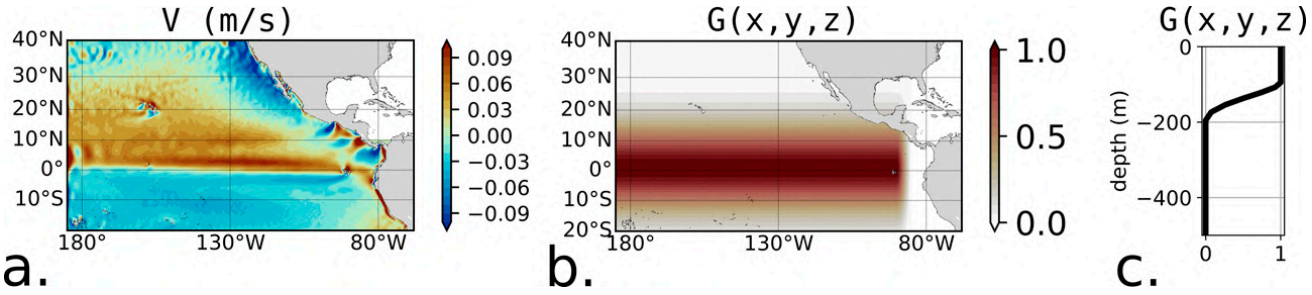

FIG. 4. Damping framework. (a) Meridional current annual climatology in the control experiment (TIWs-RUN). (b) Horizontal and (c) vertical structure of the nudging geometry $G(x, y, z)$.

These diagnostics allow delineating the spatial (including vertical) region of prominent TIW-induced mesoscale activity.

b. *Damping methodology*

To smooth out the TIWs without affecting other processes in NOTIWs-RUN, the mixed layer meridional currents v in the active TIW region (see Fig. 4) are nudged toward the monthly climatology v_0 derived from TIWs-RUN as such:

$$\frac{dv}{dt} = f(v) + G(x,y,z)\frac{v_0(t) - v(t)}{\tau}. \quad (7)$$

The left-hand part of the equation is the temporal evolution of v. The first term of the right-hand part $f(v)$ represents the evolution of v due to advection–diffusion processes. The last term of the right-hand side represents the nudging of v toward the monthly climatology v_0, computed from the control experiment (TIWs-RUN) and which does not display much trace of the TIW mesoscale features (see Fig. 4a for the annual climatology of the surface v field). Yet, the Ekman divergence at the equator is still present, indicating that the nudging of v toward v_0 is expected to damp TIW activity while keeping the mean dynamics intact. The nudging time scale τ is set to 5 days, so that both TIW modes with periods near 33 and 17 days, and commonly referred to as the Rossby and Yanai modes (Lyman et al. 2007; Wang et al. 2020), are effectively removed.

Based upon the TIW spatial features discussed above (see section 4a), the nudging geometry is restricted to the prominent region of TIW activity by applying a spatial Gaussian function $G(x, y, z)$ (see Fig. 4 and the appendix for details). This function maximizes the nudging along 1°N and reduces it poleward with a decreasing meridional rate of 10° (Fig. 4b). It is deactivated between the Galapagos Island and the coast to preserve submesoscale features in the coastal area for instance related to filaments breaking loose from the Humboldt upwelling system. Even though TIWs have been shown to radiate internal waves downward (Jing et al. 2014; Holmes and Thomas 2016; Tanaka and Hibiya 2019; Delpech et al. 2020), the nudging is concentrated within the first 200 m below the surface (Fig. 4c) where TIWs are mostly generated and active (Fig. 3d).

Note that only meridional currents are nudged. This allows an effective damping of the development of TIWs due to their strong signature in v, while keeping equatorial Kelvin waves mostly untouched, as their meridional structure in the long-wave approximation of shallow water equations is null at the equator (Cane and Sarachik 1977). Therefore, the nudging of meridional velocity only is expected to preserve the important role played by Kelvin waves in the equatorial dynamics, for instance related to the kickstarting of El Niño events (e.g., McPhaden and Yu 1999; Gushchina and Dewitte 2012). By nudging the meridional currents, the other dynamical and tracer components are expected to adjust and vanish as well.

c. *Validation of damping efficiency*

To validate to which extent the damping methodology allows smoothing out TIW variability, we first compare EKE between the NOTIWs-RUN (Fig. 5) and TIWs-RUN (Figs. 2b and 3c). These figures indicate an EKE (and associated mesoscale activity) decrease of almost 50% in the TIW active region. When separating the EKE into u'^2 and v'^2 parts reconstructed using the five first complex empirical orthogonal function (CEOF) modes (i.e., accounting together for most of the TIWs variability, see below for more details on the CEOF analysis), we observe a reduction of u'^2 and v'^2 from TIWs-RUN to NOTIWs-RUN of 62% and 94%, respectively, indicating that the remaining mesoscale activity in NOTIWs-RUN is for the most part not due to TIWs but

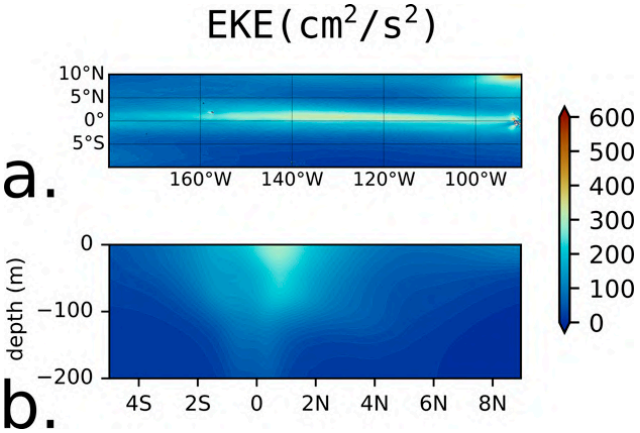

FIG. 5. EKE ($cm^2\ s^{-2}$) in NOTIWs-RUN (a) averaged over 200 m and (b) meridional section averaged between 160° and 100°W.

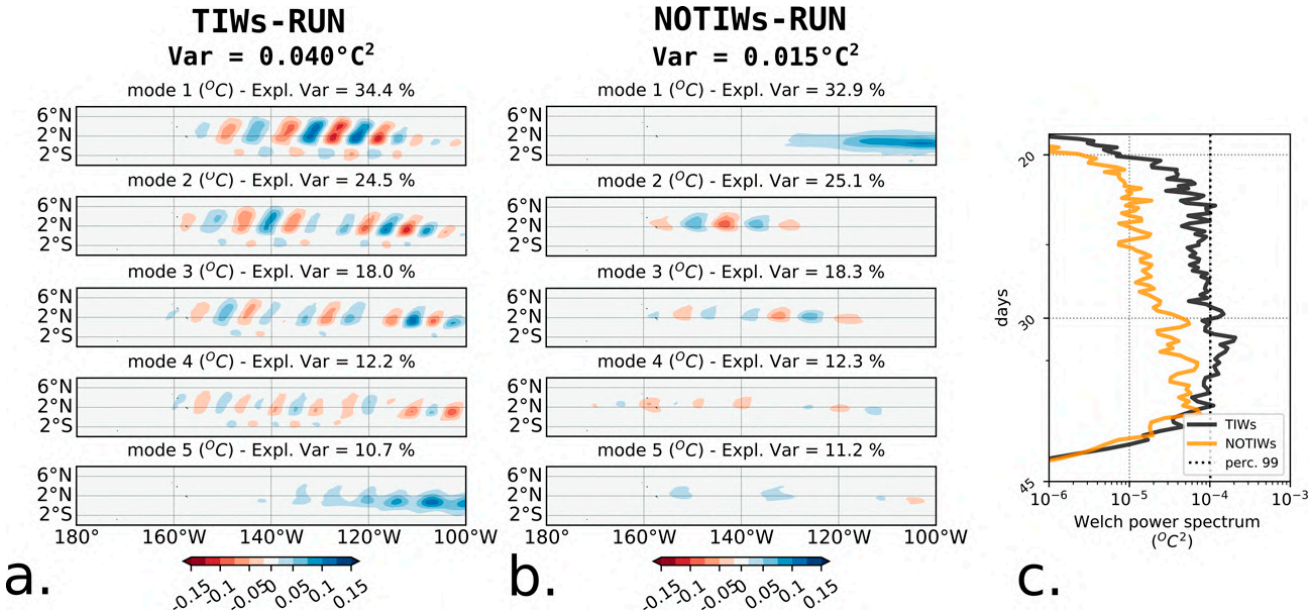

FIG. 6. First five modes' real part of the complex empirical orthogonal function (CEOF) decomposition of 20–40 days bandpassed SST anomalies performed in the TIW active region (4°S–8°N, 180°–100°W) for (a) the TIWs-RUN and (b) the NOTIWs-RUN. (c) Mean Welch power spectrum of the reconstructed SST anomaly field over maximum CEOF signal area (4°S–8°N, 140°–100°W) for each simulation using the first four CEOF modes.

instead most likely due to wind-driven currents (not shown). This also confirms the coherent adjustment of zonal currents at TIW scale to our nudging procedure applied only on v.

To investigate the TIW damping efficiency in more detail, CEOFs are estimated using the 20–40 days bandpassed SST anomaly in the TIW active region (4°S–8°N, 180°–100°W) for both simulations. CEOFs (Barnett 1983) are an efficient and extensively used way to extract the spatiotemporal characteristics of TIW intraseasonal variability, as this analysis provides both amplitude and phase information and is therefore well adapted to capture waves propagation and variability (Boucharel et al. 2013, 2016; Xue et al. 2021; Escobar-Franco et al. 2022).

The first five dominant modes are shown in Fig. 6a for TIWs-RUN and in Fig. 6b for NOTIWs-RUN. The fifth mode of TIWs-RUN and the first mode of NOTIWs-RUN could correspond to SST variations associated with the intraseasonal Madden–Julian oscillation (Madden and Julian 1994), as found by Maloney and Kiehl (2002). Similar to their results, the phase of this mode (not shown) indicates a northward propagation and seems to correspond to a potential interaction of this mode with TIWs in the TIWs-RUN, but this is beyond the scope of this paper. In the TIWs-RUN (Fig. 6a), modes 1–4 are associated with TIW variability as indicated by the alternating positive and negative nodes located between 2°S and 6°N. They are characterized by high explained variances of 34.4%, 24.5%, 18.0%, and 12.2%, respectively.

In the NOTIWs-RUN (Fig. 6b), modes 2–4 exhibit patterns resembling TIW variability, yet with small explained variances. Moreover, the total variance of the NOTIWs-RUN signal is 63% lower than that of the TIWs-RUN (standard deviation of 0.015° vs 0.04°C^2), giving even less weight to these modes of variability, and indicating that TIWs have been strongly damped in the NOTIWs-RUN sensitivity experiment. This is confirmed by the large decrease in power spectra (reconstructed using the first four CEOF modes and averaged in the TIW active region) in the TIW typical period range of 17–33 days between the two experiments (Fig. 6c).

For a more visual assessment of the efficiency of our method, we then show Hovmöller diagrams of the 20–40 days bandpassed zonal SST anomaly averaged between 2° and 5°N for TIWs-RUN in Fig. 7a and NOTIWs-RUN in Fig. 7b during the strong La Niña episodes of 2017 and 2018, i.e., periods favorable to TIW development as explained in the introduction section. In the TIWs-RUN (Fig. 7a), a strong TIW activity is observed during the boreal autumn of both years, whereas the 2015/16 winter marked by a strong El Niño event does not exhibit, as expected, any sign of TIW propagation. In contrast, in the NOTIWs-RUN (Fig. 7b), TIWs have almost fully disappeared during all three winters, indicating that their development has been effectively prevented by the nudging procedure. These results are valid throughout the entire 40-yr period.

Finally, to establish that other aspects of the equatorial dynamics, in particular related to Kelvin waves propagation, are left unaltered by our methodology, Hovmöller diagrams of the 60–130 days bandpassed thermocline depth anomaly averaged between 2°S and 2°N for TIWs-RUN and NOTIWs-RUN are shown in Figs. 7c and 7d, respectively. In both simulations, one can identify the presence of Kelvin waves by their eastward propagating signal at a phase speed of 2.3 m s^{-1}.

To sum up, the nudging procedure applied in NOTIWs-RUN effectively damps TIW activity while keeping the important Kelvin waves signal in this region untouched. Consequently,

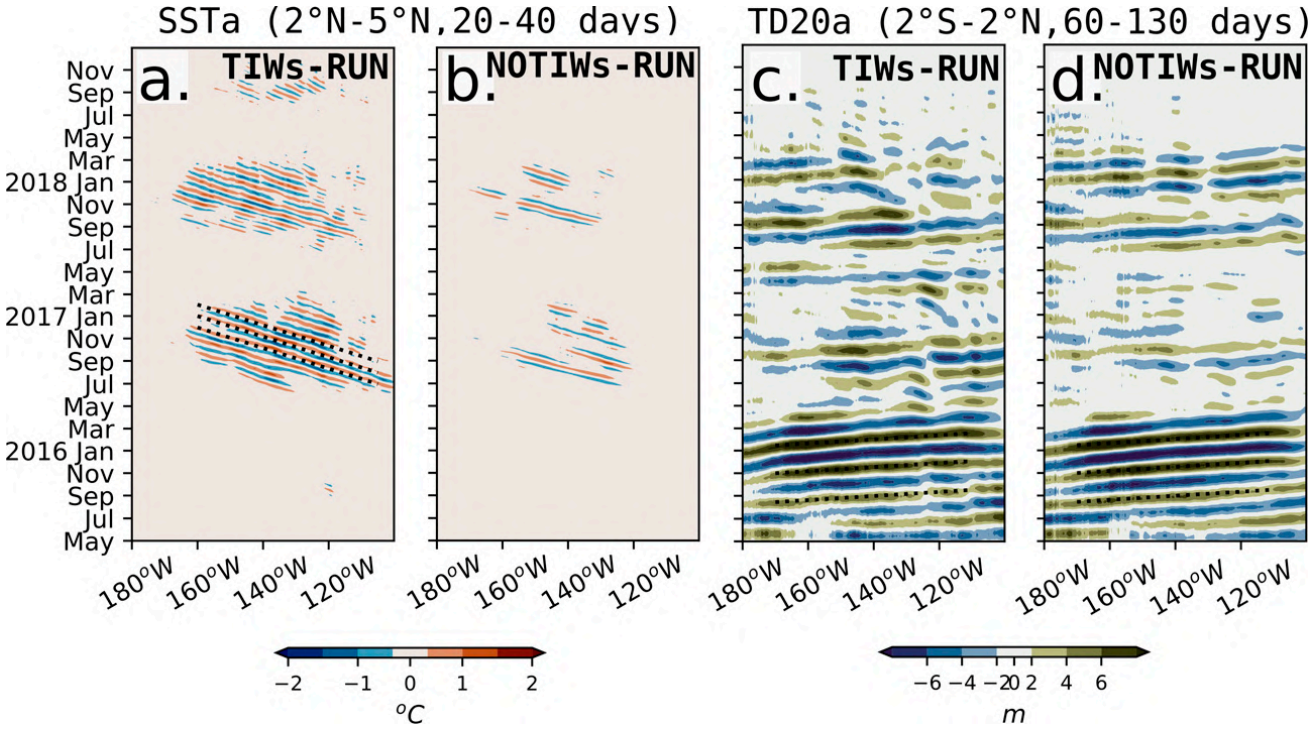

FIG. 7. Hovmöller diagrams of the 20–40 days bandpassed zonal SST anomalies averaged between 2° and 5°N for (a) TIWs-RUN and (b) NOTIWs-RUN between May 2015 and December 2017. Dotted lines represent the westward propagation at a 0.46 m s^{-1} phase speed. (c),(d) As in (a) and (b), but for the 20°C thermocline depth anomaly averaged in the 2°S–2°N latitudinal band and bandpassed between 60 and 130 days (i.e., the Kelvin waves dominant period range) for TIWs-RUN in (c) and NOTIWs-RUN in (d). Dotted lines represent the eastward propagation at a 2.3 m s^{-1} phase speed.

the differences observed between the two sensitivity experiments, which have the very same horizontal and vertical resolutions, will most likely originate from TIW-induced effects only.

5. TIW effects on the eastern tropical Pacific Ocean

The aim of this section is to investigate to which extent TIW activity alters the oceanic mean state. To do so and hereafter, TIW impacts will be assessed by subtracting NOTIWs-RUN to TIWs-RUN.

a. *Effects on the oceanic mean state*

TIW effects on mean temperature and circulation are shown in Fig. 8. At the surface, TIWs warm up the cold tongue by up to 0.4°C and cool down the surrounding waters by the same amount (Fig. 8a). In depth, the warming of the cold tongue spreads down to 150 m with a maximum of 0.50°C at 100 m while the cooling of southern and northern waters is constrained to the first 50 and 100 m, respectively (Fig. 8b).

The comparison between the two simulations also reveals a significant impact of TIWs on mean zonal and meridional currents amplitude (Figs. 8c,d), with an overall decrease of zonal currents intensity. In particular, at the subsurface, the eastward EUC is significantly reduced (by up to −0.20 m s^{-1} near the surface and −0.12 m s^{-1} in the core, i.e., more than 15%) and its upper limit is deepened from the surface to 25 m. The intensity of both the westward SEC located at the surface between 5°S and 3°N and NECC located near 7°N are also strongly reduced by −0.13 m s^{-1} (30%) and −0.06 m s^{-1} (20%), respectively. In contrast, TIWs lead to a slight increase of the equatorial Ekman divergence (oriented poleward in surface and equatorward in depth) in particular in the Northern Hemisphere by 0.02 m s^{-1} (20%) and 0.01 m s^{-1} (20%), as shown by the red shadings between 2° and 4°N, respectively.

b. *Energy exchange between oceanic mean state and TIWs*

As detailed by many others before (e.g., Qiao and Weisberg 1998; Masina and Philander 1999; Xue et al. 2021), the time evolution of long-term averaged EKE depends on the baroclinic (P_eK_e) and barotropic (K_mK_e) conversion rates, which are

$$P_eK_e = -\frac{g}{\rho_0}\overline{w'\rho'}, \tag{8}$$

$$K_mK_e = -[\overline{u'u'}\partial_x\overline{u} + \overline{u'v'}\partial_y\overline{u} + \overline{u'w'}\partial_z\overline{u} + \overline{u'v'}\partial_x\overline{v} + \overline{v'v'}\partial_y\overline{v} + \overline{v'w'}\partial_z\overline{v}] \simeq -\overline{u'v'}\partial_y\overline{u}, \tag{9}$$

where $g = 9.81$ m s^{-2} is the gravitational acceleration constant and $\rho_0 = 1025$ kg m^{-3}.

The spatial distributions of K_mK_e and P_eK_e, which represent the energy exchange from the mean kinetic energy and from the eddy available potential energy to the EKE, are

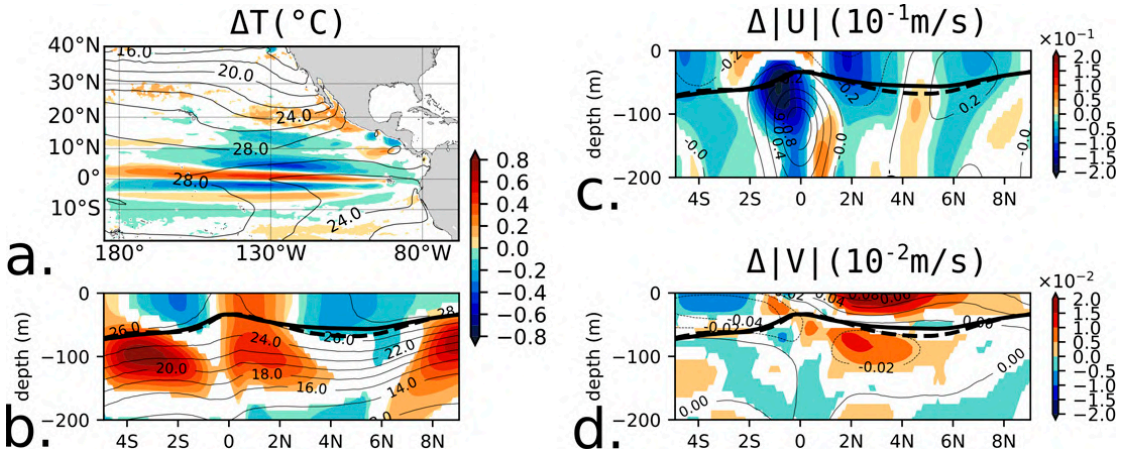

FIG. 8. Mean state differences between TIWs-RUN and NOTIWs-RUN for (a) sea surface temperature, (b) vertical section of temperature, (c) amplitude of zonal, and (d) meridional currents. Depth–latitude sections are averaged between 160° and 100°W. Only differences significant at the 99% confidence level (i.e., p value of the two-tailed Student's t test below 0.01) are displayed. Contours (every 2°C) show the mean values of temperature in the TIWs-RUN in (a) and (b), U every 0.2 m s^{-1} in (c), and V every 0.02 m s^{-1} interval (solid lines for positive and dashed lines for negative values) in (d). Thick black (dashed) line in (b)–(d) shows the mean mixed layer depth in TIWs-RUN (NOTIWs-RUN).

shown in contours in Fig. 9. Only the dominant barotropic term $-\overline{u'v'}\partial_y\overline{u}$ is shown here. Both are essentially positive (solid contours) and are increased when TIWs are present (indicated by the red shading), in particular in a zonal band north of the equator and over the first 100-m depth, indicating a source of EKE in the TIW region. The strong meridional gradient and weak stratification lead to large baroclinic conversion (Masina and Philander 1999), and the strong meridional shear of zonal currents, especially between the EUC and the northern branch of the SEC, leads to high barotropic conversion.

To complement this analysis, the rate of kinetic energy transfer across spatial scales is shown in Fig. 10 (for details on the computation, see, for instance, Marchesiello et al. 2011; Renault et al. 2019), where positive (negative) energy rates mean a transfer toward smaller (larger) scales. From 500 km to smaller scales, both experiments are characterized by a forward cascade of energy, i.e., a transfer of energy from the larger scales toward the smaller scales, which can be interpreted as the signature of submesoscale mixed layer eddies with scales of 50–200 km that form along TIW fronts as suggested by Marchesiello et al. (2011). The KE-flux spectrum at TIW scales (≈1000 km) displays negative transfer rates in the TIWs-RUN (black line) but positive values in the NOTIWs-RUN (orange line), indicating that TIWs are responsible for an inverse energy cascade, i.e., a transfer of energy from the TIWs to the larger-scale currents. This reveals a rectified effect of the TIWs onto the larger scale associated with the eastern tropical Pacific mean circulation. To sum up, this energy analysis confirms that TIWs play a central role in the energy budget of this region by in particular 1) harvesting energy from temperature meridional gradient through baroclinic instability, and from the meridional shear of currents through barotropic instability, therefore acting to reduce the mean zonal circulation,

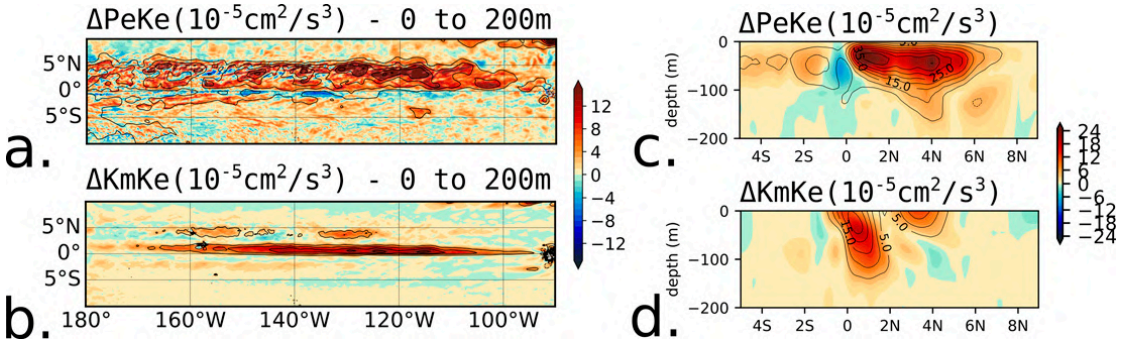

FIG. 9. Mean differences between TIWs-RUN and NOTIWs-RUN for (a),(c) baroclinic (P_eK_e) and (b),(d) dominant barotropic ($K_mK_e \simeq -\overline{u'v'}\partial_y\overline{u}$) conversion rates ($10^{-5}$ cm^2 s^{-3}). (left) Maps of conversion rates averaged over the first 200 m. (right) Depth–latitude sections averaged over 160°–100°W. Contours show the mean values of conversion rates in the TIWs-RUN every 5×10^{-5} cm^2 s^{-3} (solid lines for positive and dashed lines for negative values). A Gaussian smoothing of 1° radius was applied for maps in (b)–(d) and 5° radius for (a).

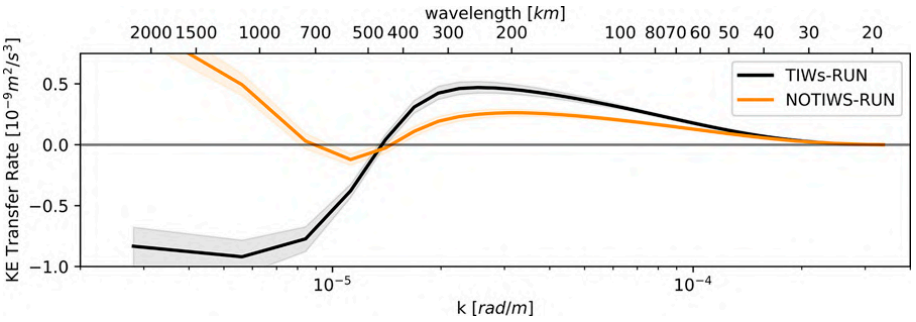

FIG. 10. Spectrum of KE transfer rate averaged between (160°–100°W, 10°S–10°N) and from surface to 50-m depth. Surfaces show the 95% confidence interval from a bootstrap method on annual averages (see section 2d).

and 2) injecting energy back into the larger scales through an inverse energy cascade responsible for a rectified effect onto the mean state.

c. *Quantification of direct and rectified effects of TIWs from a heat budget analysis*

To evaluate the mechanisms responsible for the direct and rectified effects of the TIWs onto the mean state, a heat budget is derived in both simulations. Additionally, to make a better physical sense of the TIW effects on the eastern Pacific mean state, the advection of temperature is separated into a mean and a fluctuating part through a Reynolds decomposition (see section 2e). The difference in the anomalous and mean advection terms between the two experiments will allow quantifying the TIW direct and rectified effects on the eastern tropical Pacific mean state.

The difference in the heat budget vertical structure averaged over 160°–100°W between the two simulations is presented in Fig. 11. The top panels represent the total advection, horizontal and vertical mixing (the horizontal term being negligible), and heating by atmospheric forcing terms. The other panels represent the decomposition of the advective terms into zonal, meridional, and vertical parts, and into total (X), mean (X_m), and fluctuating (X') parts.

At the surface, a compensating effect between mixing and heating by atmospheric forcing is observed with TIWs warming up the 0°–2°N band and cooling down the surrounding waters through mixing (Fig. 11b), while the forcing term exhibits

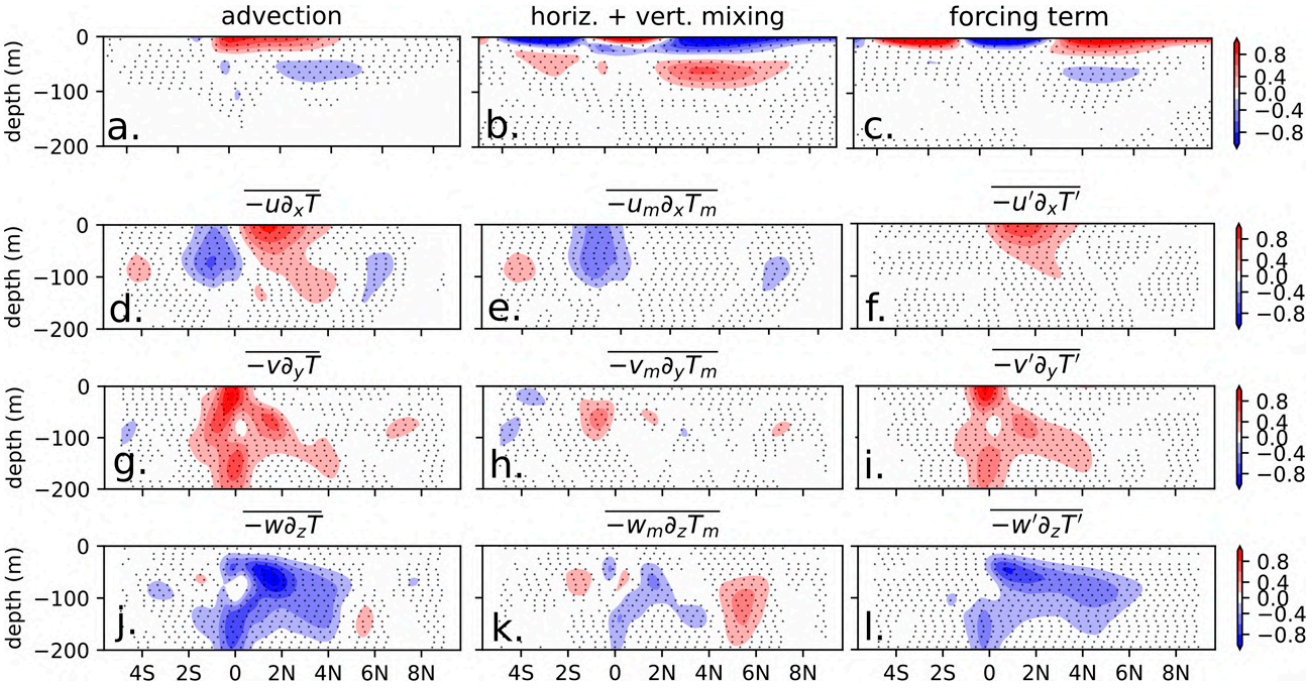

FIG. 11. Depth–latitude sections of TIW contribution to heat budget terms (i.e., TIWs-RUN minus NOTIWs-RUN; °C month^{-1}), averaged over 100°–160°W and over 40 years. Top three panels show the total (a) heat advection, (b) heat mixing, and (c) heating by atmospheric forcing terms. Other panels show the (d)–(f) zonal, (g)–(i) meridional, and (j)–(l) vertical terms of heat advection, decomposed into total parts in (d), (g), and (l); mean parts in (e), (h), and (k); and fluctuating parts in (f), (i), and (l). Dots show significant differences at the 99% confidence level (i.e., p value of the two-tailed Student's t test below 0.01).

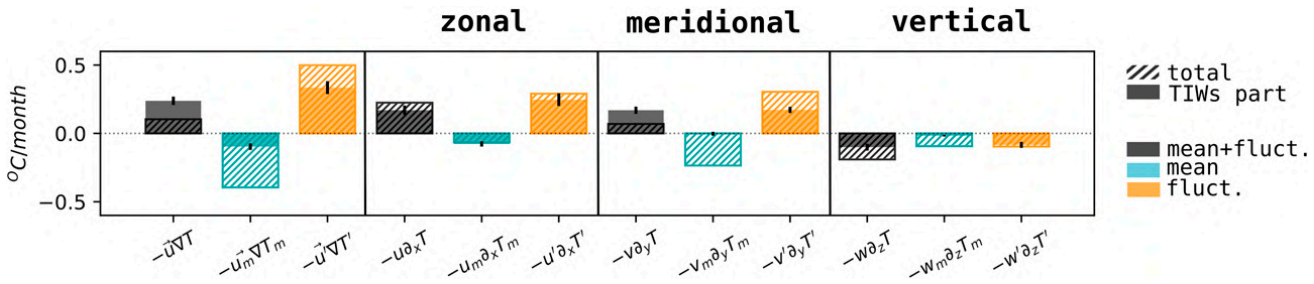

FIG. 12. Total (hatched) and residual heat advection (TIWs-RUN minus NOTIWs-RUN, plain color) averaged over 2°S–6°N and 160°–100°W, in the first 50 m. Black bars represent the total advection terms, blue bars the mean advection terms, and orange bars the fluctuating advection terms. Error bars stand for the ±1/2 annual standard deviation.

an opposite behavior (Fig. 11c). Yet, our approach does not allow assessing properly the effect of TIWs on atmospheric fluxes as the atmospheric forcing is prescribed. In the subsurface (between 50 and 100 m) TIWs tend to warm up northern waters through vertical mixing.

The overall TIW-induced advection leads to a warming of the 0°–4°N band, with a peak value of 0.8°C month^{-1} (Fig. 11a). The zonal component of TIW advection (Fig. 11d) is separated into a cooling over 2°S–0° through mean advection (i.e., rectified effect, Fig. 11e) and a warming over 0°–4°N through fluctuating advection (i.e., direct effect, Fig. 11f). The location of cooling by mean zonal advection is consistent with the weakening and deepening of the EUC by TIWs (Fig. 8c). As the presence of TIWs leads to a significant EUC weakening, less warm waters can be advected from the central-western Pacific, which could explain this cooling rectified effect. The meridional component of TIW advection (Fig. 11g) is almost fully explained by the warming through fluctuating meridional advection (Fig. 11i), which spreads from the surface to 200 m. In surface, it is constrained to the equatorial region (1°S–1°N) while it extends more meridionally with depth (2°S–4°N). The vertical component of TIW advection (Fig. 11j) cools down the 2°S–5°N band, from subsurface to 200 m. It is mostly due to fluctuating vertical advection (Fig. 11l), with only a small portion due to mean vertical advection (Fig. 11k). This highlights a complex interplay between potential changes in the upwelling/downwelling velocities and vertical temperature gradients. Unsurprisingly, the fluctuating part (i.e., the direct effect of TIWs) is found to be the largest near the surface concurrently with the large zonal and meridional fluctuating terms associated with the very strong zonal current shear (Fig. 8c) and meridional temperature gradient (Fig. 8b) concentrated in the mixed layer. The fluctuating vertical advection is constrained deeper, below the mixed layer, as found in Menkes et al. (2006).

The advection contribution to the heat budget averaged over the first 50 m and the cold tongue area (160°–100°W, 2°S–6°N) is shown in Fig. 12. This large band in latitude has been selected to be consistent with other studies such as Menkes et al. (2006). However, it should be kept in mind that there are latitudinal changes of advective components (in particular, the zonal component) within this band. The advection (gray bars) is decomposed into mean (blue) and fluctuating (orange) contributions. Hatched bars show the total value for TIWs-RUN, while plain color bars show the part due to TIWs (i.e., TIWs-RUN minus NOTIWs-RUN). Each term is decomposed into zonal, meridional, and vertical parts.

The total advection warms up the cold tongue by 0.10°C month^{-1} (hatched gray, $-\mathbf{u}\nabla T$). TIW contribution to this total advection is a warming by 0.24°C month^{-1} (plain gray, same term).

The fluctuating part leads to an overall net warming of the cold tongue by 0.50°C month^{-1} (hatched orange), 68% of which being attributed to TIW activity (plain orange). This direct TIW effect warms up the cold tongue via zonal (0.25°C month^{-1}) and meridional advection (0.17°C month^{-1}), and slightly cools it down through vertical advection (−0.08°C month^{-1}), resulting in a net warming by 0.34°C month^{-1}, which is consistent with previous studies (e.g., Menkes et al. 2006; Im et al. 2012; Graham 2014) yet a bit lower than in Menkes et al. (2006), for instance. While Menkes et al. (2006) used a simple Reynolds decomposition and attribute all the fluctuating part to the TIWs, other mesoscale processes might remain included in their analysis. The mechanisms leading to the TIWs-induced warming are explained in detail in Menkes et al. (2006) (see their Fig. 6 for a detailed sketch).

Advection by the mean flow cools down the cold tongue by 0.40°C month^{-1} (hatched blue in terms $-\mathbf{u}_m\nabla T_m$). As found in previous studies (e.g., Menkes et al. 2006) and in our data (not shown), it is a balance between the vertical advection (cooling in the equatorial upwelling and warming in the downwelling areas), meridional advection (Ekman divergence at the surface exporting cold water outside the cold tongue, and convergence in depth importing warm waters), and zonal advection (EUC bringing western warm waters in the cold tongue, SEC bringing eastern cold waters to a lesser extent). On average, the mean advection results in a cooling of the cold tongue through a subtle balance between currents and temperature gradients. Twenty-five percent of this cooling is attributed to the TIW rectified effect (−0.10°C month^{-1}, plain blue).

To summarize, on average, TIWs tend to warm up the cold tongue by 0.34°C month^{-1} through direct anomalous zonal and meridional heat advection, while their rectified effect leads to cooling by −0.10°C month^{-1} due to a reduction of mean zonal advection most likely associated with a significant weakening and deepening of the EUC. The combined TIW effects result in a net cold tongue warming by 0.24°C month^{-1}.

6. Summary and discussion

In this study, a new framework is introduced to isolate and quantify impacts of TIWs on the eastern tropical Pacific Ocean background state in a regional ocean model. This methodology is based upon the comparison between two eddy-rich sensitivity experiments, one (TIWs-RUN) reproducing realistically the regional mean state and circulation, as well as the essential TIW dynamics, and the other (NOTIWs-RUN) is identical but TIWs are damped online by nudging the meridional velocities toward their monthly climatology obtained from the TIWs-RUN. This method effectively prevents TIWs from growing and propagating, while keeping the rest of the equatorial dynamics and in particular Kelvin waves, a key dynamical feature of this region, unaltered.

By subtracting TIWs-RUN from NOTIWs-RUN, differences can mainly be attributed to TIW variability and can then be evidenced and quantified. In particular, two pathways are identified as source of changes: 1) a direct way, i.e., through TIW-induced mesoscale dynamics, and 2) a rectified way, i.e., through upscaling feedbacks from TIW variability back onto the mean state and circulation. On the one hand, TIWs are shown to pump up energy from the mean shear of zonal currents through barotropic conversion, which reduces the mean zonal circulation and in particular decreases the speed of the SEC, EUC, and NECC, respectively, by up to 30%, 15%, and 20%. On the other hand, this effect is also partly balanced by a reinjection of energy from TIWs back into the larger scales through an inverse energy cascade. Moreover, TIW activity is shown to reduce the meridional temperature gradient in the mixed layer, which tends to warm up the cold tongue and cool down surrounding warmer waters by up to 0.4°C on average.

To investigate the main physical processes behind this dual energy cascade, a heat budget has been derived in both simulations. A classic Reynolds decomposition, i.e., into mean and fluctuating terms, and their differences between the two sensitivity experiments allow disentangling and quantifying properly the TIW direct versus rectified effects. Overall, the anomalous fluctuations induced by TIW mesoscale and intraseasonal variability are shown to advect heat into the cold tongue at a rate of 0.34°C month^{-1}. A rectified effect of TIWs on the background state counterbalance this warming through the reduction of mean heat advection by −0.10°C month^{-1}. In total, TIWs are responsible for an advection of warm waters into the cold tongue of 0.24°C month^{-1}. The vertical advection of heat by TIWs is mainly located below the mixed layer, with a strong direct advection of cold waters.

Because TIWs are shown to strongly affect advection, their effect on the different components has been investigated in detail. This reveals that zonal and meridional eddy advection induce a warming of the cold tongue, which is in agreement with the literature (e.g., Kessler et al. 1998; Swenson and Hansen 1999; Jochum and Murtugudde 2006; Jochum et al. 2007; Menkes et al. 2006; Graham 2014). The rectified effect operates mostly via the reduction of mean zonal advection most likely associated with a significant decrease in the amplitude of the EUC.

Other components of the budget equations are also shown to play a not-so-insignificant role. In particular, in surface, TIW induced vertical mixing is responsible for a warming of the 0°–2°N band and a cooling of other surface waters. In depth (50–100 m), TIW-induced vertical mixing warms up the waters (Fig. 11b). Several studies have focus on the potential implication of TIWs in the modulation of vertical mixing (e.g., Lien et al. 2008; Moum et al. 2009; Holmes and Thomas 2015; Inoue et al. 2012, 2019; Cherian et al. 2021). From shipboard profiling measurements of turbulence kinetic-energy dissipation rate during an active TIW period at the equator, Moum et al. (2009) have revealed an important mixing rate induced by TIWs, leading to a cooling of the surface of 1°–2°C month^{-1}. Similarly, in an idealized 1D model, Holmes and Thomas (2015) have found a 0.6°C month^{-1} cooling of the surface due to the increase of turbulent heat fluxes by TIWs. This increase of turbulent heat flux is thought to be forced by an increased shear of the EUC due to TIWs. Recently, Cherian et al. (2021) used a 1/20° regional model of the cold tongue to demonstrate that the same mechanism takes place off-equator, in the TIW cold cusps. From an oceanic model, Menkes et al. (2006) also found an enhanced diffusivity in the cold cusps, and a reduced one in warm TIW areas, and their climatological heat budget of the cold tongue reveals a positive eddy mixing flux of 0.37°C month^{-1}. However, it should be stressed that in some studies such as Moum et al. (2009) and Wei et al. (2019), the atmospheric forcing is included in the vertical mixing term as its boundary condition in surface. In our study and others (e.g., Menkes et al. 2006; Graham 2014), the atmospheric forcing is an independent term, and the boundary condition of the vertical mixing rather depends on the wind stress. Regardless, the climatological effect of TIWs on the mixing part of the heat budget is thus still debated, and the present study tends to show a complex effect of TIW induced mixing with respect to depth and latitude. This mixing could have important implications on the oceanic biogeochemistry in this key region for the carbon cycle.

Using a forced ocean model enables us to quantify the oceanic response to changes in TIW activity. However, this approach has some limitations. In particular, using a regional forced oceanic model signifies that TIW imprint is still present in the atmospheric forcing (e.g., Seo et al. 2007; Small et al. 2009), which evidently leads to a discrepancy between the ocean state and the overlaying atmosphere.

Some studies have looked at the implication of TIWs in the ENSO asymmetry (i.e., stronger El Niños than La Niñas) (e.g., An 2008; Imada and Kimoto 2012; Graham 2014). The framework presented in this paper is an effective tool to diagnose the potential rectifying effect of TIWs onto ENSO, and to a larger extent on the seasonal and interannual variability of the climate of the eastern Pacific region. However, if Kelvin waves are kept untouched here, equatorial Rossby waves may have been impacted. As suggested by Bosc and Delcroix (2008), Rossby waves could participate to the recharge–discharge oscillator paradigm of ENSO dynamics, based on meridional advection of heat between equatorial and off-equatorial regions (Jin 1997a,b). Moreover, the atmospheric feedback is needed to accurately depict the ENSO coupled phenomenon and the interannual climate of the region. This is

a strong incentive to 1) use a coupled atmosphere–ocean regional model so that the atmosphere can react in a direct and rectified way to TIW variability, and 2) fine-tune the nudging framework to keep off-equatorial Rossby waves dynamics as unaltered as possible while efficiently removing TIWs. This work is ongoing and will be the purpose of a future study.

Acknowledgments. This project was supported by the French Agence Nationale de la Recherche project MOPGA "TROCODYN" (Grant ANR-17-MPGA-0018), the CNES TOSCA I-CASCADE and CARAMBA projects, and the MUSIC project funded by the Thomas Jefferson Fund of the FACE foundation and the Embassy of France in the United States. The authors would like to acknowledge the region Occitanie and the CALMIP center for providing access to their supercomputer Olympe. We would also like to thank two anonymous reviewers for their constructive comments.

Data availability statement. All presented data are available at https://doi.org/10.6084/m9.figshare.17129588. CFSR dataset: rda.ucar.edu/datasets/ds093.1. CFSv2 dataset: rda.ucar.edu/datasets/ds094.1. Johnson's climatology of currents: https://floats.pmel.noaa.gov/gregory-c-johnson-home-page. NOAA drifter-database: https://www.aoml.noaa.gov/phod/gdp/mean_velocity.php. NOAA Optimal Interpolation of SST version 2: https://www.emc.ncep.noaa.gov/research/cmb/sst_analysis/. SODA3.4.2 reanalysis: https://www2.atmos.umd.edu/%7Eocean/index_files/soda3.4.2_mn_download_b.htm. TropFlux products: https://incois.gov.in/tropflux/. COREv2 products: https://rda.ucar.edu/datasets/ds260.2/. CMEMS surface currents https://resources.marine.copernicus.eu/product-detail/MULTIOBS_GLO_PHY_REP_015_004/.

APPENDIX

Spatial Filter *G* for Nudging

The nudging is restrained to the TIW active region by applying a space-dependent function $G(x, y, z)$ to the nudging. It can be decomposed into individual functions of depth $J(z)$, longitude $H(x)$, and latitude $I(y)$:

$$G(x, y, z) = H(x)I(y)J(z). \tag{A1}$$

Depth $J(z)$ equals one from the surface down to z_1 = 100-m depth, then smoothly decreases and reaches zero at z_2 = 200-m depth and below (see Fig. 4c):

$$J(z) = \begin{cases} 1, & \text{if } z \le z1 \\ 3\left(\dfrac{z - z_2}{z_1 - z_2}\right)^2 - 2\left(\dfrac{z - z_2}{z_1 - z_2}\right)^3, & \text{if } z_1 \le z \le z_2. \\ 0, & \text{if } z \ge z_2 \end{cases} \tag{A2}$$

Longitude $H(x)$ equals one from the most western part of the region to x_1 = 90°W, then smoothly decreases and reaches zero at x_2 = 85°W and after:

$$H(x) = \begin{cases} 1, & \text{if } x \le x_1 \\ 3\left(\dfrac{x - x_2}{x_1 - x_2}\right)^2 - 2\left(\dfrac{x - x_2}{x_1 - x_2}\right)^3, & \text{if } x_1 \le x \le x_2. \\ 0, & \text{if } x \ge x_2 \end{cases} \tag{A3}$$

Latitude $I(y)$, given by Eq. (A4), is a Gaussian centered at μ = 1°N, with a standard deviation of σ = 10° latitude;

$$I(y) = \exp\left[-\frac{1}{2}\left(\frac{y - \mu}{\sigma}\right)^2\right]. \tag{A4}$$

Figure 4b shows the combination of these two functions $H(x) \times I(y)$.

REFERENCES

An, S.-I., 2008: Interannual variations of the tropical ocean instability wave and ENSO. *J. Climate*, **21**, 3680–3686, https://doi.org/10.1175/2008JCLI1701.1.

Barnett, T. P., 1983: Interaction of the monsoon and Pacific trade wind system at interannual time scales Part I: The equatorial zone. *Mon. Wea. Rev.*, **111**, 756–773, https://doi.org/10.1175/1520-0493(1983)111<0756:IOTMAP>2.0.CO;2.

Baturin, N. G., and P. P. Niiler, 1997: Effects of instability waves in the mixed layer of the equatorial Pacific. *J. Geophys. Res.*, **102**, 27 771–27 793, https://doi.org/10.1029/97JC02455.

Becker, J. J., and Coauthors, 2009: Global bathymetry and elevation data at 30 arc seconds resolution: SRTM30_PLUS. *Mar. Geod.*, **32**, 355–371, https://doi.org/10.1080/01490410903297766.

Bosc, C., and T. Delcroix, 2008: Observed equatorial Rossby waves and ENSO-related warm water volume changes in the equatorial Pacific Ocean. *J. Geophys. Res.*, **113**, C06003, https://doi.org/10.1029/2007JC004613.

Boucharel, J., and F.-F. Jin, 2020: A simple theory for the modulation of tropical instability waves by ENSO and the annual cycle. *Tellus*, **72A**, 1–14, https://doi.org/10.1080/16000870.2019.1700087.

——, A. Timmermann, and F.-F. Jin, 2013: Zonal phase propagation of ENSO sea surface temperature anomalies: Revisited. *Geophys. Res. Lett.*, **40**, 4048–4053, https://doi.org/10.1002/grl.50685.

——, F.-F. Jin, M. H. England, B. Dewitte, I. I. Lin, H.-C. Huang, and M. A. Balmaseda, 2016: Influence of oceanic intraseasonal Kelvin waves on eastern Pacific hurricane activity. *J. Climate*, **29**, 7941–7955, https://doi.org/10.1175/JCLI-D-16-0112.1.

Bryan, K., J. K. Dukowicz, and R. D. Smith, 1999: On the mixing coefficient in the parameterization of bolus velocity. *J. Phys. Oceanogr.*, **29**, 2442–2456, https://doi.org/10.1175/1520-0485(1999)029<2442:OTMCIT>2.0.CO;2.

Bryden, H. L., and E. C. Brady, 1989: Eddy momentum and heat fluxes and their effects on the circulation of the equatorial Pacific Ocean. *J. Mar. Res.*, **47**, 55–79, https://doi.org/10.1357/002224089785076389.

Cane, M., and E. Sarachik, 1977: Forced baroclinic ocean motions. II-the linear equatorial bounded case. *J. Mar. Res.*, **35**, 395–432,

Carton, J. A., G. A. Chepurin, L. Chen, S. Grodsky, E. Kalnay, and S. G. Penny, 2019: Soda project: SODA3 ensemble

means and standard deviations. Research Data Archive at the National Center for Atmospheric Research, Computational and Information Systems Laboratory, accessed March 2021, https://doi.org/10.5065/HBTB-R521.

Chavez, F. P., P. G. Strutton, G. E. Friederich, R. A. Feely, G. C. Feldman, D. G. Foley, and M. J. McPhaden, 1999: Biological and chemical response of the equatorial Pacific Ocean to the 1997–98 El Niño. *Science*, **286**, 2126–2131, https://doi.org/10.1126/science.286.5447.2126.

Chelton, D. B., and Coauthors, 2001: Observations of coupling between surface wind stress and sea surface temperature in the eastern tropical Pacific. *J. Climate*, **14**, 1479–1498, https://doi.org/10.1175/1520-0442(2001)014<1479:OOCBSW>2.0.CO;2.

Cherian, D. A., D. B. Whitt, R. M. Holmes, R.-C. Lien, S. D. Bachman, and W. G. Large, 2021: Off-equatorial deep-cycle turbulence forced by tropical instability waves in the equatorial Pacific. *J. Phys. Oceanogr.*, **51**, 1575–1593, https://doi.org/10.1175/JPO-D-20-0229.1.

Contreras, R. F., 2002: Long-term observations of tropical instability waves. *J. Phys. Oceanogr.*, **32**, 2715–2722, https://doi.org/10.1175/1520-0485(2002)032<2715:LTOOTI>2.0.CO;2.

Cox, M., 1980: Generation and propagation of 30-day waves in a numerical model of the Pacific. *J. Phys. Oceanogr.*, **10**, 1168–1186, https://doi.org/10.1175/1520-0485(1980)010<1168:GAPODW>2.0.CO;2.

Debreu, L., P. Marchesiello, P. Penven, and G. Cambon, 2012: Two-way nesting in split-explicit ocean models: Algorithms, implementation and validation. *Ocean Modell.*, **49–50**, 1–21, https://doi.org/10.1016/j.ocemod.2012.03.003.

Delpech, A., S. Cravatte, F. Marin, C. Ménesguen, and Y. Morel, 2020: Deep eddy kinetic energy in the tropical Pacific from Lagrangian floats. *J. Geophys. Res. Oceans*, **125**, e2020JC016313, https://doi.org/10.1029/2020JC016313.

Dolinar, E. K., X. Dong, and B. Xi, 2016: Evaluation and intercomparison of clouds, precipitation, and radiation budgets in recent reanalyses using satellite-surface observations. *Climate Dyn.*, **46**, 2123–2144, https://doi.org/10.1007/s00382-015-2693-z.

Düing, W., and Coauthors, 1975: Meanders and long waves in the equatorial Atlantic. *Nature*, **257**, 280–284, https://doi.org/10.1038/257280a0.

Escobar-Franco, M. G., J. Boucharel, and B. Dewitte, 2022: On the relationship between tropical instability waves and intraseasonal equatorial Kelvin waves in the Pacific from satellite observations (1993–2018). *Front. Mar. Sci.*, **9**, 788908, https://doi.org/10.3389/fmars.2022.788908.

Evans, W., P. G. Strutton, and F. P. Chavez, 2009: Impact of tropical instability waves on nutrient and chlorophyll distributions in the equatorial Pacific. *Deep-Sea Res. I*, **56**, 178–188, https://doi.org/10.1016/j.dsr.2008.08.008.

Fairall, C. W., E. F. Bradley, J. E. Hare, A. A. Grachev, and J. B. Edson, 2003: Bulk parameterization of air–sea fluxes: Updates and verification for the COARE algorithm. *J. Climate*, **16**, 571–591, https://doi.org/10.1175/1520-0442(2003)016<0571:BPOASF>2.0.CO;2.

Flament, P. J., S. C. Kennan, R. A. Knox, P. P. Niiler, and R. L. Bernstein, 1996: The three-dimensional structure of an upper ocean vortex in the tropical Pacific Ocean. *Nature*, **383**, 610–613, https://doi.org/10.1038/383610a0.

Gent, P. R., and J. C. Mcwilliams, 1990: Isopycnal mixing in ocean circulation models. *J. Phys. Oceanogr.*, **20**, 150–155, https://doi.org/10.1175/1520-0485(1990)020<0150:IMIOCM>2.0.CO;2.

——, J. Willebrand, T. J. McDougall, and J. C. McWilliams, 1995: Parameterizing eddy-induced tracer transports in ocean circulation models. *J. Phys. Oceanogr.*, **25**, 463–474, https://doi.org/10.1175/1520-0485(1995)025<0463:PEITTI>2.0.CO;2.

Giese, B. S., and D. E. Harrison, 1991: Eastern equatorial Pacific response to three composite westerly wind types. *J. Geophys. Res.*, **96**, 3239–3248, https://doi.org/10.1029/90JC01861.

Graham, T., 2014: The importance of eddy permitting model resolution for simulation of the heat budget of tropical instability waves. *Ocean Modell.*, **79**, 21–32, https://doi.org/10.1016/j.ocemod.2014.04.005.

Gushchina, D., and B. Dewitte, 2012: Intraseasonal tropical atmospheric variability associated with the two flavors of El Niño. *Mon. Wea. Rev.*, **140**, 3669–3681, https://doi.org/10.1175/MWR-D-11-00267.1.

Halpern, D., R. A. Knox, and D. S. Luther, 1988: Observations of 20-day period meridional current oscillations in the upper ocean along the Pacific equator. *J. Phys. Oceanogr.*, **18**, 1514–1534, https://doi.org/10.1175/1520-0485(1988)018<1514:OODPMC>2.0.CO;2.

Harrison, D. E., and B. S. Giese, 1988: Remote westerly wind forcing of the eastern equatorial Pacific; Some model results. *Geophys. Res. Lett.*, **15**, 804–807, https://doi.org/10.1029/GL015i008p00804.

Hashizume, H., S.-P. Xie, W. T. Liu, and K. Takeuchi, 2001: Local and remote atmospheric response to tropical instability waves: A global view from space. *J. Geophys. Res.*, **106**, 10 173–10 185, https://doi.org/10.1029/2000JD900684.

Holmes, R. M., and L. N. Thomas, 2015: The modulation of equatorial turbulence by tropical instability waves in a regional ocean model. *J. Phys. Oceanogr.*, **45**, 1155–1173, https://doi.org/10.1175/JPO-D-14-0209.1.

——, and ——, 2016: Modulation of tropical instability wave intensity by equatorial Kelvin waves. *J. Phys. Oceanogr.*, **46**, 2623–2643, https://doi.org/10.1175/JPO-D-16-0064.1.

Im, S.-H., S.-I. An, M. Lengaigne, and Y. Noh, 2012: Seasonality of tropical instability waves and its feedback to the seasonal cycle in the tropical eastern Pacific. *Sci. World J.*, **2012**, 612048, https://doi.org/10.1100/2012/612048.

Imada, Y., and M. Kimoto, 2012: Parameterization of tropical instability waves and examination of their impact on ENSO characteristics. *J. Climate*, **25**, 4568–4581, https://doi.org/10.1175/JCLI-D-11-00233.1.

Inoue, R., R.-C. Lien, and J. N. Moum, 2012: Modulation of equatorial turbulence by a tropical instability wave. *J. Geophys. Res.*, **117**, C10009, https://doi.org/10.1029/2011JC007767.

——, ——, ——, R. C. Perez, and M. C. Gregg, 2019: Variations of equatorial shear, stratification, and turbulence within a tropical instability wave cycle. *J. Geophys. Res. Oceans*, **124**, 1858–1875, https://doi.org/10.1029/2018JC014480.

Jin, F.-F., 1997a: An equatorial ocean recharge paradigm for ENSO. Part I: Conceptual model. *J. Atmos. Sci.*, **54**, 811–829, https://doi.org/10.1175/1520-0469(1997)054<0811:AEORPF>2.0.CO;2.

——, 1997b: An equatorial ocean recharge paradigm for ENSO. Part II: A stripped-down coupled model. *J. Atmos. Sci.*, **54**, 830–847, https://doi.org/10.1175/1520-0469(1997)054<0830:AEORPF>2.0.CO;2.

——, 2003: Strong El Niño events and nonlinear dynamical heating. *Geophys. Res. Lett.*, **30**, 1120, https://doi.org/10.1029/2002GL016356.

Jing, Z., L. Wu, D. Wu, and B. Qiu, 2014: Enhanced 2-h–8-day oscillations associated with tropical instability waves. *J. Phys. Oceanogr.*, **44**, 1908–1918, https://doi.org/10.1175/JPO-D-13-0189.1.

Jochum, M., and R. Murtugudde, 2006: Temperature advection by tropical instability waves. *J. Phys. Oceanogr.*, **36**, 592–605, https://doi.org/10.1175/JPO2870.1.

——, M. F. Cronin, W. S. Kessler, and D. Shea, 2007: Observed horizontal temperature advection by tropical instability waves. *Geophys. Res. Lett.*, **34**, L09604, https://doi.org/10.1029/2007GL029416.

Johnson, G. C., B. M. Sloyan, W. S. Kessler, and K. E. McTaggart, 2002: Direct measurements of upper ocean currents and water properties across the tropical Pacific during the 1990s. *Prog. Oceanogr.*, **52**, 31–61, https://doi.org/10.1016/S0079-6611(02)00021-6.

Kennan, S. C., and P. J. Flament, 2000: Observations of a tropical instability vortex. *J. Phys. Oceanogr.*, **30**, 2277–2301, https://doi.org/10.1175/1520-0485(2000)030<2277:OOATIV>2.0.CO;2.

Kessler, W. S., 2006: The circulation of the eastern tropical Pacific: A review. *Prog. Oceanogr.*, **69**, 181–217, https://doi.org/10.1016/j.pocean.2006.03.009.

——, L. M. Rothstein, and D. Chen, 1998: The annual cycle of SST in the eastern tropical Pacific, diagnosed in an ocean GCM. *J. Climate*, **11**, 777–799, https://doi.org/10.1175/1520-0442(1998)011<0777:TACOSI>2.0.CO;2.

Large, W. G., J. C. McWilliams, and S. C. Doney, 1994: Oceanic vertical mixing: A review and a model with a nonlocal boundary layer parameterization. *Rev. Geophys.*, **32**, 363, https://doi.org/10.1029/94RG01872.

Laurindo, L. C., A. J. Mariano, and R. Lumpkin, 2017: An improved near-surface velocity climatology for the global ocean from drifter observations. *Deep-Sea Res. I*, **124**, 73–92, https://doi.org/10.1016/j.dsr.2017.04.009.

Legeckis, R., 1977: Long waves in the eastern equatorial Pacific Ocean: A view from a geostationary satellite. *Science*, **197**, 1179–1181, https://doi.org/10.1126/science.197.4309.1179.

——, C. W. Brown, F. Bonjean, and E. S. Johnson, 2004: The influence of tropical instability waves on phytoplankton blooms in the wake of the Marquesas Islands during 1998 and on the currents observed during the drift of the Kon-Tiki in 1947. *Geophys. Res. Lett.*, **31**, L23307, https://doi.org/10.1029/2004GL021637.

Lien, R.-C., E. A. D'Asaro, and C. E. Menkes, 2008: Modulation of equatorial turbulence by tropical instability waves. *Geophys. Res. Lett.*, **35**, L24607, https://doi.org/10.1029/2008GL035860.

Lyman, J. M., G. C. Johnson, and W. S. Kessler, 2007: Distinct 17- and 33-day tropical instability waves in subsurface observations. *J. Phys. Oceanogr.*, **37**, 855–872, https://doi.org/10.1175/JPO3023.1.

Madden, R. A., and P. R. Julian, 1994: Observations of the 40–50-day tropical oscillation—A review. *Mon. Wea. Rev.*, **122**, 814–837, https://doi.org/10.1175/1520-0493(1994)122<0814:OOTDTO>2.0.CO;2.

Malardé, J.-P., C. Perigaud, P. D. Mey, and J.-F. Minster, 1987: Observation of long equatorial waves in the Pacific Ocean by SEASAT altimetry. *J. Phys. Oceanogr.*, **17**, 2273–2279, https://doi.org/10.1175/1520-0485(1987)017<2273:OOLEWI>2.0.CO;2.

Maloney, E. D., and J. T. Kiehl, 2002: MJO-related SST variations over the tropical eastern Pacific during Northern Hemisphere summer. *J. Climate*, **15**, 675–689, https://doi.org/10.1175/1520-0442(2002)015<0675:MRSVOT>2.0.CO;2.

Marchesiello, P., X. Capet, C. Menkes, and S. C. Kennan, 2011: Submesoscale dynamics in tropical instability waves. *Ocean Modell.*, **39**, 31–46, https://doi.org/10.1016/j.ocemod.2011.04.011.

Masina, S., and S. G. H. Philander, 1999: An analysis of tropical instability waves in a numerical model of the Pacific Ocean: 1. Spatial variability of the waves. *J. Geophys. Res.*, **104**, 29 613–29 635, https://doi.org/10.1029/1999JC900227.

——, ——, and A. B. G. Bush, 1999: An analysis of tropical instability waves in a numerical model of the Pacific Ocean: 2. Generation and energetics of the waves. *J. Geophys. Res.*, **104**, 29 637–29 661, https://doi.org/10.1029/1999JC900226.

McPhaden, M. J., 1996: Monthly period oscillations in the Pacific north equatorial countercurrent. *J. Geophys. Res.*, **101**, 6337–6359, https://doi.org/10.1029/95JC03620.

——, and X. Yu, 1999: Equatorial waves and the 1997–98 El Niño. *Geophys. Res. Lett.*, **26**, 2961–2964, https://doi.org/10.1029/1999GL004901.

Menkes, C. E. R., J. G. Vialard, S. C. Kennan, J.-P. Boulanger, and G. V. Madec, 2006: A modeling study of the impact of tropical instability waves on the heat budget of the eastern equatorial Pacific. *J. Phys. Oceanogr.*, **36**, 847–865, https://doi.org/10.1175/JPO2904.1.

Miller, L., D. R. Watts, and M. Wimbush, 1985: Oscillations of dynamic topography in the eastern equatorial Pacific. *J. Phys. Oceanogr.*, **15**, 1759–1770, https://doi.org/10.1175/1520-0485(1985)015<1759:OODTIT>2.0.CO;2.

Moum, J. N., R.-C. Lien, A. Perlin, J. D. Nash, M. C. Gregg, and P. J. Wiles, 2009: Sea surface cooling at the equator by subsurface mixing in tropical instability waves. *Nat. Geosci.*, **2**, 761–765, https://doi.org/10.1038/ngeo657.

Musman, S., 1989: Sea height wave form in equatorial waves and its interpretation. *J. Geophys. Res.*, **94**, 3303–3309, https://doi.org/10.1029/JC094iC03p03303.

Périgaud, C., 1990: Sea level oscillations observed with Geosat along the two shear fronts of the Pacific north equatorial countercurrent. *J. Geophys. Res.*, **95**, 7239–7248, https://doi.org/10.1029/JC095iC05p07239.

Philander, S. G. H., 1976: Instabilities of zonal equatorial currents. *J. Geophys. Res.*, **81**, 3725–3735, https://doi.org/10.1029/JC081i021p03725.

——, 1978: Instabilities of zonal equatorial currents, 2. *J. Geophys. Res.*, **83**, 3679–3682, https://doi.org/10.1029/JC083iC07p03679.

——, 1990: *El Niño, La Niña, and the Southern Oscillation.* Academic Press, 293 pp.

Praveen Kumar, B., J. Vialard, M. Lengaigne, V. S. N. Murty, and M. J. McPhaden, 2012: TropFlux: Air-sea fluxes for the global tropical oceans—Description and evaluation. *Climate Dyn.*, **38**, 1521–1543, https://doi.org/10.1007/s00382-011-1115-0.

Qiao, L., and R. H. Weisberg, 1995: Tropical instability wave kinematics: Observations from the tropical instability wave experiment. *J. Geophys. Res.*, **100**, 8677–8693, https://doi.org/10.1029/95JC00305.

——, and ——, 1998: Tropical instability wave energetics: Observations from the tropical instability wave experiment. *J. Phys. Oceanogr.*, **28**, 345–360, https://doi.org/10.1175/1520-0485(1998)028<0345:TIWEOF>2.0.CO;2.

Renault, L., M. J. Molemaker, J. C. Mcwilliams, A. F. Shchepetkin, F. Lemari, D. Chelton, S. Illig, and A. Hall, 2016: Modulation of wind work by oceanic current interaction with the atmosphere. *J. Phys. Oceanogr.*, **46**, 1685–1704, https://doi.org/10.1175/JPO-D-15-0232.1.

——, P. Marchesiello, S. Masson, and J. C. McWilliams, 2019: Remarkable control of western boundary currents by *eddy killing,* a mechanical air-sea coupling process. *Geophys. Res. Lett.*, **46**, 2743–2751, https://doi.org/10.1029/2018GL081211.

——, S. Masson, T. Arsouze, G. Madec, and J. C. McWilliams, 2020: Recipes for how to force oceanic model dynamics. *J. Adv. Model. Earth Syst.*, **12**, e2019MS001715, https://doi.org/10.1029/2019MS001715.

Rio, M.-H., S. Mulet, and N. Picot, 2014: Beyond GOCE for the ocean circulation estimate: Synergetic use of altimetry, gravimetry, and in situ data provides new insight into geostrophic and Ekman currents. *Geophys. Res. Lett.*, **41**, 8918–8925, https://doi.org/10.1002/2014GL061773.

Roberts, M. J., and Coauthors, 2004: Impact of an eddy-permitting ocean resolution on control and climate change simulations with a global coupled GCM. *J. Climate*, **17**, 3–20, https://doi.org/10.1175/1520-0442(2004)017<0003:IOAEOR>2.0.CO;2.

——, and Coauthors, 2009: Impact of resolution on the tropical Pacific circulation in a matrix of coupled models. *J. Climate*, **22**, 2541–2556, https://doi.org/10.1175/2008JCLI2537.1.

Saha, S., and Coauthors, 2010: NCEP Climate Forecast System Reanalysis (CFSR) selected hourly time-series products, January 1979 to December 2010. Research Data Archive at the National Center for Atmospheric Research, Computational and Information Systems Laboratory, accessed February 2021, https://doi.org/10.5065/D6513W89.

——, and Coauthors, 2011: NCEP Climate Forecast System version 2 (CFSV2) selected hourly time-series products. Research Data Archive at the National Center for Atmospheric Research, Computational and Information Systems Laboratory, accessed February 2021, https://doi.org/10.5065/D6N877VB.

Seo, H., M. Jochum, R. Murtugudde, A. J. Miller, and J. O. Roads, 2007: Feedback of tropical instability-wave-induced atmospheric variability onto the ocean. *J. Climate*, **20**, 5842–5855, https://doi.org/10.1175/JCLI4330.1.

Shchepetkin, A. F., 2015: An adaptive, Courant-number-dependent implicit scheme for vertical advection in oceanic modeling. *Ocean Modell.*, **91**, 38–69, https://doi.org/10.1016/j.ocemod.2015.03.006.

——, and J. C. McWilliams, 2005: The Regional Oceanic Modeling System (ROMS): A split-explicit, free-surface, topography-following-coordinate oceanic model. *Ocean Modell.*, **9**, 347–404, https://doi.org/10.1016/j.ocemod.2004.08.002.

——, and ——, 2009: Correction and commentary for "Ocean fore-casting in terrain-following coordinates: Formulation and skill assessment of the regional ocean modeling system" by Haidvogel et al., J. Comp. Phys. 227, pp. 3595–3624. *J. Comput. Phys.*, **228**, 8985–9000, https://doi.org/10.1016/j.jcp.2009.09.002.

Small, R. J., K. J. Richards, S.-P. Xie, P. Dutrieux, and T. Miyama, 2009: Damping of tropical instability waves caused by the action of surface currents on stress. *J. Geophys. Res.*, **114**, C04009, https://doi.org/10.1029/2008JC005147.

Strutton, P. G., J. P. Ryan, and F. P. Chavez, 2001: Enhanced chlorophyll associated with tropical instability waves in the equatorial Pacific. *Geophys. Res. Lett.*, **28**, 2005–2008, https://doi.org/10.1029/2000GL012166.

Swenson, M. S., and D. V. Hansen, 1999: Tropical Pacific Ocean mixed layer heat budget: The Pacific cold tongue. *J. Phys. Oceanogr.*, **29**, 69–81, https://doi.org/10.1175/1520-0485(1999)029<0069:TPOMLH>2.0.CO;2.

Tanaka, Y., and T. Hibiya, 2019: Generation mechanism of tropical instability waves in the equatorial Pacific Ocean. *J. Phys. Oceanogr.*, **49**, 2901–2915, https://doi.org/10.1175/JPO-D-19-0094.1.

Taylor, K. E., 2001: Summarizing multiple aspects of model performance in a single diagram. *J. Geophys. Res.*, **106**, 7183–7192, https://doi.org/10.1029/2000JD900719.

Valdivieso, M., and Coauthors, 2017: An assessment of air–sea heat fluxes from ocean and coupled reanalyses. *Climate Dyn.*, **49**, 983–1008, https://doi.org/10.1007/s00382-015-2843-3.

Vialard, J. R. M., C. Menkes, J.-P. Boulanger, P. Delecluse, E. Guilyardi, M. J. Mcphaden, and G. Madec, 2001: A model study of oceanic mechanisms affecting equatorial Pacific sea surface temperature during the 1997–98 El Niño. *J. Phys. Oceanogr.*, **31**, 1649–1675, https://doi.org/10.1175/1520-0485(2001)031<1649:AMSOOM>2.0.CO;2.

von Schuckmann, K., P. Brandt, and C. Eden, 2008: Generation of tropical instability waves in the Atlantic Ocean. *J. Geophys. Res.*, **113**, C08034, https://doi.org/10.1029/2007JC004712.

Wang, C., and P. C. Fiedler, 2006: ENSO variability and the eastern tropical Pacific: A review. *Prog. Oceanogr.*, **69**, 239–266, https://doi.org/10.1016/j.pocean.2006.03.004.

Wang, M., Y. Du, B. Qiu, X. Cheng, Y. Luo, X. Chen, and M. Feng, 2017: Mechanism of seasonal eddy kinetic energy variability in the eastern equatorial Pacific Ocean. *J. Geophys. Res. Oceans*, **122**, 3240–3252, https://doi.org/10.1002/2017JC012711.

——, ——, ——, S.-P. Xie, and M. Feng, 2019: Dynamics on seasonal variability of EKE associated with TIWs in the eastern equatorial Pacific Ocean. *J. Phys. Oceanogr.*, **49**, 1503–1519, https://doi.org/10.1175/JPO-D-18-0163.1.

——, S.-P. Xie, S. S. P. Shen, and Y. Du, 2020: Rossby and Yanai modes of tropical instability waves in the equatorial Pacific Ocean and a diagnostic model for surface currents. *J. Phys. Oceanogr.*, **50**, 3009–3024, https://doi.org/10.1175/JPO-D-20-0063.1.

Wang, W., P. Xie, S.-H. Yoo, Y. Xue, A. Kumar, and X. Wu, 2011: An assessment of the surface climate in the NCEP Climate Forecast System Reanalysis. *Climate Dyn.*, **37**, 1601–1620, https://doi.org/10.1007/s00382-010-0935-7.

Warner, S. J., R. M. Holmes, E. H. M. Hawkins, M. S. Hoecker-Martínez, A. C. Savage, and J. N. Moum, 2018: Buoyant gravity currents released from tropical instability waves. *J. Phys. Oceanogr.*, **48**, 361–382, https://doi.org/10.1175/JPO-D-17-0144.1.

Wei, Y., Y. Pei, and X. Kang, 2019: Assessing feedback of tropical instability wave-induced wind stress perturbations in the equatorial Pacific. *Int. J. Climatol.*, **39**, 1634–1643, https://doi.org/10.1002/joc.5906.

Xie, S.-P., M. Ishiwatari, H. Hashizume, and K. Takeuchi, 1998: Coupled ocean-atmospheric waves on the equatorial front. *Geophys. Res. Lett.*, **25**, 3863–3866, https://doi.org/10.1029/1998GL900014.

Xue, A., F.-F. Jin, W. Zhang, J. Boucharel, S. Zhao, and X. Yuan, 2020: Delineating the seasonally modulated nonlinear feedback onto ENSO from tropical instability waves. *Geophys. Res. Lett.*, **47**, e2019GL085863, https://doi.org/10.1029/2019GL085863.

——, W. Zhang, J. Boucharel, and F.-F. Jin, 2021: Anomalous tropical instability wave activity hindered the development of the 2016/17 La Niña. *J. Climate*, **34**, 5583–5600, https://doi.org/10.1175/JCLI-D-20-0399.1.

Yeager, S. G., and W. G. Large, 2008: CORE.2 global air-sea flux dataset. Research Data Archive at the National Center for Atmospheric Research, Computational and Information Systems Laboratory, accessed May 2021, https://doi.org/10.5065/D6WH2N0S.

Yoder, J. A., S. G. Ackleson, R. T. Barber, P. Flament, and W. M. Balch, 1994: A line in the sea. *Nature*, **371**, 689–692, https://doi.org/10.1038/371689a0.

Yu, J.-Y., and W. T. Liu, 2003: A linear relationship between ENSO intensity and tropical instability wave activity in the eastern Pacific Ocean. *Geophys. Res. Lett.*, **30**, 1735, https://doi.org/10.1029/2003GL017176.

Yu, Z., J. P. McCreary, and J. A. Proehl, 1995: Meridional asymmetry and energetics of tropical instability waves. *J. Phys. Oceanogr.*, **25**, 2997–3007, https://doi.org/10.1175/1520-0485(1995)025<2997:MAAEOT>2.0.CO;2.

3.3 Conclusion

3.3.1 Summary

This work quantifies the thermodynamic changes of the background state induced by TIWs. In particular, TIWs warm the SST in the cold tongue by up to 0.4°C, and cool surrounding waters by the same amount. TIWs also reduce the strength of zonal currents, with a reduction of the EUC by up to -0.20 m.s^{-1} near the surface and -0.12 m.s^{-1} in the core, which corresponds to more than 15% of its strength. I then identify, using a kinetic energy transfer diagnostic and a heat budget analysis, a direct and indirect (or rectified) TIW effect on the eastern tropical Pacific mean state. The definition of these effects is the following:

- the **direct effect** of TIWs corresponds to the instantaneous nonlinear eddy processes (*e.g.,* $v'T'$ where prime indicates intraseasonal anomalies) and the time-integration of these instantaneous fields (*e.g.,* $\overline{v'T'}$ where $\bar{\cdot}$ denotes a long-term average). This effect will potentially affect the large scale thermodynamics of the Ocean.
- The rectification of the large scale thermodynamics due to the direct effect of TIWs can then lead to other large scale changes, which is defined as an **indirect or rectified effect** of TIWs.

In particular, I show that while the direct effect of TIWs tends to warm the cold tongue through horizontal heat advection, the weakening of the Equatorial Undercurrent by TIWs leads to a rectified cooling feedback on the cold tongue. To our knowledge, this effect has not been documented before. In their study, Imada and Kimoto (2012) parameterize the TIW heat flux effect by adapting the lateral diffusion to large scale features such as the latitude, the horizontal mean currents, and stratification. In their paper, the authors did not look at the impact of this parameterization on zonal currents, but it could be interesting to see if improving TIW heat fluxes could also improve their large scale effect on the mean circulation. Nevertheless, this effect should be accounted for in the future generations of climate models through development of new TIW parameterizations or improvement of existing ones.

3.3.2 Author contributions

This is a collaborative work between my PhD advisors J. Boucharel and L. Renault, and myself. The conceptualization of the study has been initially imagined by J. Boucharel and L. Renault. I performed the simulations, the processing of the data and the original writing of the draft. We all contributed to improving the methodology, discussing the results and improving the article.

Chapter 4

TIWs & the Seasonal Cycle

Contents

4.1 Preamble

In 2021, the 2-year project "MUlti Scale Interactions in the PacifiC (MUSIC)" led by J. Boucharel, L. Renault and M. Stuecker was funded by the Thomas Jefferson fund of the French-American Cultural Exchange in Education and the Arts foundation. It aims at understanding how modes of climate variability, such as ENSO, the annual cycle, and TIWs, interact with each others in the eastern tropical Pacific. The ultimate goal is to develop parameterization of TIWs to be implemented in GCMs, in order to reduce mean state bias and improve the simulation of ENSO dynamics. As part of this project, I had the opportunity to visit the University of Hawai'i for several weeks and collaborate with climate scientists M. Stuecker and F.-F. Jin. This collaboration resulted in a study on the multi-scale interactions between the eastern tropical Pacific ocean seasonal cycle and TIWs.

The annual cycle of equatorial oceanic features in the Pacific is modulated by external forcing, such as solar heating and winds (Kessler (2006)), and by oceanic processes such as mixing (Moum et al. (2013)). Large scale events like ENSO have been shown to non-linearly interact with the annual cycle, leading to a modulation in the frequency of occurrence of these events (Stuecker et al. (2013)). Characterizing and quantifying the processes that impact the annual cycle of the main thermal and dynamical features of the tropical Pacific Ocean is a necessary step toward improving our understanding of ENSO and multi-scale interactions in the basin.

In this work, published in *Geophysical Research Letters*, I use the same set of forced ocean-only simulations described in Chapter 3 to assess the impact of TIWs on the eastern tropical Pacific seasonal variability. I also test the ability of a low horizontal resolution simulation of 1° in reproducing TIW-induced modulations of the eastern equatorial Pacific seasonal cycle, and a similar simulation without nonlinear terms, to test a less subtle technique for TIW damping. Hereafter, a copy of the study is provided as well as a summary of the main results.

4.2 Paper published in *Geophysical Research Letters*

Maillard, L., Boucharel, J., Stuecker, M. F., Jin, F.-F., & Renault, L. (2022). Modulation of the eastern equatorial Pacific seasonal cycle by tropical instability waves. Geophysical Research Letters, 49, e2022GL100991. https://doi.org/10.1029/2022GL100991

Modulation of the Eastern Equatorial Pacific Seasonal Cycle by Tropical Instability Waves

L. Maillard[1], J. Boucharel[1,2], M. F. Stuecker[3], F.-F. Jin[2], L. Renault[1]

[1]LEGOS, University of Toulouse, IRD, CNRS, CNES, UPS, Toulouse, France

[2]Department of Atmospheric Sciences, School of Ocean and Earth Science and Technology (SOEST), University of Hawai'i at Mānoa, Honolulu, HI, USA

[3] Department of Oceanography and International Pacific Research Center (IPRC), School of Ocean and Earth Science and Technology (SOEST), University of Hawai'i at Mānoa, Honolulu, HI, USA

Key Points:

- Feedbacks from Tropical Instability Waves (TIWs) on the eastern equatorial Pacific Ocean seasonal cycle are quantified.
- TIWs reduce the amplitude of the upper equatorial ocean temperature seasonal cycle by warming equatorial waters in boreal summer and fall.
- TIWs stabilize and weaken the upper Equatorial Undercurrent year-round and prevent its re-intensification in boreal fall.

Corresponding author: Lisa Maillard, `lisa.maillard@univ-tlse3.fr`

Abstract

Feedbacks from Tropical Instability Waves (TIWs) on the seasonal cycle of the eastern Pacific Ocean are studied using two eddy-rich ocean simulations, with and without TIWs. By warming the equatorial waters by up to 0.4 °C through nonlinear advection in boreal summer and fall, TIWs reduce the amplitude of the seasonal cycle in upper ocean temperatures. In addition, TIWs stabilize the upper part of the Equatorial Undercurrent (EUC) through enhanced barotropic energy conversion, leading to a year-round weakening by -0.15 m.s^{-1} and preventing an unrealistic re-intensification in boreal fall usually found in non-eddy resolving models. A coarser simulation at 1-degree horizontal resolution fails to reproduce the TIW-induced nonlinear warming of equatorial waters, but succeeds in inhibiting the EUC re-intensification. This suggests a threshold effect in TIW strength, associated with the model's ability to simulate eddies, which may be responsible for long-standing biases displayed by global climate models in this region.

Plain Language Summary

Tropical Instability Waves (TIWs) are meandering ocean waves that originate off the coast of Ecuador between June and December and propagate in the eastern equatorial Pacific Ocean. By mixing cold equatorial with warm off-equatorial waters, TIWs influence the climate of this key region for the global carbon cycle. In this study, we use a regional ocean model to quantify the impact of these waves on the upper-ocean seasonal cycle. We find that TIWs do not interact in the same way with ocean surface temperatures and currents. TIWs warm surface equatorial waters during the boreal summer and fall, reducing the amplitude of the seasonal temperature cycle. In contrast, TIWs reduce the strength of one of the strongest Pacific equatorial currents – the Equatorial Undercurrent – all year long. Moreover, TIWs prevent an unrealistic re-intensification of this current in boreal fall often found in models unable to simulate these waves accurately. In particular, we provide evidence that the horizontal resolution of most climate models is not sufficient to simulate accurately TIW impacts on the Pacific Ocean, particularly its temperatures. These findings highlight the necessity to incorporate TIW effects in the future generation of global climate models, via enhanced parameterization or increased horizontal resolution.

1 Introduction

Tropical Instability Waves (TIWs) are long waves with wavelength of 800-2,000 km and period of 15-40 days (Qiao & Weisberg, 1995; Lyman et al., 2007), that propagate westward at the surface of the equatorial Pacific Ocean. They are observed through meanders of surface tracers such as temperature, salinity and oxygen (Legeckis, 1977; Lee et al., 2012), and alternating cusps of meridional velocities (Düing et al., 1975; Qiao & Weisberg, 1995), sea surface height (Miller et al., 1985; Escobar-Franco et al., 2022), and winds (Xie et al., 1998; Chelton et al., 2001).

TIWs represent the dominant form of oceanic mesoscale activity in the tropics. They are generated by baroclinic and barotropic conversions of energy that are respectively related to the mean meridional gradient of temperature between the cold equatorial upwelled water and the surrounding warm tropical waters (Cox, 1980; Z. Yu et al., 1995; Masina et al., 1999), and to the meridional shear of zonal equatorial currents (Philander, 1976, 1978).

TIWs modulate the climate variability of the tropical Pacific through complex two-way interactions over a wide range of timescales, from intraseasonal to interannual. For instance, TIWs warm the cold tongue and reduce the meridional gradient of temperature in a direct way, mostly via meridional Nonlinear Dynamical Heating (NDH, *i.e.,* advection of anomalous temperatures by anomalous currents. See Menkes et al., 2006; Im et al., 2012; Graham, 2014). They also reduce the average strength of equatorial currents and in particular the EUC. This reduces the volume of warm subsurface water brought from the western Pacific into the cold tongue, leading to a rectified cooling effect that partly counterbalances the direct TIW warming through NDH (Maillard et al., 2022). By modulating the heat and momentum budgets, TIWs have a complex impact on the mean flow of active and passive tracers, which together with their strong effect on the vertical oceanic mixing (Lien et al., 2008; Moum et al., 2009; Inoue et al., 2012; Holmes & Thomas, 2015) can substantially influence biogeochemical properties (Eddebbar et al., 2021) in this key region for ecosystems and the global carbon cycle (Takahashi et al., 2009).

TIWs are also at the heart of another well-known nonlinear interaction between intraseasonal timescales and the El Niño-Southern Oscillation (ENSO), the strongest driver of interannual variability in this region. ENSO modulates TIW activity, enhancing it during La Niña and decreasing it during El Niño (W. Wang & McPhaden, 2000, 2001; An, 2008). In turn, TIWs warm the cold tongue more during La Niña than El Niño, leading

to an asymmetric negative feedback that may partially explain the observed asymmetry in ENSO amplitude (*e.g.,* Vialard et al., 2001; An & Jin, 2004; An, 2008). More recently, Boucharel and Jin (2020) developed an analytical formulation of the amplitude of TIWs that is modulated by both ENSO and the seasonal cycle. This formulation successfully reproduces the feedback of TIWs on ENSO, through the seasonal modulation of the NDH generated by TIWs (Xue et al., 2020, 2021). These studies highlight the central role played by the seasonal cycle in these multi-scale interactions between ENSO, TIWs, and the climate background state.

Despite a roughly constant equatorial solar shortwave heat flux, the equatorial sea surface temperature (SST) and zonal currents have a pronounced seasonal cycle. TIWs are therefore modulated at seasonal timescales (Von Schuckmann et al., 2008; Im et al., 2012; M. Wang et al., 2019). The intensification of trade winds above the cold tongue region during the second half of the calendar year increases the equatorial upwelling and meridional temperature gradient and strengthens the South Equatorial Current, enhancing TIW activity from July to February (*e.g.,* Contreras, 2002). However, the feedback of TIWs onto the eastern Pacific seasonal cycle has received much less attention since the seminal study by Im et al. (2012). Using an eddy-permitting ocean model, they suggested that the intensified TIW activity in boreal summer and fall warms the eastern equatorial Pacific SST due to in-phase NDH, by up to 1 °C month^{-1} during the active TIW period. This feedback between seasonal and intraseasonal variability requires a more in-depth study to fully understand the complex multi-scale interactions at the heart of which TIWs are embedded.

In this study, we build up on the methodology developed and validated in Maillard et al. (2022) to evaluate and quantify TIW effects on the seasonal variations of the eastern equatorial Pacific thermo-dynamical properties. More specifically, we compare twin long-term regional 1/12° ocean simulations in which TIWs freely develop (TIW-RUN) or are removed (NOTIW-RUN). This technique allows us to explicitly quantify the rectified effects of TIWs on the seasonal cycle of the main thermal and dynamical features. We also compare two additional coarser resolution simulations (1° horizontal resolution), with (LR-RUN) and without non-linear terms in the momentum equation (NONL-RUN) to investigate to which extent low-resolution simulations with distinctly degraded TIW activity can reproduce the TIW-induced modulation of the eastern Pacific seasonal cycle. In the first result section, we show that the control TIW-RUN reproduces well the main characteristics of the observed

TIW seasonal cycle. In section 2, we focus on the impact of TIWs on the seasonal cycle of thermal and thermo-dynamical features of the upper ocean. The third section details the impact of TIWs on the seasonal cycle of dynamical features, with a particular emphasis on the EUC. The last section summarizes and discusses our results.

2 Model and Methods

The numerical model and configurations are the ones employed in Maillard et al. (2022), and the following model descriptions are derived from it with minor modifications. The reader is invited to refer to that study for more details.

Ocean model simulations were performed using the coastal and regional ocean community model (CROCO, Shchepetkin & McWilliams, 2005, 2009; Debreu et al., 2012; Shchepetkin, 2015). CROCO is a free-surface, terrain-following coordinate model with split-explicit time stepping and with Boussinesq and hydrostatic approximations. CROCO is implemented over the eastern tropical Pacific ocean ($20°\mathrm{S}-40°\mathrm{N}$, $185°-68°\mathrm{W}$). Tracers, surface elevation, and horizontal velocity initial and boundary information are derived from the Simple Ocean Data Assimilation 5-day reanalysis (SODA v3.4.2 on a $1/4° \times 1/4°$ horizontal grid, Carton et al., 2018). The bathymetry is obtained from the Shuttle Radar Topography Mission (SRTM30 plus, Becker et al., 2009). The terrain-following configuration has 50 vertical σ-levels, with stretching surface and bottom parameters of $\theta_s = 7$, $\theta_b = 2$, and $h_{cline} = 200$ m. The K-profile parameterization is used to compute the vertical mixing of tracers and momentum (KPP; Large et al., 1994). The surface freshwater, heat, and momentum fluxes are estimated using the COARE bulk formulas (Fairall et al., 2003) with a surface stress-correction approach described in Renault et al. (2016, 2020). The precipitation rate, the wind field at 10-m, the shortwave and longwave radiation flux, and the temperature and specific humidity at 2-m are derived from the hourly Climate Forecast System Reanalysis (CFSR and CFSv2, Saha et al., 2010, 2011).

Four simulations are performed after a spin up of 7 years, and each four configurations is detailed hereafter and in Table S1. A set of two eddy-rich ($dx = 1/12°$) simulations is carried out:

- TIW-RUN, in which TIWs are free to develop and propagate;
- NOTIW-RUN, in which TIWs are damped. One more year of spin up is done for this simulation to ensure its stabilization.

Following Maillard et al. (2022), in NOTIW-RUN, to damp TIWs, the meridional currents v in the region of active TIWs are nudged online toward their monthly climatology calculated from TIW-RUN. This methodology removes most of TIW activity while keeping the equatorial dynamics and in particular the Kelvin wave activity mostly untouched. Indeed, only the amplitude of Kelvin waves is slightly different between TIW- and NOTIW-RUN (see Maillard et al. (2022), their Fig. 7c,d), which might be due to the TIW-Kelvin wave interactions (Holmes & Thomas, 2016; Escobar-Franco et al., 2022) or to the TIW-induced modification of the mean state. These two eddy-rich simulations are used to isolate the effect of TIWs on the ocean mean state, by subtracting the NOTIW-RUN from the TIW-RUN. Another set of two coarse-resolution ($dx = 1°$) simulations is performed:

- LR-RUN is used to test the ability of a model with similar horizontal resolution as most climate models used in the Coupled Model Intercomparison Project Phase 6 (CMIP6, Eyring et al., 2016) to reproduce TIW-induced modulations of the eastern equatorial Pacific seasonal cycle.
- NONL-RUN, in which non-linear terms in the momentum balance equation are disabled (see Gruber et al., 2011) largely reducing TIW activity through a less subtle technique.

3 Results

3.1 TIW Seasonality in the Ocean Model

To evaluate the ability of the TIW-RUN to reproduce TIW variability, we compare simulated and observed variances of intraseasonal anomalies of SST (SST'^2) and meridional surface currents (v'^2), based on 30-day high-pass filtered data. Next, a spatial high-pass filter of 12° longitude is applied to isolate fine-scale structures associated with TIWs. Note that a 5-day low-pass filter is also applied to observations to remove high frequency variability. Spatial and temporal filtering are performed by applying a centered running mean to the data.

Figures 1a and 1b show the long-term mean of SST'^2 from the TIW-RUN and the observations (daily NOAA 1/4° Optimal Interpolation SST OISST v2 from January 1981 to December 2019, Reynolds et al., 2007). The spatial patterns of SST'^2 are very similar, yet with an amplitude slightly overestimated in TIW-RUN compared to observations (+26% in the black box, $2° - 5°$N, $160° - 110°$W). The seasonal cycle of the simulated SST'^2 has the

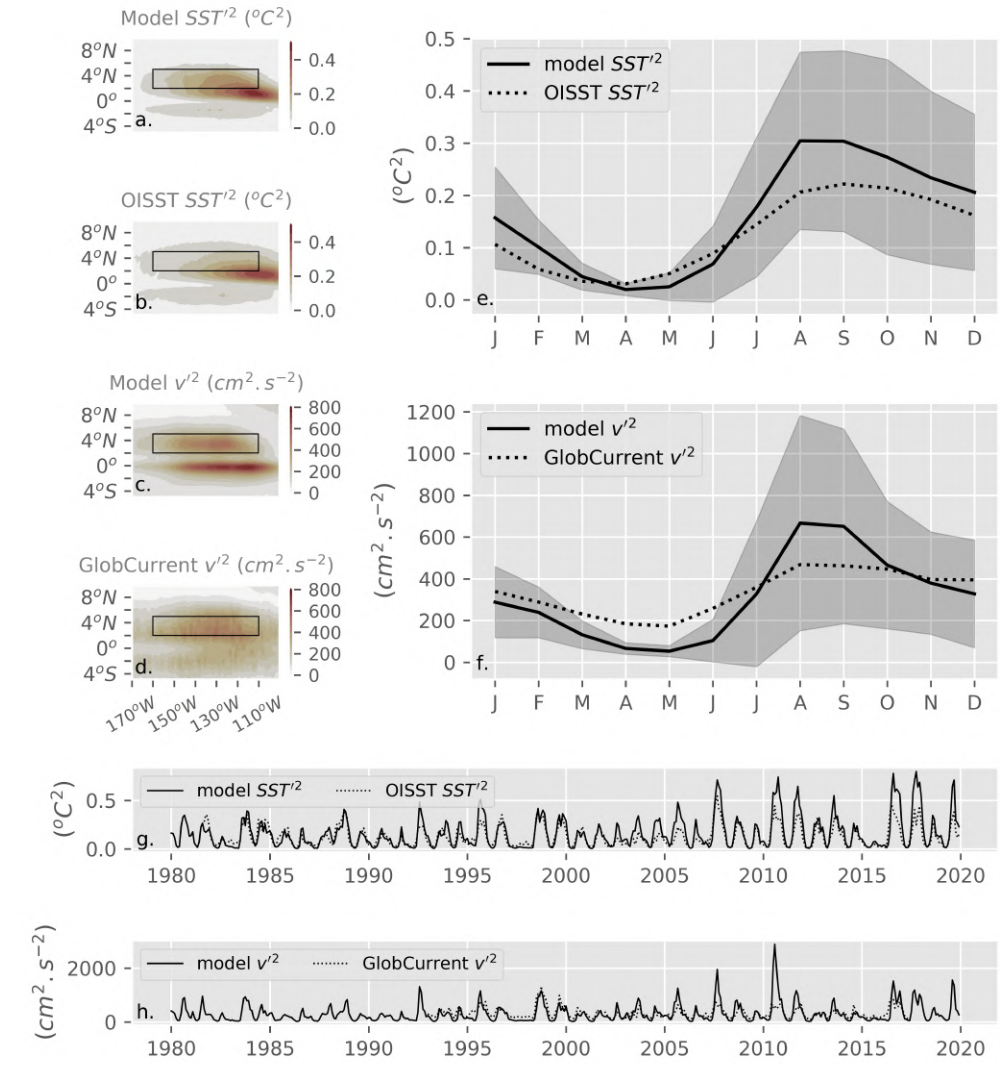

Figure 1. Maps of mean TIW variance SST'^2 in (a) the simulated TIW-RUN (1980-2019), and (b) observed OISST (1981-2019), (c,d) Same as (a,b) but for the TIW variance v'^2, in (c) the simulated TIW-RUN (1980-2019) and (d) GlobCurrent product (1993-2017). (e) Annual cycle of SST'^2 averaged over the region $2^\circ - 5^\circ$N, $160^\circ - 110^\circ$W (black box in (a,b,c,d)). Shading shows the interannual variability of the model (± 1 std). (f) Same as (e) for v'^2. (g) Monthly time series of SST'^2 averaged over the same region. (h) Same as (g) for v'^2.

same phase and displays a similar amplitude as the observations (Fig. 1e), and the monthly time-series of the simulated SST'^2 closely follows the observed interannual variations (Fig. 1g) with a Pearson correlation coefficient of 0.85 (99% confidence level, see supporting Text S1)

Figures 1c and 1d show the long-term mean of v'^2 from the TIW-RUN and the observations (daily altimetric geostrophic and modeled Ekman currents from the GlobCurrent project at 1/4° from January 1993 to May 2017, Rio et al., 2014). The model reproduces well the observed dipole structure, yet with a stronger near-equatorial peak. However, the GlobCurrent currents might not be accurate at the equator, and several reanalyses (*e.g.,* GLORYS12, HYCOM, ECCO2 and GODAS) show contrasted patterns and intensities of v'^2 (Xue et al., 2022). Nevertheless, the v'^2 pattern in TIW-RUN is consistent with most reanalyses products, and with the standard deviation pattern of v' obtained from altimeters in M. Wang et al. (2020). The box-averaged seasonality of v'^2 follows that of SST'^2 (Fig. 1f), and confirms that TIWs are active from July to February, in good agreement with the observations.

The interannual variability of TIW variance is shown in shading in Figure 1e,f, and by the monthly time-series of v'^2 and SST'^2 in Figure 1g,h. The intensity of TIW variance greatly varies from one year to another. For instance, the 2015 El Niño period leads to an almost nonexistent TIW activity whereas the TIW signal is very strong during the following La Niña events of 2016 and 2017. Boucharel and Jin (2020) demonstrated in their Figure 3c that most of this interannual variability is dominated by ENSO, and by the amplitude modulation emerging from the nonlinear interaction between ENSO and the annual cycle, the so-called combination mode (Stuecker et al., 2013).

Overall, the simulation captures well the TIW seasonal and interannual variability. In the following, a "TIW index" is defined as the monthly average of v'^2, averaged over the black box in Fig. 1. Similar results are obtained when using SST'^2 as the TIW index (Table S2). The same diagnostic is performed on NOTIW-, LR-, and NONL-RUN and compared to the TIW-RUN (Fig. S1). In the NOTIW-RUN most of TIW variability is removed (removal of 91% of v'^2 and 70% of SST'^2). The LR-RUN still reproduces half of TIW variability. In NONL-RUN, only SST'^2 is used to characterize TIW variability since this method creates a spurious noise in the velocities (Gruber et al., 2011). This last experiment simulates only 19% of SST'^2.

3.2 TIW Influence on the Upper-Ocean Temperature Seasonal Cycle

Cold upwelled waters near the equator (Fig. 2a, averaged in the region delineated by white solid-lines, and from 0 to 50 m) are subject to a strong annual cycle, being warmer

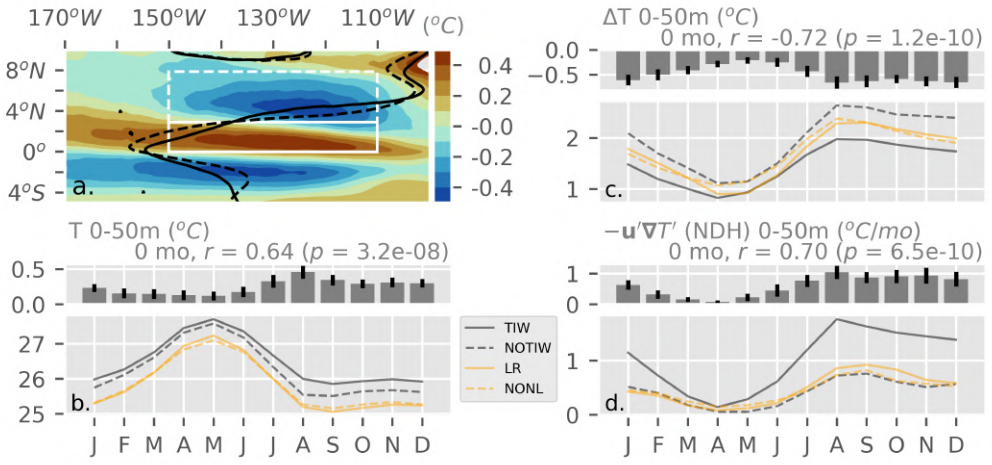

Figure 2. Impact of TIWs on the upper temperature seasonal cycle. (a) Map of the 50-m averaged temperature difference between TIW- and NOTIW-RUN (colors). The 27.5° C isotherm is shown in plain and dashed bold contours for TIW- and NOTIW-RUN respectively. (b) Seasonal cycle of TIW-RUN (solid gray line), NOTIW-RUN (dashed gray), LR-RUN (solid orange), and NONL-RUN (dashed orange), and difference between TIW- and NOTIW-RUN (gray bars) for the mean temperature averaged over the first 50 m in the plain-line white box (0° − 3°N, 150° − 110°W). (c) Same as (b) but for the meridional temperature difference between dashed-line white box (3° − 8°N, 150° − 110°W) and plain-line white box averages. (d) Same as (b) but for NDH averaged in the plain-line white box. Error bars denote the interannual variability (set to ±0.5 std for clarity). The lag (*e.g.,* " 2 mo", in month), the Pearson correlation coefficient r and its p-value are obtained from a lead-lag analysis between the TIW index and the difference between TIW- and NOTIW-RUN for the variable of interest.

from March to June and colder from August to January (Fig. 2b, curves). These cold waters are situated next to warm tropical waters, creating a similarly phased meridional gradient of temperature. Here, we use the 50-m averaged temperature difference between the northern off-equatorial (averaged in the region delineated by white dashed-lines) and equatorial (averaged in the region delineated by white solid-lines) waters as a proxy of the meridional temperature gradient (Fig. 2c). This strong gradient participates in the generation of TIWs through baroclinic instability, which in turn warms the cold upwelled waters via NDH during the period of active TIWs (Fig. 2d, solid gray line). Here, the NDH is defined as the 3-dimensional TIW nonlinear advection of heat $-\mathbf{u}'\nabla T'$ over the first 50 m, with primes denoting fluctuations from a temporal 30-day running-mean. On

average, TIWs warm waters between $0° - 3°$N by up to 0.4 °C in the first 50 m and cool the northern tropical waters by the same amount, decreasing the northward meridional temperature gradient (see Fig. 2a,c and Maillard et al., 2022). This process expands the cold tongue in the meridional direction, as depicted by the 27.5 °C isotherms of TIW-RUN (solid black line) and NOTIW-RUN (dashed black line), with their meridional extent differing by 100 km at 140°W.

In order to quantify TIW seasonal impacts on these thermal features, the differences in the annual cycles between TIW- and NOTIW-RUN are indicated in gray bars in Figure 2b–d. We also performed a lead-lag correlation analysis between the TIW-induced differences and the TIW index, to evaluate a potential delayed impact of TIWs on the thermal features. This lead-lag correlation analysis is simply giving the delay for which the two signals have the highest Pearson correlation coefficient. The impact of TIWs on upper ocean temperature, meridional temperature gradient, and NDH is shown to be highly correlated with TIW activity, with correlation coefficients of 0.64, -0.72 and 0.70 respectively (99% confidence level) and null lag values indicating a strong and sub-monthly amplitude modulation of the upper thermal oceanic structure by TIW-induced NDH, consistent with the study of Im et al. (2012). In particular, the impact of TIWs on thermal characteristics is stronger in boreal summer and fall (and stays significant until mid-winter, in particular for the meridional temperature gradient), when equatorial surface ocean temperatures are the coldest and the meridional temperature gradient is the strongest, than in boreal spring when the situation is reversed (Fig. 2b,c). This leads to a reduction of the amplitudes of both equatorial surface ocean temperatures and meridional gradient seasonal cycles.

We emphasize that while the NDH is not increased by TIWs during the non-active TIW season (Fig. 2d, bars in March-April are not significantly different from zero), we still notice a slight increase of the temperature (0.2 ± 0.1 °C in March) and a moderate decrease (-0.4 ± 0.2 °C in March) of the meridional temperature gradient in this season. Therefore, TIWs are inducing a change in the seasonal cycle, which is not restricted to the period of active TIWs. This could indicate a more long-term impact of TIWs on the mean thermal state, with an integration over time of the fluctuating changes induced by TIWs.

Compared to the TIW-RUN, the LR-RUN (solid orange line) underestimates NDH, most likely due to its reduced TIW activity described in section 3.1. Such low NDH can explain the overestimated meridional temperature gradient, and the underestimated equa-

torial temperature. However, the cold tongue temperature in the LR-RUN is 0.4 °C cooler on average than in the NOTIW-RUN, despite similar amplitude of the NDH. This suggests that reducing the horizontal resolution not only impacts TIW activity but also other circulation and dynamical features, making it difficult to disentangle the changes induced by TIWs from other changes associated with the decrease in resolution in this simulation. Compared to the LR-RUN, the NONL-RUN (dashed orange line) displays slightly weaker NDH from April to November due to weaker TIW activity, and an increased meridional temperature gradient from April to August, that is, the less active TIW period. This is counter-intuitive, as we would expect the difference to be strongest during the active TIW period. This suggests that other processes involving nonlinear momentum terms are modifying the large scale environment. Overall, the NONL-RUN is very similar to the LR-RUN, indicating no improvement in the ability of the LR-RUN to capture the TIW-induced NDH warming of equatorial waters.

3.3 TIW Influence on the Equatorial Undercurrent Seasonal Cycle

The EUC plays an essential role in the Pacific Ocean, transporting large amounts of water to the east along the equatorial thermocline. The EUC evolves zonally, getting closer to the surface as it flows eastward especially from April to May, when trade winds are weak (X. Yu & McPhaden, 1999). Here we evaluate its properties over the region where TIWs are the most active ($140° - 120°$W), that is, where they most likely are able to induce large-scale circulation changes. The seasonal cycles of the EUC peak value and of the EUC transport are shown in Figure 3a,b. The impact of TIWs on the peak value of the EUC and on its transport is illustrated by the gray bars.

The first remarkable result is the year-long TIW-induced reduction of the EUC strength of -0.15 ± 0.02 m.s^{-1} on average (Fig. 3a), highlighting a time-integrated effect of TIW activity onto the EUC annual cycle. This is confirmed by the one-to-two months lags and moderate values of correlation coefficients with TIW activity (2-, 1-month lags and -0.38, -0.54 correlation coefficients, with 85% and 99% confidence levels respectively for the peak value and transport).

To investigate the dynamical processes at play behind this seasonal rectification of the EUC, Figure 3c,d shows the climatology of $(1 - \partial_y^2 u/\beta)$ (shading) and of the dominant term of the barotropic conversion rate (thin contours) defined as $-u'v'\partial_y u$ with primes denoting

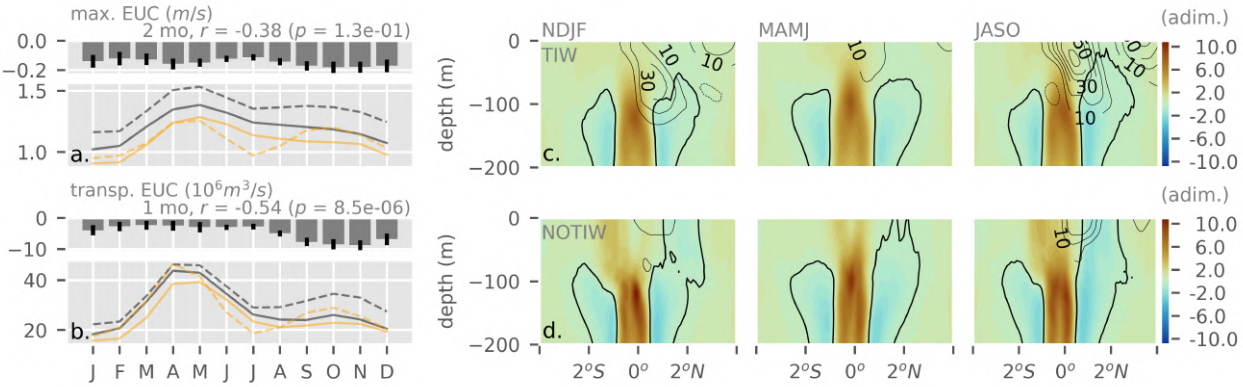

Figure 3. Impact of TIWs on the EUC seasonal cycle. (a) Seasonal cycle of TIW-RUN (solid gray line), NOTIW-RUN (dashed gray), LR-RUN (solid orange) and NONL-RUN (dashed orange), and difference between TIW- and NOTIW-RUN (gray bars) for the maximum value of EUC (maximum of the eastward u averaged between $140^\circ - 120^\circ$W, in the 4°S-3°N and $0-200$ m range). (b) Same as (a) but for the mean value of the EUC transport (eastward u integrated between 4°S-3°N, $140^\circ - 120^\circ$W, $0-200$ m). (c) Depth-latitude sections of the barotropic instability criterion (shading) and barotropic conversion rate (thin contours every 10×10^{-5} $cm^2.s^{-2}$) for TIW-RUN for each climatological season (November to February (left), March to June (middle) and July to October (right)), averaged between $140^\circ - 120^\circ$W. (d) Same as (c) but for the NOTIW-RUN. Bold contours depict the zero value of the instability criterion, that is, the locations satisfying the Rayleigh criterion of barotropic instability.

deviations from a temporal 30-day running mean only. According to the Rayleigh-Kuo's inflection theorem (lan Kuo, 1949), a necessary condition for a flow to be barotropically unstable is that the gradient of the absolute vorticity, $\beta - \partial_y^2 u$, changes sign and thus somewhere $(1 - \partial_y^2 u/\beta) = 0$. Areas where this criterion is satisfied are shown in black bold contours for TIW-RUN (Fig. 3c) and NOTIW-RUN (Fig. 3d). In both runs, this criterion is satisfied between $100 - 200$ m depth on each side of the equator. In the NOTIW-RUN, the criterion is also met in the upper 100 m in the Northern Hemisphere, all year long (see also Fig. S2) while it is most of the time maintained below 50-100 m depth in the TIW-RUN. This potential stabilization of the upper layer could occur through the barotropic conversion of energy, as indicated by the thin contours in Figure 3c. This conversion is responsible for the formation of TIWs, which highlights their key role in stabilizing the near surface ocean. By contrast, TIWs in the NOTIW-RUN are too weak to break this unstable

state by converting the mean energy contained in the EUC into eddy energy. The unstable state therefore persists all year, concurrently with the observed permanent stronger EUC in the absence of TIWs.

The second intriguing result is the near disappearance of the second seasonal maximum in EUC intensity and transport during the second half of the calendar year, in the TIW-RUN (Fig. 3b). Indeed, the EUC transport in the NOTIW-RUN is shown to increase again in June, reaching a second maximum in October, which is associated with a re-strengthening and shoaling of the EUC (Fig. S3). However, as the EUC starts to decrease in spring and remains weak throughout the rest of the year, this second maximum mostly disappears in the TIW-RUN. The EUC re-intensification seems partly inhibited by the increased TIW activity starting in May/June in the TIW-RUN. Again, this could be linked to mechanisms of TIW-induced stabilization of the near surface flow (Fig. 3c,d). This re-intensification of the EUC in the eastern Pacific is not observed in SODA v3.4.2 ocean reanalysis product (Figs. S4 and S5), nor in in-situ observations (X. Yu and McPhaden (1999), their Figure 4). Note that due to the scarcity of EUC observations, we cannot apply the same diagnostics because it requires data over the entire latitudinal extent of the EUC. Thus, we can only hypothesize that this strong semi-annual cycle is not realistic.

Because the LR-RUN does not reproduce TIW variability accurately (see section 3.1), it should be expected that the EUC seasonal cycle shape resembles that of the NOTIW-RUN. However, even though LR-RUN exhibits a weak EUC, its seasonal cycle matches that of the TIW-RUN, with no clear EUC re-intensification in October. The NONL-RUN, however, shows a very clear EUC semi-annual cycle, even more pronounced than in the NOTIW-RUN, even if the second peak in the transport, driven by the intensification of the core, is not accompanied by a shoaling like in NOTIW-RUN (Fig. S3). This may indicate that a 1° horizontal resolution simulation resolves TIWs with sufficient strength to trigger this effect on the seasonal zonal equatorial circulation. This suggests the existence of a threshold in TIW activity beyond which the TIW-induced barotropic conversion is strong enough to stabilize the large-scale circulation, inhibiting the EUC re-intensification and preventing a potentially unrealistic semi-annual cycle.

4 Summary and Discussion

In this study, we assess the modulation of the eastern tropical Pacific seasonality by TIWs, using a regional ocean model. Following the methodology of Maillard et al. (2022), we compare a 1/12° regional eddy-rich simulation to one where TIWs are removed. We also consider a 1° simulation in which the coarse resolution prevents TIWs to be fully resolved, and a similar configuration where the nonlinear terms in the momentum equation are turned off to reduce the TIW activity even further.

Overall, our results highlight two types of seasonal changes of the eastern equatorial Pacific climate induced by TIWs:

- A direct (sub-monthly) effect on the upper ocean equatorial heat budget. This effect is driven by the TIW-induced NDH, which is itself modulated by the seasonal cycle. It leads to a meridional extension of the cold tongue, and to the weakening of the seasonal amplitude of the upper equatorial temperature and the meridional temperature gradient. This effect is not well captured by our 1° horizontal resolution simulation due to an underestimation of TIW activity.
- A rectified and delayed (one-to-two months) effect on the subsurface equatorial circulation that induces (i) a year-long weakening of the EUC of 0.15 m s^{-1} on average, most likely induced by the barotropic energy conversion that generates TIWs and leads to a stabilisation of the upper ocean, along with (ii) a change in the EUC seasonal phasing (*i.e.,* an annualization of a potentially unrealistic semi-annual variability of the EUC in the absence of TIWs). This last effect does not seem proportional to TIW strength but rather triggered when TIW activity passes a certain threshold.

Note that these results hold when TIW-RUN is degraded to the similar coarse horizontal resolution as the LR-RUN (Fig. S6).

The semi-annual variability of the eastern EUC has been noticed in several simulations of the eastern Pacific Ocean (*e.g.,* Harrison et al. (2001) their Figure 1, Keenlyside and Kleeman (2002) their Figure 6b). To our knowledge, it has not been noticed in observations (X. Yu & McPhaden, 1999) that are nonetheless very sparse for the EUC, nor in the SODA v3.4.2 ocean reanalysis. Failing to simulate the eastern EUC seasonal cycle in low-resolution models could for instance cause an inaccurate shoaling of the EUC that may impact Kelvin waves through stratification changes, and influence ENSO initiation.

Using a simple conceptual 1-dimensional linear model, Boucharel and Jin (2020) have shown that the seasonal modulation of TIW activity (and thus of TIW induced NDH) could lead to a nonlinear rectification of the upper eastern Pacific temperatures (their Fig. 6b). Based on their results, one would expect that TIWs could impact circulation via $u'\nabla v'$ in the same way that TIWs impact temperature via NDH. It is not the case here, indicating that a new formulation of the theoretical framework of Boucharel and Jin (2020) is needed to better delineate the rectification effects of TIWs on both temperature and currents.

Finally, interestingly, the LR-RUN fails to reproduce the NDH effects of TIWs but manages to reproduce the seasonal cycle of the EUC. This indicates a need to develop scale-aware parameterizations in low-resolution models that do not properly resolve TIWs in order to reproduce more accurately the eastern Pacific Ocean.

5 Open Research

The CROCO model used in this study can be found here `https://www.croco-ocean.org/`. The data used to generate the figures can be found here `https://doi.org/10.6084/m9.figshare.20597793.v1`.

Acknowledgments

The NOAA Optimum Interpolation (OI) SST V2 dataset can be found here `https://psl.noaa.gov/data/gridded/data.noaa.oisst.v2.html`. The GlobCurrent dataset can be found here `http://globcurrent.ifremer.fr/`.

This work was partly supported by the Thomas Jefferson Fund, a program of the FACE Foundation launched in collaboration with the French Embassy in the U.S. LM and JB are funded through the French Agence Nationale de la Recherche project Make Our Planet Great Again MOPGA "Trocodyn" (ANR-17-MPGA-0018) and the Région Occitanie. LR is funded through the French ANR EUREC4 project, the CNES TOSCA I-CASCADE project and the CARAMBA project. F.-F.J. is funded through the U.S. National Science Fundation Grant AG-S-1813611 and the U.S. Department of Energy Grant D-E-SC0005110. In addition, MFS was supported by NSF grant AGS-2141728 and NOAA's Climate Program Office's Modeling, Analysis, Predictions, and Projections (MAPP) program grant NA20OAR4310445. We thank the CALMIP and GENCI centers for providing access to the supercomputers Olympe and Irene (project 13051). We thank two anonymous reviewers

for their constructive comments. This is SOEST publication 11598 and IPRC contribution 1585.

References

An, S.-I. (2008). Interannual Variations of the Tropical Ocean Instability Wave and ENSO. *Journal of Climate*, *21*(15), 3680–3686. doi: 10.1175/2008JCLI1701.1

An, S.-I., & Jin, F.-F. (2004). Nonlinearity and asymmetry of ENSO. *Journal of Climate*, *17*(12), 2399 - 2412. doi: 10.1175/1520-0442(2004)017⟨2399:NAAOE⟩2.0.CO;2

Becker, J. J., Sandwell, D. T., Smith, W. H. F., Braud, J., Binder, B., Depner, J., ... Weatherall, P. (2009). Global Bathymetry and Elevation Data at 30 Arc Seconds Resolution: SRTM30_PLUS. *Marine Geodesy*, *32*(4), 355–371. doi: 10.1080/01490410903297766

Boucharel, J., & Jin, F.-F. (2020). A simple theory for the modulation of tropical instability waves by ENSO and the annual cycle. *Tellus A: Dynamic Meteorology and Oceanography*, *72*(1), 1–14. doi: 10.1080/16000870.2019.1700087

Carton, J. A., Chepurin, G. A., & Chen, L. (2018). SODA3: A new ocean climate reanalysis. *Journal of Climate*, *31*(17), 6967 - 6983. doi: 10.1175/JCLI-D-18-0149.1

Chelton, D. B., Esbensen, S. K., Schlax, M. G., Thum, N., Freilich, M. H., Wentz, F. J., ... Schopf, P. S. (2001). Observations of Coupling between Surface Wind Stress and Sea Surface Temperature in the Eastern Tropical Pacific. *Journal of Climate*, *14*(7), 1479–1498. doi: 10.1175/1520-0442(2001)014⟨1479:OOCBSW⟩2.0.CO;2

Contreras, R. F. (2002). Long-Term Observations of Tropical Instability Waves. *Journal Of Physical Oceanography*, *32*, 8. doi: 10.1175/1520-0485(2002)032⟨2715:LTOOTI⟩2.0.CO;2

Cox, M. (1980). Generation and propagation of 30-day waves in a numerical model of the Pacific. *Journal of Physical Oceanography, American Meteorological Society*, *10*, 1168 - 1186. doi: https://doi.org/10.1175/1520-0485(1980)010⟨1168:GAPODW⟩2.0.CO;2

Debreu, L., Marchesiello, P., Penven, P., & Cambon, G. (2012). Two-way nesting in split-explicit ocean models: Algorithms, implementation and validation. *Ocean Modelling*, *49-50*, 1-21. doi: https://doi.org/10.1016/j.ocemod.2012.03.003

Düing, W., Hisard, P., Katz, E., Meincke, J., Miller, L., Moroshkin, K. V., ... Weisberg, R. (1975). Meanders and long waves in the equatorial Atlantic. *Nature*, *257*(5524), 280–284. doi: https://doi.org/10.1038/257280a0

Eddebbar, Y. A., Subramanian, A. C., Whitt, D. B., Long, M. C., Verdy, A., Mazloff, M. R., & Merrifield, M. A. (2021). Seasonal Modulation of Dissolved Oxygen in the Equatorial Pacific by Tropical Instability Vortices. *Journal of Geophysical Research: Oceans*, *126*(11). doi: https://doi.org/10.1029/2021JC017567

Escobar-Franco, M. G., Boucharel, J., & Dewitte, B. (2022). On the Relationship Between Tropical Instability Waves and Intraseasonal Equatorial Kelvin Waves in the Pacific From Satellite Observations (1993–2018). *Frontiers in Marine Science*, *9*, 788908. doi: 10.3389/fmars.2022.788908

Eyring, V., Bony, S., Meehl, G. A., Senior, C. A., Stevens, B., Stouffer, R. J., & Taylor, K. E. (2016). Overview of the Coupled Model Intercomparison Project Phase 6 (CMIP6) experimental design and organization. *Geoscientific Model Development*, *9*(5), 1937–1958. doi: 10.5194/gmd-9-1937-2016

Fairall, C. W., Bradley, E. F., Hare, J. E., Grachev, A. A., & Edson, J. B. (2003). Bulk Parameterization of Air–Sea Fluxes: Updates and Verification for the COARE Algorithm. *Journal of Climate*, *16*(4), 571–591. doi: 10.1175/1520-0442(2003)016⟨0571:BPOASF⟩2.0.CO;2

Graham, T. (2014). The Importance of Eddy Permitting Model Resolution for Simulation of the Heat Budget of Tropical Instability Waves. *Ocean Modelling*, *79*, 21–32. doi: 10.1016/j.ocemod.2014.04.005

Gruber, N., Lachkar, Z., Frenzel, H., Marchesiello, P., Münnich, M., McWilliams, J. C., ... Plattner, G.-K. (2011). Eddy-induced reduction of biological production in eastern boundary upwelling systems. *Nature geoscience*, *4*(11), 787–792. doi: https://doi.org/10.1038/ngeo1273

Harrison, D. E., Romea, R. D., & Vecchi, G. A. (2001). Central equatorial Pacific zonal currents. II: The seasonal cycle and the boreal spring surface eastward surge. *Journal of Marine Research*, *59*(6), 921-948. doi: 10.1357/00222400160497715

Holmes, R. M., & Thomas, L. N. (2015). The Modulation of Equatorial Turbulence by Tropical Instability Waves in a Regional Ocean Model. *Journal of Physical Oceanography*, *45*(4), 1155–1173. doi: 10.1175/JPO-D-14-0209.1

Holmes, R. M., & Thomas, L. N. (2016). Modulation of Tropical Instability Wave Intensity by Equatorial Kelvin Waves. *Journal of Physical Oceanography*, *46*(9), 2623–2643. doi: 10.1175/JPO-D-16-0064.1

Im, S.-H., An, S.-I., Lengaigne, M., & Noh, Y. (2012). Seasonality of Tropical Instability

Waves and Its Feedback to the Seasonal Cycle in the Tropical Eastern Pacific. *The Scientific World Journal*, *2012*, 1–11. doi: 10.1100/2012/612048

Inoue, R., Lien, R.-C., & Moum, J. N. (2012). Modulation of Equatorial Turbulence by a Tropical Instability Wave. *Journal of Geophysical Research: Oceans*, *117*(C10). doi: 10.1029/2011JC007767

Keenlyside, N., & Kleeman, R. (2002). Annual cycle of equatorial zonal currents in the Pacific. *Journal of Geophysical Research: Oceans*, *107*(C8), 8-1-8-13. doi: https://doi.org/10.1029/2000JC000711

lan Kuo, H. (1949). Dynamic instability of two-dimensional nondivergent flow in a barotropic atmosphere. *Journal of Atmospheric Sciences*, *6*(2), 105 - 122. doi: 10.1175/1520-0469(1949)006⟨0105:DIOTDN⟩2.0.CO;2

Large, W. G., McWilliams, J. C., & Doney, S. C. (1994). Oceanic vertical mixing: A review and a model with a nonlocal boundary layer parameterization. *Reviews of Geophysics*, *32*(4), 363. doi: 10.1029/94RG01872

Lee, T., Lagerloef, G., Gierach, M. M., Kao, H.-Y., Yueh, S., & Dohan, K. (2012). Aquarius reveals salinity structure of tropical instability waves. *Geophysical Research Letters*, *39*(12). doi: 10.1029/2012GL052232

Legeckis, R. (1977). Long Waves in the Eastern Equatorial Pacific Ocean: A View from a Geostationary Satellite. *Science*, *197*(4309), 1179–1181. doi: 10.1126/science.197.4309.1179

Lien, R.-C., D'Asaro, E. A., & Menkes, C. E. (2008). Modulation of equatorial turbulence by tropical instability waves. *Geophysical Research Letters*, *35*(24). doi: https://doi.org/10.1029/2008GL035860

Lyman, J. M., Johnson, G. C., & Kessler, W. S. (2007). Distinct 17- and 33-Day Tropical Instability Waves in Subsurface Observations. *Journal of Physical Oceanography*, *37*(4), 855–872. doi: 10.1175/JPO3023.1

Maillard, L., Boucharel, J., & Renault, L. (2022). Direct and rectified effects of Tropical Instability Waves on the eastern tropical Pacific mean state in a regional ocean model. *Journal of Physical Oceanography*, *52*(8), 1817 - 1834. doi: 10.1175/JPO-D-21-0300.1

Masina, S., Philander, S. G. H., & Bush, A. B. G. (1999). An analysis of tropical instability waves in a numerical model of the Pacific Ocean: 2. Generation and energetics of the waves. *Journal of Geophysical Research: Oceans*, *104*(C12), 29637–29661. doi: 10.1029/1999JC900226

Menkes, C. E. R., Vialard, J. G., Kennan, S. C., Boulanger, J.-P., & Madec, G. V. (2006). A Modeling Study of the Impact of Tropical Instability Waves on the Heat Budget of the Eastern Equatorial Pacific. *Journal of Physical Oceanography*, *36*(5), 847–865. doi: 10.1175/JPO2904.1

Miller, L., Watts, D. R., & Wimbush, M. (1985). Oscillations of dynamic topography in the Eastern Equatorial Pacific. *Journal of Physical Oceanography*, *15*(12), 1759 - 1770. doi: 10.1175/1520-0485(1985)015⟨1759:OODTIT⟩2.0.CO;2

Moum, J. N., Lien, R.-C., Perlin, A., Nash, J. D., Gregg, M. C., & Wiles, P. J. (2009). Sea surface cooling at the Equator by subsurface mixing in Tropical Instability Waves. *Nature Geoscience*, *2*(11), 761–765. doi: 10.1038/ngeo657

Philander, S. G. H. (1976). Instabilities of zonal equatorial currents. *Journal of Geophysical Research*, 11.

Philander, S. G. H. (1978). Instabilities of zonal equatorial currents, 2. *Journal of Geophysical Research*, *83*(C7), 3679. doi: 10.1029/JC083iC07p03679

Qiao, L., & Weisberg, R. H. (1995). Tropical instability wave kinematics: Observations from the Tropical Instability Wave Experiment. *Journal of Geophysical Research*, *100*(C5), 8677. doi: 10.1029/95JC00305

Renault, L., Masson, S., Arsouze, T., Madec, G., & McWilliams, J. C. (2020). Recipes for How to Force Oceanic Model Dynamics. *Journal of Advances in Modeling Earth Systems*, *12*(2). doi: 10.1029/2019MS001715

Renault, L., Molemaker, M. J., Mcwilliams, J. C., Shchepetkin, A. F., Lemarié, F., Chelton, D., ... Hall, A. (2016). Modulation of Wind Work by Oceanic Current Interaction with the Atmosphere. *Journal of Physical Oceanography*, *46*, 20.

Reynolds, R. W., Smith, T. M., Liu, C., Chelton, D. B., Casey, K. S., & Schlax, M. G. (2007). Daily high-resolution-blended analyses for sea surface temperature. *Journal of Climate*, *20*(22), 5473 - 5496. doi: 10.1175/2007JCLI1824.1

Rio, M.-H., Mulet, S., & Picot, N. (2014). Beyond GOCE for the ocean circulation estimate: Synergetic use of altimetry, gravimetry, and in situ data provides new insight into geostrophic and Ekman currents. *Geophysical Research Letters*, *41*(24), 8918-8925. doi: https://doi.org/10.1002/2014GL061773

Saha, S., Moorthi, S., Pan, H.-L., Wu, X., Wang, J., Nadiga, S., ... Goldberg, M. (2010). *NCEP climate forecast system reanalysis (CFSR) selected hourly time-series products, january 1979 to december 2010.* Boulder CO: Research Data Archive at the National

513 Center for Atmospheric Research, Computational and Information Systems Labora-
514 tory.

515 Saha, S., Moorthi, S., Wu, X., Wang, J., Nadiga, S., Tripp, P., ... Becker, E. (2011).
516 *NCEP Climate Forecast System Version 2 (CFSv2) selected hourly time-series prod-*
517 *ucts.* Boulder CO: Research Data Archive at the National Center for Atmospheric
518 Research, Computational and Information Systems Laboratory. doi: https://doi.org/
519 10.5065/D6N877VB

520 Shchepetkin, A. F. (2015). An adaptive, Courant-Number-Dependent implicit scheme for
521 vertical advection in oceanic modeling. *Ocean Modelling*, *91*, 38–69. doi: 10.1016/
522 j.ocemod.2015.03.006

523 Shchepetkin, A. F., & McWilliams, J. C. (2005). The regional oceanic modeling sys-
524 tem (ROMS): A split-explicit, free-surface, topography-following-coordinate oceanic
525 model. *Ocean Modelling*, 58.

526 Shchepetkin, A. F., & McWilliams, J. C. (2009). Correction and commentary for
527 "Ocean forecasting in terrain-following coordinates: Formulation and skill assess-
528 ment of the regional ocean modeling system" by Haidvogel et al., J. Comp. Phys.
529 227, pp. 3595–3624. *Journal of Computational Physics*, *228*(24), 8985–9000. doi:
530 10.1016/j.jcp.2009.09.002

531 Stuecker, M. F., Timmermann, A., Jin, F.-F., McGregor, S., & Ren, H.-L. (2013). A
532 combination mode of the annual cycle and the El Niño/Southern Oscillation. *Nature*
533 *Geoscience*, *6*(7), 540–544.

534 Takahashi, T., Sutherland, S. C., Wanninkhof, R., Sweeney, C., Feely, R. A., Chipman,
535 D. W., ... de Baar, H. J. (2009). Climatological mean and decadal change in surface
536 ocean pCO2, and net sea–air CO2 flux over the global oceans. *Deep Sea Research Part*
537 *II: Topical Studies in Oceanography*, *56*(8), 554-577. (Surface Ocean CO2 Variability
538 and Vulnerabilities) doi: https://doi.org/10.1016/j.dsr2.2008.12.009

539 Vialard, J. R. M., Menkes, C., Boulanger, J.-P., Delecluse, P., Guilyardi, E., Mcphaden,
540 M. J., & Madec, G. (2001). A Model Study of Oceanic Mechanisms Affecting Equato-
541 rial Pacific Sea Surface Temperature during the 1997–98 El Niño. *Journal of Physical*
542 *Oceanography*, *31*, 27.

543 Von Schuckmann, K., Brandt, P., & Eden, C. (2008). Generation of Tropical Instability
544 Waves in the Atlantic Ocean. *Journal of Geophysical Research*, *113*(C8), C08034. doi:
545 10.1029/2007JC004712

Wang, M., Du, Y., Qiu, B., Xie, S.-P., & Feng, M. (2019). Dynamics on Seasonal Variability of EKE Associated with TIWs in the Eastern Equatorial Pacific Ocean. *Journal of Physical Oceanography*, *49*(6), 1503–1519. doi: 10.1175/JPO-D-18-0163.1

Wang, M., Xie, S.-P., Shen, S. S. P., & Du, Y. (2020). Rossby and Yanai Modes of Tropical Instability Waves in the Equatorial Pacific Ocean and a Diagnostic Model for Surface Currents. *Journal of Physical Oceanography*, *50*(10), 3009–3024. doi: 10.1175/JPO-D-20-0063.1

Wang, W., & McPhaden, M. J. (2000). The surface-layer heat balance in the equatorial pacific ocean. part II: Interannual variability. *Journal of Physical Oceanography*, *30*(11), 2989 - 3008. doi: 10.1175/1520-0485(2001)031⟨2989:TSLHBI⟩2.0.CO;2

Wang, W., & McPhaden, M. J. (2001). Surface layer temperature balance in the equatorial pacific during the 1997–98 El Niño and 1998–99 La Niña. *Journal of Climate*, *14*(16), 3393 - 3407. doi: 10.1175/1520-0442(2001)014⟨3393:SLTBIT⟩2.0.CO;2

Xie, S.-P., Ishiwatari, M., Hashizume, H., & Takeuchi, K. (1998). Coupled ocean-atmospheric waves on the equatorial front. *Geophysical Research Letters*, *25*(20), 3863–3866. doi: 10.1029/1998GL900014

Xue, A., Jin, F.-F., Zhang, W., & Boucharel, J. (2022). Quantifying ENSO-Tropical Instability Waves (TIWs) interaction by nonlinear Eddy thermal diffusivity. *Submitted to Journal of Geophysical Research - Ocean*.

Xue, A., Jin, F.-F., Zhang, W., Boucharel, J., Zhao, S., & Yuan, X. (2020). Delineating the Seasonally Modulated Nonlinear Feedback Onto ENSO From Tropical Instability Waves. *Geophysical Research Letters*, *47*(7). doi: 10.1029/2019GL085863

Xue, A., Zhang, W., Boucharel, J., & Jin, F.-F. (2021). Anomalous Tropical Instability Wave activity hindered the development of the 2016/17 La Niña. *Journal of Climate*, *34*(13), 5583 - 5600. doi: 10.1175/JCLI-D-20-0399.1

Yu, X., & McPhaden, M. J. (1999). Seasonal variability in the equatorial pacific. *Journal of Physical Oceanography*, *29*(5), 925 - 947. doi: 10.1175/1520-0485(1999)029⟨0925:SVITEP⟩2.0.CO;2

Yu, Z., McCreary, J. P., & Proehl, J. A. (1995). Meridional asymmetry and energetics of tropical instability waves. *Journal of Physical Oceanography*, *25*(12), 2997 - 3007. doi: 10.1175/1520-0485(1995)025⟨2997:MAAEOT⟩2.0.CO;2

4.3 Supporting Information

Supporting Information for "Modulation of the Eastern Equatorial Pacific seasonal cycle by Tropical Instability Waves"

L. Maillard[1], J. Boucharel[1,2], M. F. Stuecker[3], F.-F. Jin[2], L. Renault[1]

[1]LEGOS, University of Toulouse, IRD, CNRS, CNES, UPS, Toulouse, France

[2]Department of Atmospheric Sciences, School of Ocean and Earth Science and Technology (SOEST), University of Hawai'i at Mānoa, Honolulu, HI, USA

[3] Department of Oceanography and International Pacific Research Center (IPRC), School of Ocean and Earth Science and Technology (SOEST), University of Hawai'i at Mānoa, Honolulu, HI, USA

Contents of this file

Text S1: Confidence level of a correlation

Confidence levels for the correlations are obtained from a null hypothesis of non-correlation. For instance, the hypothesis of non correlation is rejected at a 99% confidence level if the associated p-value is less than 0.01. The p-value is based on the effective degrees of freedom estimated from the auto-correlation function. For a time series of a red noise, $n = N/2L$ with n the effective degrees of freedom, N the sample size and L the e-folding time-scale of the auto-correlation function.

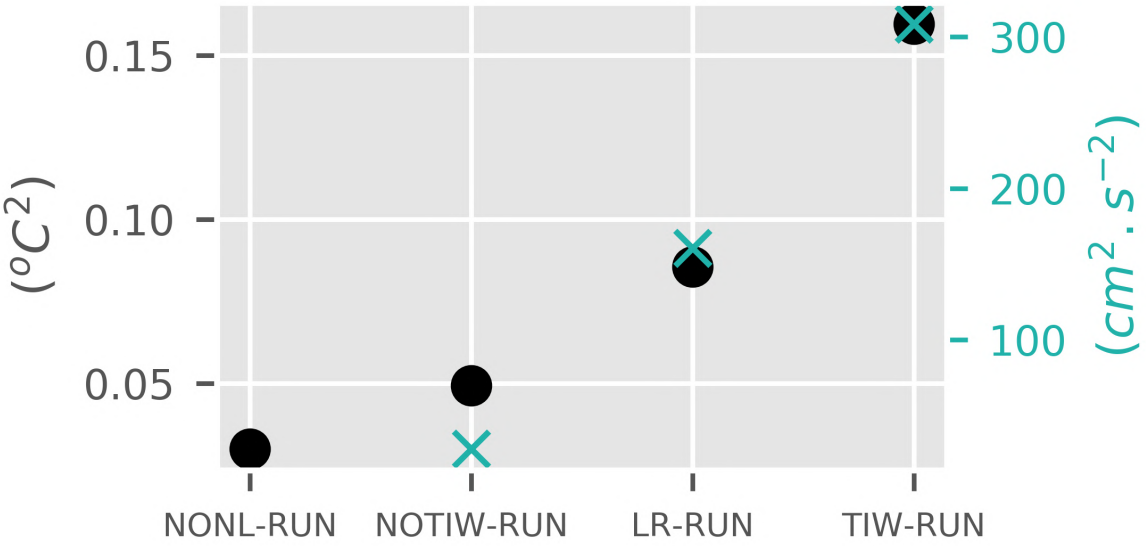

Figure S1. Mean values of TIW variance SST'^2 (black dots) and v'^2 (blue cross) averaged over the 40 simulated years and over 2°– 5°N, 160°– 110°W, for each simulations.

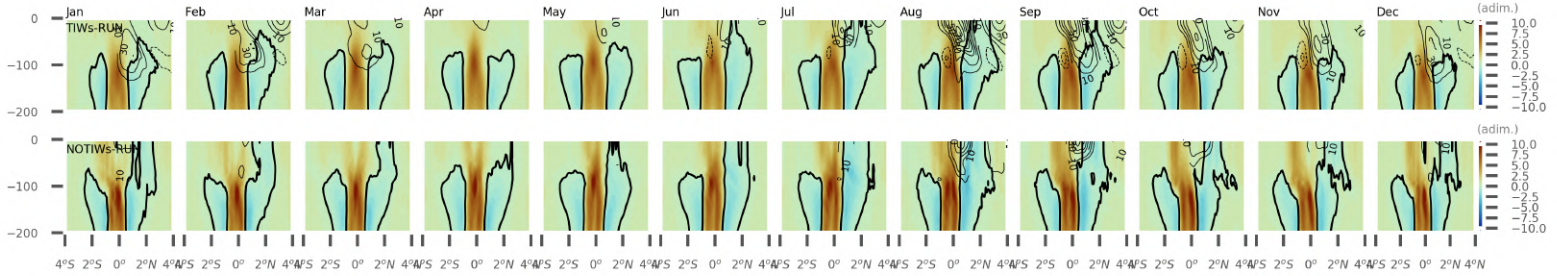

Figure S2. (up) Depth-latitude sections of the barotropic instability criterion ($1 - \partial_y^2 u/\beta$, colors) and barotropic conversion rate ($-\overline{u'v'}\partial_y\overline{u}$, contours every 10×10^{-5} $cm^2.s^{-2}$) for TIW-RUN for each climatological months, averaged between 140°– 120°W. (down) Same as (up) for the NOTIW-RUN. Bold contours depict the zero value of the instability criterion, i.e. the positions meeting the Rayleigh criterion of barotropic instability.

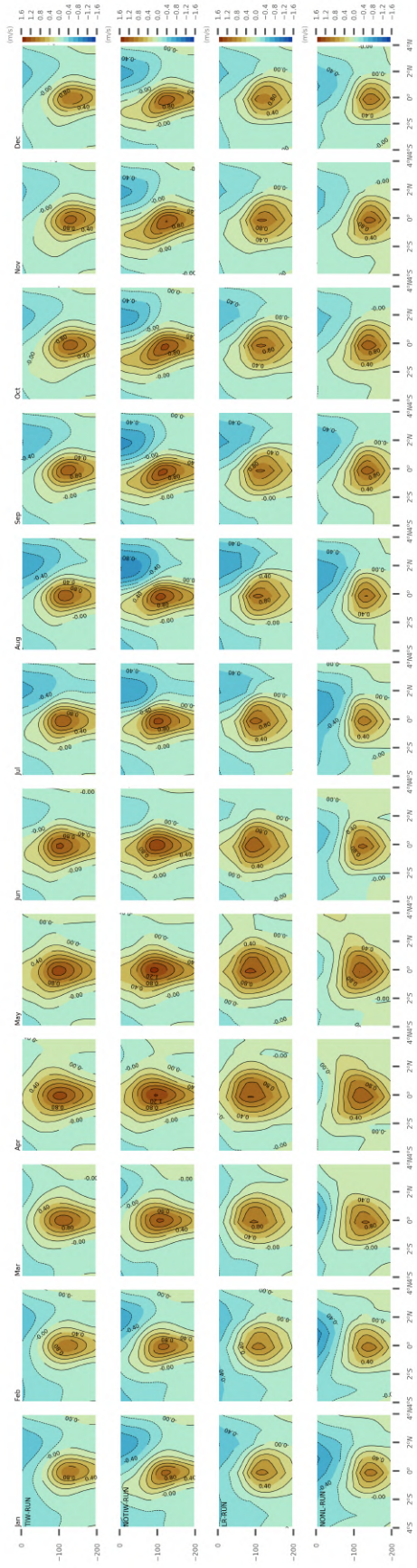

Figure S3. Depth-latitude sections of the mean zonal current for each climatological months, averaged between 140°–120°W, in (first line) TIW-RUN, (second line) NOTIW-RUN, (third line) LR-RUN and (fourth line) NONL-RUN.

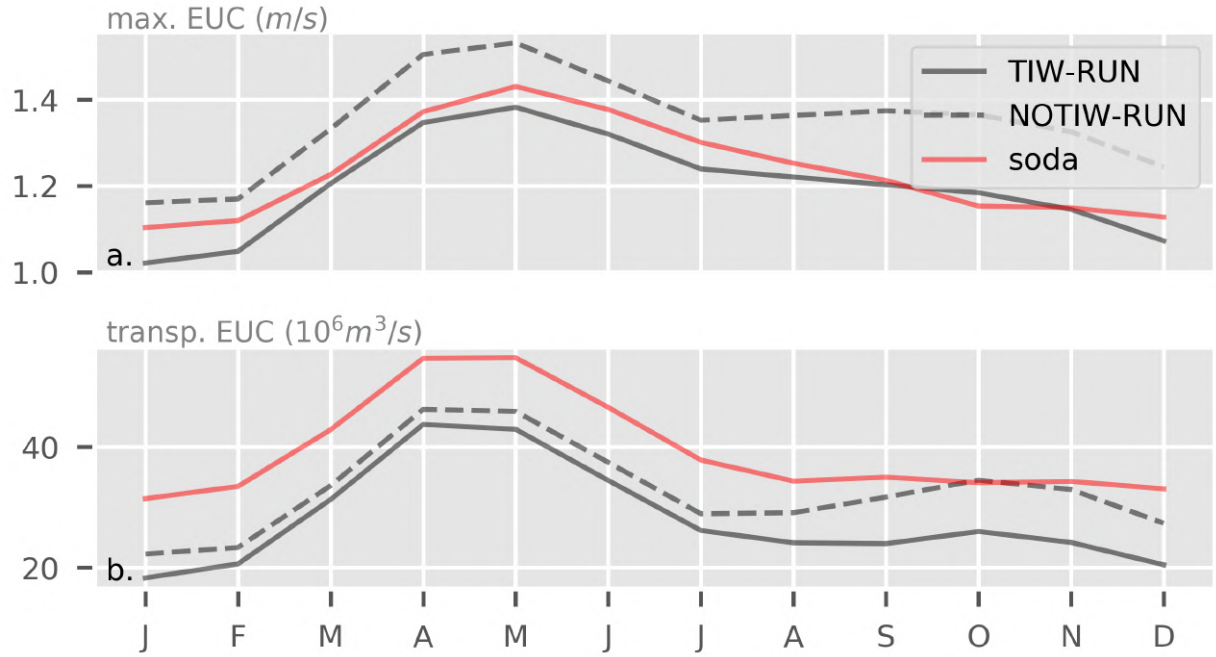

Figure S4. Seasonal cycle of (a) maximum and (b) transport of EUC, for TIW-RUN (solid black line), NOTIW-RUN (dashed black line), and SODA v3.4.2 (solid red line). The EUC is defined here as the positive u velocities averaged between 140°– 120°W, and located between 4°S – 3°N and 0 – 200 m.

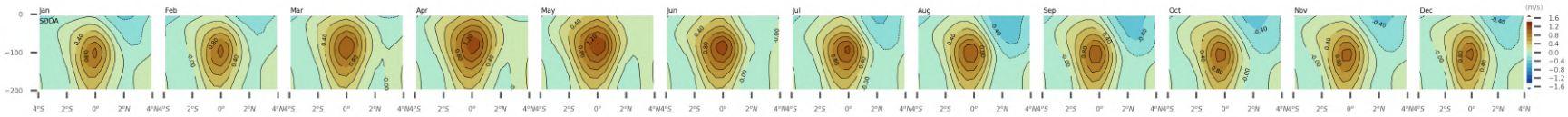

Figure S5. Depth-latitude sections of the mean zonal current for each climatological months, averaged between 140°–120°W, in SODA v3.4.2

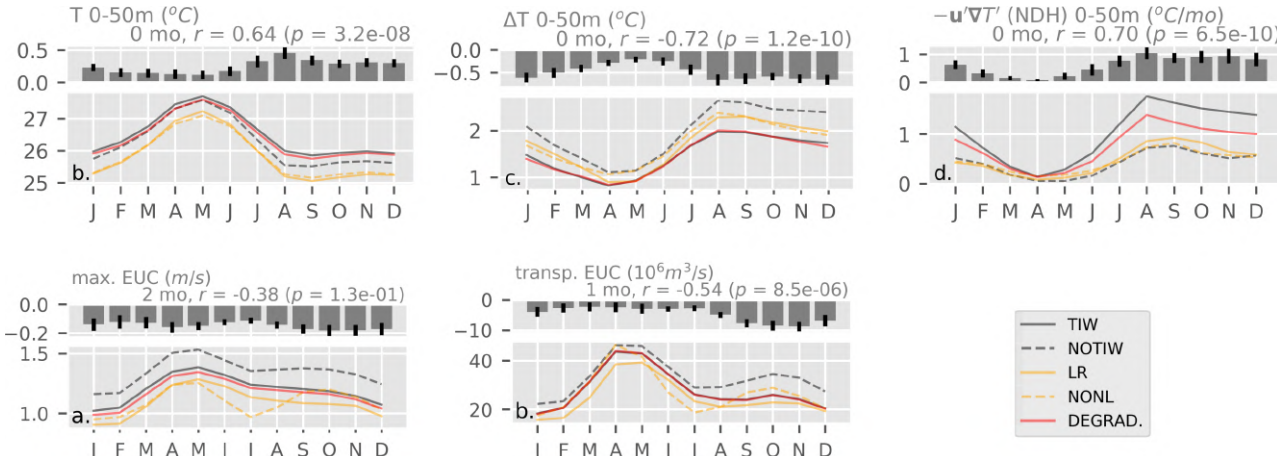

Figure S6. Seasonal cycles of the main features described in the manuscript, for TIW-, NOTIW-, LR-, NONL-RUN and degraded TIW-RUN to the same grid as LR-RUN, i.e., 1° horizontal resolution (DEGRAD-RUN, red line).

Table S1. Configuration of each ocean simulations used in the study

	horizontal resolution	Nudging of v	nonlinear momentum terms
TIW-RUN	1/12 °	no	activated
NOTIW-RUN	1/12 °	yes	activated
LR-RUN	1°	no	activated
NONL-RUN	1°	no	deactivated

Table S2. lead-lag analysis of TIW impacts for several TIW index

	TIW index v'^2		TIW index T'^2	
	lag (months)	r	lag (months)	r
EUC_{max}	2	-0.38	2	-0.38
EUC_{transp}	1	-0.54	1	-0.60
T	0	0.64	0	0.63
ΔT	0	-0.72	0	-0.72
$-\mathbf{u}'\nabla T'$	0	0.70	0	0.79

4.4 Conclusion

4.4.1 Summary

This work highlights a non-negligible TIW-induced modulation of the annual cycle amplitude of upper temperature in the cold tongue region by up to 0.4°C, mainly explained by an increased warming through nonlinear eddy advection in boreal summer and fall. The results also indicate that TIWs modulate the seasonal cycle of the EUC, stabilizing and weakening it by -0.15 m.s^{-1} throughout the year, preventing what appears to be an unrealistic re-intensification in boreal autumn. This re-intensification is thought to be unrealistic as it has not been noticed in observations nor in SODA v3.4.2 reanalysis. However, it often seems to be found in low resolution climate models that do not simulate eddies properly. Moreover, the coarser simulation (LR-RUN, 1° horizontal resolution) fails to reproduce the TIW-induced nonlinear warming of equatorial waters, but succeeds in inhibiting the EUC re-intensification in boreal autumn. This suggests a threshold effect in TIW strength associated with the ability of the model to simulate eddies, which indicates a need to develop scale-aware parameterizations of TIWs in low-resolution models.

The seasonally modulated direct effect of TIWs through NDH on ENSO has been conceptualized by Xue et al. (2020) based on the theoretical approach by Boucharel and Jin (2020), with the idea of parameterize the TIW induced NDH into simple ENSO models, and ultimately into GCMs. The study presented here could serve as the foundation of a similar theoretical work to quantify the seasonally modulated TIW effect on zonal momentum and circulation, to improve the understanding of ENSO-TIWs interaction and perfect the TIWs parameterization schemes.

4.4.2 Author contributions

This work comes from a collaboration between my PhD advisors J. Boucharel and L. Renault, scientists from the University of Hawai'i M. Stuecker and F.-F. Jin, and myself. All authors contributed to the conceptualization of the study, during the visit of J. Boucharel, L. Renault and myself to the University of Hawai'i. I performed the simulations, the processing of the data and the original writing of the draft. We all contributed to improving the methodology, discussing the results and improving the article.

Chapter 5

TIWs & El Niño – Southern Oscillation

Contents

5.1 Preamble

In previous Chapters, we have established that TIWs interact with the eastern tropical Pacific oceanic variability over a multitude of time scales through direct and indirect (or rectified, *i.e.,* through modification of larger scale features) feedbacks. Direct and indirect effects have also been observed in the atmosphere.

Locally, TIW-induced (and more generally, mesoscale and submesoscale-induced) fluctuations of SST and oceanic currents can influence the low-level winds, the surface wind stress variability, and the turbulent heat fluxes through two main feedbacks: the Thermal Feedback (TFB) and the Current Feedback (CFB). TFB represents the influence of the SST on the overlying atmosphere. It has a "top-down" (*i.e.,* induced by the overlying atmosphere) effect on the wind and surface stress (Chelton et al. (2001); O'Neill et al. (2012)) through two distinct mechanisms (Small et al. (2008)). On the one hand, in the lower troposphere, large eddies and turbulence are influenced by the local SST, that also affects the atmospheric stability. Over warmer waters, the destabilized atmosphere causes a larger vertical mixing and more intense surface winds. On the other hand, local SST gradients also cause a thermodynamic adjustment of the air density, which can modulate the surface wind through pressure gradient. Mesoscale TFB also has a direct influence on the turbulent heat fluxes by altering the temperature and humidity gradients between the atmosphere and the ocean and by altering, as described above, the wind. It is also worth noting that mesoscale TFB can also have an influence on the clouds and precipitation, as shown by Frenger et al. (2013). The CFB (*e.g.,* Bye (1985); Duhaut and Straub (2006); Renault et al. (2016b)) has a "bottom-up" (*i.e.,* induced by the underlying ocean) effect by directly modifying the surface stress through changes in ocean current anomalies, that can in turn alter the low-level winds. Turbulent heat fluxes can also be to a less degree modified by CFB. For more details on these feedbacks, the reader is invited to refer to Small et al. (2008) and to the introductory section of Renault et al. (2019a), which provides a comprehensive overview of the processes involved in these two feedbacks and their implications. Overall, these effects have been shown to damp the TIW activity (Pezzi (2004); Seo et al. (2007b); Small et al. (2009); Zhang (2014)).

At larger scale, the atmosphere can influence TIWs mainly through modifications of the oceanic mean state. For instance, Imada et al. (2012) found that despite the above mentioned local negative atmospheric impact on TIWs, increasing the horizontal resolution of the atmospheric component in a coupled model improves the large scale wind curl representation in the ITCZ, which in turn lead to an enhanced SEC/NECC shear, stronger barotropic instability and thus strengthened TIW activity.

Rectifying effects of the oceanic waves onto the atmosphere have also been noticed in several studies. For instance, Hashizume et al. (2001) found evidences in observations of remote TIW-induced ITCZ variability during the 1999 La Niña, with clouds and precipitation patterns at 7°N correlated to TIW pattern located further south. By comparing atmospheric simulations forced either by only climatological SST, or by climatological SST plus monthly SST anomalies induced by TIWs, Jochum et al. (2007b) investigated the long-term effect of TIWs on the atmosphere. They found an increase in rainfall and wind stress interannual

variability, reaching 35% in the tropical band. Other modelling studies based on adding or not the TIW-induced wind stress (due to mesoscale TFB) feedback onto the ocean (Zhang and Busalacchi (2008); Zhang (2014); Pezzi (2004)) suggest that this feedback goes beyond local effects, and can rectify the large scale thermodynamics of the ocean. For instance, Pezzi (2004) showed that the negative feedback of the atmosphere on TIW activity (*i.e.,* a damping of the TIW activity) leads to stronger equatorial currents and cooler cold tongue, due to a reduced momentum and heat transport.

Such noticeable TIW effects on the oceanic and atmospheric variability in the tropical Pacific are likely to trigger significant changes in the characteristics of the El Niño - Southern Oscillation (ENSO), the strongest driver of the interannual air-sea coupled variability in this region (see Chapter 1 for more details). Figure 5.1a shows the evolution of the interannual SST anomalies averaged in the widely-used Niño 3 box (4°S – 4°N, 150°– 90°W, black line) and of the interannual anomaly of the "TIW-index" (blue line) defined as the TIW-induced SST variance SST'^2 averaged over the region 2°– 5°N, 160°– 110°W (see Chapter 3) in the ocean-only simulation TIW-RUN. A significant (at the 99% confidence level, p-value ≤ 0.01) anti-correlation of -0.58 between the two time series reveals that ENSO and TIW interannual variability are strongly related, with in particular an increase in TIW activity during La Niña episodes, and a decrease during El Niño episodes. This modulation of TIWs by ENSO has been noticed and described in observational (Wang and McPhaden (2000); Wu and Bowman (2007)) and modelling (Vialard et al. (2001); Yu and Liu (2003)) studies, and reviewed by An et al. (2020). For instance, using a 28-year long ocean-atmosphere coupled simulation Yu and Liu (2003) found that this modulation is due to the cooling of the cold tongue during La Niña events, which increases the meridional temperature gradient, thus reinforcing the baroclinic instability that triggers TIWs. Conversely, the weak baroclinic instability during warm El Niño events attenuates TIW activity.

On this basis, Xue et al. (2020) introduced a new index, Niño D, defined as the meridional difference in SST anomalies between off-equatorial (3°N – 8°N, 150°– 110°W) and equatorial (3°S – 3°N, 150°– 110°W) water. Compared to the traditional Niño 3 and Niño 3.4 indices, this index better accounts for the changes in meridional temperature gradient induced by ENSO, which modulate TIW activity at interannual time scales. The interannual anomalies of Niño D and of the TIW index (SST'^2) are shown in Figure 5.1b. The correlation coefficient between these two curves reaches 0.71 (99% confidence level, p-value < 0.01), revealing a stronger relationship between TIW activity and Niño D than the one obtained using Niño 3 (Fig. 5.1a).

In turn, TIWs may influence the El Niño-Southern Oscillation (ENSO) evolution in several ways. First, modelling (Holmes and Thomas (2016)) and observational (Escobar-Franco et al. (2022b)) studies revealed a nonlinear interaction between TIWs and intraseasonal Kelvin waves, that could potentially modify the air–sea coupled feedbacks necessary to amplify ENSO events.

Second, TIWs can feedback onto ENSO through their induced stochastic ocean variability. In a recent study, Holmes et al. (2019) complemented the large body of research on the effect of chaotic atmospheric variability on ENSO (*e.g.,* Moore and Kleeman (1999); Levine et al.

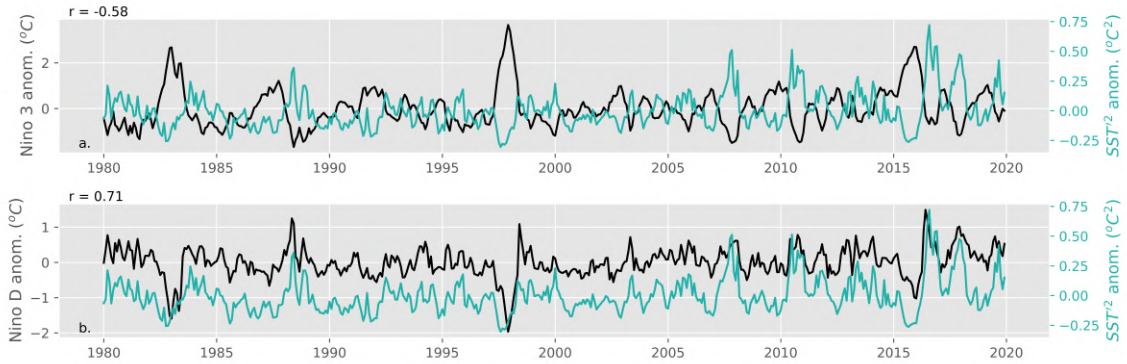

Figure 5.1: Monthly time series of SST interannual anomalies averaged in the (a) Niño 3 box and (b) Niño D box (black lines) and interannual anomalies of TIW associated SST variance SST'^{2} averaged over the region 2° – 5°N, 160° – 110°W (blue line), in the ocean-only TIW-RUN. The correlation coefficient r between the time series is indicated in the upper left corner.

(2016); Hayashi and Watanabe (2017)) by quantifying the contribution of ocean internal variability to the strength of an El Niño event. In particular, using an ensemble of ocean model simulations at 1/4° horizontal resolution coupled to a simple atmospheric model and initiated by a wind burst in the western Pacific to trigger an El Niño event, they found that TIWs induce a spread in the Niño 3 index of ±0.34°C, corresponding to ±45% of the ensemble mean. This indicates that ENSO irregularity might be increased due to the TIW-induced oceanic mesoscale variability.

Lastly, through their anomalous meridional heat advection into the cold tongue, TIWs can feedback onto the ENSO cycle. During La Niña, the increased TIW activity leads to a warm anomaly in the cold tongue, which attenuates La Niña. Conversely, the decrease of TIW activity during El Niño leads to a cold anomaly in the cold tongue, which also attenuates El Niño. Because this anomalous TIW effect on ENSO is stronger during La Niña than El Niño, TIWs act as a negative feedback onto ENSO (An (2008); Wang and McPhaden (2000, 2001); Boucharel and Jin (2020); Xue et al. (2020)), potentially explaining the ENSO cycle asymmetry (An and Jin (2004)). Note that in terms of raw signal (not anomalies), we can expect a weak/moderate El Niño to have a small TIW activity, which could have a positive feedback on it. However, during a strong El Niño without TIW activity, the instability waves will not exert any feedback on this event since they are not generated.

In particular, using an ocean reanalysis, An (2008) found that the interannual anomaly of heat flux convergence (equivalent to NDH) due to TIWs was stronger during La Niña than El Niño events: an increase of 1°C in Niño 3.4 leads to TIW-induced NDH of -0.048°C month^{-1}, while a decrease of 1°C in Niño 3.4 leads to TIW-induced NDH of $+0.077$°C month^{-1}. Incorporating the TIW-induced NDH into the classic recharge-discharge ENSO conceptual model (Jin (1997a)), An (2008) found that the TIW feedback could indeed partly explain the El Niño-La Niña amplitude asymmetry, with an increase of 0.47 in the eastern Pacific SST anomaly skewness (*i.e.,* the third-order statistical moment).

Using observational and reanalysis products, Xue et al. (2021a) compared the development of the 1998/99 and 2016/17 La Niña, with a particular focus on the role of TIW activity. While the 1998/99 La Niña is strong, the 2016/17 La Niña seems inhibited by an important TIW activity arising from increased baroclinic instabilities triggered by a stronger than normal meridional SST gradient in the eastern Pacific. The authors hypothesized that the long-lasting ENSO meridional discharge of heat that occurred after the 2015/16 El Niño contributed to the warm off-equatorial SST anomalies and thus to an enhanced meridional gradient. They also found that the delayed 1983/84 La Niña might also have been hindered by a comparably delayed strong TIW activity, in a similar fashion as the 2016/17 La Niña. As concluded by the authors,

> "ENSO diversity requires careful assessment of each event's individual time evolution."

Although the wide regime-spanning (Kug et al. (2009)) and irregularity (An et al. (2020)) of ENSO make it difficult to study its interaction with TIWs, the role of TIWs in the ENSO cycle and in particular in the development of La Niña events requires a thorough understanding in order to be considered in ENSO forecasts and improve predictions.

In this Chapter, the TIW-damping methodology detailed in Chapter 2 is used in a coupled ocean-atmosphere model to investigate and quantify the complex feedbacks of TIWs onto ENSO. To motivate the use of a coupled model and as a preliminary diagnostic, Figure 5.2 shows the relationship between the interannual anomalies of the TIW index SST'^2, and of Niño D in both the TIW-RUN (black) and NOTIW-RUN (magenta) ocean-only simulations (see Chapter 3 and Chapter 4).

The time series of the raw Niño D is shown in Figure 5.2a. Strong Niño and Niña events are defined as events with a Niño D anomaly index higher (respectively lower) than 0.3^oC (respectively -0.3^oC) in the TIW-RUN, during at least 3 consecutive months and indicated respectively in orange and green shaded areas. Several interesting features are noticed: (1) the Niño D is seasonally modulated, being stronger in the second half of the year; (2) this seasonal cycle is different between TIW- and NOTIW-RUN, especially during the strong phase of the cycle which corresponds to the period of active TIWs (Fig. 5.2d, and Chapter 4); (3) This last observation is not true during the strongest El Niño events of 1983, 1987, 1997, and 2015, during which the two signals are identical, probably due to the absence of TIWs during these events;

The next step is to compute the interannual anomalies of Niño D, to provide a better picture of the impact of TIW on the interannual variability. Two methods can be used to compute the interannual anomalies:

- The first method is to consider each run as two separate worlds. The interannual anomalies are thus computed as the deviation from each run's monthly climatology depicted in Figure 5.2d. The time series is shown in Figure 5.2b. In that case, strong

Niño events are weaker in TIW- than in NOTIW-RUN, while strong Niña events are similar.

- The second method consists in considering both runs as a part of the same world. The interannual anomalies are computed as the deviation from a common climatology depicted in cyan in Figure 5.2d. The time series (Fig. 5.2c) now indicates that La Niña events are weaker in TIW- than in NOTIW-RUN, while El Niño events are similar.

As the real net effect observed in the raw Niño D signal indicates no changes during El Niño events and weaker values during La Niña events in TIW-RUN, I chose to use the second definition of interannual anomalies, *i.e.,* a departure from a common climatology, because it preserves the above-mentioned information. However, this choice may be questioned. Indeed, we could interpret the first method as an indication that the seasonal decrease of Niño D induced by TIWs is not stronger during La Niña events than during normal years. This choice thus requires further considerations.

Using the second definition of interannual anomalies, the scatter plot of Niño D anomaly versus SST'^2 anomaly (Fig. 5.3a) confirms the nonlinear relationship between the ENSO phase and the strength of TIW activity found in previous studies (An (2008); Boucharel and Jin (2020); Xue et al. (2020)). In particular, a stronger TIW activity is associated in both simulations with increased values of Niño D (*i.e.,* a strengthened SST meridional gradient) as we saw in Figure 5.1b. The restriction of this scatter plot to either El Niño (Fig. 5.3b) or La Niña (Fig. 5.3c) events only essentially confirms this nonlinear relationship. While no changes in the El Niño-TIW strength relationship is evidenced between the two simulations, the correlations between Niño D and the TIW index increases by 0.29 (going from 0.40 to 0.69) during La Niña in the absence of TIWs.

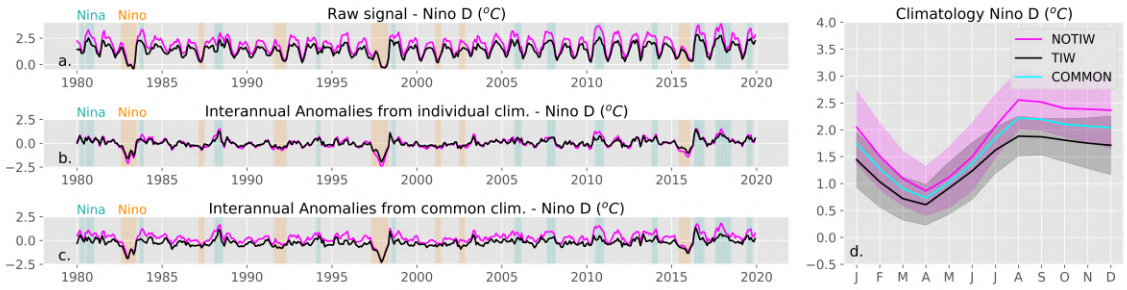

Figure 5.2: Influence of TIWs on the meridional gradient of temperature (Niño D) in the ocean-only simulations. (a – c) Time series of (a) raw Niño D, (b) interannual anomalies of Niño D computed from individual climatologies, and (c) interannual anomalies of Niño D computed from a common climatology. (d) Monthly climatologies of Niño D from TIW-, NOTIW-RUN and the common climatology to both runs, with shading indicating the ±1 interannual standard deviation. Strong Niño (Niña) events are indicated by orange (green) shaded areas, and defined as events with a Niño D anomaly index higher (lower) than 0.3^oC (-0.3^oC) in the TIW-RUN, during at least 3 consecutive months.

While such results are in line with the nonlinear asymmetrical feedback of TIWs onto

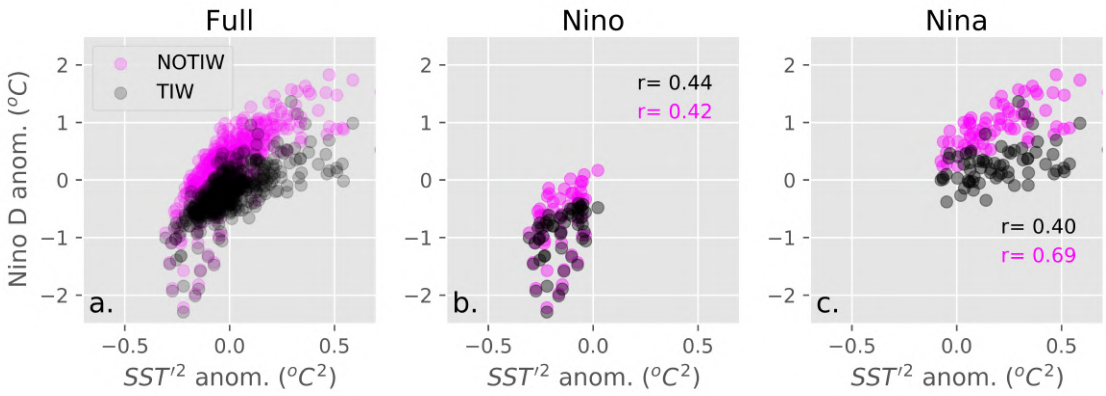

Figure 5.3: Scatter plots of interannual anomalies of Niño D computed from a common climatology, versus the interannual anomalies of TIW-index (SST'^2), for (a) all, (b) strong El Niño events and (c) strong La Niña events. r indicate the Pearson correlation coefficient between Niño D anomaly and anomalous TIW-index.

ENSO evidenced in earlier studies, using ocean-only simulations to diagnose TIW effects onto the air-sea coupled ENSO phenomenon presents serious limitations. For instance, the TIW imprint remains present in the atmospheric forcing (*e.g.,* Seo et al. (2007a); Small et al. (2009)), which evidently leads to a discrepancy between the oceanic state and the overlaying atmosphere. Therefore, ocean-atmosphere coupled simulations are needed to fully account for all air-sea interactions induced by the presence of TIWs. In this Chapter, the ENSO-TIW relationship is investigated in an ensemble of ocean-atmosphere coupled simulations of the 2015-2018 ENSO cycle using the damping methodology previously described. In the First Section, the ocean and atmosphere models are described and the simulations are validated with respect to a multitude of observational data sets and reanalyse products. In Section 2, the effects of TIWs on the ENSO cycle are investigated. The Last Section summarizes and discusses our findings.

5.2 Data and Methods

This section aims at describing the ocean-atmosphere coupled simulations and their validation.

5.2.1 Models

The oceanic model - CROCO

The oceanic part is performed using the CROCO model at a spatial resolution of 1/14° with 50 vertical σ levels, and stretching parameters $h_{cline} = 200$ m, $\theta_b = 2$, and $\theta_s = 7$. The model domain is 185°W-70°W, 15°S-20°N. Note that the size of the domain is reduced with respect to the previous forced ocean-only simulations, for two reasons: (1) to reduce computational costs and (2) to better constrain ENSO events, that are present in the boundary forcing.

It is initiated and forced at the boundaries using data derived from the Simple Ocean Data Assimilation 5-day reanalysis (SODA 3.4.2 on a 1/4° × 1/4° grid, Carton et al. (2019)). The K-profile parameterization (KPP; Large et al. (1994)) is used for vertical mixing of tracers and momentum. The bathymetry is obtained from the Shuttle Radar Topography Mission (SRTM30 plus, Becker et al., 2009). The model is spun up for 11 years starting from the SODA v3.4.2 January 1st 2014 conditions, and forced by atmospheric fluxes derived from the hourly Climate Forecast System Reanalysis (Saha et al. (2010, 2011)) until the kinetic energy and tracers fields are stabilized (Fig. 5.4).

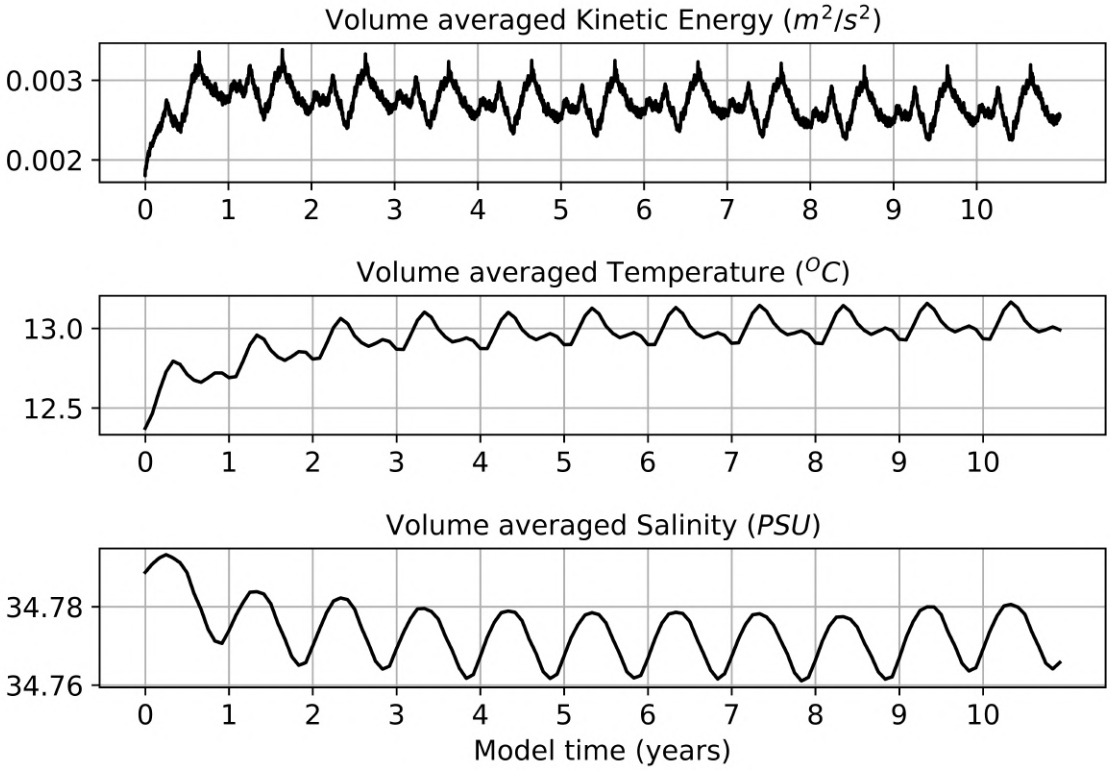

Figure 5.4: Volume averaged kinetic energy, temperature and salinity fields from the ocean model during the 11 spinup years

The atmospheric model - Weather Research and Forecast

The atmospheric part is performed using the Weather Research and Forecast (WRF) model version 4.2, using a single grid over the same eastern Pacific region but slightly larger than the CROCO grid and with a horizontal spatial resolution of about ∼25 km. The model is initialized from the atmospheric ECMWF Reanalysis v5 (ERA5, Hersbach et al. (2020), ∼25 km spatial resolution) produced by the Copernicus Climate Change Service (C3S). We used the hybrid vertical coordinate with 50 vertical levels and the following stretching parameters ($dzstretch\_u = 1.3$; $dzstretch\_s = 1.3$; $dzbot = 20$; $max\_dz = 1000$; $p\_top\_requested =$

1000), allowing us to have the first level set at 10 m over the ocean and about half of them in the lowest 1.5 km.

Several parameterizations were tested, in particular related to the droplet concentration and the cumulus convection scheme. Figures 5.5 – 5.7 present ocean-atmosphere simulations from January 2014 to September 2014, that take into account or not the droplet concentration ("drop"/"nodrop" (Jousse et al. (2016)), in solid/dashed lines), and with two different convective parameterization schemes ("cu11": multi-scale Kain–Fritsch convective scheme (Zheng et al. (2016)); "cu14": scale-aware New Simplified Arakawa-Schubert scheme (Kwon and Hong (2017)), in orange/blue lines), and their bias compared to observations. We chose the "cu11" scheme, as the "cu14" scheme leads strong cold SST bias reaching -2°C in the cold tongue, which is our main region of interest. In the "cu11" simulations, the "drop" one was selected as it reproduces a more accurate seasonal cycle in terms of SST, shortwave radiation and net heat flux. Yet, this "cu11 drop" simulation displays a time delay of 2 month in the shortwave radiation seasonal cycle compared to observations (Fig. 5.6).

Finally, the set of parameterizations found to be the most adequate in representing the mean state and seasonal to interannual variability of the Eastern tropical Pacific is the following : the 6-class microphysics scheme Hong and Lim (2006) taking into account droplet concentration Jousse et al. (2016), the multi-scale Kain–Fritsch convective parameterization scheme Zheng et al. (2016), the Goddard scheme for longwave and shortwave radiations Chou and Suarez (1999), the Noah land surface model Skamarock et al. (2008), the Revised MM5 Monin-Obukhov scheme for surface layers, and the YSU planetary boundary layer scheme Hong et al. (2006). As we will see in the following, it seems that the horizontal resolution of the atmospheric model may lead to bias in the stratocumulus cloud deck, that does not seem improved after tuning the convection scheme. One solution would be to increase the spatial resolution to explicitly resolve the convection of clouds. However, this would require a high resolution, from the current ∼25 km to ∼2 km, which would generate a high computational cost.

5.2.2 Coupled Experiments

Ocean-Atmosphere coupled simulations are performed using the coupler OASIS3MCT-2.5 (Craig et al. (2017)), which allows exchanging hourly-averaged of heat (net shortwave radiation, net heat flux), momentum, and freshwater fluxes from WRF to CROCO and SST and currents data from CROCO to WRF, every hour.

The control simulations (TIW-RUN) consist in an ensemble of 5 members starting from slightly perturbed oceanic conditions. The perturbations are done by using the initial conditions from the five last model time steps of the spinup. The damping of TIWs (NOTIW-RUN) in the oceanic model is done using the nudging methodology detailed in Chapter 2 and used in Chapter 3 and Chapter 4, although with some minor methodological differences. The meridional currents are nudged at a 5-day time scale toward the monthly climatology estimated from the 5-members ensemble. The Gaussian standard deviation used for the spatial filtering

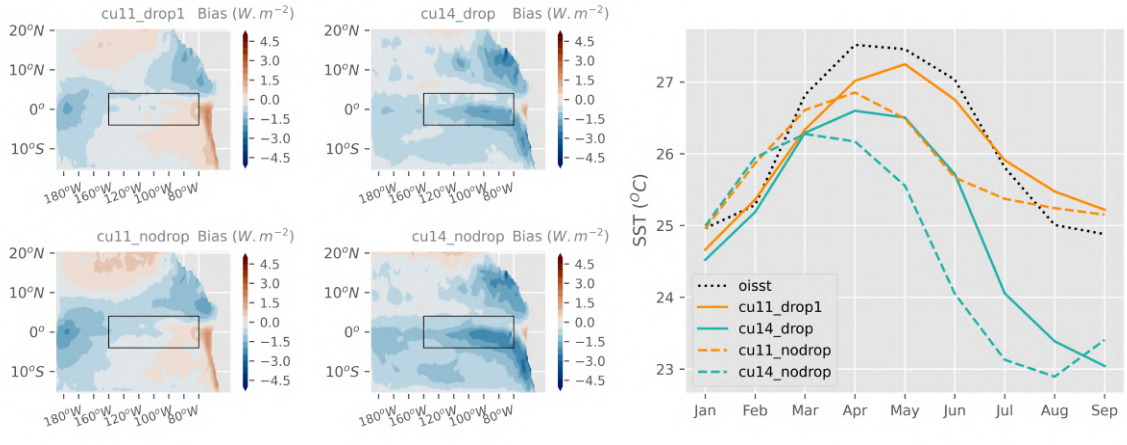

Figure 5.5: SST mean and seasonal biases between observations (OISST) and several ocean-atmosphere simulations with changing droplet concentrations ("drop": solid lines, "nodrop": dashed lines) and convection schemes ("cu11": orange lines, "cu14": blue lines), between January 1st 2014 and September 30th 2014 (see text for details). The seasonal cycle is obtained by averaging the SST in the Niño 3 box, shown in black lines on the maps.

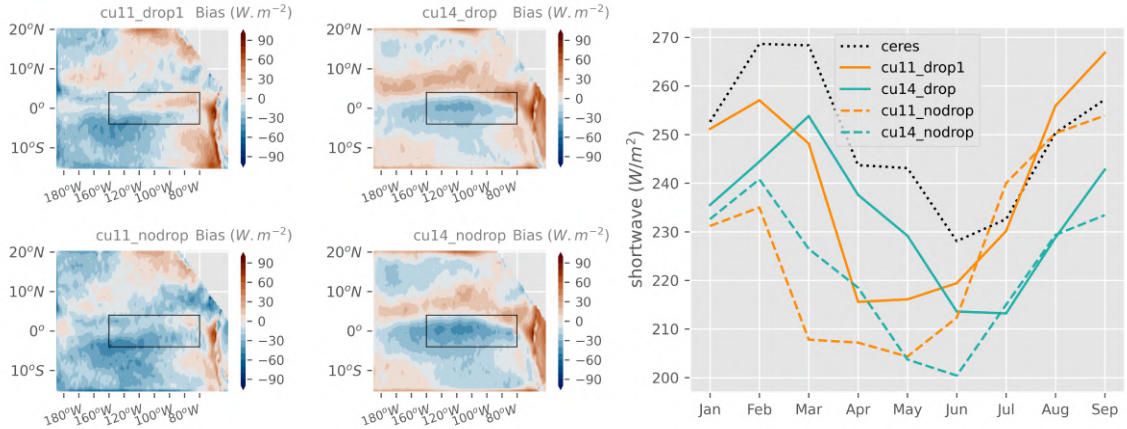

Figure 5.6: Same as Fig. 5.5 for shortwave radiation (observations: CERES)

is decreased from 10° in the ocean-only simulation to 5°in the coupled runs in order to reduce potential impacts of the nudging on the propagation and amplitude of off-equatorial Rossby Waves (see Chapter 2 for details).

The ocean and atmosphere models are forced at the boundaries by the Simple Ocean Data Assimilation 5-day reanalysis on 1/4° × 1/4° horizontal grid (SODA v3.4.2 , Carton et al. (2019)) in CROCO, and ERA-5 reanalyses in WRF, over the 2014-2018 period, with 2014 used as a spin-up year and discarded from the following analyses. This period includes a strong El Niño episode, followed by two successive La Niña events. Considering the relatively small spatial domain (185°W-70°W, 15°S-20°N), the coupled simulations are expected to be well constrained by the reanalyses-derived open boundary conditions and thus to reproduce

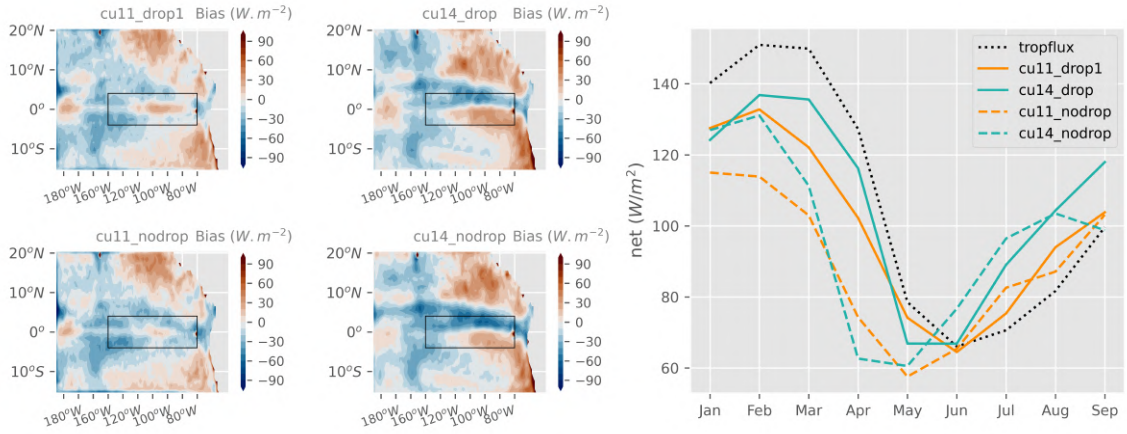

Figure 5.7: Same as Fig. 5.5 for net heat flux (observations: TROPFLUX)

the ENSO cycle rather realistically. This will be verified in the following.

5.3 Validation of the Model

A validation of the model is performed using one member of the TIW-RUN. We confront modeled atmospheric and oceanic components to observations and reanalysis over the 2014-2018 period.

5.3.1 Mean state and seasonal cycle

We evaluate the performance of the ocean-atmosphere coupled model with respect to both observations and the forced ocean simulation. However, we should keep in mind that both the spatial extent of the domain and its horizontal resolution differ slightly between the coupled and forced simulations.

First, we show in Figure 5.8a the seasonal evolution and mean biases in SST between observations (OISST) and both the coupled and forced simulations. Similarly, Figure 5.8b and c show the seasonal evolution and mean biases in shortwave radiation and net surface heat flux between observations (respectively CERES and TROPFLUX) and both the coupled simulation and CFSR reanalysis product used as atmospheric forcing for the ocean-only simulation.

Patterns of mean biases in the coupled ocean-atmosphere simulation are very distinct from the ones found in the forced ocean model, which suggests that they originate from different deficiencies in the simulation of the eastern tropical Pacific heat and momentum properties.

As noted previously (Chapter 3), the forced ocean-only simulation displays a warm SST bias over the entire domain (Fig. 5.8.a.2) most likely originating from an overall overesti-

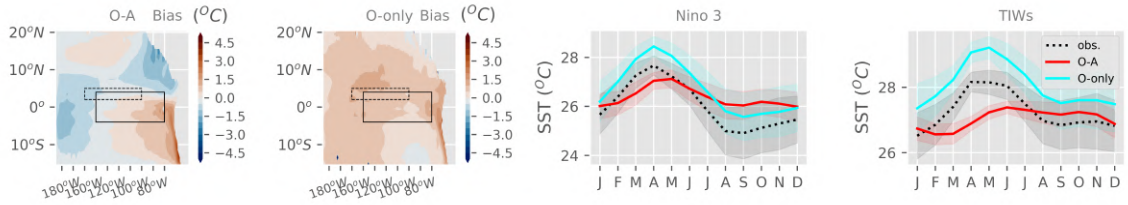

(a) Sea Surface Temperature

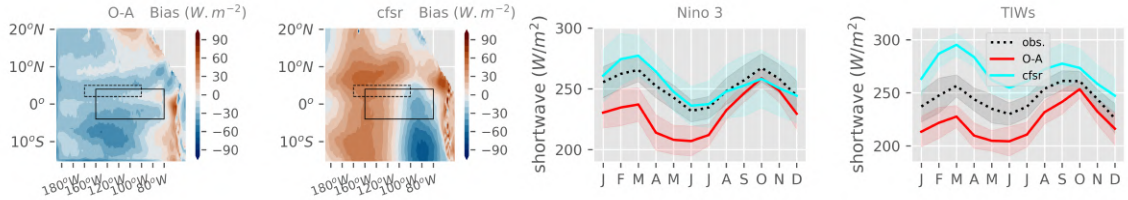

(b) Shortwave radiation

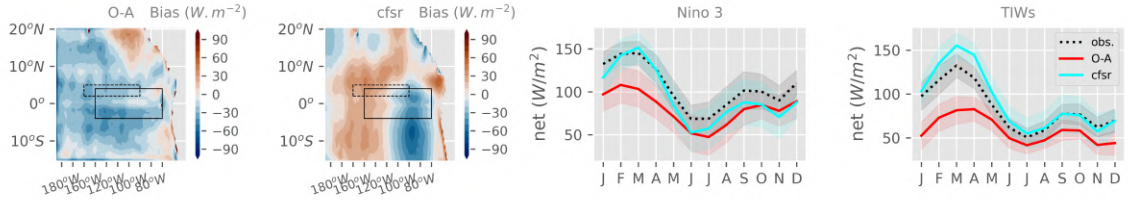

(c) Net surface heat flux

Figure 5.8: Model Validation. (a) Mean SST biases between observations (OISST) and the coupled ocean-atmosphere (a1) and forced ocean-only (a2) simulations. (a3,a4) SST seasonal cycle averaged in (a3) Niño 3 region (black solid-line box) and (a4) TIW region (2°– 5°N, 160°– 110°W, black dashed-line box) for the observations (dotted lines), the forced (blue lines) and coupled (red line) simulations. Shading shows the range of one standard deviation. (b) Same as (a) for the shortwave radiation biases with CERES observations, of the coupled ocean-atmosphere and CFSR reanalysis product. (c) Same as (a) for the net surface heat flux biases with TROPFLUX observations, of the coupled ocean-atmosphere and CFSR reanalysis product.

mation of shortwave radiation due to a poorly simulated cloudiness in CFSR (Dolinar et al. (2016)). Biases in the coupled ocean-atmosphere simulation, however, exhibit a more complicated spatial structure with essentially a warm bias in the cold tongue and a cold bias in the ITCZ region (Figure 5.8.a.1). The warm bias in the cold tongue, and in particular along the Peruvian coast, seems to arise from a too strong shortwave radiation (Figure 5.8.b.1) likely indicating a poor representation of the stratocumulus cloud deck, which is a classic deficiency of atmospheric models. Other parameterizations may be more adequate for this region but would deteriorate the realism of the simulations over the equatorial region.

On the other hand, the cold SST bias in the ITCZ linked to a weak shortwave radiation possibly originates from deficiencies in simulating the formation of towering cumulus or cumulonimbus in this region characterized by a strong convective activity. These biases could

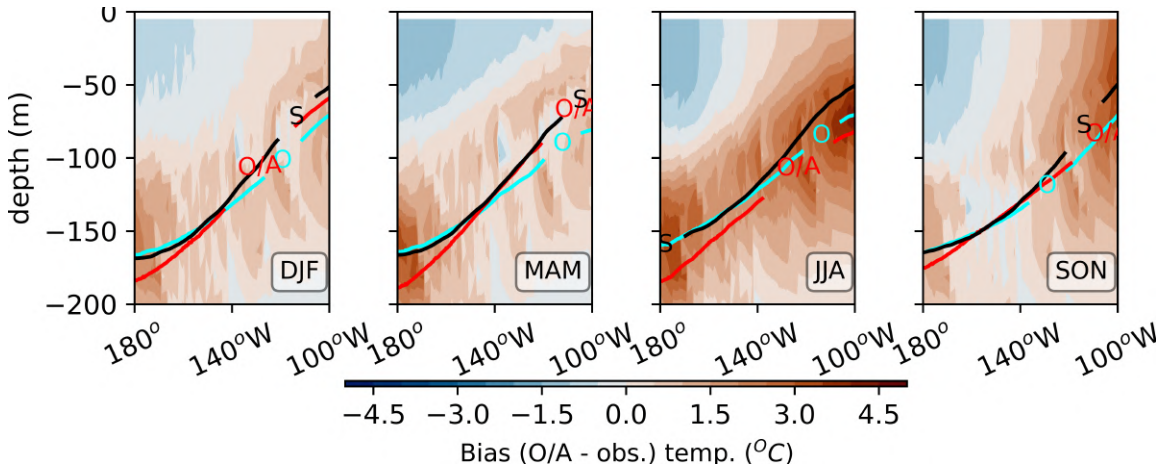

Figure 5.9: Seasonal variations of the depth of the thermocline (diagnosed as the 20°C-isotherm, averaged in the 1°S-1°N latitudinal band) in the coupled ocean-atmosphere ("O/A", red line), forced ocean-only ("O", cyan line) simulations and SODA3.4.2 reanalysis ("S", black line), over the period 2014-2018. Shadings correspond to the temperature bias in the coupled ocean-atmosphere simulation

be reduced by changing some parameterizations, or by increasing the spatial resolution of the atmospheric model to explicitly resolve the cloud cover. However, such a sensitivity study is beyond the scope of the present study.

In addition to this thermodynamic origin, biases can also originate from failures in the simulation of some dynamical processes, as indicated by the biases in the mean depth of the thermocline simulated by the forced and coupled model (Fig. 5.9). In the forced simulation, the thermocline is too deep in the eastern Pacific, demonstrating a weak upwelling that potentially participates in the warm SST bias. This could arise from a poor wind stress curl representation (Sun et al. (2021)) in CFSR, or an inaccurate equatorial wave dynamics injected at the western boundary. Conversely, in the coupled simulation, the thermocline position in the eastern Pacific seems in good agreement with observations in winter and spring, but remains too deep the rest of the year. In the West, the thermocline is too deep all year long again potentially due to biases in the open boundary conditions, or in the wind stress.

In terms of seasonal cycles, two main points are noticeable. First, the maximum SST in the coupled model occurs one-to-two months later than observations in the region of active TIWs (Fig. 5.8.a.2). Second, the seasonal cycles of SST and atmospheric fluxes appear much weaker in the coupled runs only. It is not surprising to have a more realistic forced simulation, as it is strongly constrained at the surface and the open boundaries by reanalysis products. Moreover, the weak seasonal cycle in the coupled model could arise from too weak large scale atmosphere-ocean feedbacks, or from a too coarse resolution of the atmospheric component making it unable to simulate an accurate synoptic variability.

5.3.2 ENSO cycle

We now evaluate the ability of the model to reproduce the interannual variability in the eastern tropical Pacific. The time series of interannual anomalies of SST averaged in the Niño 3 box, and of the meridional temperature gradient characterized by the Niño D index are shown in Figure 5.10 for all members of the coupled ocean-atmosphere ensemble (red lines, ensemble of 5 members), forced ocean-only (cyan line) and observations (OISST, black dashed line).

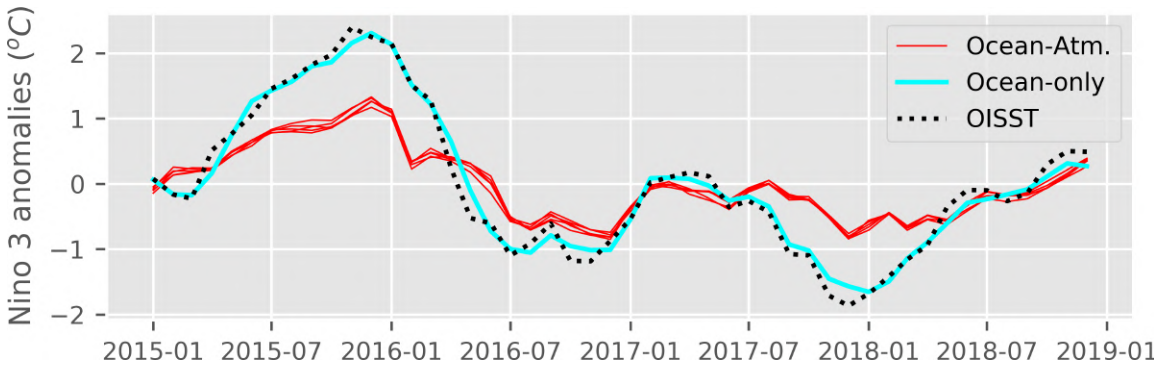

(a) Niño 3

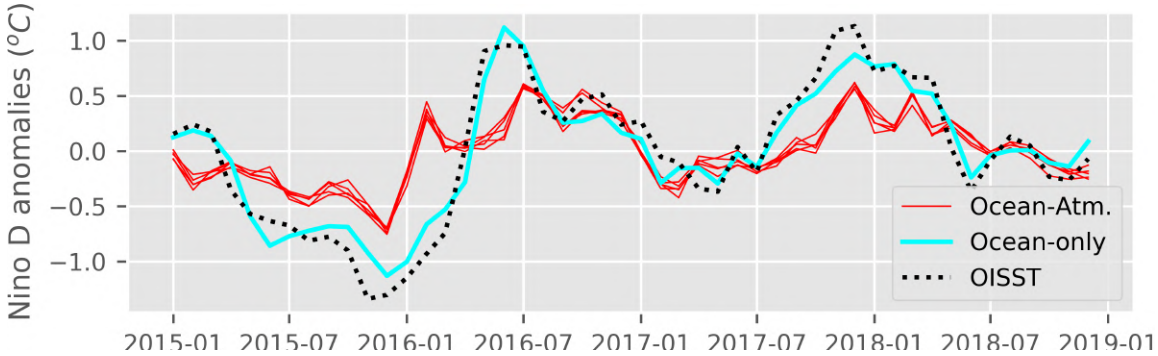

(b) Niño D

Figure 5.10: Interannual anomalies of SST averaged in the (a) Niño 3 and (b) Niño D regions, in the coupled ocean-atmosphere (red lines), forced ocean-only (cyan line) and OISST observations (black dashed line)

This 2015-2018 period is characterized by a strong El Niño peaking during the 2015/16 boreal fall and winter inducing warm SST anomalies (Fig. 5.10a) and a negative anomaly of meridional temperature gradient (Fig. 5.10b), followed a double-year La Niña, in 2016/17 and 2017/18, marked by cold SST anomalies and a positive anomaly of meridional temperature gradient.

While the ocean-only forced simulation captures with accuracy the timing and amplitude of interannual variations, the ocean-atmosphere coupled simulations produce a weaker and slightly shifted ENSO cycle, with an amplitude reduced by half compared to the observations.

Overall, the ocean-atmosphere coupled simulation produces weak seasonal and ENSO cycles and different mean state biases compared to the forced simulation and to observations. This could be due to flaws in the representations of large scale atmosphere-ocean feedbacks or of local air-sea interactions potentially related to an inadequate parameterization of convection in the ITCZ region, which remain to be investigated. Options to look into this issue in more details include testing the dependency of the coupled model to other reanalysis products at the boundaries; testing other convection schemes; increasing the horizontal resolution of the atmospheric model to resolve explicitly the cloud cover. Regardless, hereafter, the coupled simulation ensemble will be compared to a sensitivity experiment in which only the TIW mesoscale activity is damped. The aforementioned large scale mean biases are expected to be similar in all experiments and therefore cancel out when evaluating the specific effect of TIWs onto the 2015 – 2018 ENSO cycle.

5.3.3 TIW representation

To study the ability of our coupled model to simulate TIWs, the variance of TIW-induced surface meridional currents and SST is computed as v'^2 and SST'^2. To specifically focus on TIW activity, fluctuations are obtained by removing 30-day and 12° longitude centered running means to the raw data. In addition, a 5-day running mean is applied to the observation (OISST) to remove small-scale variability (see Chapter 4). Note that the spatial running mean is used only for comparison with observations.

The comparison between observed and simulated TIW variability is presented in Figure 5.11. The spatial pattern of SST'^2 is in good agreement with observations (OISST, January 2015 to December 2018). The amplitude of SST'^2 however is underestimated by 45% in the region of strong TIW activity (black box in panels a–d), which might come from large scale bias in the simulation of temperature and currents. The spatial pattern of v'^2 is similar to observations (GlobCurrent, January 2015 to May 2017) for the off-equatorial peak, but the equatorial peak is different, an issue that has been discussed in the previous Chapter. While as expected, TIW activity is strong during the 2016/17 and 2017/18 La Niña episodes and almost nonexistent during the 2015/16 El Niño, the time series are shifted by about 2 months compared to the observations (Fig. 5.11e–h). This shift can be attributed to the seasonal shift in SST (see Section 5.3.1), or in the timing of ENSO feedbacks simulated by the coupled model (see Section 5.3.2), both of which being most likely the result of the large scale mean biases identified earlier.

5.4 TIW – ENSO interactions

In this section, preliminary results on the effects of TIW activity on the ENSO cycle are presented. In this part, the intraseasonal anomalies related to TIWs and noted X' will refer to fluctuations from a 30-day running mean only, so that the Reynolds decomposition can be applied.

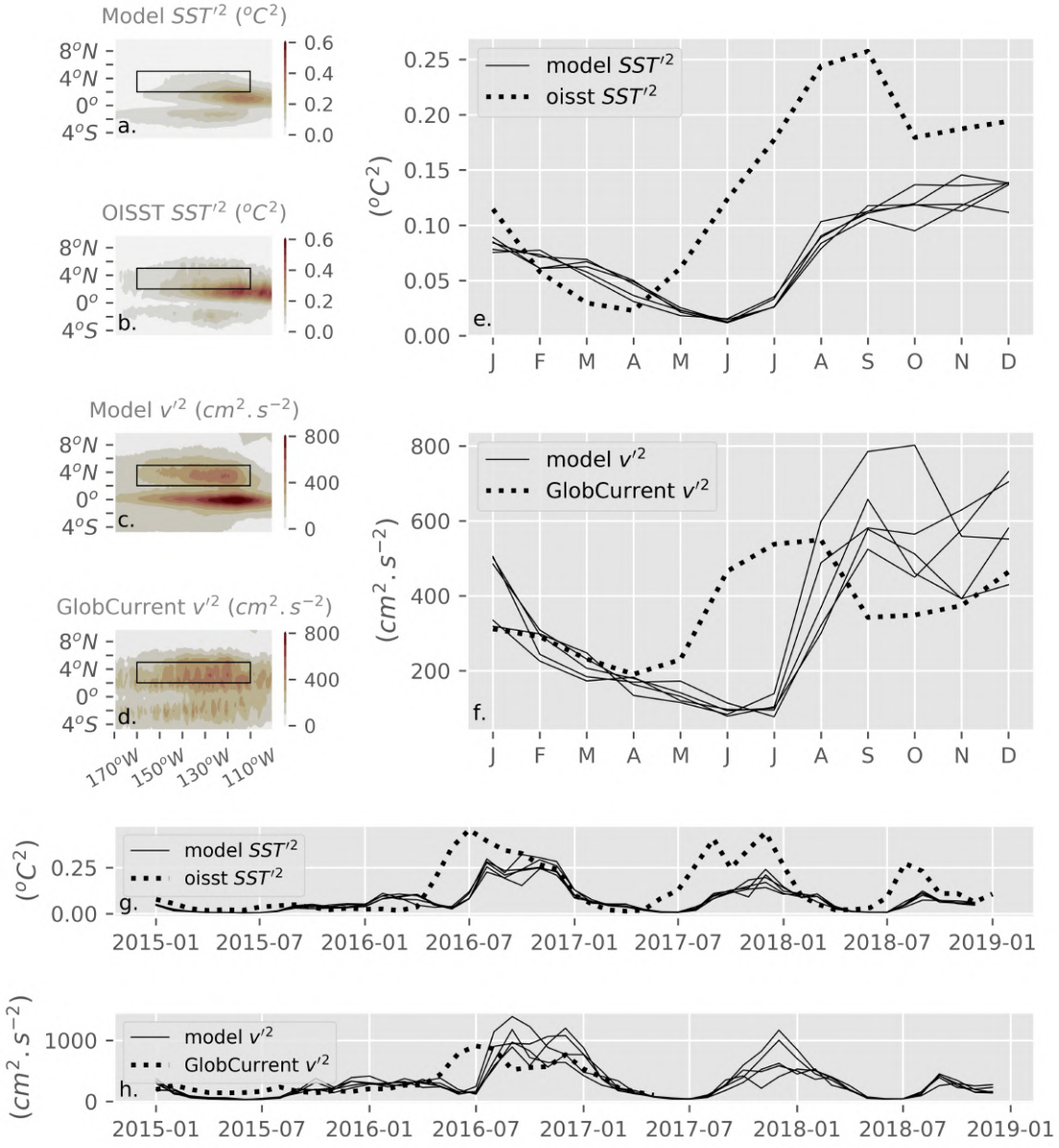

Figure 5.11: Maps of mean TIW variance SST'^2 for (a) the ensemble averaged of the ocean-atmosphere coupled runs and (b) OISST, from January 2015 to December 2018. (c,d) Same as (a,b) but for the TIW variance v'^2 in (c) the ensemble average of the coupled runs and (d) GlobCurrent product, from January 2015 to May 2017. (e) Seasonal cycle of SST'^2 averaged in the region delineated by black lines in a–d (2°– 5°N, 160°– 110°W) from January 2015 to December 2018. (f) Same as (e) but for v'^2 from January 2015 to May 2017. (g) Time series of SST'^2. (h) Same as (g) but for v'^2.

5.4.1 A detailed ENSO cycle

First, we focus on describing the dynamics of the ENSO cycle in the TIW-RUN coupled simulations ensemble mean. To do so, we show in Figure 5.12 Hovmöller diagrams of interannual anomalies of SST, thermocline depth, zonal wind and currents in the equatorial band (4°S-4°N) to describe the air-sea feedback responsible for the temporal evolution of the 2015-2018 ENSO cycle.

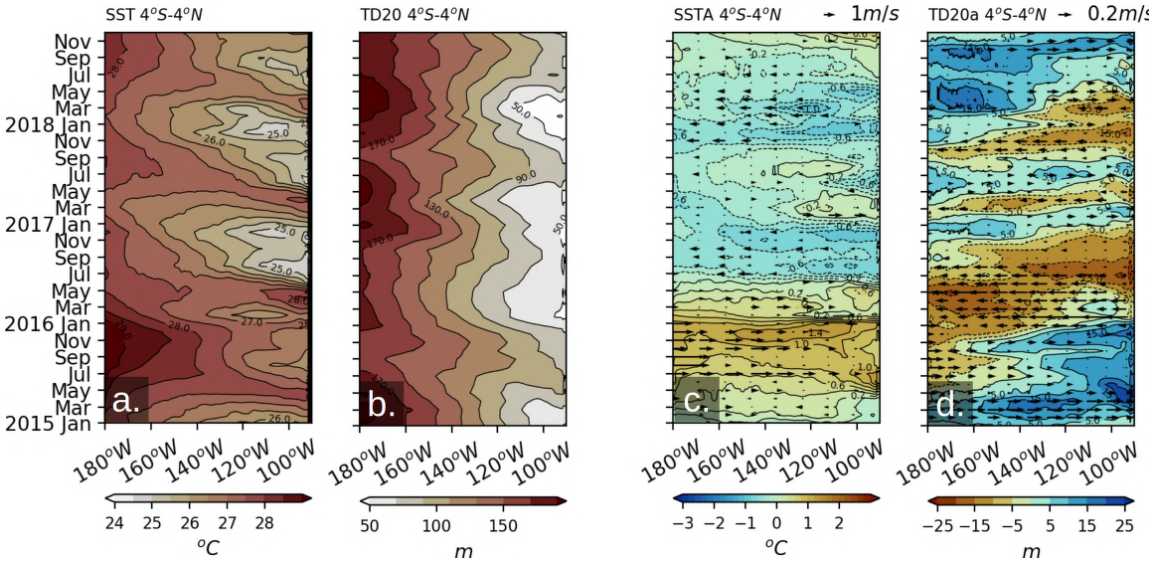

Figure 5.12: Hovmöller diagrams of the TIW-RUN ensemble mean of (a) SST, (b) thermocline depth (isotherm 20°C), (c) SST (shading) and zonal low-level wind (arrows) interannual anomalies and (d) thermocline depth (shading) and surface zonal currents (arrows) interannual anomalies, zonally averaged between 4°S and 4°N.

During the spring preceding the 2015/16 El Niño, positive SST anomalies emerge over the central and western Pacific, respectively (Fig. 5.12c). In the subsequent months, the atmospheric response is characterized by westerly wind anomalies (Fig. 5.12c) that trigger a downwelling Kelvin wave (Fig. 5.12d) starting in the west at the very beginning of 2015, and resulting in the deepening of the equatorial thermocline and anomalous eastward zonal currents. This Kelvin wave propagates eastward and contributes to the anomalous warming in the eastern Pacific in May of the same year, through thermocline and zonal advective feedback (see Chapter 1). This kickstarts an El Niño episode peaking during the 2015/16 winter, characterized by a nearly complete disappearance of the cold tongue (Fig. 5.12a) and a deep thermocline in the east (Fig. 5.12b).

In November 2015, an upwelling Kelvin wave crosses the basin in about 2 months and results in a shoaling of the thermocline and anomalous westward zonal currents, accompanied by a cold SST anomaly that reaches the eastern Pacific in July 2016. These 2016/17 La Niña conditions persist until March 2017, when a return to neutral conditions is observed in both the eastern Pacific temperature and thermocline depth.

A succession of upwelling Kelvin waves and anomalous easterly winds in fall/winter of 2017 leads to the return of the 2017/18 La Niña episode with SST similar to La Niña 2016/17, but with a shallower thermocline (20 meters shallower at 110°W).

This double-year La Niña event is composed of two successive episodes that exhibit different characteristics. The 2016/17 La Niña episode begins in July and lasts until January of the following year, with cold waters reaching the central Pacific and staying there for a long time. The 2017/18 La Niña episode begins in October and lasts until July of the following year. As will be seen in Section 5.4.4, the dynamics of these two La Niña episodes differ most notably in the respective contribution of the dominant ENSO feedbacks in the growth of the cold SST anomalies.

5.4.2 TIW impacts on ENSO: Niño indices as proxy of ENSO

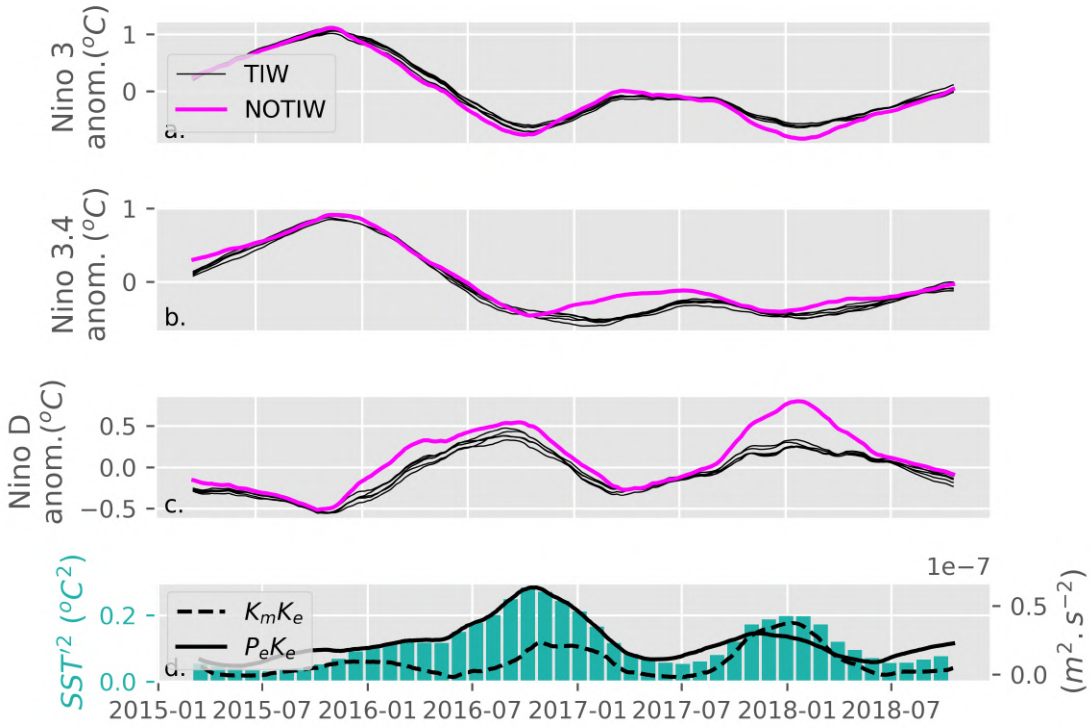

Figure 5.13: Effect of TIWs on interannual anomalies of SST averaged in (a) Niño 3, (b) Niño 3.4 and (c) Niño D boxes. (d) TIW-induced SST variance SST'^2 and 50-meters averaged baroclinic (P_eK_e) and barotropic (K_mK_e) conversion rates, averaged in the same black box as in figure 5.11. A 5-month running-mean has been applied to all variables. The interannual anomalies are computed as fluctuations from a common monthly climatology from the NOTIW-RUN and the mean of the 5 ensembles of TIW-RUN.

We now evaluate how differences in TIW activity modulate the ENSO cycle. Figure 5.13 shows different traditional Niño indices from the TIW- and NOTIW-RUN simulations. Again,

note that we compute interannual anomalies as fluctuations from a common monthly mean climatology obtained by averaging NOTIW-RUN with the TIW-RUN ensemble mean.

The impacts of TIWs on each Niño indices are the following,

- The Niño 3 index (Fig. 5.13a) shows no significant differences between TIW- and NOTIW-RUN during El Niño and 2016/17 La Niña. However, the TIW-RUN members are slightly warmer than NOTIW-RUN during the 2017/18 La Niña, with +0.2°C in February 2018.

- The Niño 3.4 index (Fig. 5.13b) shows a different picture than the Niño 3 index. If the El Niño still remains similar in both runs, the 2016/17 La Niña is extended in presence of TIWs, and the 2017/18 La Niña is not significantly changed.

- The Niño D index (Fig. 5.13c), a proxy for the meridional gradient of temperature, shows significant TIW-induced decrease of the gradient during the two La Niña episodes, in particular during the 2017/18 La Niña with -0.53°C in February 2018.

However, those Niño indices are averaged over different areas. The Niño 3.4 box is centered at the equator and located close to the central Pacific (5°S-5°N, 170°W-120°W). The Niño 3 box is also centered at the equator, and in the eastern Pacific (4°S-4°N, 150°W-90°W). The Niño D index is the difference between an off-equatorial box (3°N-8°N, 150°W-110°W) and an equatorial box (3°S-3°N, 150°W-110°W). The variety of responses of each Niño index to TIWs indicates that the TIW-induced modifications of the SST have a complex temporal and spatial pattern. Thus, focusing on only one Niño index to characterize the effect of TIWs on ENSO might not be sufficient. A more in-depth process study is needed.

Overall, the Niño indices show that each La Niña episode appears to respond differently to TIWs, which could be due to the different nature of La Niña episodes of this double-year La Niña, and of the associated TIW bursts.

As briefly explained in the previous section, and as it will be detailed in Section 5.4.4, the 2016/17 and 2017/18 La Niña episodes differ in terms of the contribution from the different feedbacks to the growth of the anomalies. As a response, the TIW activity during these two episodes differ both in their timing and generating processes (Fig. 5.13d). TIWs are seen to start early during the first half of the year and peak in November during the 2016/17 La Niña episode, while they start later in the second half of the year and peak in January during the 2017/18 La Niña episode (green bars). Moreover, their generation process differ. A strong baroclinic (P_eK_e, solid line) conversion of energy generate the first wave burst, while a mixture of baroclinic and barotropic (K_mK_e, dashed line) conversion of energy generate the second burst of 2017/18.

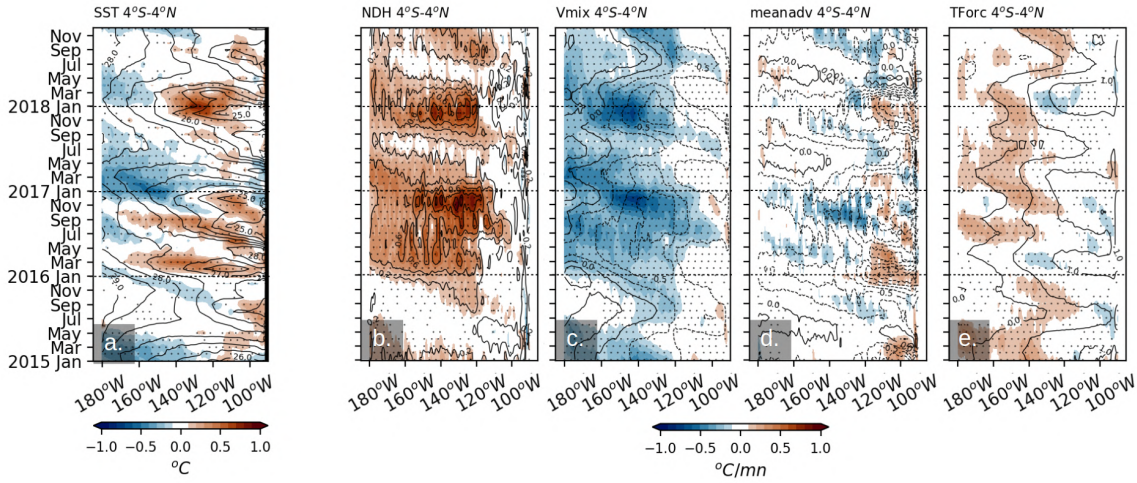

Figure 5.14: Hovmöller diagrams of differences (shading) between TIW- and NOTIW-RUN for (a) SST and (b-e) 50-meter averaged heat budget terms. The heat budget terms are (b) the 3-dimensional TIW-induced intraseasonal NDH, (c) the vertical mixing, (d) the 3-dimensional mean advection and (e) the forcing by the atmosphere. Contours show the mean values in TIW-RUN. Dots indicate significant differences at 95% confidence (one sample two-tailed student t-test on differences between NOTIW-RUN and each member of TIW-RUN, with the null hypothesis $H_0 = 0$)

5.4.3 TIW impacts on ENSO: an intraseasonal heat budget analysis

Figure 5.14a shows the effect of TIWs on the time evolution of the ENSO cycle (SST), as well as the dominant thermodynamic feedbacks as Hovmöller diagrams of the differences between TIW- and NOTIW-RUN averaged in the 4°S-4°N band. This heat budget is obtained using daily averaged fields, and the advective terms are separated into an intraseasonal (noted x') and a mean (noted x_m) contribution.

Red shading indicates a TIW-induced warming in the central and eastern Pacific, sometimes reaching 170°W, occurring predominantly during the multi-year La Niña event (looking back at Figure 5.13a, the warming during the 2016/17 was not significant probably because of the 5-month running mean applied to the time series). As extensively explained in previous Chapters and in literature, and shown in Figure 5.14b, this warming is mainly due to TIW-induced intraseasonal nonlinear dynamical heating (NDH, advection of anomalous temperature by anomalous currents).

Interestingly, a TIW-induced cooling is observed in the western-to-central part of the basin, especially during the second half of the 2016/17 La Niña. This cooling appears to be generated through vertical mixing processes (Fig. 5.14c), with an anomalous cooling rate occurring during each TIW burst and reaching 180°W in January-April 2017. Although the TIW-induced mixing cooling rate occurs during both La Niña episodes, the 2016/17 is much more pronounced. It is likely helped by the anomalous cooling rate by mean advective

processes (an indirect, or rectified, effect due to the reduced strength of the EUC, see Chapter 3), in the center of the basin in fall 2016.

This combination of warming by intraseasonal NDH and cooling by vertical mixing during each Niña episode explains the different variations in the Niño index seen in the previous section : the 2016/17 La Niña is reduced by TIW-induced intraseasonal NDH, but a very intense TIW-induced cooling through vertical mixing helps the Niña to extend a few months more. The 2017/18 La Niña is strongly damped by TIW-induced intraseasonal NDH which dominates over cooling through vertical mixing.

Understanding why this TIW-induced cooling through vertical mixing occurs in the western part of the basin, and why it interacts differently with intraseasonal NDH for different successive episodes of one double-year La Niña events remain open questions. TIWs are known to enhance vertical mixing in the upper part of the EUC (Lien et al. (2008); Moum et al. (2009); Inoue et al. (2012); Holmes and Thomas (2015)). However, the changes in vertical mixing observed might not only be due to TIW-scale processes (*i.e.,* a direct effect), but could also be due to a modification of the large scale processes reflecting a potential indirect effect. A study of diffusion, thermocline, stratification, shear, could help understanding which process controls this mixing rate.

- quick note on the heat budget -

At time step n, the temperature T of the TIW-RUN is

$$T_n^{TIW} = T_{n-1}^{TIW} + dt * \partial_t T_n^{TIW} \tag{5.1}$$

Same for NOTIW-RUN.

Thus, the difference of temperature between the TIW- and NOTIW-RUN is

$$\Delta T_n = \Delta T_{n-1} + dt * \Delta \partial_t T_n \tag{5.2}$$

where Δ is the difference operator between the two simulations.

Hence, we can look at the contribution of each term of this heat budget to the temperature change at a time step n. Note that this temperature change also depends on the temperature change at time step $n-1$.

5.4.4 TIW impacts on ENSO: an interannual heat budget analysis

The heat budget can also be decomposed into ENSO feedbacks, by looking this time at interannual anomalies. The new heat budget averaged in the first 50 meters is now:

$$\begin{aligned}\partial_t T_a = & \underbrace{-\overline{u}\partial_x T_a - \overline{v}\partial_y T_a}_{DD} \underbrace{-\overline{w}\partial_z T_a}_{TCF} \\ & \underbrace{-u_a\partial_x \overline{T}}_{ZAF} \underbrace{-v_a\partial_y \overline{T}}_{MAF} \underbrace{-w_a\partial_z \overline{T}}_{UPW} \\ & \underbrace{-u_a\partial_x T_a - v_a\partial_y T_a - w_a\partial_z T_a}_{NDH} + \underbrace{\epsilon}_{RES}\end{aligned} \tag{5.3}$$

with x_a are the interannual anomalies (*i.e.,* anomalies from the common monthly climatology), and $\overline{x}$ are the climatological terms. The temperature tendency is the combination of the dynamical damping or mean current effect (DD), the thermocline feedback (TCF), the zonal advective feedback (ZAF), the meridional advective feedback (MAF), the upwelling or Ekman feedback (UPW), the interannual nonlinear dynamical heating (NDH), and the residual (RES). As this heat budget is computed from monthly averaged fields, the residual contains the contribution of intraseasonal terms to the heat budget. It also contains diffusive processes, heat fluxes and possible errors from approximations. In the literature, the DD, TCF, ZAF and UPW are recognized as key contributors to ENSO development (Suarez and Schopf (1988); Battisti and Hirst (1989); Jin (1997a)). The MAF is often found negligible (Jin et al. (2006); Kim and Jin (2011)), and the interannual NDH is often low but thought to explain in part the ENSO amplitude asymmetry (*e.g.,* An and Jin (2004)).

To avoid large errors that occur in the computation of the heat budget close to the coast where σ-levels are shallower, each term of the heat budget is averaged over a slightly shorter region (4°S – 4°N, 150°– 100°W) than Niño 3 (4°S – 4°N, 150°– 90°W). Each term is then evaluated during the development phase of each La Niña episode, defined as the period between the phase transition (T_a becomes negative) and the beginning of the decaying phase of La Niña (grey shaded areas in Fig. 5.15 up).

ENSO feedbacks during the multi-year La Niña

In each La Niña episode, the positive feedbacks (*i.e.,* that leads to a decreasing temperature tendency) are the DD, TCF, ZAF, MAF and UPW, while negative feedbacks (*i.e.,* that counteract the decreasing temperature tendency) are the interannual NDH and the RES.

Interesting, despite a large number of studies finding a negative contribution of the DD feedback (*e.g.,* Jin et al. (2006); Kim and Jin (2011); Kim et al. (2014); Boucharel et al. (2015); Ferrett and Collins (2019)), and only a some studies finding a positive contribution (Battisti (1988); Kang et al. (2001); Zhu and Kumar (2018)), our DD feedback makes an important positive contribution to La Niña development, especially during the 2016/17 La Niña episode. This might come from a different definition of the DD feedback, but a more detailed study is needed to understand the respective contribution of each zonal and meridional term of this feedback.

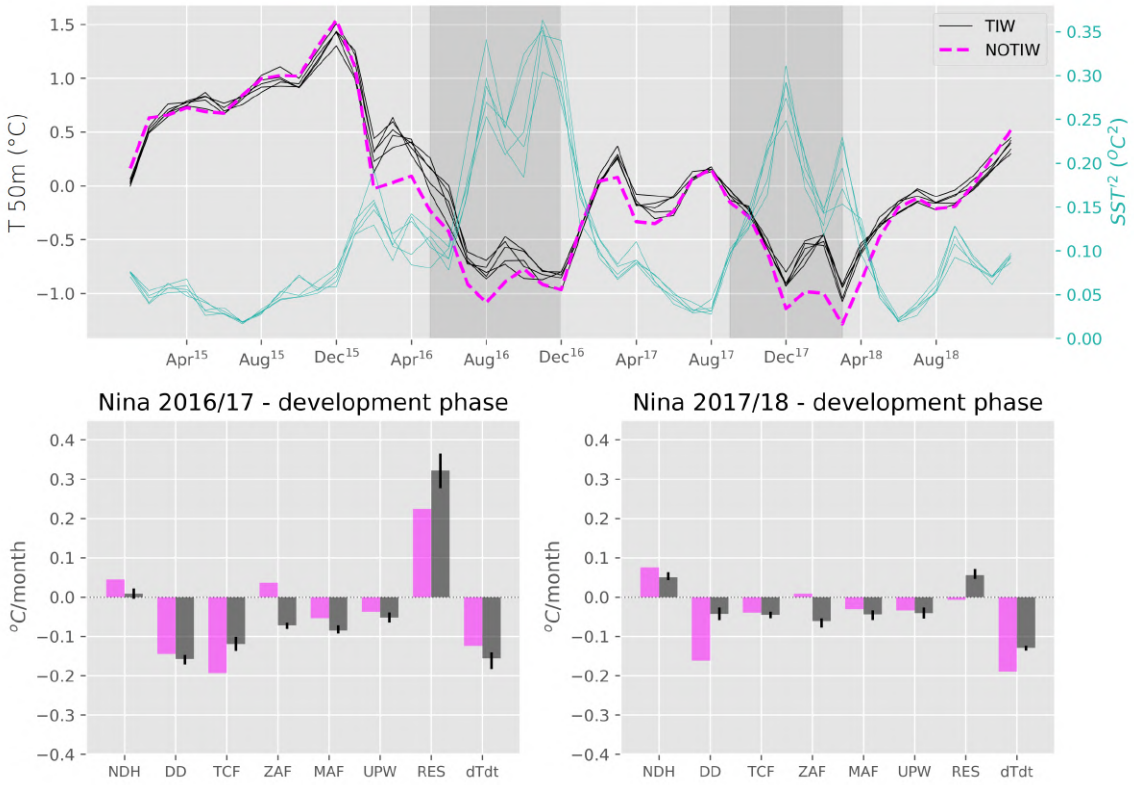

Figure 5.15: ENSO feedbacks on the upper 50 meters over 4°S – 4°N, 150°– 100°W. (up) time series of the temperature interannual anomaly in TIW-RUNs (black) and NOTIW-RUN (dashed magenta), and of the TIW-index in TIW-RUN (SST'^2 as in Fig. 5.11). (down) Contribution of each ENSO feedback to the temperature tendency during each La Niña development phase. Errors bars in grey bars indicate the spread of the 5 members in TIW-RUN. The development phase of each Niña episodes is indicated in shaded grey areas in (up).

In the 2016/17 La Niña episode, the dominant terms are the DD, TCF and RES. In the 2017/18 La Niña however, all terms have a similar small contribution, with a slight dominance of the ZAF. This difference in the contribution of ENSO feedbacks for each episode of this multi-year La Niña could come from the difference in transition phase: a strong El Niño precedes the 2016/17 La Niña episode, while a normal state precedes the 2017/18 episode. In the first case, a large discharge of equatorial ocean heat content most probably occurs during the decay of the strong 2015/16 El Niño. This discharge state is partly recharged during the 2016/17 La Niña through TCF and DD (probably through $-\overline{v}\partial_y T_a$). In that case, the recharge process is expected to be much weaker during the 2017/18 La Niña. Hence, this potential large discharge after El Niño could explain the larger contributions of TCF and DD in the development of the 2016/17 La Niña than of the 2017/18 La Niña.

The important TCF feedback during the 2016/17 La Niña episode, and the slight dominance of the ZAF feedback during the 2017/18 La Niña episode is in line with the results of Liu et al. (rev.) in which the authors investigate the oceanic processes responsible for the multi-year La Niña based on observations and reanalysis datasets. They found that during a

typical multi-year La Niña, the TCF and ZAF make equal contributions during the first La Niña episode while only the ZAF contribute to the second episode. However, they did not investigate the contribution of other feedbacks, despite the fact that they seem to play an important role in our results.

The potential large off-equatorial discharge of heat that precedes the development of the 2016/17 La Niña could explain the large meridional temperature gradient (Niño D, see Fig. 5.13c), and therefore the large baroclinic conversion rate that generates TIWs (Fig. 5.13d).

During the 2016/17 La Niña, the residual term has a very large contribution to the temperature tendency (more than 0.3°C month^{-1}). Conversely, its contribution is relatively small (less than 0.1°C month^{-1}). This difference might come from differences in intraseasonal NDH, mixing, or heat fluxes between these two La Niña episodes, as inferred by the intraseasonal heat budget (Section 5.4.3).

ENSO feedbacks modulated by TIWs

By comparing the TIW-RUNs (black) with NOTIW-RUN (magenta), the impact of TIWs on the ENSO feedbacks during the development phase of each La Niña is assessed. This section is a work in progress. Hence, only the most striking result will be detailed here.

One major effect of TIWs on ENSO feedback is observed in the ZAF. While this feedback was positively contributing to the development of both La Niña in the TIW-RUNs, it becomes a negative feedback in the NOTIW-RUN. This result indicates that TIWs are directly or indirectly responsible for the strength and sign of the ZAF. This feedback is the zonal advection of mean temperature by anomalous zonal currents ($-u_a \partial_x \overline{T}$). Therefore the contribution of each of these terms, u_a and $\partial_x \overline{T}$, to the change induced by TIWs on the ZAF could shed light on the mechanisms by which TIWs are modulating this key feedback in ENSO dynamics.

5.5 Synthesis and discussion

In this Chapter, a coupled ocean-atmosphere model is used to simulate the 2015-2018 ENSO cycle, consisting in a strong El Niño event followed by a double-year La Niña event, and to investigate its interaction with TIW activity. The model represents well the equatorial dynamics, although the seasonal and ENSO cycles amplitudes are underestimated most likely due to a too coarse resolution of the atmospheric component as well as an inadequate parameterization of convection in the ITCZ region and representation of the stratocumulus deck and associated cloud formation in the eastern Pacific cold tongue. This bias could also come from an underestimated wind response to SST forcing. The model also reproduces well TIW activity although with a slight temporal lag compared to observations, that seems to be related to a similar shift in the SST seasonal cycle and in the development of the La Niña episodes. We first show that the TIW activity is increased during both La Niña episodes and triggered by their induced large scale climate background in particular associated with a strengthened

meridional temperature gradient and shear of currents. However, the contribution from these two mechanisms of generation (baroclinic and barotropic energy conversion respectively) differ between the two La Niña events. In particular, a strong baroclinic conversion occurs during the 2016/17 La Niña episode, while a more balanced combination of baroclinic and barotropic conversions is evidenced during the 2017/18 La Niña episode. This could be linked with the respective contribution from large scale feedbacks involved in the La Niña cold SST anomalies growth rate.
The first 2016/17 La Niña event seems to develop through the classic Sverdrup dynamics associated with the thermocline feedback and meridional dynamical damping, that are linked to the strong off-equatorial heat discharge. This discharge strengthen the meridional SST gradient (and baroclinic instability) in the eastern tropical Pacific, which generates TIWs. The development of the following 2017/18 La Niña seems to be due to a combination of feedbacks, with a dominance of the zonal advective feedback. This could could cause an increased shear of zonal currents along with a slight strengthening of the meridional temperature gradient, which both trigger barotropic and baroclinic instabilities.

We then used the methodology developed in Maillard et al. (2022a) (Chapter 2 and Chapter 3) to properly isolate and quantify TIW effects on the ENSO cycle. More specifically, we compare different simulations: a 5-members ensemble (TIW-RUN) in which TIWs freely develop and a simulation in which they are subtly removed (NOTIW-RUN). This methodology allows to accurately distinguish TIW effects on the ENSO cycle and coupled dynamics. A decrease of the meridional gradient of temperature is noticed in both Niña episodes overall reducing their strength and the ENSO cycle asymmetry. However, looking at typical Niño index as proxy of ENSO does not seem to be sufficient to capture the complexity of the changes induced by TIWs.

A more in-depth study has been started by looking at the heat budget of the first 50-meter in the equatorial band. It reveals a warming of the cold tongue through non-linear dynamical heating associated with TIWs during both La Niña episodes. Interestingly, an intense cooling of western equatorial waters through vertical mixing is noticed during the 2016/17 La Niña episode, resulting in a temporal extension of this episode. This cooling through vertical mixing also occurs during the 2017/18 La Niña episode, but the NDH seems to dominate. Moreover, an interannual heat budget revealed a important contribution of TIWs to the sign of the zonal advective feedback, and in particular to make it a positive feedback that help the cold anomaly to grow into a La Niña.

This case study on this double-year La Niña events tells us that there is a complex feedback of TIWs on La Niña which seems to depend on each episode of the double-year event. In-depth diagnostics are needed to understand the origin of (1) the TIW-induced cooling through mixing and (2) of the TIW-induced change of sign of the zonal advective feedback. In particular, is the changes in the mixing cooling rate a direct or indirect effect of TIWs ? What are the involved processes explaining these changes ? Do these results hold for all multi-year La Niña ? This last question could be answered from a similar study on a longer period, which could also be used to evaluate the processes that differ between single-year and multi-year La Niña.

Conclusion and Perspectives

– Conclusions –

As the tropics become increasingly populated and threatened in a changing climate, there is an urgent need to better understand the complex processes that influence climate variability in these tropical regions, especially regarding El Niño – Southern Oscillation (ENSO), the most important driver of tropical interannual fluctuations which has widespread effects on weather, climate and societies. Tropical instability waves (TIWs) represent the dominant form of mesoscale oceanic transient activity in the tropics and have been shown to interact with ocean temperatures and circulation over a wide range of time scales, and in particular with ENSO. This thesis focuses on the impact of TIWs on oceanic variability in the eastern tropical Pacific Ocean, with a number of contributions that improve our understanding of the interactions between TIWs and the larger scale thermodynamic state and variability.

First, based on the Coastal and Regional Ocean Community (CROCO) model, I developed a model-based tool to isolate the effects of TIWs on the eastern tropical Pacific Ocean (Chapter 2). The approach consists in removing the oceanic variability associated with TIWs in a simulation of the eastern Pacific Ocean (NOTIW-RUN), and in comparing it to a similar control simulation (TIW-RUN) in which TIWs freely develop. In NOTIW-RUN, removing TIWs is done online *i.e.,* during the simulation, by nudging the meridional velocity v toward its monthly climatology obtained from TIW-RUN. Owing to the transient and random nature of TIWs, TIW-RUN has to be run over a period long enough to allow estimating a monthly climatology that does not contain signatures of the waves but retains the main characteristics of the meridional circulation, in particular related to the equatorial Ekman divergence. Nudging the instantaneous meridional velocity to this climatology at a sufficiently short 5-day time scale allows to efficiently smooth out TIWs in the NOTIW-RUN. This technique gives robust results, and keeps Kelvin waves, an essential aspect of the equatorial dynamics, untouched. However, it proves difficult to avoid the alteration of Rossby waves as they share similar characteristics with TIWs. Nevertheless, efforts have been made throughout the thesis to reduce their alteration, in particular during the study of TIWs-ENSO interactions in Chapter 5, by reducing the meridional extent of the region over which the nudging is applied. Overall, this methodology damps TIWs effectively while barely affecting other processes, thus allowing to accurately delineate their impacts on the eastern Pacific mean thermodynamic state and variability.

Second, I used this methodology to investigate the changes induced by TIWs on the mean thermodynamic components of the eastern Pacific, using forced eddy-resolving (horizontal resolution of $1/12°$) ocean-only simulations over a time period of 40-year (1980-2019), with and without TIWs (Chapter 3). Using a kinetic energy transfer diagnostic, I first show that TIWs are involved in an inverse energy cascade, *i.e.,* giving back kinetic energy to larger scale features. TIWs change the upper-layer temperature spatial distribution,

with a warming of the cold tongue and cooling of off-equatorial waters. The zonal dynamics is also affected by TIWs, in particular with a weakening and deepening of the Equatorial Undercurrent (EUC). A subsequent heat budget analysis allows to understand the pathways by which TIWs modulate the upper ocean in the cold tongue. First, as a direct effect, the waves are responsible for an advection of heat into the cold tongue, which warm its water at a rate of 0.34°C month^{-1}. Second, as an indirect or rectified effect, the waves weaken the EUC, which in turn advect less heat eastward, counterbalancing in part the direct effect of TIWs with a cooling rate of −0.10°C month^{-1}.

Third, I focused on the feedbacks of TIWs on the seasonal cycle, an effect that has been little documented (Chapter 4). In previous studies, TIWs have been shown to be phase locked with the eastern tropical Pacific annual cycle, due to the seasonal modulation of the barotropic and baroclinic instabilities that are responsible for the generation of TIWs. These instabilities occur predominantly from July to February, when the cold tongue is the coldest and the shear of zonal currents the strongest. From the same 40-year forced ocean-only simulations described in the above paragraph, results show that TIWs induce a decrease of 0.4°C in the annual amplitude of the upper temperature in the cold tongue region (0°– 3°N, 150°– 110°W), by warming equatorial waters in boreal summer and fall. TIWs also modulate the EUC seasonal cycle by stabilizing and weakening it year-round therefore preventing what appears to be an unrealistic re-intensification found in boreal fall in some non-eddy resolving models.

Finally, I investigated the feedbacks of TIWs onto ENSO through the case study of the 2015-2018 ENSO cycle (Chapter 5). I used coupled ocean-atmosphere simulations of the eastern Pacific, using CROCO and the Weather Research and Forecast (WRF) model. Ensemble simulations with spatial resolutions of 1/14° in the ocean and 1/4° in the atmosphere are run over the period 2015-2018. During this period, an intense El Niño (2015/16) is followed by a double-year La Niña (2016/17 and 2017/18). While El Niño events generally end rapidly after their mature phase and exhibit an already established transition to the cold phase by the following summer, many La Niña events tend to persist throughout the second year and even re-intensify the following winter. Although many mechanisms have been proposed, no consensus has yet been reached and the essential physical processes responsible for the multi-year behavior of La Niña remain to be illustrated. Using the TIW- versus NOTIW-RUN methodology, we aim to establish in this part of the thesis the potentially distinct TIW effects occurring during such two consecutive episodes of a multi-year La Niña. Preliminary results suggest a complex temporal and spatial effects of TIWs on ENSO resulting from a combination of warming through increased intraseasonal nonlinear dynamical heating and of cooling through increased vertical mixing in the presence of TIWs. An interannual heat budget also revealed an implication of TIWs in the traditional ENSO feedbacks, in particular on the zonal advective feedback. The different processes that control each episode of the multi-year La Niña could explain the different TIW activity and TIW-induced impacts obtained on each episode. More work is needed to fully understand the processes involved here, and simulations on a longer period and involving several one-year and multi-year La Niña events could help having a better picture of TIWs-ENSO interactions with statistical results.

– Discussion –

As explained in the Background Chapter, most CMIP5 and CMIP6 models have horizontal ocean resolutions close to 1°. These non eddy-resolving resolutions are not sufficient to fully capture the sharp and narrow structures that constitute the cusps and edges of TIWs (*e.g.,* Graham (2014)). We have seen in Chapter 4 that a 1° horizontal resolution regional ocean model could not capture the intraseasonal NDH associated with TIWs, and lead to a cold bias in the mean and annual cycle of the cold tongue. However, this low-resolution simulation manages to capture – at least partially – the EUC-TIWs interactions, and in particular it simulates an accurate seasonal cycle of the EUC, with no re-intensification in boreal autumn. Based on these results, we can expect non eddy resolving CMIP models and GCMs in general to capture some part of TIW dynamics and effects, while not resolving others. Therefore, scale-aware parameterizations of TIWs are needed to properly represent non-resolved TIW effects.

Studies of Boucharel and Jin (2020); Xue et al. (2020, sub) developed analytical formulations for the modulation of TIW amplitude and associated intraseasonal NDH, by (i) ENSO, (ii) the seasonal cycle, and (iii) nonlinear interactions between the two. These formulations successfully reproduce the seasonally modulated TIW-induced NDH feedback onto ENSO. These analytical formulations are based on either the Niño 3 or Niño D indices (*i.e.,* on the interannual anomalous temperature over these regions). As such, they cannot be implemented online in climate models in which only the raw signal (and not anomalies) is known at each time step. However, these analytical formulations could easily be incorporated into simple conceptual models such as the 1-dimensional Recharge-Discharge Oscillator model (Jin (1997a,b); Jin et al. (2020)) or even into intermediate complexity models such as the Zebiak and Cane model (Cane et al. (1986); Zebiak and Cane (1987)) thanks to the spatial extension of the NDH-TIWs parameterization proposed in Xue et al. (sub). This would lead to a substantial improvement of our understanding of ENSO dynamics, in particular related to the multi-scale interaction in the eastern tropical Pacific and its role on ENSO amplitude asymmetry. In this PhD work, other effects involving TIWs are evidenced, with in particular a seasonal rectification of zonal currents not directly in phase and correlated with v'^2 and T'^2 (*i.e.,* TIW activity). Therefore, a new formulation of the theoretical framework based on Boucharel and Jin (2020); Xue et al. (2020, sub) is needed to better understand and determine the TIW rectification effect on the $\overline{u'v'}$ flux and on circulation in general. This could allow accounting for TIW effects on the zonal advective feedback, with potential implications for a better understanding of the dynamics of multi-year La Niña events.

Some limitations remain in the damping methodology presented in this manuscript, in particular related to the alteration of intraseasonal (and most probably of interannual) Rossby waves, as described in Chapter 2. These waves have an important role on the life-cycle of ENSO events, as described in the delayed oscillator model (Suarez and Schopf (1988); Battisti and Hirst (1989)). Within the framework of the coupled ocean-atmosphere simulation, the methodology has been improved (Chapter 5) by reducing the latitudinal extent of the nudging window. As tested on a forced ocean-only model, this technique reduces the impact of nudging

on off-equatorial intraseasonal Rossby waves (Fig. 2.7). Despite our efforts, it is not trivial to quantify how much the differences between TIW- and NOTIW-RUN originate from the alteration of Rossby waves. A way forward could be to compare our results with those obtained using other damping methodologies. For instance, we could implement the sponge layer methodology described in Chapter 2. However, the increase in viscosity could artificially change the mean zonal currents. An other way would be to smooth out TIW imprint online using the OASIS coupler: at each time step (or several time steps), the ocean model would send the field of interest, such as the meridional currents over the first 100 meters, to OASIS, which would perform a zonal filter to smooth out TIW imprint (with a cut-off frequency of approximately $12^{\circ-1}$), and send it back to the ocean model to replace the original field. However, such a methodology would need to be applied carefully in particular given that we are using a σ-level coordinates oceanic model. First, only a zonal filtering should be done, as a meridional filter would impact the large scale structures such as SST gradient or zonal current shear, depending on which variable is chosen to apply the smoothing. Second, the filter should be applied in depth (at least in the first 100 meters) to successfully filter out TIWs. Therefore, for the deep ocean, the σ-levels should be designed to be mostly flat in the first 100 meters and the spatial filter should be applied away from the shallow regions in order to avoid spurious mixing along σ-levels.

– Perspectives –

Overall, this thesis work has contributed to improving our understanding of fine-scale processes in the tropics and their interactions with the background environment and low frequency climate variability. The TIW damping methodology represents an efficient tool that can easily be implemented in high-resolution ocean models, and can help understand the multi-scale interaction effects associated with TIWs and more generally the mesoscale activity. You will find below a non exhaustive list of ongoing and future studies in which I'm involved and, for some of them, could benefit from this damping approach.

1. TIWs & air-sea coupling

As explained in the preamble of Chapter 5, the atmosphere impacts and is influenced back by TIWs. Using the same set of coupled ocean-atmosphere simulations described in this Chapter, I assessed the extent to which TIWs alter fine-scale atmospheric features and modulate large scale atmospheric processes.

Local effects

The atmosphere is locally impacted by the TIW-induced oceanic variability, as shown by the regression of the latent heat (LH) flux and surface wind on the first CEOF mode of SST intraseasonal variability (Fig. 5.16). In particular, the LH flux is well correlated with

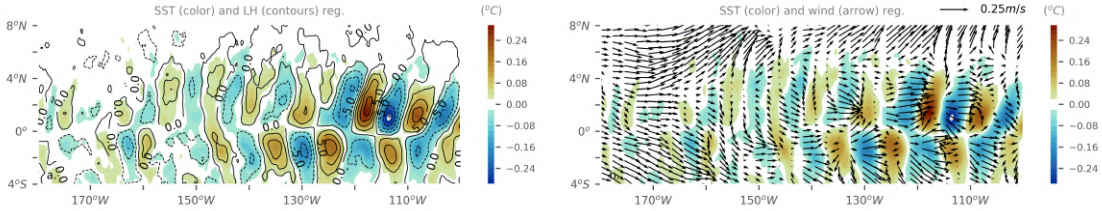

Figure 5.16: Fluctuating fields of SST (colors), latent heat flux (a, contours) and wind at 1st level (b, arrows) regressed on the 1st CEOF mode on SST intraseasonal anomaly (with 5-40 day band-pass, see Chapter 3 for details on the CEOF analysis).
Champs de SST (couleurs), du flux de chaleur latente (a, contours) et du vent au 1er niveau (b, flèches) régressés sur le 1er mode CEOF sur l'anomalie intrasaisonnière de SST (avec une bande passante de 5-40 jours) Se réferer au Chapter 3 pour les détails sur l'analyse CEOF).

the SST pattern at the TIW scale, with in particular negative values of LH flux above cold SST anomalies (*i.e.,* the ocean is cooling the atmosphere). This correlation was observed in previous studies such as Thum et al. (2002) and Seo et al. (2007c) and is thought to arise from the slow adjustment of the atmosphere to the SST gradient, which induces a temperature difference between the ocean surface and the atmosphere (Small et al. (2008)). The patterns of surface wind regression reveals a weakening/strengthening of trade winds above cold/warm SST anomalies. This finding is in line with results from the observational study by Hashizume et al. (2001), who interpret this in-phase wind-SST pattern in terms of atmospheric mixing response. Indeed, let's imagine a wind profile following a logarithmic law in the planetary boundary layer. The vertical shear induced by this profile produces atmospheric mixing. Above a warm SST anomaly, enhanced mixing weakens the wind shear, which increases surface wind speed. The response of air temperature and moisture to surface fluxes also modifies the atmospheric pressure, which generates pressure gradients that might also be responsible for wind anomalies over SST anomalies (Small et al. (2008)). Chelton et al. (2001) also noticed a linear relationship between the TIW-induced SST gradient and the wind stress curl and divergence: (1) a positive wind stress divergence occurs when the wind direction is parallel to the SST gradient, as the wind stress amplitude increases; (2) a positive wind stress curl occurs when the wind direction is perpendicular to the SST gradient, as the wind is surrounded by slower winds to its left and faster winds to its right. These air-sea coupling processes over fronts and eddies have been shown to induce changes in cloudiness (Deser et al. (1993); Frenger et al. (2013)).

Integrated effects

Due to the non-linearity of the interactions between TIWs and the mean state detailed in previous chapters, TIW-induced local atmospheric effects are likely to rectify the large scale atmospheric features in a similar fashion as the oceanic environment. Figure 5.17 shows the integrated effect of TIWs on different climate variables on the simulated 2015-2018 period. These maps are obtained by subtracting the 2015-2018 averaged values in NOTIW-RUN, with the averaged values of the 5-members ensemble from TIW-RUN. Only the significant

differences are shown, at a 95% confidence level. As explained earlier, TIWs warm and broaden the eastern Pacific cold tongue, and cool equatorial waters to the west, and off-equatorial waters to the north of the cold tongue (Fig. 5.17a). Changes in LH flux are shown to follow changes in SST: more warming from the ocean to the atmosphere above the cold tongue (reaching $+10\ W\ m^{-2}$, *i.e.,* 11% of the value); less warming elsewhere (reaching $-8\ W\ m^{-2}$ at 0°N,180°W, *i.e.,* 8%). Around the equator, the change in shortwave radiation also seems to follow the change in SST with stronger radiation above colder waters and weaker radiation above warmer waters (Fig. 5.17e). This could be due to an increased convection above warm anomalies producing more clouds and thus weaker shortwave radiation, and *vice versa*. Close to the equator, the LH flux and shortwave radiations are thus reacting to SST changes, and counterbalancing them in part. Away from the equator, between 5°– 10°N, the shortwave radiation is increased, indicating a decrease of the cloud cover. This is also noticed in the change in precipitation rate, being reduced by up to 3 mm/day (*i.e.,* 40% of the value) in the ITCZ from 180°– 110°W (Fig. 5.17d). Significant changes in the low-level wind field are also noticed. In particular, trade winds are increased along the equator and decreased elsewhere.

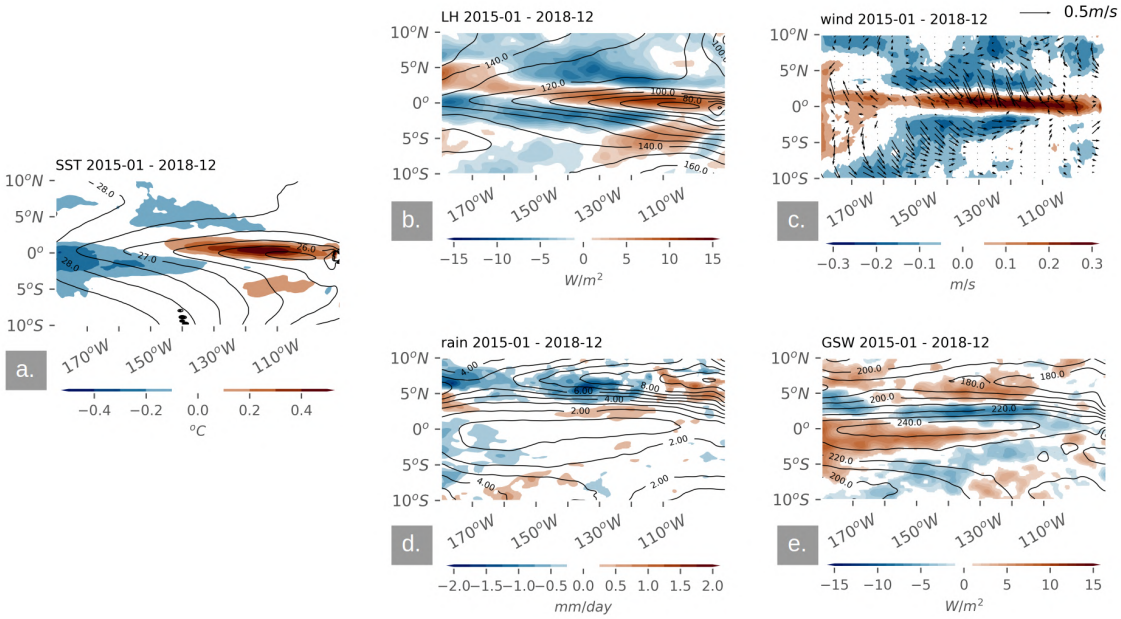

Figure 5.17: TIW-induced mean state differences for (a) SST, (b) latent heat flux, (c) low-level wind, (d) precipitation and (e) shortwave radiation over the 2015-2018 period. Contours show the values of the averaged 5 ensemble members of TIW-RUN. Colors show significant differences between TIW- and NOTIW-RUN at 95% confidence.
Différences d'état moyen induits par les TIWs pour (a) la SST, (b) le flux de chaleur latente, (c) le vent à basse altitude, (d) les précipitations et (e) le rayonnement à shortwave, sur la période 2015-2018. Les contours montrent les valeurs de la moyenne des 5 membres de l'ensemble TIW-RUN. Les couleurs indiquent les différences significatives entre TIW- et NOTIW-RUN, à un niveau de confiance de 95 %

These large scale changes might arise from a combination of direct TIW effects (*i.e.,* the integration in time of the local changes described above), and to indirect effects (*i.e.,* large scale modifications that induce other large scale modifications).

Such changes, in particular in the strength of the ITCZ, could trigger other TIW-induced indirect atmospheric changes, for instance related to tropical cyclone activity in the north eastern Pacific basin, which is the second most active basin in the world. However, a proper assessment of TIW-induced changes in tropical cyclone genesis and intensity would require longer simulations.

Current Feedback (CFB) and Thermal Feedback (TFB)

As shown in the literature an described in the preamble of Chapter 5, the mesoscale air-sea coupling influences the low-level winds, the surface wind stress variability, and the turbulent heat flux. In turn, these perturbations can alter TIW activity. On the one hand, TFB, by inducing turbulent heat fluxes should induce a sink of potential energy from the ocean to the atmosphere (Bishop et al. (2020)), potentially damping the TIWs. On the other hand, CFB should have a dual effect on TIWs: (i) a damping through the eddy killing process (Renault et al. (2016b)); and (ii) an indirect reduction of the TIW generation caused by the slow-down of the mean circulation (Luo et al. (2005)). Mesoscale TFB and CFB may also indirectly alter ENSO.

Based on a similar coupled ocean-atmosphere model than the one used in Chapter 5 (the only difference being an increase in vertical levels in CROCO), Ryan Holmes (University of Sydney) started a study that aim to disentangle TFB and CFB effects on TIWs and ENSO, a study I had the opportunity to collaborate on during R. Holmes's visit to LEGOS. The strategy is similar to the one used by *e.g.,* Renault et al. (2019b), where the authors used the OASIS coupler to spatially smooth the SST sent to the atmospheric model. In their study, Renault et al. (2019b) apply this strategy over a realistic tropical channel in order to unravel the different coupling coefficients. However, the equatorial region needs to be handled carefully as a classic isotropic filter used *e.g.,* by Renault et al. (2019b), would smooth out not only the TIW imprint but also the meridional temperature gradients, potentially altering the large scale wind curl and thus the equatorial dynamics. To overcome this issue, TIW imprint is removed by applying only a zonal filter (centered running mean of 12° longitude). A set of 4 simulations are developed:

- a control simulation, which considers the full coupling
- a no mesoscale TFB, which smoothes out the mesoscale SST seen by the atmosphere
- a no mesoscale CFB, which smoothes out the mesoscale surface currents seen by the atmosphere
- a no CFB, which does not include the CFB at all by setting the surface currents seen by the atmosphere to zero.

Snapshots illustrating each field sent to the atmospheric model are shown in Figure 5.18.

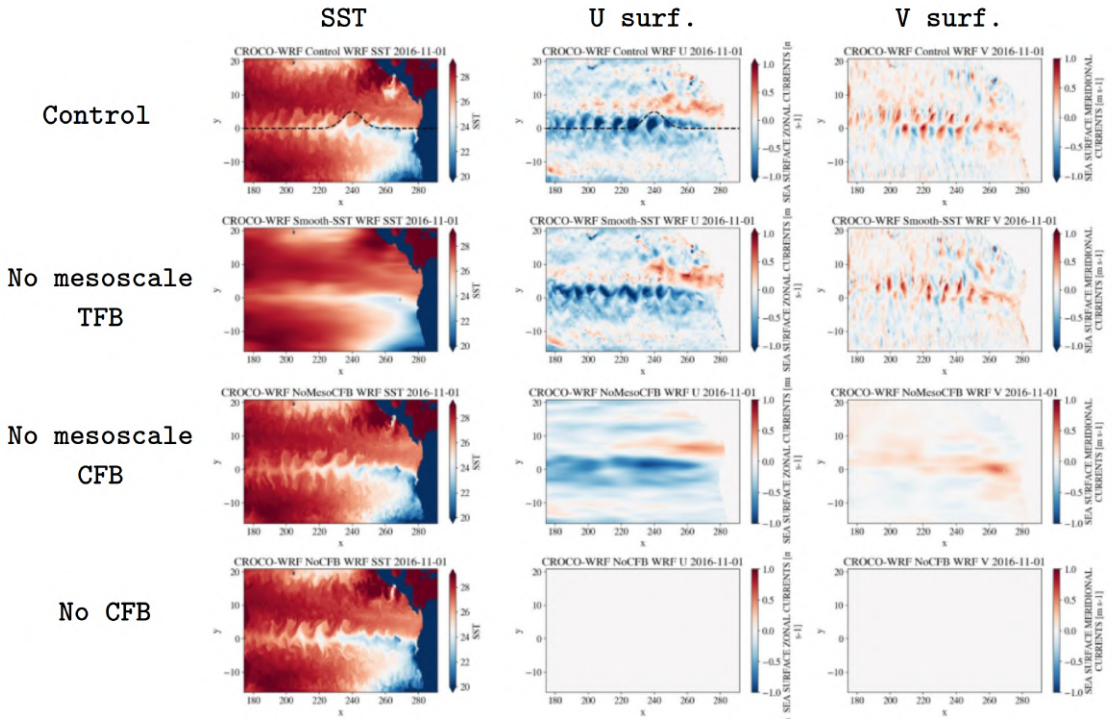

Figure 5.18: Snapshots (1^{st} November 2016) of SST and oceanic currents sent to the atmospheric model, in each experiment. Courtesy of R. Holmes.
Carte (1^{er} Novembre 2016) de la SST et des courants océaniques envoyés au modèle atmosphérique, dans chaque expérience. Avec l'aimable autorisation de R. Holmes.

Preliminary results reveal (1) a reduction by half of SST variance in the 2°S – 6°N, 150°–90°W region, due to the mesoscale TFB most probably caused by turbulent heat fluxes, and (2) a damping of meridional velocity variance due to both mesoscale (eddy killing) and large scale (indirect of reduction of TIW generation) CFB. For the CFB damping, the relative importance of the eddy killing *vs.* the reduction of TIW generation strongly depends on the latitude. Interestingly this is usually not the case, for example for western boundary currents where the eddy killing effect largely dominates (Renault et al. (2016a)). These results are only preliminary, and a more thorough study will allow understanding the impact of mesoscale TFB on heat fluxes, the detailed mechanisms responsible for the damping of TIWs in each experiment, and the impact of each feedback on the mean ocean and atmosphere components.

2. TIWs & biogeochemical processes

Marine organisms, which act as a biological pump for carbon sequestration, play a key role in the global biogeochemical cycle. A better understanding of their large spatial and temporal fluctuations can lead to great improvement in marine biogeochemical predictions (*e.g.,* Krumhardt et al. (2020)), and therefore to a better assessment and anticipation of

the worldwide marine fish catch. While diverse challenges still remain in particular due to the very limited availability of biogeochemical data as well as the difficulty in assimilating these data in numerical models (*e.g.,* , Song et al. (2016)), large efforts have been achieved to understand the climate connection to marine biogeochemical variability at seasonal to interannual time scales. Recent studies (Yoder et al. (1994); Chavez et al. (1999); Legeckis et al. (2004); Gorgues et al. (2005); Evans et al. (2009); Shi and Wang (2021)) suggest in particular that TIWs strongly modulate both the productivity and the oxygen concentration of the eastern Pacific Ocean, a key region for the global carbon cycle. More recently, modelling studies have shown that the TIW-induced chlorophyll-a can act as a negative feedback on TIW intensity and induces changes of the large scale SST, by modulating the incoming solar radiation that can penetrate into the mixed layer (Tian et al. (2018)), which can ultimately feed back onto ENSO (Tian et al. (2019)). Therefore, understanding the multi-scale interactions between physical and biogeochemical processes is of high interest. During my thesis, I had the opportunity to work with Feng Jiang, a PhD candidate from the University of Information Science & Technology in China. Based on my CROCO configurations of the eastern tropical Pacific and using my TIW damping methodology, she aims at understanding in particular the direct and indirect effects of TIWs on the productivity and variability of the Oxygen Minimum Zone (Paulmier and Ruiz-Pino (2009)). To that end, she uses simulations of CROCO coupled with the biogeochemical model BioEBUS (a simple NPZD model, Gutknecht et al. (2013)). Again, two simulations are carried out, one with TIWs and one without TIWs, over a time-period of 20-year (2000-2020). Figure 5.19 shows the meandering of TIWs observed through the surface chlorophyll concentration obtained from the CROCO-BioEBUS simulation.

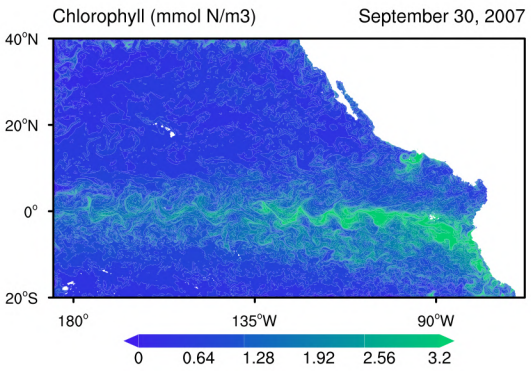

Figure 5.19: Snapshot of the surface chlorophyll concentration on September 30, 2007 obtained from the coupled CROCO-BioEBUS numerical simulation of the eastern tropical Pacific. Courtesy of Feng Jiang.
Carte de la concentration de chlorophylle en surface le 30 septembre 2007 obtenue à partir de la simulation numérique couplée CROCO-BioEBUS du Pacifique tropical Est. Avec l'aimable autorisation de Feng Jiang.

3. TIWs & mixing above the EUC core

Observational studies have shown that the upper EUC is most often in a state of marginal instability (Smyth and Moum (2013)) reflecting a near-equilibrium state in which the forcing by trade winds induces destabilisation and turbulence, and turbulence re-stabilizes the state. To better understand this process, the sand-pile analogy was used in the poster presentation of W.D. Smyth and J.N. Moum during the Ocean Science meeting of 2014 [1]: when sand is

[1] https://www.eposters.net/pdfs/marginal-instability-and-the-deep-cycle-of-equatorial-turbulence.pdf

poured onto a sand pile, small avalanches occur when the critical slope of the pile exceeds a threshold, allowing the sand-pile to stay in a near-equilibrium state. In this analogy, the sand source is equivalent to wind forcing, and avalanches to turbulence. The slope of the sand pile is an analogy for the Richardson number $Ri = \frac{N^2}{S^2}$, which is the ratio of stratification $N^2 = -\frac{g}{\rho}\partial_z\rho$ over shear $S^2 = (\partial_z u)^2 + (\partial_z v)^2$. The marginal stability occurs for $Ri = 1/4$. Several studies have shown that TIWs modulate the vertical mixing in the upper EUC (Lien et al. (2008); Moum et al. (2009); Inoue et al. (2012)), and might drive the upper EUC away from marginal stability, in a shear instability state that enhances turbulence (Holmes and Thomas (2015)). This could have high implication on the cold tongue heat budget, and could explain the modification of vertical mixing obtained in Chapter 3 and Chapter 5. More work could be done on this aspect of TIWs, with a particular focus on the ability of the chosen turbulence parameterization scheme (in this thesis, K-profile parameterization KPP) to reproduce the observed turbulence and turbulence cycles (Holmes and Thomas (2015); Cherian et al. (2021)).

4. TIWs & the generation of deep jets

In low latitude regions, the circulation below the thermocline is shaped by intense alternating eastward and westward jets that have been documented only recently thanks to the Argo float deployment in 2000. Still, the origins of these equatorial deep jets remain poorly understood. Intraseasonal variability associated with TIWs have been detected down to 2000 meters (Tuchen et al. (2018)), as they can propagate as downward Rossby and Yanai waves (Farrar (2011); Lee et al. (2022); Delpech et al. (2020)). This TIW-induced intraseasonal variability in depth is thought to be a major driver of equatorial deep jets (Ascani et al. (2015); Greatbatch et al. (2018)). Using the TIW damping methodology developed in this thesis could help highlighting potential interactions between TIWs and equatorial deep jets.

– Concluding Note –

All this thesis work is based on numerical simulations. As a young modeling scientist, I often feel disconnected from my object of study. To reconnect with reality, here is a natural-light photograph showing the front of a tropical instability wave (Fig. 5.20).

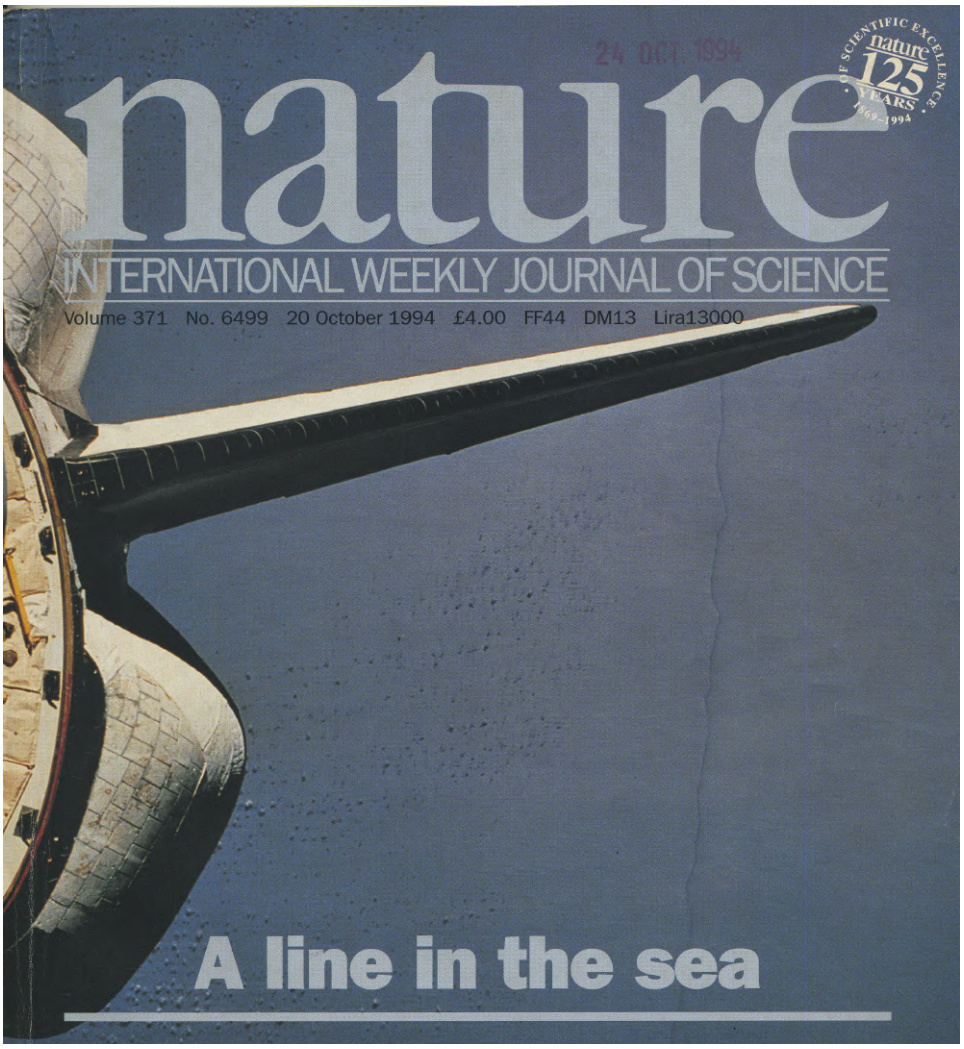

Figure 5.20: *"along a front where cool and warm waters meet in the equatorial Pacific Ocean, enhanced primary production creates a dark line. This line was visible from an altitude of 230 km to the mission STS-46 space shuttle crew, as revealed in this natural-light photograph. (NASA photo S46-79-17)"*, from Nature Vol. 371, No 6499, October 20th 1994

Conclusion et Perspectives

– Conclusions –

Alors que les tropiques sont de plus en plus peuplés et menacés par un climat changeant, il y a un besoin urgent de mieux comprendre les processus complexes qui influencent la variabilité climatique dans ces régions tropicales, en particulier en ce qui concerne l'Oscillation Australe – El Niño (ENSO) qui est le moteur le plus important de la variabilité tropicale interannuelle, et dont les effets touchent à la fois la météo, le climat et nos sociétés. Les ondes tropicales d'instabilité (TIWs) représentent la principale activité océanique de méso-échelle dans les tropiques, et interagissent avec les propriétés thermales et la circulation de l'océan équatorial sur une large gamme d'échelles temporelles, en particulier avec ENSO. Cette thèse se concentre sur l'impact qu'ont les TIWs sur la variabilité océanique de l'océan Pacifique tropical Est, avec apporte un certain nombre de contributions améliorant notre compréhension des interactions entre les TIWs et l'état thermodynamique et la variabilité climatique.

D'abord, à partir du modèle Coastal and Regional Ocean Community (CROCO), j'ai développé un outil permettant d'isoler les effets des TIWs sur l'océan Pacifique tropical Est (Chapitre 2). L'approche consiste à supprimer la variabilité océanique associée aux TIWs dans une simulation de l'océan Pacifique Est (NOTIW-RUN), et à la comparer à une simulation de contrôle (TIW-RUN) dans laquelle les TIWs se développent librement. Dans NOTIW-RUN, la suppression des TIWs est faite en ligne, c'est-à-dire au cours de la simulation numérique, en rappelant la vitesse méridienne v vers la climatologie mensuelle de v calculée à partir du TIW-RUN. En raison de la nature transitoire et aléatoire des TIWs, TIW-RUN doit être exécuté sur une période suffisamment longue pour permettre l'estimation d'une climatologie mensuelle qui ne contient pas les signatures des ondes, mais conserve les principales caractéristiques de la circulation méridienne, en particulier celles liées à la divergence équatoriale d'Ekman. Le rappel de la vitesse méridienne instantanée vers cette climatologie à une fréquence suffisamment courte (5 jours) permet de lisser efficacement les TIWs dans le NOTIW-RUN. Cette technique donne des résultats robustes, et permet de ne pas toucher aux ondes de Kelvin, un aspect essentiel de la dynamique équatoriale. Cependant, il s'avère difficile d'éviter l'altération des ondes de Rossby car elles partagent des caractéristiques similaires aux TIWs. Néanmoins, des efforts ont été faits tout au long de la thèse pour réduire leur altération, en particulier lors de l'étude des interactions TIWs-ENSO dans le Chapitre 5, en réduisant l'étendue méridionale de la région sur laquelle le rappel est appliqué. Dans l'ensemble, cette méthodologie permet d'atténuer efficacement les TIWs tout en affectant relativement peu les autres processus, permettant ainsi de délimiter avec précision leurs impacts sur l'état thermodynamique moyen et la variabilité du Pacifique Est.

Dans un second temps, j'ai utilisé cette méthodologie pour étudier les changements induits par les TIWs sur les caractéristiques thermodynamiques moyennes du Pacifique Est, en utilisant des simulations océaniques forcées au 1/12° sur une période

de 40 ans (1980-2019), avec et sans TIWs (Chapitre 3). Un diagnostic de transfert d'énergie cinétique permet de montrer que les TIWs sont impliquées dans une cascade d'énergie inverse, redonnant de l'énergie cinétique à la plus grande échelle. Les TIWs changent la distribution spatiale de la température de la couche de surface, en réchauffant la "cold tongue" et en refroidissant les eaux off-equatoriales. La circulation zonale est également affectée par les TIWs, avec en particulier un affaiblissement et approfondissement du sous-courant équatorial (EUC). Une analyse du bilan thermique permet de comprendre les voies par lesquelles les TIWs modulent la température de la "cold tongue". Tout d'abord, les TIWs sont responsables d'une advection de chaleur dans la "cold tongue" de 0.34 °C mois^{-1}. Enfin, les TIWs affaiblissent l'EUC, qui en retour advecte moins de chaleur vers l'Est ce qui contrebalançe en partie l'effet initial des TIWs par un refroidissement de -0.10°C mois^{-1}.

Je me suis ensuite concentrée sur les rétroactions des TIWs sur le cycle saisonnier, un effet peu documenté jusque là (Chapitre 4). Lors de précédentes études, il a été démontré que les TIWs sont synchronisées avec le cycle annuel du Pacifique tropical Est en raison de la modulation saisonnière des instabilités barotropiques et baroclines, elles même responsables de la génération des TIWs. Ces instabilités se produisent principalement de juillet à février, lorsque la "cold tongue" est la plus froide et le cisaillement des courants zonaux le plus fort. À partir des mêmes simulations océaniques forcées sur 40 ans décrites dans le paragraphe précédent, les TIWs semblent induire une diminution de l'amplitude annuelle du cycle saisonnier de la température en surface de 0.4°C dans la région de la "cold tongue" (0°– 3°N, 150°– 110°W), en réchauffant les eaux équatoriales en été et en automne boréaux. Les TIWs modulent également le cycle saisonnier de l'EUC en le stabilisant et en l'affaiblissant tout au long de l'année, empêchant ainsi ce qui semble être une réintensification irréaliste trouvée en automne boréal dans certains modèles de basse résolution.

Enfin, j'ai étudié les rétroactions des TIWs sur le cycle ENSO de 2015-2018 (Chapitre 5). J'ai pour cela utilisé des simulations couplées océan-atmosphère du Pacifique Est, obtenue avec le couplage de CROCO et du modèle Weather Research and Forecast (WRF) par le coupler OASIS. Des simulations d'ensemble de 1/14° dans l'océan et 1/4° dans l'atmosphère sont faites sur la période 2015-2018. Au cours de cette période, un El Niño intense (2015/16) est suivi d'une double année de La Niña (2016/17 et 2017/18). Alors que les événements El Niño se terminent généralement rapidement après leur phase de maturité et présentent une transition déjà établie vers la phase froide l'été suivant, de nombreux événements La Niña persistent et se réintensifient l'année suivante. Bien que de nombreux mécanismes aient été proposés, aucun consensus n'a encore été atteint et les processus physiques essentiels responsables du comportement pluriannuel de La Niña restent encore à élucider. En utilisant la méthodologie TIW- *versus* NOTIW-RUN, nous visons à éclaircir l'effet des TIWs se produisant pendant ces deux épisodes consécutifs de La Niña. Des résultats préliminaires suggèrent des effets temporels et spatiaux complexes des TIWs sur ENSO résultant d'une combinaison de réchauffement par l'augmentation de l'advection intrasaisonnière non linéaire de chaleur, et de refroidissement par l'augmentation du mélange vertical, en présence de TIWs. Un bilan de chaleur interannuel a également révélé une implication des TIWs dans les processus qui régissent le cycle de vie d'ENSO, en particulier sur la rétroaction advective zonale. Les différents processus qui régissent chaque épisode d'un La Niña pluriannuel pour-

raient expliquer les différences d'activité et d'impact des TIWs. Des travaux supplémentaires sont nécessaires pour comprendre pleinement les processus impliqués ici, et des simulations sur une période plus longue impliquant plusieurs événements La Niña pourraient mener à une meilleure compréhension de l'interaction TIWs-ENSO avec des résultats statistiques.

– Discussion –

Comme expliqué dans l'Introduction, la plupart des modèles CMIP5 et CMIP6 ont des résolutions océaniques horizontales de l'ordre d'1°. Ces résolutions ne sont pas suffisantes pour reproduire les fines structures associées aux TIWs (*e.g.,* Graham (2014)). Nous avons vu dans Chapitre 4 qu'un modèle océanique régional au 1° ne pouvait pas capturer la NDH intrasaisonnière associée aux TIWs, conduisant à un biais froid dans la "cold tongue". Cependant, cette simulation basse résolution parvient à capturer – au moins partiellement – les interactions EUC-TIWs, en simulant un cycle saisonnier relativement réaliste de l'EUC, sans ré-intensification en automne boréal. Sur la base de ces résultats, nous pouvons nous attendre à ce que les modèles CMIP de basse résolution et les GCMs en général capturent une partie des effets des TIWs, mais n'en résolvent pas d'autres. Par conséquent, des paramétrisations des TIWs tenant compte de la résolution sont nécessaires pour représenter correctement les effets non résolus des TIWs.

Les études de Boucharel and Jin (2020); Xue et al. (2020, sub) ont développé des formulations analytiques de la modulation de l'amplitude des TIWs et de la NDH intrasaisonnière, par (i) ENSO, (ii) le cycle saisonnier du Pacifique tropical Est, et (iii) les interactions non linéaires entre les deux. Ces formulations reproduisent avec succès la modulation saisonnière du NDH induit par les TIWs, et rétro-agissant sur ENSO. Ces formulations analytiques se basent sur les indices Niño 3 ou Niño D (*i.e.,* sur l'anomalie interannuelle de température dans ces régions). Ainsi, elles ne peuvent pas être implémentées directement dans les modèles climatiques dans lesquels seul le signal brut (et non les anomalies) est connu à chaque pas de temps. Cependant, ces formulations analytiques pourraient facilement être incorporées dans des modèles conceptuels simples tels que le modèle unidimensionnel Recharge-Discharge Oscillator (Jin (1997a,b); Jin et al. (2020)) ou même dans des modèles de complexité intermédiaire comme le modèle de Zebiak et Cane (Cane et al. (1986); Zebiak and Cane (1987)), grâce à l'extension spatiale de la paramétrisation NDH-TIWs proposée dans Xue et al. (sub). Cela améliorerait notre compréhension de la dynamique d'ENSO, en particulier en ce qui concerne l'interaction multi-échelle dans le Pacifique tropical Est et son rôle sur l'asymétrie d'amplitude d'ENSO. Dans cette thèse, d'autres effets impliquant les TIWs sont mis en évidence, avec notamment une rectification saisonnière des courants zonaux qui n'est pas directement en phase et corrélée avec v'^2 et T'^2 (*i.e.,* activité des TIWs). Par conséquent, une nouvelle formulation analytique basée sur les travaux de Boucharel and Jin (2020); Xue et al. (2020, sub) est nécessaire pour tenir compte de l'effet de rectification des TIWs sur la circulation. Cela pourrait également permettre de tenir compte de l'effet des TIWs sur la rétroaction advective zonale, et ainsi conduire à une meilleure compréhension de la dynamique des événements pluriannuels La Niña.

Certaines limites existent encore dans la méthodologie de suppression des TIWs présentée dans ce manuscrit, notamment en ce qui concerne l'altération des ondes de Rossby intrasaisonnières (et très probablement interannuelles), décrite dans le Chapitre 2. Ces ondes jouent un rôle important dans le cycle de vie des événements ENSO, comme le décrit le modèle d'oscillateur retardé (Suarez and Schopf (1988); Battisti and Hirst (1989)). Dans le cadre de la simulation couplée océan-atmosphère, la méthodologie a été améliorée (Chapitre 5) en réduisant l'étendue latitudinale de la fenêtre de rappel. Testée sur un modèle océanique forcé, cette technique réduit l'impact du rappel sur les ondes de Rossby intrasaisonnières hors équateur (Fig. 2.7). Malgré nos efforts, il n'est pas trivial de quantifier dans quelle mesure les différences entre TIW- et NOTIW-RUN proviennent de l'altération des ondes de Rossby. Une piste à suivre consisterait à comparer nos résultats avec ceux obtenus par d'autres techniques de suppression des TIWs. Par exemple, nous pourrions appliquer la méthodologie de la "sponge layer" (ou "couche éponge") décrite dans le Chapitre 2. Cependant, l'augmentation de la viscosité pourrait modifier artificiellement les courants zonaux. Une autre façon serait de lisser les TIWs en ligne en utilisant le coupleur OASIS : à chaque pas de temps (ou plusieurs pas de temps), le modèle océanique enverrait le champ d'intérêt, tel que les courants méridiens sur les 100 premiers mètres, à OASIS qui effectuerait un filtre zonal pour lisser la signature des TIWs (avec une fréquence de coupure d'environ $12^{\circ-1}$), et renverrait le champ lissé au modèle océanique pour remplacer le champ original. Cependant, une telle méthodologie devrait être appliquée avec précaution, notamment parce que nous utilisons un modèle océanique utilisant des coordonnées σ. Premièrement, seul un filtrage zonal devrait être effectué, car un filtre méridional aurait un impact sur les structures méridiennent telles que le gradient de SST ou le cisaillement des courants zonaux. Deuxièmement, le filtre doit être appliqué en profondeur (au moins dans les 100 premiers mètres) pour réussir à filtrer les TIWs. Par conséquent, pour l'océan profond, les niveaux σ doivent être conçus pour être principalement plats dans les 100 premiers mètres et le filtre spatial doit être appliqué loin des régions peu profondes afin d'éviter les mélanges parasites le long des niveaux σ.

– Perspectives –

Ce travail de thèse a contribué à améliorer notre compréhension des processus de fine échelle dans les tropiques, et de leurs interactions avec l'état océanique moyen et la variabilité climatique. La méthodologie de suppression des TIWs est un outil efficace qui peut facilement être implémenté dans des modèles océaniques de haute résolution, afin d'aider à la compréhension des effets d'interaction multi-échelles associés aux TIWs, et plus généralement à l'activité méso-échelle. Vous trouverez ci-dessous une liste non exhaustive d'études en cours et à venir dans lesquelles je suis impliquée et qui, pour certaines d'entre elles, pourraient bénéficier de cette approche de suppression des TIWs.

1. TIWs & couplage air-mer

Comme détaillé dans le préambule du Chapitre 5, l'atmosphère affecte les TIWs, qui l'influencent en retour. En utilisant le même ensemble de simulations couplées océan-atmosphère décrit dans ce Chapitre, la modulation des caractéristiques atmosphériques de fine et grande échelles est évaluée.

Effets locaux

L'atmosphère est localement affectée par la variabilité océanique induite par les TIWs, comme le montre la régression du flux de chaleur latente (LH) et du vent de surface sur le premier mode CEOF de la variabilité intrasaisonnière de la SST (Fig. 5.16). Le flux LH est corrélé à la SST, avec notamment des valeurs négatives du flux LH au-dessus des anomalies SST froides (*i.e.,* l'océan refroidit l'atmosphère). Cette corrélation a été observée dans des études antérieures telles que Thum et al. (2002) et Seo et al. (2007c) et serait due à l'ajustement lent de l'atmosphère au gradient de SST induisant une différence de température entre la surface de l'océan et l'atmosphère (Small et al. (2008)).

Les vents de surface révèlent un affaiblissement/renforcement des alizés au-dessus des anomalies froides/chaudes de la SST. Cette constatation est en accord avec les résultats de l'étude de Hashizume et al. (2001) basée sur des observations, qui interprète ce pattern vent-SST en termes de réponse du mélange atmosphérique. En effet, imaginons un profil de vent suivant une loi logarithmique dans la couche limite planétaire. Le cisaillement vertical induit par ce profil produit un mélange atmosphérique. Au-dessus d'une anomalie de SST chaude, le mélange accru affaiblit le cisaillement du vent, ce qui augmente la vitesse du vent de surface. La réponse de la température et de l'humidité de l'air aux flux de surface modifie également la pression atmosphérique, générant des gradients de pression qui pourraient également être responsables des anomalies de vent au dessus d'anomalies de SST (Small et al. (2008)). Chelton et al. (2001) a également remarqué une relation linéaire entre le gradient de SST induit par les TIWs, et le rotationnel et la divergence du stress du vent : (1) une divergence positive du stress du vent se produit lorsque la direction du vent est parallèle au gradient de SST, car l'amplitude du stress du vent augmente ; (2) un rotationnel positif du stress du vent se produit lorsque la direction du vent est perpendiculaire au gradient de SST, car le vent est entouré de vents plus lents à sa gauche et de vents plus rapides à sa droite. Il a également été démontré que ces processus de couplage air-mer sur les fronts et les tourbillons induisent des changements dans la couverture nuageuse (Deser et al. (1993); Frenger et al. (2013)).

Effets Intégrés

En raison de la non-linéarité d'interaction entre les TIWs et l'état moyen détaillée dans les chapitres précédents, les effets atmosphériques locaux induits par les TIWs sont susceptibles de rectifier les caractéristiques atmosphériques à grande échelle de la même manière que pour l'océan. La Figure 5.17 montre l'effet intégré des TIWs sur différentes variables climatiques

sur la période 2015-2018. Ces cartes sont obtenues en soustrayant les valeurs moyennes de 2015-2018 dans NOTIW-RUN, avec les valeurs moyennes de l'ensemble de 5 membres de TIW-RUN. Seules les différences significatives sont indiquées, à un niveau de confiance de 95 %. Comme nous l'avons expliqué précédemment, les TIWs réchauffent et élargissent la "cold tongue" du Pacifique équatorial Est, et refroidissent les eaux équatoriales à l'Ouest, ainsi que les eaux hors équateur au nord de la "cold tongue" (Fig. 5.17a). Les changements du flux de LH suivent les changements de la SST : un réchauffement plus important de l'océan vers l'atmosphère au-dessus de la "cold tongue" (atteignant $+10\ W\ m^{-2}$, soit 11% de la valeur) ; un réchauffement moindre ailleurs (atteignant $-8\ W\ m^{-2}$ à 0°N,180°W, soit 8%). Près de l'équateur, le changement du rayonnement shortwave semble également suivre le changement de la SST avec un rayonnement plus fort au-dessus des eaux plus froides et un rayonnement plus faible au-dessus des eaux plus chaudes (Fig. 5.17e). Cela pourrait être dû à une convection accrue au-dessus des anomalies chaudes produisant plus de nuages et donc un rayonnement shortwave plus faible, et *vice versa*. Près de l'équateur, le flux de LH et les radiations shortwave réagissent donc aux changements de SST, et les contrebalancent en partie. A l'écart de l'équateur, entre 5°– 10°N, le rayonnement shortwave augmente, indiquant une diminution de la couverture nuageuse. Cela se remarque également dans le changement du taux de précipitations, qui est réduit jusqu'à 3 mm/jour (soit 40 % de la valeur totale) dans l'ITCZ entre 180°et 110°W (Fig. 5.17d). Des changements significatifs dans le champ de vent à basse altitude sont également observés. En particulier, les alizés augmentent le long de l'équateur et diminuent ailleurs.

Ces changements de grande échelle peuvent résulter d'une combinaison d'effets directs des TIWs (c'est-à-dire l'intégration dans le temps des changements locaux décrits ci-dessus), et d'effets indirects (c'est-à-dire des modifications de la grande échelle qui induisent d'autres modifications de grande échelle).

De tels changements, notamment en ce qui concerne l'ITCZ, pourraient déclencher d'autres changements atmosphériques, par exemple liés à l'activité des cyclones tropicaux dans le bassin Pacifique Nord Est, qui est le deuxième bassin le plus actif au monde. Cependant, une évaluation correcte des changements induits par les TIWs dans la genèse et l'intensité des cyclones tropicaux nécessiterait des simulations plus longues.

Current Feedback (CFB) et Thermal Feedback (TFB)

Comme le montre la littérature et comme le décrit le préambule du Chapitre 5, le couplage air-mer de méso-échelle influence les vents de basse altitude, la variabilité du stress du vent de surface, et le flux de chaleur turbulent. À leur tour, ces perturbations peuvent altérer l'activité des TIWs.

D'une part, le TFB, en induisant des flux de chaleur turbulents, pourrait induire un puits d'énergie potentielle de l'océan vers l'atmosphère (Bishop et al. (2020)), amortissant potentiellement les TIWs. D'autre part, le CFB pourrait avoir un double effet sur les TIWs: (i) un amortissement par "eddy-killing", *i.e.,* destruction de la méso-échelle (Renault et al.

(2016b)); et (ii) une réduction indirecte de la génération de TIWs causée par le ralentissement de la circulation moyenne (Luo et al. (2005)). La TFB et CFB de méso-échelle peuvent également modifier indirectement ENSO.

Sur la base d'un modèle couplé océan-atmosphère similaire à celui utilisé dans le Chapitre 5 (la seule différence étant une augmentation du nombre de niveaux verticaux dans CROCO), Ryan Holmes (Université de Sydney) a lancé une étude visant à démêler les effets du TFB et du CFB sur les TIWs et ENSO, une étude à laquelle j'ai eu l'occasion de collaborer lors de la visite de R. Holmes au LEGOS.

Cette stratégie est similaire à celle utilisée par Renault et al. (2019b), où les auteurs ont utilisé le coupleur OASIS pour lisser spatialement la SST envoyée au modèle atmosphérique. Dans leur étude, Renault et al. (2019b) appliquent cette stratégie sur un canal tropical réaliste afin de démêler les différents coefficients de couplage. Cependant, la région équatoriale doit être traitée avec précaution car un filtre isotrope classique, utilisé par Renault et al. (2019b), ne lisserait pas seulement l'empreinte des TIWs mais aussi les gradients méridiens de température, potentiellement altérant le rotationnel du vent à grande échelle, et donc la dynamique équatoriale. Pour pallier à ce problème, l'empreinte TIWs est supprimée en appliquant uniquement un filtre zonal (moyenne glissante centrée de 12° longitude). Un ensemble de 4 simulations est développé :

- une simulation de contrôle, comprenant le couplage air-mer complet
- une simulation sans TFB de méso-échelle, qui lisse la SST de méso-échelle vue par l'atmosphère
- une simulation sans CFB de méso-échelle, qui lisse les courants de surface de méso-échelle vus par l'atmosphère
- une simulation sans CFB, qui n'inclut pas du tout la CFB en fixant à zéro les courants de surface vus par l'atmosphère.

Les snapshots illustrant chaque champ envoyé au modèle atmosphérique sont présentés dans la Figure 5.18.

Les premiers résultats révèlent (1) une réduction de moitié de la variance de la SST dans la région 2°S – 6°N, 150°– 90°W due au TFB de méso-échelle, très probablement causé par les flux de chaleur turbulents, et (2) un amortissement de la variance de la vitesse méridienne dû à la fois au CFB à méso-échelle ("eddy-killing") et à grande échelle (réduction indirecte de la génération des TIWs). Pour l'amortissement du CFB, l'importance relative du "eddy-killing" dépend fortement de la latitude. Il est intéressant de noter que ce n'est généralement pas le cas, par exemple pour les courants de bord ouest où l'effet "eddy-killing" domine largement (Renault et al. (2016a)). Ces résultats ne sont que préliminaires, et une étude plus approfondie permettra de comprendre l'impact des TFB de méso-échelle sur les flux de chaleur, les mécanismes détaillés responsables de l'amortissement des TIWs dans chaque

expérience, et l'impact de chaque rétroaction sur les composantes moyennes de l'océan et de l'atmosphère.

2. TIWs & processus biogéochimiques

Les organismes marins, qui agissent comme une pompe biologique pour la séquestration du carbone, jouent un rôle clef dans le cycle biogéochimique global. Une meilleure compréhension de leurs importantes fluctuations spatiales et temporelles conduirait à une grande amélioration des prévisions biogéochimiques marines (*e.g.,* Krumhardt et al. (2020)), et donc à une meilleure évaluation et anticipation de la pêche mondiale. Bien que divers défis restent à relever, notamment en raison de la disponibilité très limitée des données biogéochimiques et de la difficulté à assimiler ces données dans les modèles numériques (*e.g.,* , Song et al. (2016)), d'importants efforts ont été réalisés pour comprendre le lien entre le climat et la variabilité biogéochimique marine aux échelles saisonnières et interannuelles. Des études récentes (Yoder et al. (1994); Chavez et al. (1999); Legeckis et al. (2004); Gorgues et al. (2005); Evans et al. (2009); Shi and Wang (2021)) suggèrent notamment que les TIWs modulent fortement à la fois la productivité et la concentration en oxygène de l'océan Pacifique Est, une région clef pour le cycle global du carbone.

Plus récemment, des études de modélisation ont montré que la chlorophylle-a induite par les TIWs peut agir comme une rétroaction négative sur l'intensité des TIWs et induire des changements de la SST à grande échelle, en modulant le rayonnement solaire qui pénètre dans la couche de mélange océanique (Tian et al. (2018)), et pouvant finalement rétroagir sur ENSO (Tian et al. (2019)). Par conséquent, la compréhension des interactions multi-échelles entre les processus physiques et biogéochimiques présente un grand intérêt.

Au cours de ma thèse, j'ai eu l'occasion de travailler avec Feng Jiang, doctorante de l'Université des Sciences de l'Information & Technologie en Chine. En se basant sur mes configurations CROCO du Pacifique tropical Est et en utilisant ma méthodologie de suppression des TIWs, F. Jiang cherche à comprendre les effets directs et indirects des TIWs sur la productivité et la variabilité de la zone de minimum d'oxygène (Paulmier and Ruiz-Pino (2009)). Pour cela, elle utilise des simulations de CROCO couplées au modèle biogéochimique BioEBUS (un modèle NPZD simple, Gutknecht et al. (2013)). Là encore, deux simulations sont effectuées, l'une avec TIWs et l'autre sans, sur une période de 20 ans (2000-2020). La Figure 5.19 illustre les méandres des TIWs observés à travers la concentration de chlorophylle de surface obtenue à partir de la simulation CROCO-BioEBUS.

3. TIWs & mélange au dessus du coeur de l'EUC

Des études observationnelles ont montré que la partie supérieure de l'EUC est le plus souvent dans un état d'instabilité marginale (Smyth and Moum (2013)) reflétant un état de quasi-équilibre dans lequel le forçage par les alizés induit une déstabilisation et de la turbulence, et la turbulence re-stabilise l'état. Pour mieux comprendre ce processus, l'analogie du tas de sable

a été utilisée dans le poster de W.D. Smyth et J.N. Moum lors de l'Ocean Science meeting de 2014 [2] : lorsque du sable est versé sur un tas de sable, de petites avalanches se produisent lorsque la pente critique du tas dépasse un seuil, permettant au tas de sable de rester dans un état de quasi-équilibre. Dans cette analogie, la source de sable est équivalente au forçage du vent, et les avalanches à la turbulence. La pente du tas de sable est une analogie pour le nombre de Richardson $Ri = \frac{N^2}{S^2}$, qui est le rapport de la stratification $N^2 = -\frac{g}{\rho}\partial_z\rho$ sur le cisaillement $S^2 = (\partial_z u)^2 + (\partial_z v)^2$. La stabilité marginale se produit pour $Ri = 1/4$. Plusieurs études ont montré que les TIWs modulent le mélange vertical dans la partie supérieure de l'EUC (Lien et al. (2008); Moum et al. (2009); Inoue et al. (2012)), et l'éloigne de la stabilité marginale, vers un état d'instabilité de cisaillement qui renforcerait la turbulence (Holmes and Thomas (2015)). Ceci pourrait avoir une forte implication sur le bilan thermique de la "cold tongue", et pourrait expliquer la modification du mélange vertical obtenue dans les Chapitre 3 et Chapitre 5. Des travaux supplémentaires pourraient être effectués sur cet aspect des TIWs, avec une attention particulière sur la capacité du schéma de parametrisation de la turbulence choisi (dans cette thèse, parametrisation K-profile KPP) à reproduire la turbulence et les cycles de turbulence observés (Holmes and Thomas (2015); Cherian et al. (2021)).

4. TIWs & la génération de jets profonds

Dans les régions de basse latitude, la circulation sous la thermocline est façonnée par d'intenses jets qui n'ont été documentés que récemment grâce au déploiement du flotteur Argo en l'an 2000. Cependant, les origines de ces jets équatoriaux profonds restent mal comprises. La variabilité intrasaisonnière associée aux TIWs a été détectée jusqu'à 2000 mètres de profondeur (Tuchen et al. (2018)), car elles peuvent se propager comme des ondes de Rossby et de Yanai descendantes (Farrar (2011); Lee et al. (2022); Delpech et al. (2020)). Cette variabilité intrasaisonnière induite par les TIWs et détectée en profondeur pourrait être un facteur important de la génération des jets équatoriaux profonds (Ascani et al. (2015); Greatbatch et al. (2018)). L'utilisation de la méthodologie de suppression des TIWs développée dans cette thèse pourrait aider à mettre en évidence les interactions potentielles entre les TIWs et les jets profonds équatoriaux.

– Note Finale –

Tous ces travaux de thèse sont basés sur des simulations numériques. En tant que jeune modélisatrice, je me sens souvent déconnectée de mon objet d'étude. Pour renouer avec la réalité, voici une photographie prise en lumière naturelle montrant le front d'une onde tropicale d'instabilité (Fig. 5.20).

[2] https://www.eposters.net/pdfs/marginal-instability-and-the-deep-cycle-of-equatorial-turbulence.pdf

Appendix A: Scripts (Python and Fortran) for Nudging in CROCO

clim_u_v_nudging.py

```
# Author: L. Maillard
# Date:   August 1st 2022

# convert a netcdf file containing monthly climatological values
# of u,v into a netcdf file readable by CROCO Fortran script for nudging
# This is the version for non XIOS outputs.

#require python 3
from __future__ import print_function
import xarray as xr
import numpy as np
from datetime import date

######################
####  USER INPUT  ###
######################
clim_path     = '/my/clim/path/'
grid_path     = '/my/grid/path/'
clim_path     = '/my/save/path/'
fn_clm  = clim_path+'filename_of_monthly_climatology_uv.nc'
fn_grd  = grid_path+'filename_of_croco_grid.nc'
fn_save = save_path+'filename_of_climatology_for_nudging.nc'
######################
##  Reading data  ###
######################
ds_clm  = xr.open_dataset(fn_clm)
ds_grd  = xr.open_dataset(fn_grd)
######################
##### GRID FILE #####
######################
type_file = 'CLIMATOLOGY file obtain from CROCO averaged u,v files from TIW-RUN' ;
time_arr = np.arange(15.2188,351,30.4375) # days : middle of each month
cycle = 365.25                            # length of a typical climatological year

## add time attributes
```

```
ds_clm['tstart'] =  time_arr[0 ]
ds_clm['tend'  ] =  time_arr[-1]

## Create global attributes
today = date.today()
ds_clm.attrs['date'] = str(today)
ds_clm.attrs['clim_file'] = fn_clm
ds_clm.attrs['grid_file'] = fn_grd
ds_clm.attrs['type'] = type_file

ds_clm['time_counter'] = time_arr
ds_clm['v'] = ds_clm.v.rename({"time":"vclm_time"})
ds_clm['u'] = ds_clm.u.rename({"time":"uclm_time"})

## add cycling attributes
ds_clm.u.attrs        ['calendar'] = '365.25 days in every year'
ds_clm.u.attrs        ['cycle_length'] = cycle
ds_clm.v.attrs        ['calendar'] = '365.25 days in every year'
ds_clm.v.attrs        ['cycle_length'] = cycle
ds_clm.vclm_time.attrs['calendar'] = '365.25 days in every year'
ds_clm.vclm_time.attrs['cycle_length'] = cycle
ds_clm.uclm_time.attrs['calendar'] = '365.25 days in every year'
ds_clm.uclm_time.attrs['cycle_length'] = cycle
ds_clm.time.attrs     ['calendar'] = '365.25 days in every year'
ds_clm.time.attrs     ['cycle_length'] = cycle

######################
######save netcdf####
######################
ds_clm.to_netcdf(fn_save)
#end of script
```

clim_u_v_nudging_xios.py

```
# Author: L. Maillard
# Date:   August 1st 2022

# convert a netcdf file containing monthly climatological values
# of u,v into a netcdf file readable by CROCO Fortran script for nudging
# This is the version for XIOS outputs.

#require python 3
from __future__ import print_function
import xarray as xr
import numpy as np
from datetime import date

######################
####  USER INPUT  ###
######################
clim_path     = '/my/clim/path/'
grid_path     = '/my/grid/path/'
clim_path     = '/my/save/path/'
fn_clm  = clim_path+'filename_of_monthly_climatology_uv.nc'
fn_grd  = grid_path+'filename_of_croco_grid.nc'
fn_save = save_path+'filename_of_climatology_for_nudging.nc'
######################
##  Reading data  ###
######################
ds_clm  = xr.open_dataset(fn_clm)
ds_grd  = xr.open_dataset(fn_grd)
######################
##### GRID FILE #####
######################
type_file = 'CLIMATOLOGY file obtain from CROCO averaged u,v files from TIW-RUN' ;

time_arr = np.arange(15.2188,351,30.4375) # days : middle of each month
cycle = 365.25                            # length of a typical climatological year

## add time attributes
ds_clm['tstart'] =  time_arr[0 ]
ds_clm['tend'  ] =  time_arr[-1]

## Create global attributes
```

```
today = date.today()
ds_clm.attrs['date'] = str(today)
ds_clm.attrs['clim_file'] = fn_clm
ds_clm.attrs['grid_file'] = fn_grd
ds_clm.attrs['type'] = type_file

ds_clm['time_counter'] = time_arr
ds_clm['v'] = ds_clm.v.rename({"time_counter":"vclm_time"})
ds_clm['u'] = ds_clm.u.rename({"time_counter":"uclm_time"})
ds_clm['v'] = ds_clm.v.rename({"y_v":"eta_v"})
ds_clm['v'] = ds_clm.v.rename({"x_v":"xi_rho"})
ds_clm['u'] = ds_clm.u.rename({"y_u":"eta_rho"})
ds_clm['u'] = ds_clm.u.rename({"x_u":"xi_u"})
ds_clm['lon_rho'] = ds_grd.lon_rho
ds_clm['lat_rho'] = ds_grd.lat_rho
ds_clm['lon_u'] = ds_grd.lon_u
ds_clm['lat_u'] = ds_grd.lat_u
ds_clm['lon_v'] = ds_grd.lon_v
ds_clm['lat_v'] = ds_grd.lat_v
ds_clm = ds_clm.drop(['nav_lon_u','nav_lat_u','nav_lon_v','nav_lat_v'])
ds_clm = ds_clm.rename({'time_counter':'time'})
ds_clm = ds_clm.drop(['time_centered_bounds','time_counter_bounds'])
ds_clm = ds_clm.drop(['time_centered'])

## add cycling attributes
ds_clm.u.attrs        ['calendar'] = '365.25 days in every year'
ds_clm.u.attrs        ['cycle_length'] = cycle
ds_clm.v.attrs        ['calendar'] = '365.25 days in every year'
ds_clm.v.attrs        ['cycle_length'] = cycle
ds_clm.vclm_time.attrs['calendar'] = '365.25 days in every year'
ds_clm.vclm_time.attrs['cycle_length'] = cycle
ds_clm.uclm_time.attrs['calendar'] = '365.25 days in every year'
ds_clm.uclm_time.attrs['cycle_length'] = cycle
ds_clm.time.attrs     ['calendar'] = '365.25 days in every year'
ds_clm.time.attrs     ['cycle_length'] = cycle

## replace NaN by zeros
ds_clm.u.values = ds_clm.u.fillna(0.0)
ds_clm.v.values = ds_clm.v.fillna(0.0)

######################
######save netcdf####
######################
ds_clm.to_netcdf(fn_save)
```

modification in CROCO: `cppdefs.F`

```
/* Configuration Name */
# define EPACIFIC
# define NUDGIN_TIWS /* Nudging toward climato to remove Tropical Inst. Waves */
# ifdef NUDGIN_TIWS
#  define NUDGIN_VONLY /* Nudging toward climato of v only */
# endif
```

modification in CROCO: `climat.h`
In bold are the added lines :

```
[commandchars=\\\{\}]
#if defined SOLVE3D && defined M3CLIMATOLOGY
#   ifdef M3NUDGING
      real M3nudgcof(GLOBAL_2D_ARRAY)
      common /climat_M3nudgcof/M3nudgcof
\userinput{#       ifdef NUDGIN_TIWS}
\userinput{      real M3nudgcof3D(GLOBAL_2D_ARRAY,N)}
\userinput{      common /climat_M3nudgcof3D/M3nudgcof3D}
\userinput{#       endif}
#   endif
#   ifndef ANA_M3CLIMA
      real uclima(GLOBAL_2D_ARRAY,N,2)
      real vclima(GLOBAL_2D_ARRAY,N,2)
      common /climat_uclima/uclima /climat_vclima/vclima
#   endif
#endif
```

modification in CROCO: `set_nudgcof.F`
In the variables declaration section:

```
    # if defined NUDGIN_TIWS
      real    lonmax1, lonmax2, Zmax1, Zmax2
      real    cff,cff2,cff3,cffz,cffxy, sigma, mu
      real    wrk2(PRIVATE_2D_SCRATCH_ARRAY)
      real    wrk3(PRIVATE_2D_SCRATCH_ARRAY)
```

In the core of the script (in the " add configuration specific stuff" section for instance):

```
#     ifdef NUDGIN_TIWS
          lonmax1 = 270.0 !degree east. sponge starts to decrease
          lonmax2 = 275.0 !degree east. sponge is zero after
          Zmax1   = 100.0 !meter. sponge starts to decrease
          Zmax2   = 200.0 !meter. sponge is zero after
          sigma = 10.0 !standard deviation of the gaussian
          mu = 1.0 !center of the gaussian (in latitude)
          tau = 5.0*24.0*60.0*60.0 !relaxation time (sec) for nudging toward climato field
          do j=max(-1,JstrR-1),JendR
            do i=max(-1,IstrR-1),IendR
              wrk2(i,j) =(1.0/tau)*exp(-.5*((latr(i,j)-mu)/sigma)**2)
            enddo
          enddo
          do j=JstrR,JendR
            do i=IstrR,IendR
              do k=1,N
                 cffz = 1.0
                if (abs(z_r(i,j,k)) .lt. Zmax1) then
                  cffz = 1.0
                else if ((abs(z_r(i,j,k)) .lt. Zmax2)
     &          .and.    (abs(z_r(i,j,k)) .ge. Zmax1)) then
                  cffz =
     &            3.0*
     &            ((abs(z_r(i,j,k)) - Zmax2)/(Zmax1 -Zmax2))**2 -
     &            2.0*
     &            ((abs(z_r(i,j,k)) - Zmax2)/(Zmax1 -Zmax2))**3
                else
                  cffz = 0.0
                end if
                ! compute coef for sponge in lon, lat
                if (lonr(i,j) .lt. lonmax1) then
                  cffxy = 1.0
                else if ((lonr(i,j) .lt. lonmax2)
     &             .and. (lonr(i,j) .ge. lonmax1)) then
                  cffxy =
     &            3.0*((lonr(i,j) - lonmax2)/(lonmax1 - lonmax2))**2 -
     &            2.0*((lonr(i,j)-  lonmax2)/(lonmax1 - lonmax2))**3
                else
                  cffxy = 0.0
                end if
#       ifdef M3NUDGING
            ! create an array M3 3D
                M3nudgcof3D(i,j,k)=wrk2(i,j)*cffz*cffxy
#       endif
```

```
              enddo
            enddo
          enddo
#     endif
```

modification in CROCO: `step3d_uv2.F`
In bold are the added lines :

```
[commandchars=\\\{\}]
!-----------------------------------------------------------------------
!  Set 3D Momemtum nudging
!-----------------------------------------------------------------------
!
# if defined M3NUDGING && defined M3CLIMATOLOGY

#  ifdef ZONAL_NUDGING
       if (iic.eq.ntstart .or. mod(iic,10).eq.0) then
         call zonavg_3d(istr,iend,jstr,jend,
     &                          u(START_2D_ARRAY,1,nnew),uzon)
         call zonavg_3d(istr,iend,jstr,jend,
     &                          v(START_2D_ARRAY,1,nnew),vzon)
       endif
       if (iic.eq.ntstart) then
         call zonavg_3d(istr,iend,jstr,jend,
     &                          uclm(START_2D_ARRAY,1),uclmzon)
         call zonavg_3d(istr,iend,jstr,jend,
     &                          vclm(START_2D_ARRAY,1),vclmzon)
       endif
#  endif /* ZONAL_NUDGING */

       do k=1,N
         do j=JU_RANGE
           do i=IU_RANGE
             u(i,j,k,nnew)=u(i,j,k,nnew)
#  ifdef ZONAL_NUDGING
     &                 +dt*M3nudgcof(i,j)*(uclmzon(j,k)-uzon(j,k))
#    ifdef MASKING
     &                                          *umask(i,j)
#    endif
#    ifdef WET_DRY
     &                                       *umask_wet(i,j)
#    endif
#  else
```

```
\userinput{#    ifdef NUDGIN_TIWS}
\userinput{#       if !defined NUDGIN_VONLY}
\userinput{     &                +dt*M3nudgcof3D(i,j,k)*(uclm(i,j,k)-u(i,j,k,nnew))}
\userinput{#          ifdef MASKING}
\userinput{     &                                          *umask(i,j)}
\userinput{#          endif}
\userinput{#          ifdef WET_DRY}
\userinput{     &                                      *umask_wet(i,j)}
\userinput{#          endif}
\userinput{#       endif /* NUDGIN_VONLY */}
\userinput{#    else}
\userinput{     &                +dt*M3nudgcof(i,j)*(uclm(i,j,k)-u(i,j,k,nnew))}
\userinput{#          ifdef MASKING}
\userinput{     &                                          *umask(i,j)}
\userinput{#          endif}
\userinput{#          ifdef WET_DRY}
\userinput{     &                                      *umask_wet(i,j)}
\userinput{#          endif}
\userinput{#    endif /* NUDGIN_TIWS */}
#  endif /* ZONAL_NUDGING */
          enddo
        enddo
      enddo
      do k=1,N
        do j=JV_RANGE
          do i=IV_RANGE
            v(i,j,k,nnew)=v(i,j,k,nnew)+
#  ifdef ZONAL_NUDGING
     &                 dt*M3nudgcof(i,j)*(vclmzon(j,k)-vzon(j,k))
\userinput{#  else}
\userinput{#    ifdef NUDGIN_TIWS}
\userinput{     &                 dt*M3nudgcof3D(i,j,k)*(vclm(i,j,k)-v(i,j,k,nnew))}
\userinput{#    else}
\userinput{     &                 dt*M3nudgcof(i,j)*(vclm(i,j,k)-v(i,j,k,nnew))}
\userinput{#    endif /* NUDGIN_TIWS */}
#  endif
#  ifdef MASKING
     &                                          *vmask(i,j)
#  endif
# ifdef WET_DRY
     &                                      *vmask_wet(i,j)
# endif
          enddo
        enddo
```

```
      enddo
# endif
!
```

Bibliography

Abram, N., Gattuso, J.P., Prakash, A., Cheng, L., Chidichimo, M., Crate, S., Enomoto, H., Garschagen, M., Gruber, N., Harper, S., Holland, E., Kudela, R., Rice, J., Steffen, K., von Schuckmann, K., 2019. Framing and Context of the Report. In: *The Ocean and Cryosphere in a Changing Climate: Special Report of the Intergovernmental Panel on Climate Change*. Cambridge University Press. p. 73–130. doi:10.1017/9781009157964.003.

An, S.I., 2008. Interannual Variations of the Tropical Ocean Instability Wave and ENSO. Journal of Climate 21, 3680–3686. doi:10.1175/2008JCLI1701.1.

An, S.I., Jin, F.F., 2004. Nonlinearity and asymmetry of ENSO. Journal of Climate 17, 2399 – 2412. doi:10.1175/1520-0442(2004)017<2399:NAAOE>2.0.CO;2.

An, S.I., Tziperman, E., Okumura, Y.M., Li, T., 2020. ENSO Irregularity and Asymmetry, in: McPhaden, M.J., Santoso, A., Cai, W. (Eds.), Geophysical Monograph Series. first ed.. Wiley, pp. 153–172. doi:10.1002/9781119548164.ch7.

Arias, P., Bellouin, N., Coppola, E., Jones, R., Krinner, G., Marotzke, J., Naik, V., Palmer, M., Plattner, G.K., Rogelj, J., et al., 2021. Climate Change 2021: The Physical Science Basis. Contribution of Working Group I to the Sixth Assessment Report of the Intergovernmental Panel on Climate Change. Cambridge University Press, Cambridge, United Kingdom and New York, NY, USA. pp. 33–144. doi:10.1017/9781009157896.002.

Ascani, F., Firing, E., McCreary, J.P., Brandt, P., Greatbatch, R.J., 2015. The Deep Equatorial Ocean Circulation in Wind-Forced Numerical Solutions. Journal of Physical Oceanography 45, 1709–1734. doi:10.1175/JPO-D-14-0171.1.

Battisti, D.S., 1988. Dynamics and Thermodynamics of a Warming Event in a Coupled Tropical Atmosphere–Ocean Model. Journal of the Atmospheric Sciences 45, 2889–2919. doi:10.1175/1520-0469(1988)045<2889:DATOAW>2.0.CO;2.

Battisti, D.S., Hirst, A.C., 1989. Interannual variability in a tropical atmosphere–ocean model: Influence of the basic state, ocean geometry and nonlinearity. Journal of Atmospheric Sciences 46, 1687 – 1712. doi:10.1175/1520-0469(1989)046<1687:IVIATA>2.0.CO;2.

Baturin, N.G., Niiler, P.P., 1997. Effects of instability waves in the mixed layer of the equatorial Pacific. Journal of Geophysical Research: Oceans 102, 27771–27793. doi:10.1029/97JC02455.

Bayr, T., Latif, M., Dommenget, D., Wengel, C., Harlaß, J., Park, W., 2018. Mean-state dependence of ENSO atmospheric feedbacks in climate models. Climate Dynamics 50, 3171–3194. doi:10.1007/s00382-017-3799-2.

Becker, J.J., Sandwell, D.T., Smith, W.H.F., Braud, J., Binder, B., Depner, J., Fabre, D., Factor, J., Ingalls, S., Kim, S.H., Ladner, R., Marks, K., Nelson, S., Pharaoh, A., Trimmer,

R., Von Rosenberg, J., Wallace, G., Weatherall, P., 2009. Global Bathymetry and Elevation Data at 30 Arc Seconds Resolution: SRTM30_PLUS. Marine Geodesy 32, 355–371. doi:10.1080/01490410903297766.

Bishop, S.P., Small, R.J., Bryan, F.O., 2020. The global sink of available potential energy by mesoscale air-sea interaction. Journal of Advances in Modeling Earth Systems 12, e2020MS002118. doi:https://doi.org/10.1029/2020MS002118. e2020MS002118 10.1029/2020MS002118.

Bjerknes, J., 1966. A possible response of the atmospheric Hadley circulation to equatorial anomalies of ocean temperature. Tellus 18, 820–829. doi:10.1111/j.2153-3490.1966.tb00303.x.

Bjerknes, J., 1969. Atmospheric teleconnections from the equatorial Pacific. Monthly Weather Review 97, 163 – 172. doi:10.1175/1520-0493(1969)097<0163:ATFTEP>2.3.CO;2.

Boucharel, J., 2010. Modes de variabilité climatique dans l'océan Pacifique tropical : quantification des non-linéarités et rôle sur les changements de régimes climatiques. Ph.D. thesis. Université de Toulouse, Université Toulouse III - Paul Sabatier.

Boucharel, J., Jin, F.F., 2020. A simple theory for the modulation of Tropical Instability Waves by ENSO and the annual cycle. Tellus A: Dynamic Meteorology and Oceanography 72, 1–14. doi:10.1080/16000870.2019.1700087.

Boucharel, J., Timmermann, A., Santoso, A., England, M.H., Jin, F.F., Balmaseda, M.A., 2015. A surface layer variance heat budget for ENSO. Geophysical Research Letters 42, 3529–3537. doi:https://doi.org/10.1002/2015GL063843.

Bryden, H.L., Brady, E.C., 1989. Eddy momentum and heat fluxes and their effects on the circulation of the equatorial Pacific Ocean. Journal of Marine Research 47, 55–79. doi:10.1357/002224089785076389.

Bye, J.A., 1985. Large-scale momentum exchange in the coupled atmosphere-ocean, in: Elsevier oceanography series. Elsevier. volume 40, pp. 51–61. doi:https://doi.org/10.1016/S0422-9894(08)70702-5.

Cai, W., Santoso, A., Wang, G., Wu, L., Collins, M., Lengaigne, M., Power, S., Timmermann, A., 2020. ENSO Response to Greenhouse Forcing, in: McPhaden, M.J., Santoso, A., Cai, W. (Eds.), Geophysical Monograph Series. first ed.. Wiley, pp. 289–307. doi:10.1002/9781119548164.ch13.

Cai, W., Wang, G., Dewitte, B., Wu, L., Santoso, A., Takahashi, K., Yang, Y., Carréric, A., McPhaden, M.J., 2018. Increased variability of eastern Pacific El Niño under greenhouse warming. Nature 564, 201–206. doi:10.1038/s41586-018-0776-9.

Cane, M., Sarachik, E., 1977. Forced baroclinic ocean motions. II-the linear equatorial bounded case. Journal of Marine Research 35.

Cane, M.A., Zebiak, S.E., Dolan, S.C., 1986. Experimental forecasts of El Niño. Nature 321, 827–832. doi:https://doi.org/10.1038/321827a0.

Carreric, A., 2019. La diversité d'ENSO et le changement climatique. Ph.D. thesis. Université de Toulouse, Université Toulouse III - Paul Sabatier.

Carton, J.A., Chepurin, G.A., Chen, L., Grodsky, S., Kalnay, E., Penny, S.G., 2019. SODA project: SODA3 ensemble means and standard deviations.

Chavez, F.P., Strutton, P.G., Friederich, G.E., Feely, R.A., Feldman, G.C., Foley, D.G., McPhaden, M.J., 1999. Biological and Chemical Response of the Equatorial Pacific Ocean to the 1997-98 El Niño. Science 286, 2126–2131. doi:10.1126/science.286.5447.2126.

Chelton, D.B., Esbensen, S.K., Schlax, M.G., Thum, N., Freilich, M.H., Wentz, F.J., Gentemann, C.L., McPhaden, M.J., Schopf, P.S., 2001. Observations of Coupling between Surface Wind Stress and Sea Surface Temperature in the Eastern Tropical Pacific. Journal of Climate 14, 1479–1498. doi:10.1175/1520-0442(2001)014<1479:OOCBSW>2.0.CO;2.

Chen, H.C., Jin, F.F., 2020. Fundamental Behavior of ENSO Phase Locking. Journal Of Climate 33, 16. doi:https://doi.org/10.1175/JCLI-D-19-0264.1.

Cherian, D.A., Whitt, D.B., Holmes, R.M., Lien, R.C., Bachman, S.D., Large, W.G., 2021. Off-Equatorial Deep-Cycle Turbulence Forced by Tropical Instability Waves in the Equatorial Pacific. Journal of Physical Oceanography 51, 1575–1593. doi:10.1175/JPO-D-20-0229.1.

Chou, M.D., Suarez, M.J., 1999. A solar radiation parameterization for atmospheric studies. Technical Report. NASA.

Contreras, R.F., 2002. Long-Term Observations of Tropical Instability Waves. Journal Of Physical Oceanography 32, 8. doi:https://doi.org/10.1175/1520-0485(2002)032<2715:LTOOTI>2.0.CO;2.

Cox, M., 1980. Generation and propagation of 30-day waves in a numerical model of the Pacific. Journal of Physical Oceanography, American Meteorological Society 10, 1168 – 1186. doi:https://doi.org/10.1175/1520-0485(1980)010<1168:GAPODW>2.0.CO;2.

Craig, A., Valcke, S., Coquart, L., 2017. Development and performance of a new version of the oasis coupler, oasis3-mct_3.0. Geoscientific Model Development 10, 3297–3308. doi:10.5194/gmd-10-3297-2017.

Cravatte, S., Picaut, J., Eldin, G., 2003. Second and first baroclinic kelvin modes in the equatorial Pacific at intraseasonal timescales. Journal of Geophysical Research: Oceans 108.

Cromwell, T., 1953. Circulation in a meridional plane in the central equatorial Pacific. J. mar. Res. 12, 196–213.

Cromwell, T., Bennett, E.B., 1959. Surface drift charts for the eastern tropical Pacific ocean. Bulletin of the Inter-American Tropical Tuna Commission 3, 217–237.

Cromwell, T., Montgomery, R.B., Stroup, E.D., 1954. Equatorial undercurrent in Pacific ocean revealed by new methods. Science 119, 648–649. doi:10.1126/science.119.3097.648.

Debreu, L., Marchesiello, P., Penven, P., Cambon, G., 2012. Two-way nesting in split-explicit ocean models: Algorithms, implementation and validation. Ocean Modelling 49-50, 1–21. doi:https://doi.org/10.1016/j.ocemod.2012.03.003.

Delpech, A., Cravatte, S., Marin, F., Ménesguen, C., Morel, Y., 2020. Deep Eddy Kinetic Energy in the Tropical Pacific From Lagrangian Floats. Journal of Geophysical Research: Oceans 125. doi:10.1029/2020JC016313.

Deser, C., Wahl, S., Bates, J.J., 1993. The Influence of Sea Surface Temperature Gradients on Stratiform Cloudiness along the Equatorial Front in the Pacific Ocean. Journal of Climate 6, 1172–1180. doi:10.1175/1520-0442(1993)006<1172:TIOSST>2.0.CO;2.

DiNezio, P.N., Deser, C., 2014. Nonlinear controls on the persistence of La Niña. Journal of Climate 27, 7335 – 7355. doi:10.1175/JCLI-D-14-00033.1.

Dolinar, E.K., Dong, X., Xi, B., 2016. Evaluation and intercomparison of clouds, precipitation, and radiation budgets in recent reanalyses using satellite-surface observations. Climate Dynamics 46, 2123–2144. doi:10.1007/s00382-015-2693-z.

Duhaut, T.H., Straub, D.N., 2006. Wind stress dependence on ocean surface velocity: Implications for mechanical energy input to ocean circulation. Journal of physical oceanography 36, 202–211. doi:https://doi.org/10.1175/JPO2842.1.

Düing, W., Hisard, P., Katz, E., Meincke, J., Miller, L., Moroshkin, K.V., Philander, G., Ribnikov, A.A., Voigt, K., Weisberg, R., 1975. Meanders and long waves in the equatorial Atlantic. Nature 257, 280–284. doi:10.1038/257280a0.

Escobar-Franco, M.G., Boucharel, J., Dewitte, B., 2022a. On the Relationship Between Tropical Instability Waves and Intraseasonal Equatorial Kelvin Waves in the Pacific From Satellite Observations (1993–2018). Frontiers in Marine Science 9, 788908. doi:10.3389/fmars.2022.788908.

Escobar-Franco, M.G., Boucharel, J., Dewitte, B., 2022b. On the Relationship Between Tropical Instability Waves and Intraseasonal Equatorial Kelvin Waves in the Pacific From Satellite Observations (1993–2018). Frontiers in Marine Science 9, 788908. doi:10.3389/fmars.2022.788908.

Evans, W., Strutton, P.G., Chavez, F.P., 2009. Impact of Tropical Instability Waves on nutrient and chlorophyll distributions in the equatorial Pacific. Deep Sea Research Part I: Oceanographic Research Papers 56, 178–188. doi:10.1016/j.dsr.2008.08.008.

Farrar, J.T., 2011. Barotropic Rossby Waves Radiating from Tropical Instability Waves in the Pacific Ocean. Journal of Physical Oceanography 41, 1160–1181. doi:10.1175/2011JPO4547.1.

Ferrett, S., Collins, M., 2019. ENSO feedbacks and their relationships with the mean state in a flux adjusted ensemble. Climate Dynamics 52, 7189–7208. doi:https://doi.org/10.1007/s00382-016-3270-9.

Fiedler, P.C., Talley, L.D., 2006. Hydrography of the eastern tropical Pacific: A review. Progress in Oceanography 69, 143–180. doi:10.1016/j.pocean.2006.03.008.

Flament, P.J., Kennan, S.C., Knox, R.A., Niiler, P.P., Bernstein, R.L., 1996. The three-dimensional structure of an upper ocean vortex in the tropical Pacific Ocean. Nature 383, 610–613. doi:10.1038/383610a0.

Frenger, I., Gruber, N., Knutti, R., Münnich, M., 2013. Imprint of southern ocean eddies on winds, clouds and rainfall. Nature geoscience 6, 608–612. doi:https://doi.org/10.1038/ngeo1863.

Gill, A.E., 1982. Chapter eleven - the tropics, in: Atmosphere—Ocean Dynamics. Academic Press. volume 30 of *International Geophysics*, pp. 429–491. doi:10.1016/S0074-6142(08)60036-4.

Gorgues, T., Menkes, C., Aumont, O., Vialard, J., Dandonneau, Y., Bopp, L., 2005. Biogeochemical impact of Tropical Instability Waves in the equatorial Pacific. Geophysical Research Letters 32, L24615. doi:10.1029/2005GL024110.

Graham, T., 2014. The importance of eddy permitting model resolution for simulation of the heat budget of Tropical Instability Waves. Ocean Modelling 79, 21–32. doi:10.1016/j.ocemod.2014.04.005.

Greatbatch, R.J., Claus, M., Brandt, P., Matthießen, J.D., Tuchen, F.P., Ascani, F., Dengler, M., Toole, J., Roth, C., Farrar, J.T., 2018. Evidence for the Maintenance of Slowly Varying Equatorial Currents by Intraseasonal Variability. Geophysical Research Letters 45, 1923–1929. doi:10.1002/2017GL076662.

Gutknecht, E., Dadou, I., Le Vu, B., Cambon, G., Sudre, J., Garçon, V., Machu, E., Rixen, T., Kock, A., Flohr, A., Paulmier, A., Lavik, G., 2013. Coupled physical/biogeochemical modeling including o_2-dependent processes in the eastern boundary upwelling systems: application in the benguela. Biogeosciences 10, 3559–3591. doi:10.5194/bg-10-3559-2013.

Hansen, D.V., Paul, C.A., 1984. Genesis and effects of long waves in the equatorial Pacific. Journal of Geophysical Research 89, 10431. doi:10.1029/JC089iC06p10431.

Hashizume, H., Xie, S.P., Liu, W.T., Takeuchi, K., 2001. Local and remote atmospheric response to Tropical Instability Waves: A global view from space. Journal of Geophysical Research: Atmospheres 106, 10173–10185. doi:10.1029/2000JD900684.

Hastenrath, S., Lamb, P., 1978. On the dynamics and climatology of surface flow over the equatorial oceans. Tellus 30, 436–448. doi:https://doi.org/10.3402/tellusa.v30i5.10387.

Hayashi, M., Jin, F.F., Stuecker, M.F., 2020. Dynamics for El Niño-La Niña asymmetry constrain equatorial-Pacific warming pattern. Nature Communications 11, 4230. doi:10.1038/s41467-020-17983-y.

Hayashi, M., Watanabe, M., 2017. ENSO complexity induced by state dependence of westerly wind events. Journal of Climate 30, 3401 – 3420. doi:10.1175/JCLI-D-16-0406.1.

Hersbach, H., Bell, B., Berrisford, P., Hirahara, S., Horányi, A., Muñoz-Sabater, J., Nicolas, J., Peubey, C., Radu, R., Schepers, D., et al., 2020. The ERA5 global reanalysis. Quarterly Journal of the Royal Meteorological Society 146, 1999–2049. doi:https://doi.org/10.1002/qj.3803.

Holmes, R.M., 2016. Tropical Instability Waves and Mixing in the Equatorial Pacific Ocean. Ph.D. thesis. Stanford University.

Holmes, R.M., McGregor, S., Santoso, A., England, M.H., 2019. Contribution of Tropical Instability Waves to ENSO irregularity. Climate Dynamics 52, 1837–1855. doi:10.1007/s00382-018-4217-0.

Holmes, R.M., Thomas, L.N., 2015. The Modulation of Equatorial Turbulence by Tropical Instability Waves in a Regional Ocean Model. Journal of Physical Oceanography 45, 1155–1173. doi:10.1175/JPO-D-14-0209.1.

Holmes, R.M., Thomas, L.N., 2016. Modulation of Tropical Instability Wave Intensity by Equatorial Kelvin Waves. Journal of Physical Oceanography 46, 2623–2643. doi:10.1175/JPO-D-16-0064.1.

Hong, S., Lim, J.O.J., 2006. The WRF single-moment 6-class microphysics scheme (WSM6). Asia-pacific Journal of Atmospheric Sciences 42, 129–151.

Hong, S.Y., Noh, Y., Dudhia, J., 2006. A new vertical diffusion package with an explicit treatment of entrainment processes. Monthly Weather Review 134, 2318 – 2341. doi:10.1175/MWR3199.1.

Horel, J.D., 1982. On the Annual Cycle of the Tropical Pacific Atmosphere and Ocean. Monthly Weather Review 110, 1863–1878. doi:10.1175/1520-0493(1982)110<1863:OTACOT>2.0.CO;2.

Im, S.H., An, S.I., Kim, S.T., Jin, F.F., 2015. Feedback processes responsible for El Niño-La Niña amplitude asymmetry. Geophysical Research Letters 42, 5556–5563. doi:10.1002/2015GL064853.

Im, S.H., An, S.I., Lengaigne, M., Noh, Y., 2012. Seasonality of Tropical Instability Waves and Its Feedback to the Seasonal Cycle in the Tropical Eastern Pacific. The Scientific World Journal 2012, 1–11. doi:10.1100/2012/612048.

Imada, Y., Kimoto, M., 2012. Parameterization of Tropical Instability Waves and Examination of Their Impact on ENSO Characteristics. Journal of Climate 25, 4568–4581. doi:10.1175/JCLI-D-11-00233.1.

Imada, Y., Kimoto, M., Chen, X., 2012. Impact of the atmospheric mean state on tropical instability wave activity. Journal of Climate 25, 2341 – 2355. doi:10.1175/2011JCLI4244.1.

Inoue, R., Lien, R.C., Moum, J.N., 2012. Modulation of equatorial turbulence by a tropical instability wave. Journal of Geophysical Research: Oceans 117, n/a–n/a. doi:10.1029/2011JC007767.

Inoue, R., Lien, R.C., Moum, J.N., Perez, R.C., Gregg, M.C., 2019. Variations of Equatorial Shear, Stratification, and Turbulence Within a Tropical Instability Wave Cycle. Journal of Geophysical Research: Oceans 124, 1858–1875. doi:10.1029/2018JC014480.

Jin, F.F., 1997a. An equatorial ocean recharge paradigm for ENSO. part i: Conceptual model. Journal of the Atmospheric Sciences 54, 811 – 829. doi:10.1175/1520-0469(1997)054<0811:AEORPF>2.0.CO;2.

Jin, F.F., 1997b. An equatorial ocean recharge paradigm for ENSO. part ii: A stripped-down coupled model. Journal of the Atmospheric Sciences 54, 830 – 847. doi:10.1175/1520-0469(1997)054<0830:AEORPF>2.0.CO;2.

Jin, F.F., Chen, H.C., Zhao, S., Hayashi, M., Karamperidou, C., Stuecker, M.F., Xie, R., Geng, L., 2020. Simple ENSO Models, in: McPhaden, M.J., Santoso, A., Cai, W. (Eds.), Geophysical Monograph Series. first ed.. Wiley, pp. 119–151. doi:10.1002/9781119548164.ch6.

Jin, F.F., Kim, S.T., Bejarano, L., 2006. A coupled-stability index for ENSO. Geophysical Research Letters 33. doi:https://doi.org/10.1029/2006GL027221.

Jin, F.F., Neelin, J.D., Ghil, M., 1994. El Niño on the Devil's Staircase: Annual Subharmonic Steps to Chaos. Science 264, 70–72. doi:10.1126/science.264.5155.70.

Jochum, M., Cronin, M.F., Kessler, W.S., Shea, D., 2007a. Observed horizontal temperature advection by Tropical Instability Waves. Geophysical Research Letters 34. doi:10.1029/2007GL029416.

Jochum, M., Danabasoglu, G., Holland, M., Kwon, Y.O., Large, W.G., 2008. Ocean viscosity and climate. Journal of Geophysical Research 113, C06017. doi:10.1029/2007JC004515.

Jochum, M., Deser, C., Phillips, A., 2007b. Tropical atmospheric variability forced by oceanic internal variability. Journal of Climate 20, 765 – 771. doi:10.1175/JCLI4044.1.

Jochum, M., Malanotte-Rizzoli, P., Busalacchi, A., 2004. Tropical Instability Waves in the Atlantic Ocean. Ocean Modelling 7, 145–163. doi:10.1016/S1463-5003(03)00042-8.

Jochum, M., Murtugudde, R., 2006. Temperature Advection by Tropical Instability Waves. Journal of Physical Oceanography 36, 592–605. doi:10.1175/JPO2870.1.

Jousse, A., Hall, A., Sun, F., Teixeira, J., 2016. Causes of WRF surface energy fluxes biases in a stratocumulus region. Climate Dynamics 46, 571–584. doi:https://doi.org/10.1007/s00382-015-2599-9.

Kang, I.S., An, S.I., Jin, F.F., 2001. A Systematic Approximation of the SST Anomaly Equation for ENSO. Journal of the Meteorological Society of Japan. Ser. II 79, 1–10. doi:10.2151/jmsj.79.1.

Kang, I.S., Kug, J.S., 2002. El Niño and La Niña sea surface temperature anomalies: Asymmetry characteristics associated with their wind stress anomalies. Journal of Geophysical Research: Atmospheres 107, ACL 1–1–ACL 1–10. doi:https://doi.org/10.1029/2001JD000393.

Kao, H.Y., Yu, J.Y., 2009. Contrasting Eastern-Pacific and Central-Pacific Types of ENSO. Journal of Climate 22, 615–632. doi:10.1175/2008JCLI2309.1.

Karamperidou, C., Stuecker, M.F., Timmermann, A., Yun, K.S., Lee, S.S., Jin, F.F., Santoso, A., McPhaden, M.J., Cai, W., 2020. ENSO in a Changing Climate: Challenges, Paleo-Perspectives, and Outlook, in: McPhaden, M.J., Santoso, A., Cai, W. (Eds.), Geophysical Monograph Series. first ed.. Wiley, pp. 471–484. doi:10.1002/9781119548164.ch21.

Kennan, S.C., Flament, P.J., 2000. Observations of a Tropical Instability Vortex. Journal Of Physical Oceanography 30, 25. doi:https://doi.org/10.1175/1520-0485(2000)030<2277:OOATIV>2.0.CO;2.

Kessler, W.S., 2002. Is ENSO a cycle or a series of events? Geophysical Research Letters 29, 40–1–40–4. doi:10.1029/2002GL015924.

Kessler, W.S., 2006. The circulation of the eastern tropical Pacific: A review. Progress in Oceanography 69, 181–217. doi:10.1016/j.pocean.2006.03.009.

Kessler, W.S., Rothstein, L.M., Chen, D., 1998. The Annual Cycle of SST in the Eastern Tropical Pacific, Diagnosed in an Ocean GCM*. Journal of Climate 11, 777–799. doi:10.1175/1520-0442(1998)011<0777:TACOSI>2.0.CO;2.

Kim, S.T., Cai, W., Jin, F.F., Yu, J.Y., 2014. ENSO stability in coupled climate models and its association with mean state. Climate dynamics 42, 3313–3321. doi:https://doi.org/10.1007/s00382-013-1833-6.

Kim, S.T., Jin, F.F., 2011. An ENSO stability analysis. part I: Results from a hybrid coupled model. Climate dynamics 36, 1593–1607. doi:https://doi.org/10.1007/s00382-010-0796-0.

Klein, S.A., Hartmann, D.L., 1993. The seasonal cycle of low stratiform clouds. Journal of Climate 6, 1587 – 1606. doi:10.1175/1520-0442(1993)006<1587:TSCOLS>2.0.CO;2.

Krumhardt, K.M., Lovenduski, N.S., Long, M.C., Luo, J.Y., Lindsay, K., Yeager, S., Harrison, C., 2020. Potential predictability of net primary production in the ocean. Global Biogeochemical Cycles 34, e2020GB006531. doi:https://doi.org/10.1029/2020GB006531.

Kug, J.S., Jin, F.F., An, S.I., 2009. Two types of El Niño events: Cold tongue El Niño and warm pool El Niño. Journal of Climate 22, 1499 – 1515. doi:10.1175/2008JCLI2624.1.

Kwon, Y.C., Hong, S.Y., 2017. A mass-flux cumulus parameterization scheme across gray-zone resolutions. Monthly Weather Review 145, 583 – 598. doi:10.1175/MWR-D-16-0034.1.

Large, W.G., McWilliams, J.C., Doney, S.C., 1994. Oceanic vertical mixing: A review and a model with a nonlocal boundary layer parameterization. Reviews of Geophysics 32, 363. doi:10.1029/94RG01872.

Lee, K.N., Jeon, C., Seung, Y., Shin, H.R., Son, S.K., Park, J.H., 2022. Observational Evidence of Generation and Propagation of Barotropic Rossby Waves Induced by Tropical Instability Waves in the Northeastern Pacific. Geophysical Research Letters 49. doi:10.1029/2022GL098327.

Lee, T., Lagerloef, G., Gierach, M.M., Kao, H.Y., Yueh, S., Dohan, K., 2012. Aquarius reveals salinity structure of Tropical Instability Waves. Geophysical Research Letters 39, n/a–n/a. doi:10.1029/2012GL052232.

Legeckis, R., 1977. Long Waves in the Eastern Equatorial Pacific Ocean: A View from a Geostationary Satellite. Science 197, 1179–1181. doi:10.1126/science.197.4309.1179.

Legeckis, R., Brown, C.W., Bonjean, F., Johnson, E.S., 2004. The influence of Tropical Instability Waves on phytoplankton blooms in the wake of the Marquesas Islands during 1998 and on the currents observed during the drift of the Kon-Tiki in 1947. Geophysical Research Letters 31. doi:10.1029/2004GL021637.

Levine, A., Jin, F.F., McPhaden, M.J., 2016. Extreme noise–extreme El Niño: How state-dependent noise forcing creates El Niño–La Niña asymmetry. Journal of Climate 29, 5483 – 5499. doi:10.1175/JCLI-D-16-0091.1.

Levine, A.F.Z., Jin, F.F., 2010. Noise-induced instability in the ENSO recharge oscillator. Journal of the Atmospheric Sciences 67, 529 – 542. doi:10.1175/2009JAS3213.1.

Li, G., Du, Y., Xu, H., Ren, B., 2015. An intermodel approach to identify the source of excessive equatorial Pacific cold tongue in cmip5 models and uncertainty in observational datasets. Journal of Climate 28, 7630 – 7640. doi:10.1175/JCLI-D-15-0168.1.

Lien, R.C., D'Asaro, E.A., Menkes, C.E., 2008. Modulation of equatorial turbulence by Tropical Instability Waves. Geophysical Research Letters 35, L24607. doi:10.1029/2008GL035860.

Liu, C., Fang, L., Köhl, A., Liu, Z., Smyth, W.D., Wang, F., 2019a. The Subsurface Mode Tropical Instability Waves in the Equatorial Pacific Ocean and Their Impacts on Shear and Mixing. Geophysical Research Letters 46, 12270–12278. doi:10.1029/2019GL085123.

Liu, C., Wang, X., Köhl, A., Wang, F., Liu, Z., 2019b. The Northeast-Southwest Oscillating Equatorial Mode of the Tropical Instability Wave and Its Impact on Equatorial Mixing. Geophysical Research Letters 46, 218–225. doi:10.1029/2018GL080226.

Liu, F., Zhang, W., Jin, F.F., Jiang, F., Boucharel, J., Hu, S., rev. New insight into multi-year La Niña dynamics from the perspective of a near-annual ocean process. Currently under review, submitted to *Journal of Climate*.

Luo, J.J., Masson, S., Roeckner, E., Madec, G., Yamagata, T., 2005. Reducing climatology bias in an ocean–atmosphere cgcm with improved coupling physics. Journal of Climate 18, 2344 – 2360. doi:10.1175/JCLI3404.1.

Lyman, J.M., Johnson, G.C., Kessler, W.S., 2007. Distinct 17- and 33-Day Tropical Instability Waves in Subsurface Observations*. Journal of Physical Oceanography 37, 855–872. doi:10.1175/JPO3023.1.

Maillard, L., Boucharel, J., Renault, L., 2022a. Direct and rectified effects of Tropical Instability Waves on the eastern tropical Pacific mean state in a regional ocean model. Journal of Physical Oceanography 52, 1817 – 1834. doi:10.1175/JPO-D-21-0300.1.

Maillard, L., Boucharel, J., Stuecker, M.F., Jin, F.F., Renault, L., 2022b. Modulation of the eastern equatorial pacific seasonal cycle by tropical instability waves. Geophysical Research Letters 49, e2022GL100991. doi:https://doi.org/10.1029/2022GL100991. e2022GL100991 2022GL100991.

Marzeion, B., Timmermann, A., Murtugudde, R., Jin, F.F., 2005. Biophysical feedbacks in the tropical Pacific. Journal of Climate 18, 58 – 70. doi:10.1175/JCLI3261.1.

Masina, S., Philander, S.G.H., Bush, A.B.G., 1999. An analysis of Tropical Instability Waves in a numerical model of the Pacific Ocean: 2. Generation and energetics of the waves. Journal of Geophysical Research: Oceans 104, 29637–29661. doi:10.1029/1999JC900226.

Menkes, C.E., Lengaigne, M., Vialard, J., Puy, M., Marchesiello, P., Cravatte, S., Cambon, G., 2014. About the role of Westerly Wind Events in the possible development of an El Niño in 2014. Geophysical Research Letters 41, 6476–6483. doi:10.1002/2014GL061186.

Menkes, C.E.R., Vialard, J.G., Kennan, S.C., Boulanger, J.P., Madec, G.V., 2006. A Modeling Study of the Impact of Tropical Instability Waves on the Heat Budget of the Eastern Equatorial Pacific. Journal of Physical Oceanography 36, 847–865. doi:10.1175/JPO2904.1.

Miller, L., Watts, D.R., Wimbush, M., 1985. Oscillations of Dynamic Topography in the Eastern Equatorial Pacific. Journal of Physical Oceanography 15, 1759–1770. doi:10.1175/1520-0485(1985)015<1759:OODTIT>2.0.CO;2.

Mitchell, T.P., Wallace, J.M., 1992. The Annual Cycle in Equatorial Convection and Sea Surface Temperature. Journal of Climate 5, 1140–1156. doi:10.1175/1520-0442(1992)005<1140:TACIEC>2.0.CO;2.

Moore, A.M., Kleeman, R., 1999. Stochastic forcing of ENSO by the intraseasonal oscillation. Journal of Climate 12, 1199 – 1220. doi:10.1175/1520-0442(1999)012<1199:SFOEBT>2.0.CO;2.

Moum, J.N., Lien, R.C., Perlin, A., Nash, J.D., Gregg, M.C., Wiles, P.J., 2009. Sea surface cooling at the Equator by subsurface mixing in Tropical Instability Waves. Nature Geoscience 2, 761–765. doi:10.1038/ngeo657.

Moum, J.N., Perlin, A., Nash, J.D., McPhaden, M.J., 2013. Seasonal sea surface cooling in the equatorial Pacific cold tongue controlled by ocean mixing. Nature 500, 64–67. doi:10.1038/nature12363.

Okumura, Y.M., 2019. ENSO Diversity from an Atmospheric Perspective. Current Climate Change Reports 5, 245–257. doi:10.1007/s40641-019-00138-7.

Olivier, L., Reverdin, G., Hasson, A., Boutin, J., 2020. Tropical Instability Waves in the Atlantic Ocean: Investigating the Relative Role of Sea Surface Salinity and Temperature From 2010 to 2018. Journal of Geophysical Research: Oceans 125. doi:10.1029/2020JC016641.

O'Neill, L.W., Chelton, D.B., Esbensen, S.K., 2012. Covariability of surface wind and stress responses to sea surface temperature fronts. Journal of Climate 25, 5916 – 5942. doi:10.1175/JCLI-D-11-00230.1.

Paek, H., Yu, J.Y., Qian, C., 2017. Why were the 2015/2016 and 1997/1998 extreme El Niños different?: Contrasting 1997/1998 and 2015/2016 El Niños. Geophysical Research Letters doi:10.1002/2016GL071515.

Paulmier, A., Ruiz-Pino, D., 2009. Oxygen minimum zones (omzs) in the modern ocean. Progress in Oceanography 80, 113–128. doi:https://doi.org/10.1016/j.pocean.2008.08.001.

Périgaud, C., 1990. Sea level oscillations observed with Geosat along the two shear fronts of the Pacific North Equatorial Countercurrent. Journal of Geophysical Research 95, 7239. doi:10.1029/JC095iC05p07239.

Pezzi, L.P., 2004. Influence of ocean-atmosphere coupling on the properties of Tropical Instability Waves. Geophysical Research Letters 31, L16306. doi:10.1029/2004GL019995.

Philander, S., Hurlin, W., Seigel, A., 1987. Simulation of the seasonal cycle of the tropical Pacific ocean. Journal of Physical Oceanography 17, 1986–2002. doi:https://doi.org/10.1175/1520-0485(1987)017<1986:SOTSCO>2.0.CO;2.

Philander, S.G., 1990. El Niño, La Niña, and the southern oscillation. Number 46 in International geophysics series, Academic Press, San Diego. .

Pörtner, H.O., Roberts, D.C., Adams, H., Adler, C., Aldunce, P., Ali, E., Begum, R.A., Betts, R., Kerr, R.B., Biesbroek, R., et al., 2022. Climate Change 2022: Impacts, Adaptation and Vulnerability. Contribution of Working Group II to the Sixth Assessment Report of the Intergovernmental Panel on Climate Change. Cambridge University Press, Cambridge, United Kingdom and New York, NY, USA. p. 3068.

Qiao, L., Weisberg, R.H., 1995. Tropical instability wave kinematics: Observations from the Tropical Instability Wave Experiment. Journal of Geophysical Research 100, 8677. doi:10.1029/95JC00305.

Qiao, L., Weisberg, R.H., 1998. Tropical Instability Wave Energetics: Observations from the Tropical Instability Wave Experiment. Journal Of Physical Oceanography 28, 16. doi:https://doi.org/10.1175/1520-0485(1998)028<0345:TIWEOF>2.0.CO;2.

Rayner, N.A., 2003. Global analyses of sea surface temperature, sea ice, and night marine air temperature since the late nineteenth century. Journal of Geophysical Research 108, 4407. doi:10.1029/2002JD002670.

Renault, L., 2008. Impact des jets cotiers atmospheriques sur l'upwelling du système de courants de Humboldt. Ph.D. thesis. Université de Toulouse, Université Toulouse III - Paul Sabatier.

Renault, L., Masson, S., Oerder, V., Jullien, S., Colas, F., 2019a. Disentangling the Mesoscale Ocean-Atmosphere Interactions. Journal of Geophysical Research: Oceans 124, 2164–2178. doi:10.1029/2018JC014628.

Renault, L., Masson, S., Oerder, V., Jullien, S., Colas, F., 2019b. Disentangling the mesoscale ocean-atmosphere interactions. Journal of Geophysical Research: Oceans 124, 2164–2178. doi:https://doi.org/10.1029/2018JC014628.

Renault, L., Molemaker, M.J., Gula, J., Masson, S., McWilliams, J.C., 2016a. Control and stabilization of the gulf stream by oceanic current interaction with the atmosphere. Journal of Physical Oceanography 46, 3439 – 3453. doi:10.1175/JPO-D-16-0115.1.

Renault, L., Molemaker, M.J., Mcwilliams, J.C., Shchepetkin, A.F., Lemari, F., Chelton, D., Illig, S., Hall, A., 2016b. Modulation of Wind Work by Oceanic Current Interaction with the Atmosphere. Journal Of Physical Oceanography 46, 20. doi:https://doi.org/10.1175/JPO-D-15-0232.1.

Roberts, M.J., Banks, H., Gedney, N., Gregory, J., Hill, R., Mullerworth, S., Pardaens, A., Rickard, G., Thorpe, R., Wood, R., 2004. Impact of an Eddy-Permitting Ocean Resolution on Control and Climate Change Simulations with a Global Coupled GCM. Journal Of Climate 17, 18. doi:https://doi.org/10.1175/1520-0442(2004)017<0003:IOAEOR>2.0.CO;2.

Roberts, M.J., Clayton, A., Demory, M.E., Donners, J., Vidale, P.L., Norton, W., Shaffrey, L., Stevens, D.P., Stevens, I., Wood, R.A., Slingo, J., 2009. Impact of Resolution on the Tropical Pacific Circulation in a Matrix of Coupled Models. Journal of Climate 22, 2541–2556. doi:10.1175/2008JCLI2537.1.

Saha, S., Moorthi, S., Pan, H.L., Wu, X., Wang, J., Nadiga, S., Tripp, P., Kistler, R., Woollen, J., Behringer, D., Liu, H., Stokes, D., Grumbine, R., Gayno, G., Wang, J., Hou, Y.T., Chuang, H.Y., Juang, H.M.H., Sela, J., Iredell, M., Treadon, R., Kleist, D., Delst, P.V., Keyser, D., Derber, J., Ek, M., Meng, J., Wei, H., Yang, R., Lord, S., van den Dool, H., Kumar, A., Wang, W., Long, C., Chelliah, M., Xue, Y., Huang, B., Schemm, J.K., Ebisuzaki, W., Lin, R., Xie, P., Chen, M., Zhou, S., Higgins, W., Zou, C.Z., Liu, Q., Chen, Y., Han, Y., Cucurull, L., Reynolds, R.W., Rutledge, G., Goldberg, M., 2010. NCEP climate forecast system reanalysis (CFSR) selected hourly time-series products, january 1979 to december 2010.

Saha, S., Moorthi, S., Wu, X., Wang, J., Nadiga, S., Tripp, P., Behringer, D., Hou, Y.T., ya Chuang, H., Iredell, M., Ek, M., Meng, J., Yang, R., Mendez, M.P., van den Dool, H.,

Zhang, Q., Wang, W., Chen, M., Becker, E., 2011. NCEP climate forecast system version 2 (CFSv2) selected hourly time-series products.

Sakamoto, T.T., Komuro, Y., Nishimura, T., Ishii, M., Tatebe, H., Shiogama, H., Hasegawa, A., Toyoda, T., Mori, M., Suzuki, T., Imada, Y., Nozawa, T., Takata, K., Mochizuki, T., Ogochi, K., Emori, S., Hasumi, H., Kimoto, M., 2012. MIROC4h—A New High-Resolution Atmosphere-Ocean Coupled General. Journal of the Meteorological Society of Japan 90, 35. doi:https://doi.org/10.2151/jmsj.2012-301.

Seo, H., Jochum, M., Murtugudde, R., Miller, A.J., Roads, J.O., 2007a. Feedback of Tropical Instability-Wave-Induced Atmospheric Variability onto the Ocean. Journal of Climate 20, 5842–5855. doi:10.1175/JCLI4330.1.

Seo, H., Jochum, M., Murtugudde, R., Miller, A.J., Roads, J.O., 2007b. Feedback of tropical instability-wave-induced atmospheric variability onto the ocean. Journal of Climate 20, 5842 – 5855. doi:10.1175/JCLI4330.1.

Seo, H., Miller, A.J., Roads, J.O., 2007c. The Scripps Coupled Ocean–Atmosphere Regional (SCOAR) Model, with Applications in the Eastern Pacific Sector. Journal of Climate 20, 381–402. doi:10.1175/JCLI4016.1.

Shchepetkin, A.F., 2015. An adaptive, Courant-number-dependent implicit scheme for vertical advection in oceanic modeling. Ocean Modelling 91, 38–69. doi:10.1016/j.ocemod.2015.03.006.

Shchepetkin, A.F., McWilliams, J.C., 2005. The regional oceanic modeling system (ROMS): A split-explicit, free-surface, topography-following-coordinate oceanic model. Ocean Modelling , 58doi:https://doi.org/10.1016/j.ocemod.2004.08.002.

Shchepetkin, A.F., McWilliams, J.C., 2009. Correction and commentary for "Ocean forecasting in terrain-following coordinates: Formulation and skill assessment of the regional ocean modeling system" by Haidvogel et al., J. Comp. Phys. 227, pp. 3595–3624. Journal of Computational Physics 228, 8985–9000. doi:10.1016/j.jcp.2009.09.002.

Shi, W., Wang, M., 2021. Tropical instability wave modulation of chlorophyll-a in the Equatorial Pacific. Scientific Reports 11, 22517. doi:10.1038/s41598-021-01880-5.

Skamarock, W., Klemp, J., Dudhia, J., Gill, D., Barker, D., 2008. A description of the Advanced Research WRF version 3. Technical Report. NCAR. doi:10.5065/D68S4MVH.

Skamarock, W.C., Klemp, J.B., Dudhia, J., Gill, D.O., Liu, Z., Berner, J., Wang, W., Powers, J.G., Duda, M.G., Barker, D.M., et al., 2019. A description of the advanced research WRF model version 4. National Center for Atmospheric Research: Boulder, CO, USA 145, 145.

Small, R., deSzoeke, S., Xie, S., O'Neill, L., Seo, H., Song, Q., Cornillon, P., Spall, M., Minobe, S., 2008. Air–sea interaction over ocean fronts and eddies. Dynamics of Atmospheres and Oceans 45, 274–319. doi:https://doi.org/10.1016/j.dynatmoce.2008.01.001.

Small, R.J., Richards, K.J., Xie, S.P., Dutrieux, P., Miyama, T., 2009. Damping of Tropical Instability Waves caused by the action of surface currents on stress. Journal of Geophysical Research 114, C04009. doi:10.1029/2008JC005147.

Smyth, W.D., Moum, J.N., 2013. Marginal instability and deep cycle turbulence in the eastern equatorial Pacific Ocean. Geophysical Research Letters 40, 6181–6185. doi:10.1002/2013GL058403.

Song, H., Edwards, C.A., Moore, A.M., Fiechter, J., 2016. Data assimilation in a coupled physical–biogeochemical model of the california current system using an incremental lognormal 4-dimensional variational approach: Part 1—model formulation and biological data assimilation twin experiments. Ocean Modelling 106, 131–145. doi:https://doi.org/10.1016/j.ocemod.2016.04.001.

Specht, M.S., Jungclaus, J., Bader, J., 2021. Identifying and Characterizing Subsurface Tropical Instability Waves in the Atlantic Ocean in Simulations and Observations. Journal of Geophysical Research: Oceans 126. doi:10.1029/2020JC017013.

Strutton, P.G., Ryan, J.P., Chavez, F.P., 2001. Enhanced chlorophyll associated with Tropical Instability Waves in the equatorial Pacific. Geophysical Research Letters 28, 2005–2008. doi:10.1029/2000GL012166.

Stuecker, M.F., Jin, F.F., Timmermann, A., 2015. El Niño-southern oscillation frequency cascade. Proceedings of the National Academy of Sciences 112, 13490–13495. doi:10.1073/pnas.1508622112.

Stuecker, M.F., Timmermann, A., Jin, F.F., Chikamoto, Y., Zhang, W., Wittenberg, A.T., Widiasih, E., Zhao, S., 2017. Revisiting ENSO/indian ocean dipole phase relationships. Geophysical Research Letters 44, 2481–2492. doi:https://doi.org/10.1002/2016GL072308.

Stuecker, M.F., Timmermann, A., Jin, F.F., McGregor, S., Ren, H.L., 2013. A combination mode of the annual cycle and the El Niño/Southern Oscillation. Nature Geoscience 6, 540–544.

Suarez, M.J., Schopf, P.S., 1988. A delayed action oscillator for ENSO. Journal of Atmospheric Sciences 45, 3283 – 3287. doi:10.1175/1520-0469(1988)045<3283:ADAOFE>2.0.CO;2.

Sun, Z., Small, J., Bryan, F., heng Tseng, Y., Liu, H., Lin, P., 2021. The impact of wind corrections and ocean-current influence on wind stress forcing on the modeling of Pacific north equatorial countercurrent. Ocean Modelling 166, 101876. doi:https://doi.org/10.1016/j.ocemod.2021.101876.

Tanaka, Y., Hibiya, T., Sasaki, H., 2015. Downward lee wave radiation from Tropical Instability Waves in the central equatorial P acific O cean: A possible energy pathway to turbulent mixing. Journal of Geophysical Research: Oceans 120, 7137–7149. doi:10.1002/2015JC011017.

Thomas, L.N., Tandon, A., Mahadevan, A., 2008. Submesoscale processes and dynamics, in: Hecht, M.W., Hasumi, H. (Eds.), Geophysical Monograph Series. American Geophysical Union, Washington, D. C.. volume 177, pp. 17–38. doi:10.1029/177GM04.

Thum, N., Esbensen, S.K., Chelton, D.B., Mcphaden, M.J., 2002. Air–Sea Heat Exchange along the Northern Sea Surface Temperature Front in the Eastern Tropical Pacific. Journal Of Climate 15, 18. doi:https://doi.org/10.1175/1520-0442(2002)015<3361:ASHEAT>2.0.CO;2.

Tian, F., Zhang, R.H., Wang, X., 2018. A Coupled Ocean Physics-Biology Modeling Study on Tropical Instability Wave-Induced Chlorophyll Impacts in the Pacific. Journal of Geophysical Research: Oceans 123, 5160–5179. doi:10.1029/2018JC013992.

Tian, F., Zhang, R.H., Wang, X., 2019. A Positive Feedback Onto ENSO Due to Tropical Instability Wave (TIW)-Induced Chlorophyll Effects in the Pacific. Geophysical Research Letters 46, 889–897. doi:10.1029/2018GL081275.

Timmermann, A., An, S.I., Kug, J.S., Jin, F.F., Cai, W., Capotondi, A., Cobb, K.M., Lengaigne, M., McPhaden, M.J., Stuecker, M.F., et al., 2018. El Niño–Southern Oscillation complexity. Nature 559, 535–545. doi:10.1038/s41586-018-0252-6.

Tuchen, F.P., Brandt, P., Claus, M., Hummels, R., 2018. Deep Intraseasonal Variability in the Central Equatorial Atlantic. Journal Of Physical Oceanography 48, 15. doi:https://doi.org/10.1175/JPO-D-18-0059.1.

Tziperman, E., Stone, L., Cane, M.A., Jarosh, H., 1994. El Niño Chaos: Overlapping of Resonances Between the Seasonal Cycle and the Pacific Ocean-Atmosphere Oscillator. Science 264, 3. doi:DOI:10.1126/science.264.5155.72.

Vialard, J., Delecluse, P., Menkes, C., 2002. A modeling study of salinity variability and its effects in the tropical Pacific Ocean during the 1993-1999 period. Journal of Geophysical Research: Oceans 107, SRF 6–1–SRF 6–14. doi:10.1029/2000JC000758.

Vialard, J.R.M., Menkes, C., Boulanger, J.P., Delecluse, P., Guilyardi, E., Mcphaden, M.J., Madec, G., 2001. A Model Study of Oceanic Mechanisms Affecting Equatorial Pacific Sea Surface Temperature during the 1997–98 El Niño. Journal Of Physical Oceanography 31, 27. doi:https://doi.org/10.1175/1520-0485(2001)031<1649:AMSOOM>2.0.CO;2.

Wang, M., Xie, S.P., Shen, S.S.P., Du, Y., 2020. Rossby and Yanai Modes of Tropical Instability Waves in the Equatorial Pacific Ocean and a Diagnostic Model for Surface Currents. Journal of Physical Oceanography 50, 3009–3024. doi:10.1175/JPO-D-20-0063.1.

Wang, W., Mcphaden, M.J., 2000. The Surface-Layer Heat Balance in the Equatorial Pacific Ocean. Part II: Interannual Variability. Journal Of Physical Oceanography 30, 20. doi:https://doi.org/10.1175/1520-0485(2001)031<2989:TSLHBI>2.0.CO;2.

Wang, W., McPhaden, M.J., 2000. The surface-layer heat balance in the equatorial Pacific ocean. part ii: Interannual variability. Journal of Physical Oceanography 30, 2989 – 3008. doi:10.1175/1520-0485(2001)031<2989:TSLHBI>2.0.CO;2.

Wang, W., McPhaden, M.J., 2001. Surface Layer Temperature Balance in the Equatorial Pacific during the 1997–98 El Niño and 1998–99 La Niña. Journal of Climate 14, 3393–3407. doi:10.1175/1520-0442(2001)014<3393:SLTBIT>2.0.CO;2.

Willett, C.S., Leben, R.R., Lavín, M.F., 2006. Eddies and Tropical Instability Waves in the eastern tropical Pacific: A review. Progress in Oceanography 69, 218–238. doi:10.1016/j.pocean.2006.03.010.

Wu, Q., Bowman, K.P., 2007. Interannual variations of Tropical Instability Waves observed by the tropical rainfall measuring mission. Geophysical Research Letters 34. doi:https://doi.org/10.1029/2007GL029719.

Wu, X., Okumura, Y.M., DiNezio, P.N., 2019. What controls the duration of El Niño and La Niña events? Journal of Climate 32, 5941 – 5965. doi:10.1175/JCLI-D-18-0681.1.

Wyrtki, K., 1965. Surface currents of the eastern tropical Pacific ocean. Fishery Bulletin 63, 355–372.

Xie, S.P., Ishiwatari, M., Hashizume, H., Takeuchi, K., 1998. Coupled ocean-atmospheric waves on the equatorial front. Geophysical Research Letters 25, 3863–3866. doi:10.1029/1998GL900014.

Xue, A., Jin, F.F., Zhang, W., Boucharel, J., sub. Quantifying the nonlinear feedback on enso from tropical instability waves (tiws) by nonlinear eddy thermal diffusivity. Submitted to *Climate Dynamics*.

Xue, A., Jin, F.F., Zhang, W., Boucharel, J., Zhao, S., Yuan, X., 2020. Delineating the Seasonally Modulated Nonlinear Feedback Onto ENSO From Tropical Instability Waves. Geophysical Research Letters 47. doi:10.1029/2019GL085863.

Xue, A., Zhang, W., Boucharel, J., Jin, F.F., 2021a. Anomalous tropical instability wave activity hindered the development of the 2016/17 La Niña. Journal of Climate 34, 5583 – 5600. doi:10.1175/JCLI-D-20-0399.1.

Xue, A., Zhang, W., Boucharel, J., Jin, F.F., 2021b. Anomalous Tropical Instability Wave activity hindered the development of the 2016/2017 La Niña. Journal of Climate , 1doi:10.1175/JCLI-D-20-0399.1.

Yang, L., Murtugudde, R., Zheng, S., Liang, P., Tan, W., Wang, L., Feng, B., Zhang, T., 2022. Seasonal variability of the Pacific south equatorial current during the argo era. Journal of Physical Oceanography doi:10.1175/JPO-D-21-0311.1.

Yoder, J.A., Ackleson, S.G., Barber, R.T., Flament, P., Balch, W.M., 1994. A line in the sea. Nature 371, 689–692. doi:10.1038/371689a0.

Yu, J.Y., Liu, W.T., 2003. A linear relationship between ENSO intensity and tropical instability wave activity in the eastern Pacific Ocean. Geophysical Research Letters 30. doi:10.1029/2003GL017176.

Yu, X., McPhaden, M.J., 1999. Seasonal Variability in the Equatorial Pacific. Journal of Physical Oceanography 29, 925–947. doi:10.1175/1520-0485(1999)029<0925:SVITEP>2.0.CO;2.

Zebiak, S.E., Cane, M.A., 1987. A model El Niño – Southern Oscillation. Monthly Weather Review 115, 2262–2278. doi:https://doi.org/10.1175/1520-0493(1987)115<2262:AMENO>2.0.CO;2.

Zhang, R.H., 2014. Effects of tropical instability wave (TIW)-induced surface wind feedback in the tropical Pacific ocean. Climate Dynamics 42, 467–485. doi:https://doi.org/10.1007/s00382-013-1878-6.

Zhang, R.H., Busalacchi, A.J., 2008. Rectified effects of tropical instability wave (TIW)-induced atmospheric wind feedback in the tropical Pacific. Geophysical Research Letters 35. doi:https://doi.org/10.1029/2007GL033028.

Zheng, G., Li, X., Zhang, R.H., Liu, B., 2020. Purely satellite data–driven deep learning forecast of complicated Tropical Instability Waves. Science Advances 6, eaba1482. doi:10.1126/sciadv.aba1482.

Zheng, Y., Alapaty, K., Herwehe, J.A., Genio, A.D.D., Niyogi, D., 2016. Improving high-resolution weather forecasts using the weather research and forecasting (WRF) model with an updated kain–fritsch scheme. Monthly Weather Review 144, 833 – 860. doi:10.1175/MWR-D-15-0005.1.

Zhu, J., Kumar, A., 2018. Influence of surface nudging on climatological mean and ENSO feedbacks in a coupled model. Climate Dynamics 50, 571–586. doi:10.1007/s00382-017-3627-8.